CRANFIELD UNIVERSITY

JAMES ELGY

Bistatic SAR for Building Wall Material Characterisation

Centre for Electronic Warfare, Information, and Cyber
PhD

PhD
Academic Year: 2019 - 2020

Supervisor: Dr Daniel Andre
July 2020

CRANFIELD UNIVERSITY

Centre for Electronic Warfare, Information, and Cyber
PhD

PhD

Academic Year 2019 - 2020

JAMES ELGY

Bistatic SAR for Building Wall Material Characterisation

Supervisor: Dr Daniel Andre
July 2020

ABSTRACT

This thesis addresses the problem of using radar to extract interpretable information concerning both the structure and electrical properties of a wall, and the environment behind it. This is broken down into two subproblems: how to determine the thickness and electromagnetic properties of the wall without being in direct contact with it, and how to obtain the most accurate images of what lies beyond the wall.

Existing research in the area is evaluated and a theoretical study is presented on the use of monostatic, bistatic, and multistatic Synthetic Aperture Radar (SAR) in both one and two dimensional apertures. New methods of determining the wall properties are evaluated by both computer simulation and with laboratory radar measurements, where a wall of concrete blocks is constructed. The robustness of the asymmetric SAR geometry approach is evaluated with the addition of complex objects placed behind the wall. The uncertainty associated with estimating the wall properties is evaluated and consequential improvements to image quality are discussed.

It was found that an asymmetric bistatic SAR geometry accurately extracts the refractive index and thickness of a wall. The method is applicable to both cluttered environments and non-parallel wall trajectories without loss of accuracy. Applying a compensation for refraction in the SAR imagery results in better positional accuracy but does not necessarily result in better image focusing. Volumetric multistatic image formation benefits from applied refraction compensation. SAR image formation, and in particular volumetric image formation, can be significantly accelerated via a spatially variant basebanding technique followed by zero padding. Spatially variant basebanding is sub-optimal when applied to a Through-Wall radar scenario where there is a visible wall signature in the image.

Keywords:

Through-Wall radar, Multistatic radar, Multidimensional signal processing, Electromagnetic propagation, Radar imaging

ACKNOWLEDGEMENTS

Firstly, I would like to acknowledge and thank my parents. Without their continual support and input, all of this would not have been possible. Secondly, I must recognise the input and support my supervisor has given me. Dan has been both encouraging and the source of many great technical discussions, most of which have contributed in some form to this thesis. Finally, I extend a formal thank you to Dstl for sponsoring the project and to Cemex UK for the donation of the concrete blocks used throughout the project.

TABLE OF CONTENTS

LIST OF FIGURES

LIST OF TABLES

LIST OF ABBREVIATIONS

EM	Electromagnetic
SAR	Synthetic Aperture Radar
VNA	Vector Network Analyser
GBSAR	Ground Based Synthetic Aperture Radar
PFA	Polar Format Algorithm
TWR	Through-Wall Radar
CCD	Coherent Change Detection
SNR	Signal to Noise Ratio
RCS	Radar Cross Section
NRW	Nicolson-Ross-Weir
InSAR	Interferometric SAR
DEM	Digital Elevation Model
GPR	Ground Penetrating Radar
MIMO	Multiple Input Multiple Output
MUSIC	Multiple Signal Classification
ESPRIT	Estimation of Signal Parameters via Rotational Invariance Technique
CMP	Common Midpoint Processing
PSF	Point Spread Function
MSE	Mean Squared Error
WMSE	Weighted Mean Squared Error

LIST OF SYMBOLS

In addition to the list below, this thesis follows the convention that i is used to represent the imaginary unit such that $i^2 = -1$.

n	Refractive Index
ε	Material permittivity
μ	Material permeability
σ	Material conductivity
ε'	The real component of the material permittivity
ε''	The imaginary component of the material permittivity
B	Radar signal bandwidth
λ	The wavelength of the electromagnetic wave
λ_c	Waveguide cut-off wavelength
Γ	Reflection coefficient
$\boldsymbol{E}$	Electric field vector, $\boldsymbol{E} = [E_x, E_y, E_z]$
$\boldsymbol{H}$	Magnetic field vector, $\boldsymbol{H} = [H_x, H_y, H_z]$
$\boldsymbol{D}$	Electric flux density, $\boldsymbol{D} = \varepsilon\boldsymbol{E}$
$\boldsymbol{B}$	Magnetic flux density, $\boldsymbol{B} = \mu\boldsymbol{H}$
α	Attenuation constant for the material
v	Electromagnetic propagation speed in a material
c	Speed of light in a vacuum
f_c	Radar centre frequency
L_{syn}	Synthetic aperture length
$\Delta\theta$	Angular variation due to the SAR system
W	Radiator size
R_{res}	System range resolution
CR_{res}	System cross-range resolution
Z	Characteristic impedance of the material
ε_r	Relative permittivity between two media
μ_r	Relative permeability between two media

u	Harmonic mode of propagation in a dielectric waveguide
F_{c_u}	Cut-off frequency at mode u
S_{11}	The scattering coefficient relating the radiation emitted from port 1 and received by port 1
S_{21}	The scattering coefficient relating the radiation emitted from port 1 and received by port 2
γ	Propagation constant
$\Delta R_{trihedral}$	Down range shift due to the presence of a wall
δ	Wall thickness
θ_i	Horizontal incidence angle
ϑ_i	Vertical incidence angle
θ_t	Transmission angle
$\boldsymbol{T}$	Vector coordinate for the transmitting antenna
$\boldsymbol{R}$	Vector coordinate for the receiving antenna
$\boldsymbol{V}$	Bistatic baseline vector
D	Standoff distance from transmitter to wall
$\boldsymbol{r}$	Ray component in Cartesian coordinates
n	Refractive Index
θ_r	Horizontal angle of refraction
ϑ_r	Vertical angle of refraction
θ_B	Bistatic angle
p	Discrete number of pulses used in a SAR collection
m	Discrete number of frequency samples used per pulse
$\mathcal{P}$	Complex phase history represented as an $m \times p$ array
ρ	Range profile intensity
f	Frequency of the SAR collection
w	Percentage water content of the material
β	Phase term
ω	Angular Frequency
R_{Front}	Bistatic range to the front face of the wall, given specular reflection

R_{Back}	Bistatic range to the back face of the wall, given specular reflection
ΔR	Range separation between front and back faces
$\boldsymbol{P}$	Vector coordinate for a pixel in a SAR image.
h_{guide}	Half width of the dielectric waveguide used to calculate modal cut-off frequencies
Δh	RMS error in depth due to a rough material surface
$D_{fraunhofer}$	Fraunhofer distance to distinguish between near and far field.
R_s	Power reflection coefficient for S polarisation
R_p	Power reflection coefficient for P polarisation
P_r	Received power
P_t	Transmitted power
L	Dielectric loss per unit length
T	Transmission coefficient $T = 1 - R_s = 1 - R_p$
F_{xyz}	Three-dimensional unambiguous spatial-frequency extent
$\boldsymbol{B}_{\boldsymbol{vec}}$	Bistatic vector used for basebanding

LIST OF PUBLICATIONS

Published

Elgy J., Andre D., Morrow IL., Finnis M. Remote asymmetric determination bistatic radar of building geometries material characteristics using asymmetric bistatic radar geometries. Proceedings of the European Conference on Synthetic Aperture Radar, EUSAR. 2018.

Elgy J., Andre D., Finnis M., Blacknell D. Data Driven Corrections to Multistatic 3D Through-Wall Radar Imagery. Proceedings of the Institute of Acoustics. Lerici, Italy; 2018. pp. 199–208.

Elgy J., Andre D. GBSAR-Proc. 2019. Available at: DOI:10.17862/cranfield.rd.9693581.v2 (Accessed: 25 November 2019)

Elgy J., Andre D., Finnis M. Volumetric SAR near-field upsampling and basebanding. Electronic Letters. 2020; 56(12): 622–624.

In Review

Elgy, J, Andre D, Finnis M, Extraction of Wall Material Properties in Cluttered Environments via Bistatic SAR, IET Radar Sonar and Navigation, 2019, To Be Published.

1 Introduction

Since its inception in the late 19th century, the underlying principle and core functionality of radar, *RA*dio *D*etection *A*nd *R*anging, has remained broadly unchanged. Using low frequency electromagnetic (EM) radiation, a time of flight estimation is made to and from any points of reflection in the surveyed area. Naturally, using the speed of light, this can be converted into a distance from the radar to the object. By combining the time of flight estimation with a non-uniform EM radiation pattern, the spatial position of each object in the surveyed area can be established.

The developments in radar technology have been largely driven by two competing desires: lower cost and finer measurement precision. Improving the precision of the distance measurements is generally straightforward, by simply increasing the transmitted signal bandwidth. Measuring the directionality of the objects, on the other hand, is significantly more problematic. To achieve finer measurement precision (dubbed 'resolution') perpendicular to the direction of the EM pulse, the antenna beamwidth must be reduced. In general, beamwidth is inversely proportional to the antenna size, thus to half the beamwidth, and achieve finer resolution, the antenna aperture must be doubled. For obvious reasons, a larger pair of antennas very quickly becomes both impractical and expensive.

The concept of 'Synthetic Aperture Radar' (SAR) exists as a means to overcome the beamwidth limitation of a single antenna. In essence it works as a form of data fusion, similar in concept to a phased array, whereby measurements from multiple different antenna positions are used in conjunction in order to emulate a single physically larger antenna. This circumvents some of the practical limitations with a large antenna, reduces cost, and provides a much greater flexibility with regards to the radar platform. For example, the original SAR patent featured a radar system mounted to the back of an aircraft [1].

Since their inception SARs have seen widespread use in both civilian and military sectors. Examples include crop monitoring, archaeological surveying, and, of course, surveillance. This last example is of continual interest and innovation, as both infrastructure and people's behavioural patterns change.

As the nature of warfare becomes more and more urbanised, and radar platforms become ever smaller, there has been a push towards so called urban radar. As the name suggests, urban radar is primarily concerned with monitoring and surveillance within built up areas. Such a capability would be of great interest to law enforcement, search and rescue, and indeed military operations. Within the field that is urban radar exists a sub-field dedicated to extracting useful information about activity inside buildings. ‘Through-Wall Radar’, or less commonly ‘Through-the-Wall Radar’, has seen much interest.

1.1 Problem Statement and Aims

Through-Wall radar (TWR) is a form of remote sensing dedicated to extracting useful information concerning any and all activity inside enclosed structures. There are, however, major concerns with TWR that stop any widespread adoption of the technology:

- In an urban environment, it is often difficult to perform a large-scale SAR collection due to both spatial and temporal limitations on the collection. That is, urban environments are often cramped, and time runs at a premium.
- Due to both additional reflections, and additional electromagnetic effects, to effectively obtain imagery behind a wall, the radar system needs a large transmitting power. A high-powered radar system, while not implausible, is both costly and heavy.
- Electromagnetic refraction causes all targets behind a wall to appear in incorrect locations in the imagery, unless the refraction is explicitly compensated for in the SAR postprocessing. This positional shift changes as a function of angle, therefore it is not a linear shift. In SAR imagery, this presents as defocusing in addition to a positional shift.
- In general, walls produce comparatively strong reflections compared to other targets. This can make differentiating between target signatures and unwanted wall signatures difficult.

As will be discussed, there are of course solutions to these issues. However, they almost always require prior knowledge of the wall structure and composition to be effective. Specifically, the thickness and refractive index of the material must be known either independently in advance or obtained in situ. Unfortunately, these two parameters are often intertwined and represent an effective electrical length, thus making it difficult to obtain each parameter separately. This is, ultimately, the crux of Through-Wall radar, and is indeed the problem this thesis investigates:

How does one safely and accurately determine the properties of an unknown, and in many cases unapproachable, wall whilst simultaneously obtaining usable SAR data?

The work presented within this thesis aims to both answer this question and extend the potential sophistication of the SAR measurements. More specifically, the aims are to:

1. Establish a generalised method for remotely extracting the refractive index and thickness from a single layered wall. This should be achieved whist simultaneously obtaining usable SAR data in both two-dimensional and three-dimensional measurements.
2. Evaluate the ability of the developed method to cope with the presence of clutter and other potential sources of error.
3. Create and evaluate a method for compensating for the wall effects in any subsequent imagery. Ideally, this method should work for any wall properties and SAR collection geometry.

1.2 Statement of Novelty

Contained within this body of work are 4 distinct and novel contributions to knowledge. These are, in no particular order:

- An asymmetric bistatic method for remotely extracting both the refractive index and thickness of a wall. Unlike previous works, this has been tested in the presence of heavy clutter, showing that clutter has little impact on the extraction accuracy.
- A generalisation to three dimensional measurements is also undertaken, allowing for both volumetric image formation, and extraction of the wall properties from a single bistatic measurement.
- A volumetric method for correcting TWR SAR images through an arbitrary number of layers. This is illustrated with monostatic, bistatic, and multistatic imagery. In addition, the quality of the resultant images is assessed numerically, showing that the corrected images are better focused than non-corrected images.

However, it is also shown that this does not necessarily correspond to the greatest possible focusing.

- A rapid image upsampling method designed to reduce the computational burden with regards to forming highly sampled SAR imagery. As before, this is illustrated using volumetric images. The main contribution to knowledge is the addition and demonstration of a spatially variant baseband designed to centre the image spatial frequency support and thus achieving more accurate upsampled imagery.

1.3 Thesis Structure and Content

The remainder of this thesis is outlined as follows: Chapter 2 provides an overview of the core principles of Synthetic Aperture Radar as it pertains to a Through-Wall scenario. This covers the working principle of SAR, differentiations between the different types of measurement geometry, a discussion on near-field image formation and the problems associated with it. The chapter also provides an overview of the problems associated with TWR. A more in-depth discussion is held at the beginning of Chapters 4, 5 and 6.

Chapter 3 covers non-radar based methods for extracting the refractive index from samples of material. This is a necessity in order to validate the measurements done in later chapters. Specifically, the chapter evaluates the permittivity and conductivity of a sample of concrete in three different ways: an analysis of the material cut-off frequencies, the well documented Nicholson-Ross-Weir method, and finally via the use of a trihedral reference target. All three approaches are experimentally tested and assigned appropriate uncertainty ranges. It is shown within the chapter that although all three methods are in agreement with each other with respect to the refractive index, the conductivity of the material is not in complete agreement. As will be discussed, this is due primarily to the material sample size.

Chapter 4 introduces a bistatic method by which the thickness and refractive index of a wall can be remotely extracted. This method takes an asymmetric geometric approach to solving for each parameter. Consequently, a recursive mathematical algorithm for obtaining the necessary angles is also introduced, as is a method for obtaining an estimate of the measurement geometry directly from the measured data. Within the chapter, the sensitivity of the method is investigated by means of simulations. This is in order to assign an uncertainty to the extracted parameters. The chapter finishes with the evaluation of three different measurements: one with the bistatic SAR collection parallel to the wall, one with the collection at a slight (11°) angle with respect to the wall, and one with the addition of clutter in the form of a rudimentary office scene.

Chapter 5 uses the extracted parameters to correct the subsequent SAR images for refraction. This is preluded by an explanation of the method by which this is accomplished. Finally, the focusing image quality is quantifiably measured for over a range of different assumed parameters. This is to evaluate the compensation performance and the sensitivity of the image to errors in the extracted values for the wall thickness and refractive index.

Chapter 6 is the natural extension to Chapter 4. It extends the extraction methodology into three-dimensions, again evaluating the performance of the methodology in the presence of clutter. This allows for the production of high-quality volumetric SAR imagery, corrected for by the method discussed in the previous chapter. This culminates in a volumetric multistatic image formed via the addition of two separate images. The chapter shows that to maintain image quality, each constituent image should first be compensated.

Chapter 7 discusses a methodology by which volumetric and planar SAR image formation can be accelerated. This revolves around a pixelwise phase correction designed to centre the SAR image support followed by a symmetric zero-padding. The accuracy of the proposed method is compared to established image upsampling methods via a direct comparison between upsampled imagery and normal imagery. Finally, the effects of the proposed phase correction is discussed with regards to TWR and proposals for future development given.

Finally, Chapter 8 concludes the thesis. Here, a brief summary of the key points in the thesis is given followed by proposals for future work.

2 Radar Fundamentals

2.1 Introduction

This section is as an introduction to the core concept of Synthetic Aperture Radar, how and why it works, and an overview of the main issues within the sub-field of Through-wall Radar. The motivation behind this section is to provide the reader with enough of a background as to be able to put later sections into context, not necessarily to cover every concept in radar.

2.2 The Fourier Transform

Modern radar relies heavily on Digital Signal Processing, the most fundamental component of which is the Fourier Transform.

In radar, it is common to approach the problem from the perspective of the frequency domain. This being an analytical space whereby functions and signals are expressed in terms of frequency. The time domain is an equivalent space whereby everything is expressed in terms of time. A fundamental principle of electromagnetism is that the two domains are equivalent, such that any EM function or signal can be evaluated from either the frequency domain or the time domain.

Any signal can be represented as a sum of waves, each with a different amplitude and frequency. Therefore, the EM pulse emitted by the radar system can be represented as a range of frequencies, generally referred to as the signal bandwidth, B.

To convert between a signal's frequency domain representation and its time domain representation, the Fourier Transform is used. For a one-dimensional function, $a(f)$, the Fourier Transformed function $\hat{a}(t)$ is given by:

$$\hat{a}(t) = \mathcal{F}[a(f)] = \int_{-\infty}^{\infty} a(f) e^{2\pi i f t} d f \qquad \textbf{2-1}$$

Where f represents frequency, and t represents time [2, pp.27–28]. Equivalently, to convert between a time domain representation and a frequency domain representation, the inverse Fourier Transform is used:

$$a(f) = \mathcal{F}^{-1}[\hat{a}(t)] = \int_{-\infty}^{\infty} \hat{a}(t)e^{-2\pi ift}d\,t \tag{2-2}$$

Syntactically, the mapping of $a(f)$ to $\hat{a}(t)$ is often described as Fourier Transform pair, represented as $a(f) \leftrightarrow \hat{a}(t)$ [2, p.28].

2.2.1 Key Properties of The Fourier Transform

This section summarises the most relevant properties of the Fourier Transform as it pertains to radar. Derivations and proofs are widely available [3,4].

1. **Modulation**

   Consider an imposed time delay in the function $\hat{a}(t)$ such that the function becomes $a(t+s)$. A time delay does not change the energy content of the signal, so the magnitude of the signal will not change. Instead, this constitutes a phase change, as shown by equations 2-3, 2-4, and 2-5:

$$\mathcal{F}^{-1}[\hat{a}(t+s)] = \mathcal{F}^{-1}[\hat{a}(u)] = \int_{-\infty}^{\infty} \hat{a}(u)e^{-2\pi if(u-s)}d\,u \tag{2-3}$$

$$\mathcal{F}^{-1}[\hat{a}(u)] = \int_{-\infty}^{\infty} \hat{a}(t+s)e^{-2\pi ift}e^{2\pi ifs}d\,t \tag{2-4}$$

$$\mathcal{F}^{-1}[\hat{a}(t+s)] = e^{2\pi ifs}a(f) \tag{2-5}$$

   For reasons of symmetry, this is also true transforming from the frequency domain to the time domain. This principle is used throughout the thesis in order to apply reference shifts to the measured SAR data and is relevant in all chapters.

2. **Convolution**

   Convolution is a mathematical description of how two functions interact with regards to each other. For two functions, $f(x) \leftrightarrow \hat{f}(\xi)$ and $g(x) \leftrightarrow \hat{g}(\xi)$, the convolution theorem states that there is a tertiary function $h(x)$ such that:

$$\mathcal{F}[h(x)] = \mathcal{F}[f(x)]\mathcal{F}[g(x)] \tag{2-6}$$

$$h(x) = f(x)\otimes g(x) \tag{2-7}$$

The function $h(x)$ is a convolution of the functions $f(x)$ and $g(x)$. Therefore, multiplication in one domain is equivalent to convolution in the other domain [3, pp.95–97,4, pp.115–117].

Convolution is heavily used in radar in two main ways: in image formation, and zero-padding as a means of rapid interpolation.

2.2.2 N-Dimensional Fourier Transform

In this thesis, one-dimensional, two-dimensional, and three-dimensional Fourier Transforms are used. As such, the generalised multi-dimensional form of the Fourier Transform is defined as:

$$\hat{f}(\xi_1, \xi_2 \dots \xi_N) = \underbrace{\int_{-\infty}^{\infty} \dots \int_{-\infty}^{\infty} \int_{-\infty}^{\infty} \int_{-\infty}^{\infty}}_{N} f(x_1, x_2 \dots x_N) e^{2\pi i \sum_{k=1}^{N} x_k \xi_k} \, dx_1 dx_2 \dots dx_N \qquad \textbf{2-8}$$

An N-dimensional Fourier Transform is performed by iteratively performing a series of one-dimensional transforms for each dimension of the input function.

Syntactically, equation 2-8 is simplified via vector notation. For $\boldsymbol{x} = [x_1, x_2 \dots x_n] \in \boldsymbol{R_N}$ and $\boldsymbol{\xi} = [\xi_1, \xi_2 \dots \xi_n]$ then:

$$\hat{f}(\boldsymbol{\xi}) = \int_{\boldsymbol{R_N}} f(\boldsymbol{x}) e^{2\pi i (\boldsymbol{X} \cdot \boldsymbol{\xi})} d\boldsymbol{x} \qquad \textbf{2-9}$$

2.2.3 Discrete Fourier Transform

For finite discrete datasets, such as those generated in radar missions, a finite sum is used rather than an integration [2, pp.28–29]. Consider the discrete time series $\hat{a}(\tau)$ such that $\hat{a}(\tau) \leftrightarrow a(\nu)$ of a discrete length N. The discrete transform pair is:

$$\hat{a}(\tau) = \sum_{\tau=0}^{N-1} a(\nu) e^{\frac{2\pi i \tau \nu}{N}} \qquad \tau = 0,1,2 \dots N-1 \qquad \textbf{2-10}$$

$$a(\nu) = \frac{1}{N} \sum_{\nu=0}^{N-1} \hat{a}(\tau) e^{\frac{-2\pi i \tau \nu}{N}} \qquad \nu = 0,1,2 \dots N-1 \qquad \textbf{2-11}$$

Similarly, to the continuous Fourier Transform, an N-dimensional discrete Fourier Transform is performed by iteratively transforming each dimension of the dataset.

Fast computerised implementations of these functions are widely used in radar. Fast Fourier Transform (FFT) algorithms use a divide and conquer approach to reduce the number of iterations required to calculate $a(\nu)$ and $\hat{a}(\tau)$.

2.3 Working Principles

Given a radar platform consisting of two antennas, one transmitting and one receiving, the time of flight can be obtained using the time delay between sending an electromagnetic pulse and receiving the reflected pulse. This would give the round-trip time, from which the mean distance to the target can be inferred. This is sufficient for a single target. . However, for multiple targets, the transmitted pulse must be short enough to differentiate between separate individual responses. The minimum distance at which the radar can successfully identify separate targets is referred to as the resolution of the system. The smaller the resolution, the better. Descriptions of resolution can quite easily be misinterpreted. For example, ‘greater resolution’ can be understood to mean either better or worse performance. For this reason, descriptions of resolution shall be limited to ‘coarser’ and ‘finer’ throughout this body of work. Resolution is not synonymous with measurement precision or accuracy, the former being a measure of the measurement reliability and the former being a measure of the ‘trueness’ of the measurement.

Range resolution is proportional to the length of the transmitted signal. For example, a short pulse would provide finer resolution, whereas a long pulse would provide coarser resolution. As illustrated in Figure 2-1, a shorter pulse provides finer resolution; however, the total energy content is less.

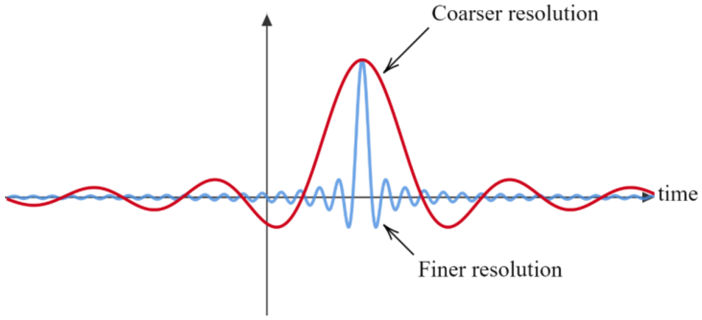

Figure 2-1 – Illustration of different pulse widths giving rise to different range resolutions

For a pulse covering a time span of $-\frac{\tau}{2}$ to $+\frac{\tau}{2}$, the distance the pulse will cover, and hence the resolution in range, is $R_{res} = c\tau$, where c represents the speed of light. One may define resolution as the distance from the peak of the signal to the first null. Therefore, the range resolution is written as $R_{res} = \frac{c\tau}{2}$ From the perspective of the frequency domain, this is equivalent to the most commonly written form of the range resolution:

$$R_{res} = \frac{c}{2B} \qquad \textbf{2-12}$$

For azimuthal resolution, one can differentiate between responses by the intensity of the received signal. For two scatters at the same distance and of the same size, the received intensity is dependent upon the beamwidth of the antenna at said distance.

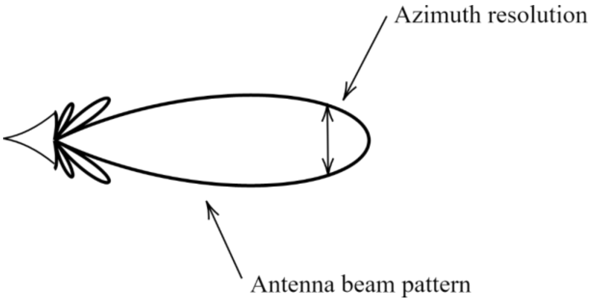

Figure 2-2 – Illustration of how azimuth resolution is tied to the antenna beam pattern.

Since beamwidth is inversely proportional to the electrical size of the antenna aperture, to achieve fine azimuthal resolution, the antenna must be very large. This very quickly becomes both expensive and impractical, so therefore a means of decoupling the azimuth resolution from the antenna size would be very much desirable.

In the 1950s, Wiley, of the then Goodyear Aircraft Company, filed a patent for the idea that a pulse by pulse comparison of radar returns from a moving aircraft would achieve finer azimuth resolution. This became the original patent for what would eventually be renamed 'Synthetic Aperture Radar' [1]. Wiley originally posed the technique as evaluating the doppler shifts from different parts of the scene, resulting in finer azimuthal resolution. However, the result is equivalent to the resolution one would achieve from a physically larger antenna. The SAR implementation used by Wiley is a 'Stripmap' mode. This is the most simplistic implementation of SAR, where the antenna is at a fixed angle relative to the trajectory of the radar platform. This results in an illuminated area parallel to the synthetic aperture, illustrated in Figure 2-3. There are other SAR modes, in particular ‘Spotlight’ and ‘Scan’ modes. Spotlight SAR aims to maintain the same illuminated area by rotating the antenna with respect to the synthetic aperture. The natural extension of spotlight mode SAR is to rotate the antennas such that any beam footprint can be achieved, this is Scan mode SAR [5, p.4].

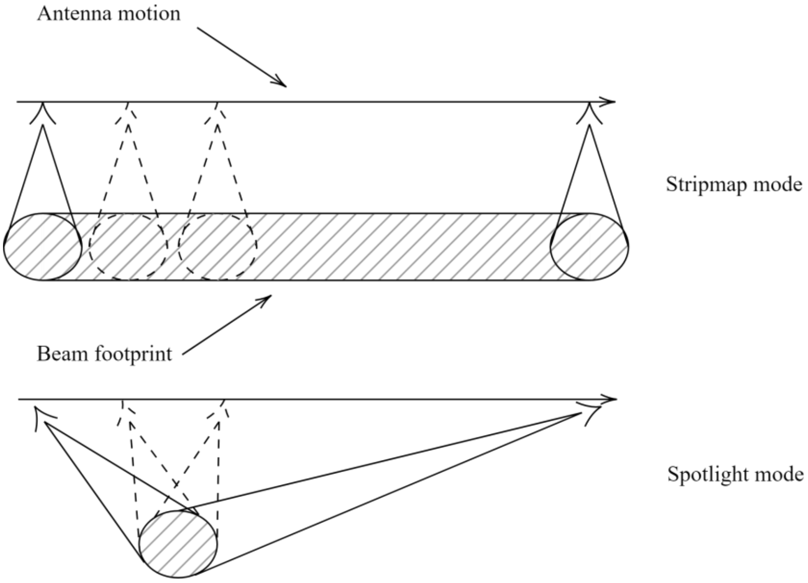

Figure 2-3 - Illustration of stripmap and spotlight mode SAR and the relation between the antenna motion and the illuminated area for each mode.

Consider a moving antenna that is traversing past a stationary target. It will eke out a dataset consisting of some frequency variation, and some angular variation. The size of the so called ‘Spatial-Frequency Support’ will ultimately determine the resolution of the target in question. In cartesian coordinates, the shape of this dataset is illustrated in Figure 2-4. The size of the support is dependent upon the received signal bandwidth and the angular variation experienced by the scattering target. Each scatterer in a SAR image will have its own support, that determines the resolution for that scatterer.

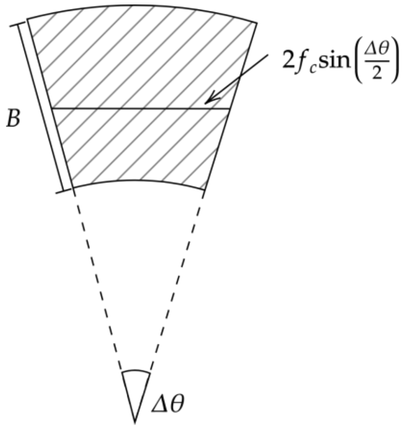

Figure 2-4 – Cartesian spatial-frequency support in a near-field SAR dataset. The extent in the range dimension is the bandwidth. The extent in the cross-range dimension is $2f_c sin(\frac{\Delta\theta}{2})$.

To evaluate the cross-range resolution CR_{res}, of a SAR system, recall that it is fundamentally limited by the size of the antenna beamwidth. The actual beamwidth is antenna dependent, however it is proportional to $\frac{\lambda}{W}$ for an antenna whose aperture size is W. For a synthetic aperture of length L_{syn}, the synthetic beamwidth is also proportional to $\frac{\lambda}{L_{syn}}$, thus increasing the size of the synthetic aperture results in finer cross range resolution. Numerically evaluating the SAR cross range resolution can be approached in multiple ways. For example, Carrara *et al* approach the problem from a geometrical perspective [5, pp.32–40], Sullivan [6, pp.17.7-17.9] approaches from the perspective of the targets apparent rotational velocity, and Jakowatz *et al* [7, pp.71–75] approach based on the size of the collection dataset in the frequency domain. Since there is no fundamental difference between the three spatial dimensions, what is true in the range dimension, must also be true in the cross-range dimension. Recall from Figure 2-4 that the cross range extent of the spatial frequency support is $2f_c \sin\left(\frac{\Delta\theta}{2}\right)$, thus the resolution in the cross-range dimension is:

$$CR_{res} = \frac{c}{4f_c \sin\left(\frac{\Delta\theta}{2}\right)} \approx \frac{c}{2f_c\Delta\theta} \qquad \textbf{2-13}$$

The most common versions of 2-13 use a small angle approximation that is valid on scales where $\Delta\theta$ is small [5,7]. This oftentimes corresponds to so called 'far-field' scenarios, where the targets are sufficiently far from the radar platform such that the propagating wavefronts are approximately straight. Where this approximation is not valid, the region is dubbed ‘near-field’. Because waves propagate spherically from an emitter, there will always be some degree of wavefront curvature. However, it is useful to define regions where this curvature is negligible, i.e. there is little variation associated with an image. The Fraunhofer Distance provides an approximate distance beyond which the propagation is considered ‘far-field’. This distance is defined as:

$$D_{fraunhofer} = \frac{2W^2}{\lambda} \qquad \textbf{2-14}$$

Where W is the largest dimension of the radiating antenna. From the point of view of the receiving antenna, the backscatter off any target is indistinguishable from a luminous target. Thus, there are two distinctions to be made when considering near or far field. The first is the antenna regime, where W represents the largest dimension of the antenna aperture. The second is the image regime, where W represents the image size. This is a useful distinction to make, since while control over the antenna size or transmit frequency may not be possible, for example so called illuminators of opportunity [2], direct control of the image size is.

In order for a passive scatterer to contribute towards the radar received signal, it must exist within the antenna beam pattern. This puts a limit on the attainable resolution of Stripmap SAR. In Stripmap SAR, the maximum synthetic aperture that will contribute towards any point in space is equal to the beam footprint at that distance [7, pp.46–47]. This puts an effective limitation on the attainable cross range resolution, as illustrated in Figure 2-5. Since the antenna beamwidth for a rectangular slit is $\sin(\theta_b) = \frac{\lambda}{W}$ [9, sect.30–1], the real aperture resolution attainable by the system is defined as:

$$Span = R\sin(\theta_b) = \frac{R\lambda}{W} \qquad \textbf{2-15}$$

For a maximum synthetic aperture length of $2Span$, the finest achievable cross range resolution is:

$$CR_{res} = \frac{R\lambda}{2Span} = \frac{W}{2} \qquad \textbf{2-16}$$

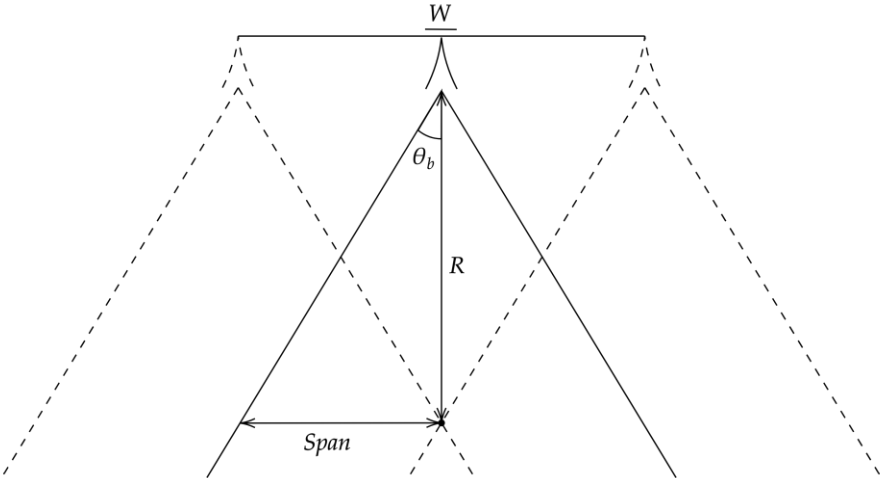

Figure 2-5 – Illustration of the cross range resolution attainable in Stripmap SAR.

2.4 Ground Based SAR

Historically SAR, and remote sensing in general, has been an airborne and spaceborne technique. However, as radar becomes less and less militarised, and costs decrease, there has been an advent of smaller ground-based SAR systems.

Ground-based SAR (GBSAR) is, as the name suggests, a SAR modality in which the radar platform is rooted to the ground. Consequently, GBSAR measurements lack the large-scale applications available to spaceborne or airborne SAR; however GBSAR systems generally benefit from greater ease of access. As such, they often serve as testbeds for larger scale systems, for observing smaller scale phenomena, and for observing underground, or otherwise obscured, activity.

A major use of GBSAR is in observing buried objects. Ground Penetrating Radar (GPR) is the field of radar dedicated to extracting information about buried objects and materials. It is the predominant use of GBSAR systems and the precursor to Through-Wall radar. GPR is used in a wide variety of subject areas, ranging from archaeology [10], groundwater content analysis [11], and more prolifically, landmine detection [12,13].

Other uses for GBSAR are predominantly urban surveillance including but not limited to through-wall scenarios, and small-scale terrain observations, such as landslide monitoring [14]

A key limitation of many GBSAR measurements is that space is limited, in particular, the physical extent of the synthetic aperture is small when compared to airborne and spaceborne SAR. For this reason, the attainable cross range resolution is limited by the physical size of the synthetic aperture rather than the antenna beam pattern. While equation 2-16 is still the finest achievable resolution, a limited synthetic aperture will cause different areas of the measurement area to exhibit different cross range resolution in accordance with equation 2-13.

Neither Scan mode nor spotlight mode SAR see heavy use for ground-based SAR platforms when compared to Stripmap SAR. This is primarily due to closer objects being persistent over a larger fraction of the synthetic aperture and practical hurdles with regards to rotating the antennas. However, small objects are often placed on a turntable to produce the equivalent of circular Spotlight SAR by rotating the object rather than the antennas. Inverse circular SAR sees some use [15,16,17, pp.69–72].

2.5 Near-Field Image Formation

Image formation, within the context of SAR, aims to convert a gathered measurement into an interpretable time domain representation.

In SAR, data is usually gathered in the frequency domain, as this allows the resolution to be decoupled from the energy of the pulse. Ergo to obtain a time domain image, one must apply a Fourier Transform at some stage during the image formation process.

The most simplistic form of image processing is pulse compression followed by azimuthal compression. In short, this is a convolution between the received and transmitted time domain responses. Following the Convolution Theorem, the same effect can be achieved by multiplying the frequency domain signals. Therefore, the image formation algorithm can be described as an N-dimensional Fourier Transform of the measurement data. While this approach is valid for a coarse resolution image, it suffers from defocusing [5]. This is due to the measurement data being gathered in a polar format, whereas efficient Fourier Transform algorithms require a Cartesian coordinate system [5,7,18]. While spherical polar FFT algorithms exist, they are not widely implemented with respect to SAR. Therefore, this method of image formation is ill suited for near-field measurements.

To combat this, the measurement data must be converted from a polar to Cartesian coordinate system. This transformation is typically done by resampling the complex power (W) recorded by the vector network analyser (VNA) for each frequency and antenna position in the measurement, collectively referred to as the phase history, to a new grid. I.e. interpolating between frequencies and aperture positions [19, pp.36–48,20]. The Polar Format Algorithm (PFA) improves the focusing quality of the image; however, it is limited by both the quality of the interpolation and the nature of the measurement. PFA suffers from range curvature errors [5,21], making it unsuitable for near-field measurements. While narrow images and a judicial choice of measurement geometry can alleviate this problem, in practice range curvature will always be present to some degree. Therefore, to remove this error completely, a more complex imaging algorithm is required. For this reason, near-field image formation is typically much more involved than far-field image formation.

Imaging algorithms that are more complex, such as the Range Migration Algorithm, Chirp Scaling, or Backprojection (Chapter 5.1.1), require a direct consideration of the measurement geometry. As such, an overview of the different modalities of SAR measurements is included.

- **Monostatic:**
  Monostatic SAR refers to a measurement paradigm wherein the transmitting and receiving antennas are co-located. Unless using a transceiver, it is not possible achieve a true monostatic measurement outside of simulation, therefore the term usually includes quasi-monostatic cases where there are two antennas, one transmitting and one receiving, exhibiting little angular separation.
- **Bistatic:**
  Bistatic measurements are characterised by the antennas being separated in space. The principle benefit for this type of measurement is a greater flexibility concerning collection geometry, allowing the radar operator to achieve greater angular variation and avoid radar cross section (RCS) nulls that may be present in the monostatic case [22]. Additional benefits include an increased resistance to electromagnetic countermeasures [23] and potential cost savings. However, this comes at the expense of increased measurement complexity. This measurement

complexity, in particular issues synchronising between antennas, is one of the main reasons that bistatic radar has historically been less common than its monostatic counterpart.

- **Multistatic:**
  The natural extension to bistatic radar is the so-called multistatic collection. In this modality, multiple antennas (> 2) are used in conjunction to produce a single coherent dataset. Since multistatic radar can consist of both monostatic and bistatic components, it can benefit from both modalities. As with the bistatic case, the spatial coordinates of all antennas must be known to avoid image distortions [23]. In addition, the same synchronicity issues are also present.

To date, monostatic SAR is by far the dominant SAR measurement modality, although bistatic and multistatic systems have seen a surge in popularity within the last two decades. This boom in popularity is driven by both decreasing costs and an uptick in compute capability due to technological improvements.

2.5.1 2D

Two-dimensional SAR, as defined in this work, refers to SAR imagery where there is no angular variation in more than one dimension. Consequently, there is no appreciable resolution in the dimension normal to the collection plane[1]. In general, this leads to projection effects whereby scatterers outside the plane are projected onto the plane, appearing in a seemingly incorrect location. This can be problematic if there are multiple scatterers existing at the same Euclidean range and azimuth angle, as these will appear at the same place in the image.

Nevertheless, 2D SAR is far more common than its 3D counterpart. This is due primarily to shorter acquisition time, a reduced complexity of (2D) collection, and a reduced computational overhead.

With regards to ground-based SAR systems, 2D SAR collections often take the form of an antenna or pair of antennas mounted to a small linear rail [24,25]. For larger scale

---

[1] There is some resolution normal to the collection due to the physical beam pattern of the antenna being three-dimensional. However, since the real aperture resolution is typically much coarser than the synthetic aperture resolution, for all intents and purposes, it can be safely neglected.

collections, it is not uncommon to retrofit a vehicle with an onboard radar system [26–28], especially in urban environments. It is also not uncommon for these systems to include multiple antennas, which can be used for multistatic measurements and for interferometric measurements.

2.5.2 3D

In two-dimensional SAR, resolution is obtained in a single plane, this being the plane defined by the range and azimuthal axes. To obtain resolution in the vertical dimension, it is necessary to generate a variation in elevation angle; the most common way of achieving this is through interferometric SAR (InSAR). InSAR, as defined by Graham [29] and later Zebker, Goldstein, and others [30–33] uses two or more SAR collections with different elevation angles to achieve a difference in phase. This difference in phase allows for the explicit calculation of a digital elevation model (DEM) of the ground [30].

This interferometric method of assessing elevation is both widely successful and widely used, for example the TanDEM-X and TerraSAR-X satellites achieved a vertical accuracy of 10m [34,35]. However, it cannot be considered a truly three-dimensional form of SAR, since the small number of interferometric collections can give rise to significant aliasing when used in conjunction to form a single volume. To avoid this aliasing, a sufficiently sampled two-dimensional aperture is required. This approach has been described exhaustively in the literature and could be considered a generalised form of cross-track multi-baseline interferometry [36–43].

While this approach to volumetric SAR is limited with regards to spaceborne radar platforms, airborne and ground-based platforms routinely employ two-dimensional apertures, most notably in the GOTCHA dataset [44,45] which has contributed towards a significant amount of publications.

Concerning ground-based platforms, the mentality is to focus more on repeatability and accuracy, rather than resolution. For this reason, along with cost saving, GBSAR systems, in the context of volumetric imaging, tend towards so-called stop-start machines, typically characterised by two orthogonal arms [41,46–48]. That said, due to the potentially small scale nature of GBSAR, handheld devices, such as those sold by IDS-GeoRadar [37] and GSSI, are becoming more popular.

The process of forming a volumetric SAR image is broadly the same as forming a two-dimensional image. The Backprojection algorithm is applicable, and widely used. Forming a volumetric image adds an additional dimensionality to the image formation. As a consequence, volumetric image formation using Backprojection can take orders of magnitude longer than its planar counterpart [21], and occupy significantly more space in computer memory.

Due to these time constraints, accelerating 3D image formation is desirable. Thankfully, techniques applicable to 2D image formation are usually also applicable to 3D. For example, decimation of the measurement data, and imaging grid [49] to accelerate the image formation.

2.6 Cranfield GBSAR

Cranfield University is one of the few institutions in the United Kingdom with a large scale dedicated GBSAR capability. Originally, this system consisted of a horizontal rail mounted to the arm of a cherry picker. The vertical motion of the Niftylift 120 cherry picker, combined with the horizontal motion of the rail formed a two-dimensional aperture, from which a volumetric SAR image can be generated. While versatile, the system was difficult to automate and had a tendency to sag slightly over time. This made it difficult to do repeat measurements. For this reason, the system was recently redesigned.

The newer system, shown in Figure 2-6, is characterised by two orthogonal motorised rails, with a horizontal rail forming a gantry by which the other rail is suspended. Featuring a large 1.5m by 3.5m 2D aperture, the system is capable of full 3D SAR measurements, over a wide range of frequencies, in both monostatic and bistatic configurations. This style of measurement rig is both easier to use, and more precise over large time frames. That said, due to the large vertical arm, there is a tendency for the arm to pendulate slightly. However, this is solved by simultaneously reducing the movement acceleration and deceleration, and increasing the time between sequential sweeps.

The GBSAR system uses a two closely mounted horn antennas connected, via microwave cables, to a stationary VNA. A VNA is a radio and microwave measurement device used to measure transmitted and received signals. A two port VNA, is capable of simultaneous measurements of both the transmitted stimulus and the received signal. During the SAR measurement, the VNA transmits a chirp signal from a minimum to a maximum frequency. The complex received signal is then recorded. The VNA is connected, via USB, to a controlling computer, once the signal has been recorded the antennas move to the next position in the SAR aperture. Because the motion of the rail is synchronised with the VNA operation, the SAR measurement is made time independent. I.e. the system will remain in one position until the desired number of frequency samples has been taken.

A key benefit compared to the cheaper Scaler Network Analyser is the ability to measure both amplitude and phase of the signal. This additional phase information allows for complex raw data manipulation, such as complex background subtraction.

Without exception, all the experimental radar work performed within this body of work was done so using this system. The wall measurements presented in Sections 4 and 6 used a Keysight N5245B VNA and a HP 8719ES VNA respectively. The Keysight N5245B VNA was rented from Keysight and was not available for both sets of measurements.

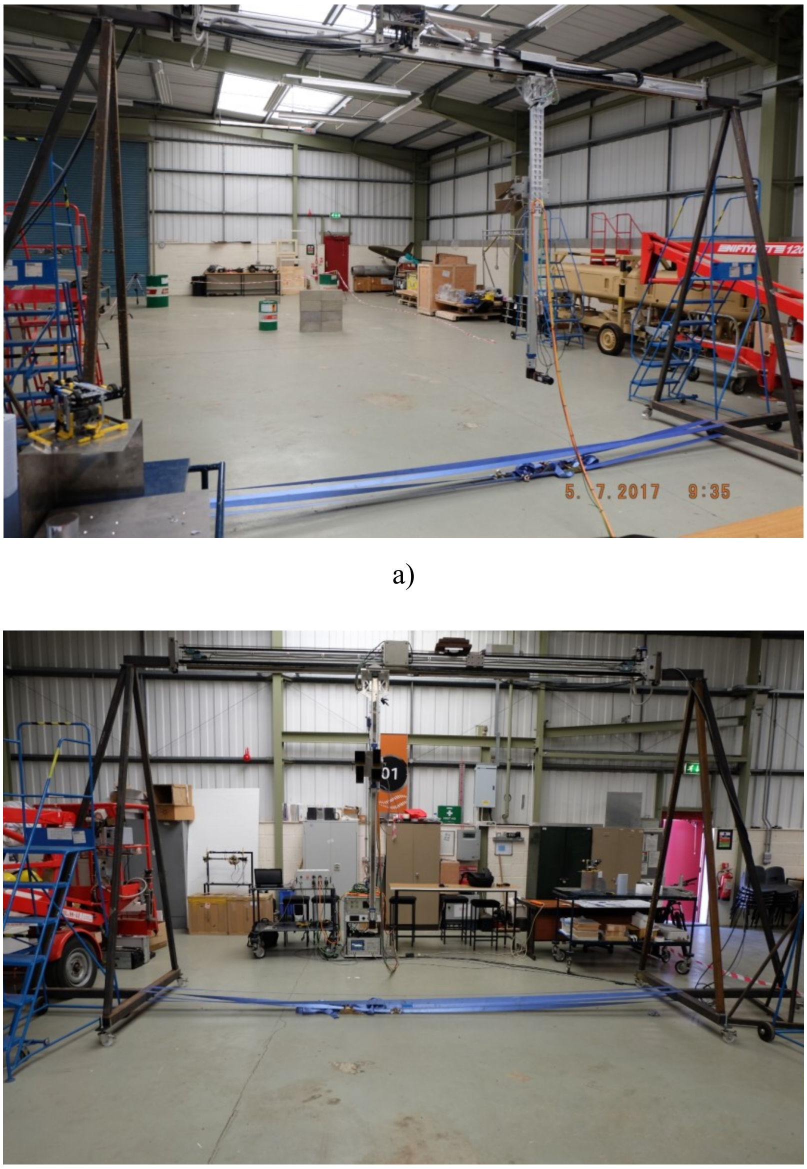

a)

b)

Figure 2-6 – Photographs of the a) back, and b) front of Cranfield’s GBSAR rig. The rig is constructed as two orthogonal arms, one supported between two metal A-frames, and the other hangs vertically from the gantry. The usable length of the rails allows for a 3.5m horizontal aperture and a 1.5m vertical aperture.

2.7 Through-Wall Radar

Through-Wall Radar (TWR) is a comparatively new topic area within the broader radar ecosystem, with uses in surveillance [50–52], search and rescue, construction [53], and material classification [54,55]. The main crux of the topic is to obtain accurate and interpretable information about activity on the far side of an obscuring wall. Supplementary to that, is to obtain information about the building or wall structure itself.

TWR can be thought of as analogous to Ground Penetrating Radar, in that the targets of interest are either part of or behind a dielectric layer. Therefore, many of the concerns associated with GPR can also be attributed to TWR. There are three main considerations when attempting to image an object behind a wall: electromagnetic refraction, electromagnetic attenuation, and reflections off of the wall.

2.7.1 Electromagnetic Refraction and Attenuation

First described mathematically by Snell in the 17th century, electromagnetic refraction is a phenomenon occurring when propagating waves change media. It is due to a change in permittivity and/or permeability[2] driving a change in phase [9, sect.31–1].

The mechanism causing this change in phase is the interaction between the propagating EM wave and charge carriers present in the material, i.e. electrons. The EM wave exerts a force on the electrons, via the Lorentz force, causing them to move; as such, the electrons generate a complementary electric field. The addition of incident and complementary fields creates a new propagating field rotated from the original. This rotation constitutes a change in direction of the newly propagating wave. Since the incident field, and the new field must be continuous at the medium boundary, the wavelength of the transmitted wave must change. Since wavelength is proportional to the speed of the propagating wave, the speed of the wave must also change. The refractive index is a unitless quantity referring to the ratio between the speed of light in a vacuum to the speed of light in a material, $n = \frac{c}{v}$, defines this change in speed.

Mathematically this phenomenon is described by Snell's Law, $n_1 \sin(\theta_1) = n_2 \sin(\theta_2)$. From a radar perspective, an unaccounted change in refractive index, n, causes a positional error in any resultant images. While this positional error can be corrected, either directly in the image formation [41] or as a focusing operator applied to a pre-generated

---

[2] In both the radar and broader EM communities, it is common to assume that a material is non-magnetic and as such, the permeability of the material is assumed equal to that of free space. This is a valid assumption for most non-reinforced building materials [197], however this assumption is not necessarily valid for all cases, e.g. ferrites.

image [56], it generally requires the inclusion of a velocity model. As such, to obtain accurate urban SAR imagery, one must know both the refractive index and thickness of any obscuring walls.

The refractive index is formally defined in terms of the materials permittivity, ε, and permeability, μ with respect to those of free space. It is also common to define the refractive index in terms of the relative permittivity and permeability, ε_r and μ_r respectively.

$$n(\varepsilon, \mu) = \sqrt{\frac{\varepsilon\mu}{\varepsilon_0\mu_0}} = \sqrt{\mu_r\varepsilon_r} \qquad \textbf{2-17}$$

The permittivity (Fm^{-1}) of a material is a measure of how easily the molecules in a material form dipoles in response to an stimulating electric field, leading to the material becoming polarised. Similarly, the permeability (Hm^{-1}) of the material is a measure of how magnetised the material becomes in response to a magnetic field. For an isotropic medium, permittivity is the ratio between the Electric field, $\boldsymbol{E}$ and the electric flux density, $\boldsymbol{D}$. Similarly, for a non-magnetised material, permeability is the ratio between the magnetic field, $\boldsymbol{H}$ and the magnetic flux density, $\boldsymbol{B}$. For a surface, $\boldsymbol{S}$, with an outward facing surface normal**,** the flux density is the surface integral of the field with respect to $\boldsymbol{S}$ divided by the area, A, of $\boldsymbol{S}$:

$$\boldsymbol{B} = \mu\boldsymbol{H} \qquad \textbf{2-18}$$

$$\boldsymbol{D} = \varepsilon\boldsymbol{E} \qquad \textbf{2-19}$$

$$\boldsymbol{B}(\boldsymbol{r}, f, t) = \frac{1}{A}\iint_S \boldsymbol{H}(\boldsymbol{r}, f, t) \cdot d\boldsymbol{S} \qquad \textbf{2-20}$$

$$\boldsymbol{D}(\boldsymbol{r}, f, t) = \frac{1}{A}\iint_S \boldsymbol{E}(\boldsymbol{r}, f, t) \cdot d\boldsymbol{S} \qquad \textbf{2-21}$$

The electric field, $\boldsymbol{E}$ (vm^{-1}) is a vector field describing the force per unit charge exerted by a charged particle at any point in space, such as an electron. Similarly, the magnetic field, $\boldsymbol{H}$ (Am^{-1}), describes the magnetic influence on a moving charge. Mathematically, the electric and magnetic fields are described by the Maxwell Equations from which the electromagnetic wave equations are derived (Appendix A.1):

$$\nabla \cdot \boldsymbol{E} = \frac{\rho}{\varepsilon}$$ Gauss' Law for Electricity **2-22**

$$\nabla \cdot \boldsymbol{H} = 0$$ Gauss' Law for Magnetism **2-23**

$$\nabla \times \boldsymbol{E} = -\mu \frac{\partial \boldsymbol{H}}{\partial t}$$ Faraday's Law **2-24**

$$\nabla \times \boldsymbol{H} = \varepsilon \frac{\partial \boldsymbol{E}}{\partial t} + \boldsymbol{J}$$ Ampere's Law **2-25**

$$\nabla^2 \mathbf{E} - \frac{1}{v^2} \ddot{\mathbf{E}} = \mu\sigma\dot{\mathbf{E}}$$ **2-26**

$$\nabla^2 \boldsymbol{H} - \frac{1}{v^2} \ddot{\boldsymbol{H}} = \mu\sigma\dot{\boldsymbol{H}}$$ **2-27**

$\boldsymbol{J}$ represents the current density. It is the amount of charge per unit time that flows through a given cross sectional area. It has units Am^{-2}. σ represents the conductivity (Sm^{-1}) of the material. It is a measure of how easily an electric current can pass through a material. It is the ratio between the current density, $\boldsymbol{J}$, and the electric field, $\boldsymbol{J} = \sigma\boldsymbol{E}$.

A solution to the wave equations is a phasor form of the electric and magnetic fields, dependent upon the wavenumber, $k = \frac{2\pi f}{c}$, the angular frequency, $\omega = 2\pi f$, time t, and a displacement vector $\boldsymbol{r}$:

$$\boldsymbol{E}(\boldsymbol{r}, f, t) = E_0 e^{i(kr - \omega t)}$$ **2-28**

$$\boldsymbol{H}(\boldsymbol{r}, f, t) = H_0 e^{i(kr - \omega t)}$$ **2-29**

Both permittivity and permeability are intrinsic to the Maxwell Equations as they are constants of proportionality between the spatial and temporal derivatives of the electric and magnetic fields via Faraday's Law, and Ampere's Law. Gauss's Laws denote the divergence of the electric and magnetic flux densities. In the case of the magnetic flux density, $\nabla \cdot B = 0$, leading to the conclusion that there are no magnetic monopoles.

Since a propagating EM wave will excite charged particles, it follows that a travelling wave will gradually lose energy to its surroundings; a process referred to as attenuation. Attenuation does not result in any positional errors in radar; in fact it can be shown, in Appendix A.1, to be independent of the phase of the propagating wave [57, pp.372–377]. Modelling the attenuation exactly requires knowledge of the material conductivity. In conjunction with the material permittivity and permeability, the attenuation term, usually referred to as α, can be explicitly calculated (Appendix A.1). Commonly, the attenuation is defined in terms of the unitless loss tangent, $\tan(\delta)$, of the material. The loss tangent is most commonly defined as the ratio between the real and imaginary components of the complex permittivity of the material, $\varepsilon = \varepsilon' - i\varepsilon''$, $\tan(\delta) = \frac{\varepsilon'}{\varepsilon''}$. A complex permittivity is a notation convention [57, pp.372–377] to account for propagation through lossy mediums and can be expressed in terms of the materials conductivity rather than as a complex number [58, p.139,59, pp.8–9]. Using the effective material conductivity and a real permittivity, the loss tangent is:

$$\tan(\delta) = \frac{\sigma}{\omega\varepsilon} \qquad \textbf{2-30}$$

It should be noted that a material's properties vary depending on the frequency of interest. For example, the refractive index of water can vary substantially across the visible spectrum, giving rise to rainbows. A material with a frequency dependent refractive index, and by extension a frequency dependent speed of light, is referred to as a dispersive medium.

For a lossy material, with a non-zero attenuation, the fields are often expressed in terms of the propagation constant, $\gamma(f) = ik(f) = \alpha(f) + i\beta(f)$. The propagation constant denotes the change per unit length of the propagating electromagnetic wave. Like the attenuation term α, and the phase term β, it has units of m^{-1}. For a non-conductive material, $\alpha = 0$ and $\beta = \frac{2\pi f}{c}$.

There are some tangible benefits to radar imaging due to refraction. From a communications perspective, the refractive index of either the troposphere, or the ionosphere is such that total internal reflection and the so called *skywave* phenomenon [60] occur, enabling short-wave propagation over the horizon.

As will be shown in Chapter 5, the decreased velocity of the EM wave within a dielectric medium leads directly to finer range resolution.

2.7.2 Fresnel Coefficients and Polarisation

Due to many different contributing factors, such as the desire to be covert, radio frequency interference, or physical limitations on the SAR platform design, TWR suffers from a chronic lack of resolution and a difficulty with differentiating targets from clutter. A somewhat effective, and common, approach to aid target discrimination from clutter is to make use of multiple polarisations in the SAR collection [61–63].

Polarisation in radar is typically described in one of three ways:

1. V and H refer to a polarisation with respect to the collection, with H being parallel to a horizontal synthetic aperture trajectory, and V being perpendicular.
2. TE and TM refer to transverse magnetic and transverse electric orientations, with TE having its electric field exclusively transverse to the direction of propagation and likewise TM with its magnetic field. Inside a waveguide, TE and TM polarisation occurs at discrete harmonics, referred to as modes. More formally, for a wave propagating in the z direction, a TE mode will have an electric field that has no z component, i.e. $E_z = 0$, whereas a TM wave will have no z component to the magnetic field $B_z = 0$. Note that both these conditions may be true simultaneously, such a wave is referred to as a TEM wave [64, p.359,65, p.390].
3. S and P polarisations refer to the polarisation with respect to the plane formed between the transmitter, receiver, and the point of reflection, with S being perpendicular to this plane, and P being parallel.

In practice, the polarisation nomenclature is dependent upon context. For example, TE and TM are typically used when referring to polarisation with respect to a device, e.g. a waveguide, whereas S and P are typically used when talking about specific reflections. Since S/P polarisation and V/H polarisation are both defined in terms of a specific plane, be it horizontal plane or the plane of incidence, they can be converted between via a basis transformation. The relation between the two is illustrated in Figure 2-7.

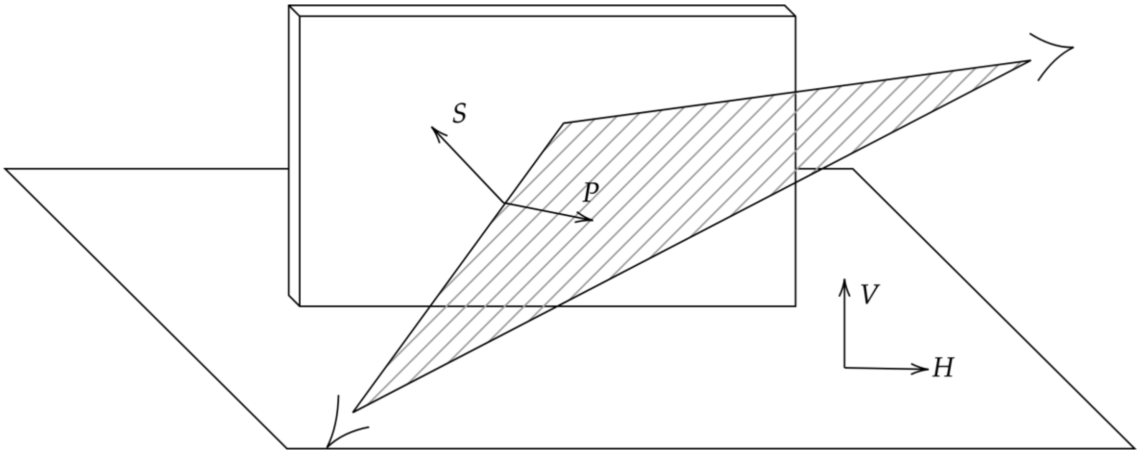

Figure 2-7 – Illustration of S/P and V/H polarisations. S/P are defined in terms of the plane formed between the antennas and the point of reflection, whereas V/H are defined in terms of the horizontal and vertical planes. A basis transformation via a rotation matrix will convert between the two.

Polarisation intrinsically affects the reflection from surfaces. As will be shown in Chapter 3, the polarisation of the EM wave directly affects waveguide behaviour, and reflection from boundaries.

For a specific polarisation, the Fresnel reflection coefficients are directly dependent upon the material refractive index. This is shown by considering specular reflection as shown in Figure 2-8.

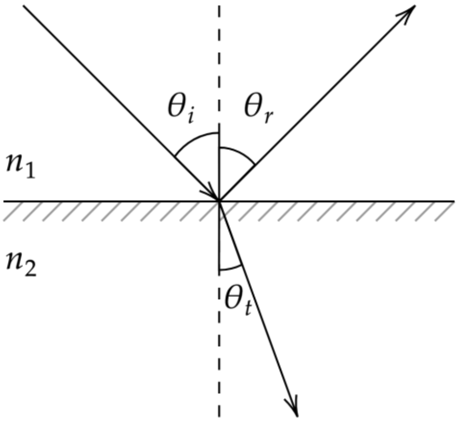

Figure 2-8 – Diagram of specular reflection and transmission between two media of different refractive indices.

From Faraday's Law (Appendix A.1), the curl of the electric field, $\boldsymbol{E} = [E_x, E_y, E_z]$, is related to the magnetic field, $\boldsymbol{H} = [H_x, H_y, H_z]$:

$$\nabla \times \mathbf{E} = \frac{\partial \mathrm{E_x}}{\partial z}\boldsymbol{a_y} = -\frac{\mu \partial H_y}{\partial t}\boldsymbol{a_y} \tag{2-31}$$

Where $\boldsymbol{a_y}$ represents the unit vector along the y dimension. For the standard phasor representations of $\boldsymbol{E}$ and $\boldsymbol{H}$, $\boldsymbol{E}(z,t) = E_0\boldsymbol{e}^{-\boldsymbol{i}(\omega t - kz)}\boldsymbol{a_x}$ and $\boldsymbol{H}(z,t) = H_0\boldsymbol{e}^{-\boldsymbol{i}(\omega t - kz)}\boldsymbol{a_y}$, this reduces to a proportionality between the electric and magnetic fields, dependent upon the intrinsic impedance, $Z(f,\mu,\varepsilon,\sigma) = \sqrt{\frac{i\omega\mu}{\sigma + i\omega\varepsilon}}$, of the material where μ and ε represent the material's permeability and permittivity respectively and σ is the material's conductivity:

$$\boldsymbol{H}(z,t) = \left(\frac{k}{\omega\mu}\right)\boldsymbol{E}(z,t) = \frac{1}{Z}\boldsymbol{E}(z,t) \tag{2-32}$$

In TE polarisation, the electric field is parallel to the boundary, whereas the magnetic field is at the angle thus:

$$E_i + E_r = E_t \tag{2-33}$$

$$H_i \cos(\theta_i) + H_r \cos(\theta_r) = H_t \cos(\theta_t) \tag{2-34}$$

For specular reflection, $\theta_i = \theta_r$. Therefore, equation 2-34 simplifies to[65, pp.366–368]:

$$\frac{1}{Z_1}(E_i + E_r)\cos(\theta_i) = \frac{1}{Z_2}E_t\cos(\theta_t) \tag{2-35}$$

For a reflection coefficient defined as the complex unitless ratio between incident and reflected electric fields, $R_{TE} = \frac{E_r}{E_i}$, and similarly a transmission coefficient, $T_{TE} = \frac{E_t}{E_i}$, then equation 2-35 yields:

$$1 - R_{TE} = \frac{Z_1\cos(\theta_i)}{Z_2\cos(\theta_t)}T_{TE} \tag{2-36}$$

The reflection coefficient can be rewritten as the well-known Fresnel coefficients:

$$R_{TE} = \frac{Z_2\cos(\theta_i) - Z_1\cos(\theta_t)}{Z_2\cos(\theta_i) + Z_1\cos(\theta_t)} \tag{2-37}$$

The same approach can be used to define the TM reflection coefficient as:

$$R_{TM} = \frac{Z_2 \cos(\theta_t) - Z_1 \cos(\theta_i)}{Z_2 \cos(\theta_t) + Z_1 \cos(\theta_i)} \qquad \textbf{2-38}$$

If the material is assumed to be non-magnetic, then the intrinsic impedance is dependent upon only the permittivity and conductivity of the material. If the complex reflection coefficient is measured, then one can backtrack to explicitly calculate the materials refractive index.

2.8 Current Methods for Extracting Wall Properties

Various methods for extracting the refractive index of a wall material are discussed. As stated in section 2.7.1, there is a distinction to be made between a real refractive index and a complex refractive index. Many options for extracting the wall material properties are specifically designed to extract either the full complex refractive index or a real approximation. In this thesis, the established framework (Appendix A.1) allows only for a real refractive index. What would have been an imaginary component is replaced by the material conductivity.

In general, methods for extracting the thickness and refractive index of a wall material can be split into three categories. These are In-situ methods, where direct access to the block is required. Target based methods, whereby a suitable reference target is used, and Bistatic methods, in which the direct backscatter from the wall is utilised. Each approach will be discussed in more detail in the relevant chapters, specifically Chapters 3 and 4.

3 In Situ Methods

3.1 Introduction

This chapter focuses primarily on extracting a value for the refractive index of the concrete wall material. This value is to be used as an independent verification for the methods presented in later chapters.

Various methods for extracting the refractive index or, more commonly, the permittivity of the material, have been proposed utilising direct access to the material. These methods generally require that the reflection and transmission coefficients be either directly measured or explicitly calculated. As such these methods often use a closed coaxial system [66–70] as a means to both hold the sample in place, and to directly measure the S_{11}, the ratio between the transmitted power emitted from port 1 and the received power as seen by port 1, and S_{21}, the transmitted power emitted from port 1 and the received power as seen by port 2[3]. S_{11} and S_{21} are both ratios between transmitted and received power, therefore they are both unitless. The scattering coefficients encapsulate multiple reflections as oppose to the single interface discussed in Section 2.7.2. However, if one assumes that there is a known number of reflections, then S_{11} and S_{21} can be directly related to the complex reflection coefficients, and by extension the material's refractive index.

$$P_{1_{recived}}(f) = S_{11}(f) P_{1_{transmitted}}(f) \qquad 3\text{-}1$$

$$P_{2_{received}}(f) = S_{21}(f) P_{1_{transmitted}}(f) \qquad 3\text{-}2$$

These methods can be broadly categorised into three somewhat distinct categories: probe-based approaches, transmission line approaches, and forward scattering methods. Each has their own benefits and drawbacks. For example, measuring the forward scattering obviously requires access to both sides of the material under test.

---

[3] A reciprocal system will have $S_{11} = S_{22}$ and $S_{12} = S_{21}$.

3.1.1 Open Ended Probes

Open ended probe based parameter extraction only requires measurement of the S_{11} reflection signal and as such this approach sees heavy use in cases where direct transmission is difficult or impossible to measure, for example GPR [71] and biological tissue. A well characterised coaxial probe is placed on a flat surface of the material under test, a broadband signal is transmitted though the probe and reflected from the material. From the reflected signal, the probe aperture admittance is calculated in terms of S_{11}, and from there, the permittivity of the material under test. The admittance of the free space aperture is usually calculated via two [72,73] or three [74,75] calibration measurements.

Recently, this probe approach has been used to characterise concrete samples, both from the perspective of probe design [72,73,75], and from a material identification perspective [76,77]. However, since porous aggregate concrete blocks present a rough surface the measurements are prone to systematic uncertainty. To avoid this, the surface should be as flat as the focal plane of the probe [74]. In addition, the material under test is usually considered to comprise one strong reflection [78] This is a valid assumption for homogeneous lossy materials, but not necessarily valid for concrete, as the aggregate will contribute towards multiple additional reflections.

In short, while open ended probes present a convenient non-destructive means of obtaining the relative permittivity of a sample, the need for an exact model of the probe, multiple calibration measurements, and a sensitivity to surface roughness makes this approach ill-suited for determining the properties of the concrete sample.

3.1.2 Transmission Lines

Transmission line approaches typically feature a sample of material inserted into a waveguide housing with ports on each side. From this setup both the S_{11} and S_{21} scattering coefficients are easy to measure. The motivation here is to solve a major concern with the afore mentioned probe method: the probed material must be non-magnetic.

Transmission line approaches centre on calculating the propagation constant directly from the reflected and transmitted signals, usually through some nonlinear combination of the two. There are numerous ways of achieving the same result, but the most common, and the most relevant to this chapter, was developed in 1970 by Nicolson and Ross [79] as a time-domain method for extracting the complex permittivity, $\varepsilon = \varepsilon' + i\varepsilon''$, from a sample of material. As with all electromagnetics, one can approach a problem either from the time-domain or from the frequency-domain. This conversion was made four years later by Weir [69] to produce finer frequency precision and the now established and extremely prolific Nicolson-Ross-Weir (NRW) method.

The NRW method [69,70,79–84] utilises the complex reflection and transmission coefficients, obtained from both the S_{11} and S_{21} scattering coefficients, to extract both the permittivity and the conductivity of the material. This is done by writing the S parameters in terms of the reflection coefficient of the material. From this, the propagation constant, and ultimately the material properties, are explicitly defined in terms of the measured S_{11} and S_{21} datasets.

While this technique does work well for samples whose thickness is $< \frac{\lambda}{4}$, it is not well suited for significantly larger samples. Specifically, samples whose thickness is a multiple of half a wavelength and exhibit low loss cause algebraic instability as S_{11} tends towards zero [80,85]. As an attempt to resolve this instability, various adaptations of the core NRW approach have been proposed. Baker-Jarvis *et al* treat the NRW method as a global optimisation problem [80], proposing an iterative approach whereby a tuning parameter, κ, is introduced as a ratio between the uncertainty in S_{21} and the uncertainty in S_{11}, along with an initial guess for the permittivity. Using their adapted method, larger scale samples can be used, and in fact are preferable. Non-iterative approaches have also been proposed, most notably by Boughriet *et al* [84], who introduce a pair of interim parameters based on the equivalent wavelength in an empty sample holder.

More recently, the NRW method has been used to estimate the dielectric constant of various samples of concrete over a wideband measurement up to 10GHz [86]. McGraw's findings align broadly with expectations. The wet concrete exhibits dispersive behaviour whereas dry concrete does not. This result has been corroborated using software directly built into modern VNAs [87].

A separate transmission line approach, utilising only S_{21}, is to treat a single concrete block sample as a rectangular dielectric waveguide. For an object to function effectively as a waveguide, the electric field outside the waveguide must be evanescent. This imposes a boundary value problem on the allowed electric field inside the guide that ultimately culminates in modal propagation tied directly to the geometry of the waveguide.

At specific wavelengths, the electric field at the waveguide boundaries will drop to zero, this corresponds to specific cutoff frequencies. The cutoff frequencies for the propagation can be utilised to extract the material permittivity directly [58,64], although it should be noted that only using the cutoff frequency does not provide information about the conductivity of the material. To extract the conductivity term, one must calculate the Q value for the cutoff trough [88]. It should also be noted that the extracted values for permittivity are only known at the cutoff frequencies, making this method ill-suited for wide-band measurements.

While there are a few pieces of work [67,86,89], closed transmission lines are rarely used to evaluate concrete. This is primarily due to high dielectric loss and the need to shave down the sample to fit inside a sample holder. As concrete samples get smaller, it becomes more difficult to describe them as homogeneous therefore it is important that as large a sample as possible is used.

3.1.3 Forward Scattering

As mentioned, these techniques often incorporate the material sample directly into a coaxial circuit, as this provides a much brighter and less noisy signal. However, with radar, such a measurement scenario is less than ideal. Ghodgaonkar, Varadan, and Varadan [82] proposed a small modification to the existing NRW methodology in order to accommodate a material sample disconnected from the probes, as part of an open circuit. By modelling the focal plane of the transmitter and receiver, and judicious time-domain gating, the S parameters, and by extension the material properties, can be accurately extracted. Conceptually, this is similar to forward scattering methodologies [90–92], wherein two antennas are placed on either side of the sample. By comparing the obscured signal to a free space measurement, the complex transmission and reflection functions are directly calculable. To calculate the permittivity from the transmission through the material, the thickness of the material must be known. Therefore, the complex reflectivity is more useful. Complex reflectivity can be established directly from backscatter, so the forward scattering approaches present little benefit over other established methods.

In this chapter, three different extraction techniques are used. The first is via an analysis of the cutoff frequencies of a single block. This sort of approach has, to my knowledge, not yet been implemented with regards to concrete, although it has been used to estimate compressive strength [93]. Secondly, an NRW approach is implemented using the same concrete block. The original intention was to develop a rapid large scale NRW technique operating over a large bandwidth. Finally a radar based backscatter approach is taken to evaluate the expected refractive index for a large structure over a specific wideband frequency range.

3.2 Material Choice

For this work, non-reinforced Cemex 1400 lightweight concrete aggregate blocks [94] are used throughout, with quoted dimensions of 215x440x100mm, although, as will be seen in Chapter 3.5, these value are not exact.

The rationale behind this choice is two-fold. Firstly, concrete is an extremely common building material, both in the UK and internationally. Secondly, a concrete block is, in general, electrically thick at microwave frequencies, leading to less interference due to edge effects.

The general material mixture for concrete is cement, sand, water, and an aggregate (typically crushed stone). The concrete block can therefore be described as a combination of a microhomogeneous host material (cement, sand, and water) and a macrohomogeneous perturbation material (aggregate).

While mixing ratios and material choices are broadly consistent between manufacturers, the exact composition will vary depending on manufacturer, and indeed on a per batch basis. This makes effective medium approximations, such as the Maxwell-Garnett approximation [95], and those used by Dobson and Hallikainen [96] untenable, as the mixing ratio and particle sizes are rarely known in advance. It is for this reason that literature concerning the electrical properties of concrete typically only considers the effective properties.

For dry non-reinforced concrete blocks, the effective material permeability is similar to that of free space [57, p.251]. The effective relative permeability is therefore approximately 1. At low frequencies ($f < 1\text{GHz}$), the permittivity of the material can vary significantly [66,67] as a function of frequency. At higher frequencies, however, the material appears to exhibit a constant permittivity [76,86,97,98].

At frequencies greater than 1GHz, the effective relative permittivity of non-reinforced concrete ranges from 2 to 9 [59,67,90,99–101]. The effective refractive index for dry non-reinforced concrete therefore ranges from $\sqrt{2}$ to 3.

It is worth noting that the addition of water, or indeed almost any liquid, increases the refractive index of the material. This can be thought as being due to the high refractive index of the liquid dragging up the average. The addition of moisture also causes the concrete to become dispersive [67,86,97,102] and drives up the loss tangent of the material. For this reason, it is important that the material be dry, otherwise radar measurements become defocused and quite dim, even for single pulse measurements.

3.3 Cut-Off Frequency Analysis

This subsection details a series of measurements concerning a single concrete block. The motivation behind this is twofold, firstly as a means to obtain a value for the refractive index of the concrete, so that there is something to compare to in Chapter 4, and secondly to give some insight into how the properties of the concrete change with water content.

A lightweight methodology for extracting permittivity from a material is to treat a sample of the material as a rectangular dielectric waveguide. A single concrete block, chosen to be representative of the entire batch, was used. Conventionally, the material under test is shaved down to a specific size, in order to accommodate a predefined number of modes and fit inside a measurement system. However, in this case, reducing the size of the concrete is problematic, due to a desire to maintain the structural integrity of the material, and due to smaller sample sizes being less homogeneous, and therefore less representative of the concrete batch as a whole. For these reasons, the block was kept intact.

Firstly, the block was thoroughly dried by placing it into a ventilated oven at a low temperature of 80$^{\text{o}}$C for 2 hours, then allowed to cool overnight. This drives off moisture without the risk that the block may crack. Finally, two small holes were drilled into the block with a longitudinal separation by 28.4cm.

Two 16.4mm coaxial probes, tuned to a frequency range of 50-510MHz, were inserted into these holes as shown in Figure 3-1. The block is situated atop a metal baseplate. This forces a strong reflection and doubles the effective thickness of the concrete block. The probes are connected to a HP8719C Vector Network Analyser , calibrated using a full 2-port calibration.

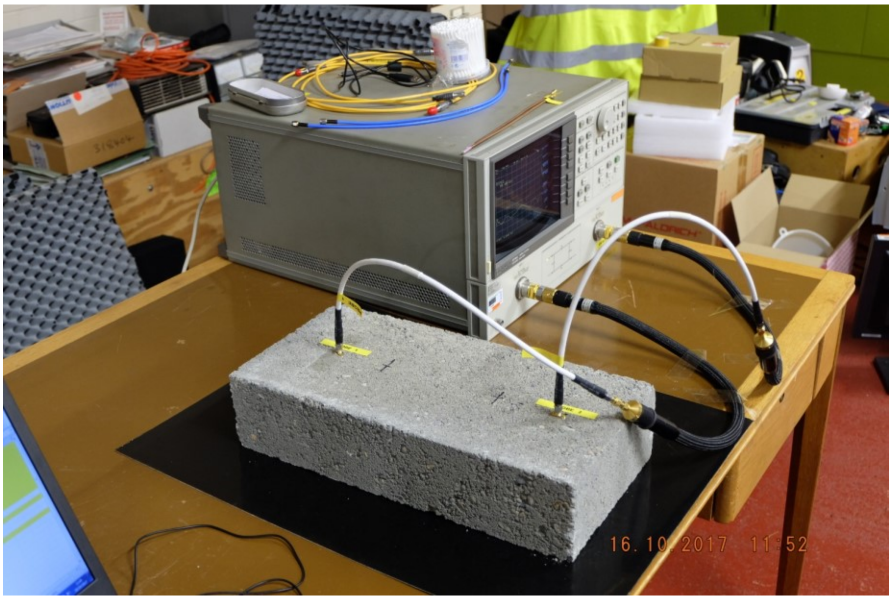

Figure 3-1 – Photograph showing the concrete sample block and coaxial probes. The block is situated atop a metal baseplate; this doubles the effective thickness of the block.

Following Balanis [58, pp.408–423], the S_{21} scattering through the block experiences periodic nulls where there is no propagation. These nulls are calculated by imposing strict boundary conditions on the waveguide, namely that there is no longitudinal propagation at the waveguide boundaries. This, in turn, imposes the condition that field inside the waveguide follow strict harmonics.

From Balanis [58, p.415,419] a slab dielectric waveguide of height $2h_{guide}$ experiences modal cut-off frequencies for both TE and TM propagation following the same formula[4]:

---

[4] The original equation in [58] for the modal cut-off frequencies is $F_{c_u} = \frac{u}{4h_{guide}\sqrt{\mu\varepsilon-\mu_0\varepsilon_0}}$. Equations 3-3 and 3-4 have both been multiplied by a factor of ½. This is because

$$F_{c_u}(\varepsilon,\mu,h_{guide}) = \frac{u}{8h_{guide}\sqrt{\mu\varepsilon - \mu_0\varepsilon_0}} \qquad \textbf{3-3}$$

$$F_{c_u}(\varepsilon,\mu,h_{guide}) = \frac{uc}{8h_{guide}\sqrt{\mu_r\varepsilon_r - 1}} \qquad \textbf{3-4}$$

Where c is the speed of light in free space, and u is a positive integer referring to the harmonic mode of propagation. I.e. $u = 1,2,3$ .... If one were to assume the material is non-magnetic, then equation 3-4 can be further simplified to:

$$F_{c_u}(\varepsilon,h_{guide}) = \frac{uc}{8h_{guide}\sqrt{\varepsilon_r - 1}} \qquad \textbf{3-5}$$

There is the special case, where $u = 0$, this fairly obviously corresponds to a cutoff frequency of 0 and therefore the zeroth mode will always propagate unattenuated.

From equation 3-5, the relative permittivity, ε_r, for a non-magnetic waveguide is derived:

$$\varepsilon_r = \left(\frac{uc}{8h_{guide}F_{c_u}}\right)^2 + 1 \qquad \textbf{3-6}$$

A dimensional analysis of equation 3-6 shows that the relative permittivity of the material is a unitless quantity, exactly as one would expect from a ratio.

The thickness of the concrete slab must be established. Using a digital calliper, the thickness of a multiple different concrete blocks was measured at 100 different positions. This produced the distribution shown in Figure 3-2. The mean value of the measurements is a thickness of 96.6mm, less than the 100mm stated by the distributor. The standard deviation associated with the distribution is 0.322mm. This standard deviation implies that the thickness of the wall material is more precisely known than any other variable. From this, the thickness of a concrete block, and hence a concrete wall is:

$$2h_{guide} = \delta = 96.6 \pm 0.322\text{mm} \qquad \textbf{3-7}$$

---

the metal baseplate acts as a strong reflector, consequently, a wave must traverse the waveguide twice. This doubles the effective thickness of the waveguide, from $2h_{guide}$ to $4h_{guide}$.

There are two caveats with this approach. Firstly, cavities are unaccountable, since a calliper cannot measure the depth of cavities. Secondly, since humans cannot properly sample random distributions, there is some unintentional bias in these measurements. In this case, large pebbles were most likely subconsciously avoided to some extent due to the difficulty in aligning the calliper with said pebble. In addition the edges of the blocks are also under represented. For these reasons, the probability distribution will have a slightly larger standard deviation than what has been measured.

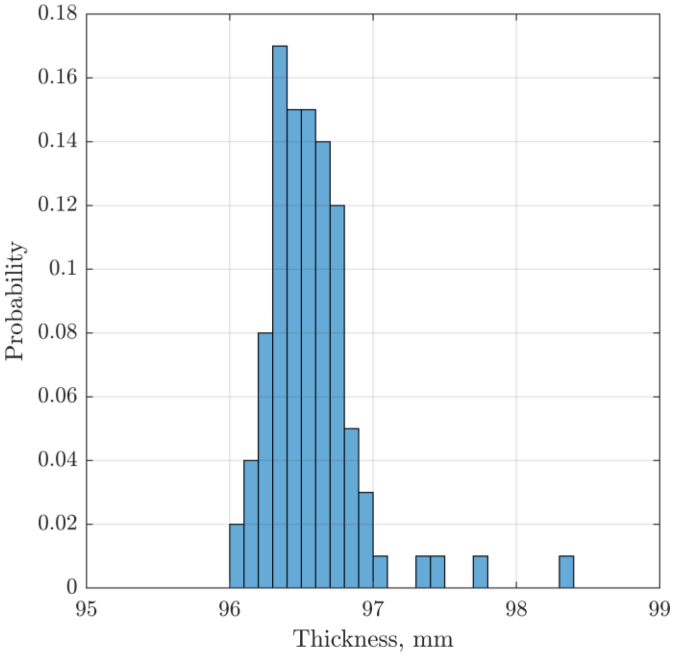

Figure 3-2 – Histogram of the thicknesses of 100 positions along the wall. The mean of the distribution is 96.6mm with a standard deviation of 0.322mm. The mean thickness of the concrete blocks is less than the quoted value of 100mm from the distributor.

When dry, the relative permittivity of the concrete slab was measured to be 5.89. This corresponds to a refractive index of 2.43. This is well within expected bounds for non-reinforced concrete. This was obtained from a TE_1 mode at a cutoff frequency of 0.1764GHz (Figure 3-3). The Q value associated with the cutoff frequency is 6.02. The loss tangent is therefore approximately $\frac{1}{6}$. This is again within the expected range for dry concrete [59, pp.8–9].

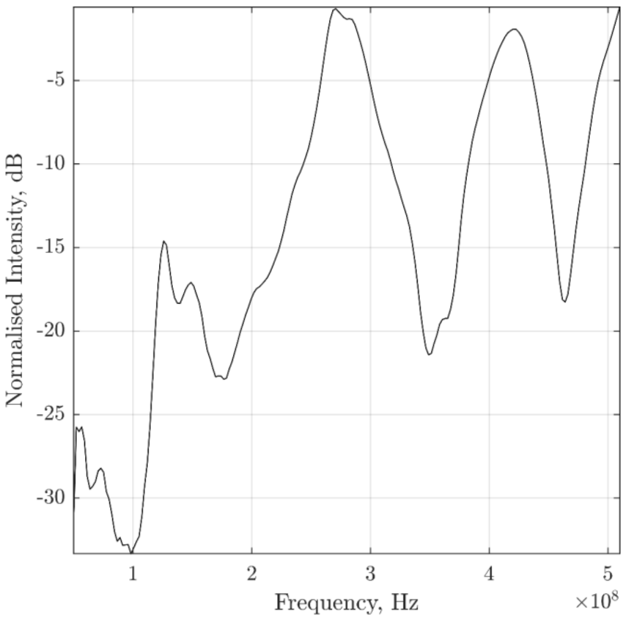

Figure 3-3 – S_{21} Frequency spectrum of the dry concrete block. The first TE mode appears at 0.1764 GHz, with a Q value of 6.02.

An error analysis of equation 3-6 now needs to be performed. The variables u and c are both known exactly, leaving the only sources of error being those associated with the height of the slab, and the cutoff frequency. Following standard rules for error propagation [103], the uncertainty associated with ε_r is:

$$\Delta\varepsilon_r = \sqrt{\left(\frac{\partial\varepsilon_r}{\partial h_{guide}}\Delta h\right)^2 + \left(\frac{\partial\varepsilon_r}{\partial F_{c_u}}\Delta F_{c_u}\right)^2} \tag{3-8}$$

$$\Delta\varepsilon_r = \sqrt{\left(-\frac{u^2c^2\Delta h_{guide}}{32h_{guide}^3F_{c_u}^2}\right)^2 + \left(-\frac{u^2c^2\Delta F_{c_u}}{32h_{guide}^2F_{c_u}^3}\right)^2} \tag{3-9}$$

Where Δ denotes an uncertainty in the associated variable. This simplifies to

$$\Delta\varepsilon_r = \frac{u^2c^2}{32F_{c_u}^3h_{guide}^3}\sqrt{\Delta h^2F_{c_u}^2 + \Delta F_{c_u}^2h_{guide}^2} \tag{3-10}$$

The uncertainty associated with the block thickness is 0.322mm. The uncertainty associated with the cut-off frequency is harder to estimate, the metric used herein is the 3dB width of the cut-off trough. For the dry concrete sample, this is 0.0293GHz. Substituting these numbers into equation 3-10 gives an uncertainty of 1.6, corresponding to an approximate 27% uncertainty. To decrease this uncertainty, one would need to increase the thickness of the material or use a higher mode. Changing the thickness of the material is possible by stacking blocks on top of each other, however this would introduce a distinct discontinuity in the material. Using a higher mode is also possible, however as seen in Figure 3-7, the 3dB width increases with mode in wet samples.

3.3.1.1 Graphical Solutions

Following Balanis, the modal cut-off frequencies can be expressed graphically by noting that the total phase term is the magnitude of its components:

$$\beta_y^2 + \beta_z^2 = \beta^2 \qquad \textbf{3-11}$$

$$\beta_z^2 - {\alpha_y}_0^2 = \beta_0^2 \qquad \textbf{3-12}$$

and therefore an equation for a circle is established:

$$\alpha_{y_0}^2 + \beta_y^2 = \beta^2 - \beta_0^2 = \omega^2(\mu\varepsilon - \mu_0\varepsilon_0) \qquad \textbf{3-13}$$

Where α_{y_0} and β_y are equal to[5]:

$$\alpha_{y_0} = \begin{cases} -\dfrac{\varepsilon_0}{2\varepsilon h}(2\beta_y h_{guide})\cot(2\beta_y h_{guide}) & \text{Even} \\ \dfrac{\varepsilon_0}{2\varepsilon h}(2\beta_y h_{guide})\tan(2\beta_y h_{guide}) & \text{Odd} \end{cases} \qquad \textbf{3-14}$$

$$\frac{(u-1)\pi}{2} \le \beta_y \le \frac{u\pi}{2} \qquad \textbf{3-15}$$

Following this, if one were to plot ${\alpha_y}_0$ against β_y then the moment the plot crosses a circle of radius $\omega^2(\mu\varepsilon - \mu_0\varepsilon_0)$ the modal phase term and attenuation term for each mode can be read off.

This is a useful because it allows for the extraction of the attenuation decoupled from the quality of the measurement data. Plotting these functions for the three modes with cut-off frequencies less than 0.5GHz shows that the attenuation term for the first and most

---

[5] Again, the height of the block has been doubled from Balanis's original equation due to the metal baseplate. For clarity, the factors of 2 have not been cancelled.

dominant TE mode is 11.1 Npm^{-1}, and 10.9 Npm^{-1} for TM. The attenuation term decreases at higher order modes. This leads to shallower cutoff troughs and a less defined signal, an observation that is corroborated in Figure 3-3 and Figure 3-7. For this reason it is best to use low frequency measurements for this technique.

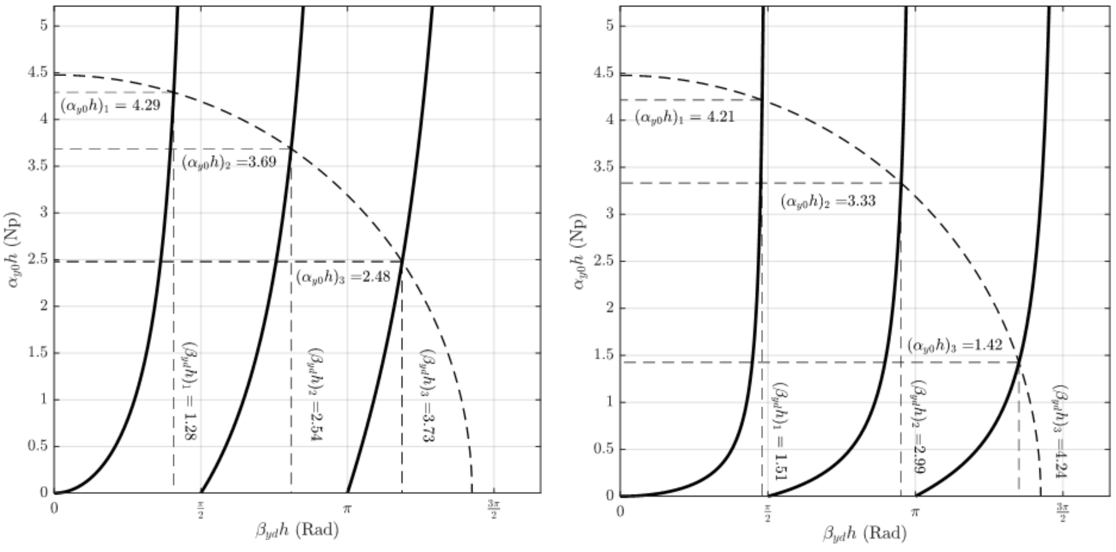

a) b)

Figure 3-4 – Graphical solutions to the waveguide propagation for first 3 cutoff frequencies of the a) TE modes and b) TM modes, given a block thickness of 96.6mm, a relative permittivity of 5.89.

3.3.2 Moisture Content Analysis

Adding moisture to the concrete, in addition to the water used in the concrete mix, directly affects the permittivity and conductivity of the material. To investigate this effect, deionised water was added to the concrete. The S_{21} measurements were repeated periodically throughout a 5 day timeframe, from which the permittivity is extracted. This provides a way to relate the permittivity of the material directly with its water content at roughly the same frequency.

Figure 3-5 – Photograph showing the concrete sample block being soaked with 5% by mass of deionised water.

The mass of the dry concrete block was measured using a Mettler PE16 weight scales, accurate to 0.1g. The dry mass of the concrete was 15.9074Kg. To investigate the change in permittivity of the concrete as the moisture content changes, 795.8g of deionised water was added to the concrete. This corresponds to roughly 5% of the mass of the block. The Mettler scales have an upper weight limit of 16Kg, thus, to measure the drying rate of the concrete, a separate block was dried then split in half. Each half was saturated with water corresponding to 5% of their mass, 373.7g and 393.4g respectively. Using both half blocks, the mean density was then periodically recorded and from that, the drying rate of the concrete material was derived. To minimise errors, the two half blocks were kept in the same location, placed on a similar metal sheet to the full block, and were moved as little as possible.

Due to the blocks being stored inside, there is little airflow. The mean temperature of the room was 19.6°C with a mean humidity of 66.1%. Over a 120 hour period, the density of the concrete was recorded. Figure 3-6 shows that the measurement data falls neatly onto an exponential decay, rapidly drying as the surface moisture evaporates and slower when there is less total moisture.

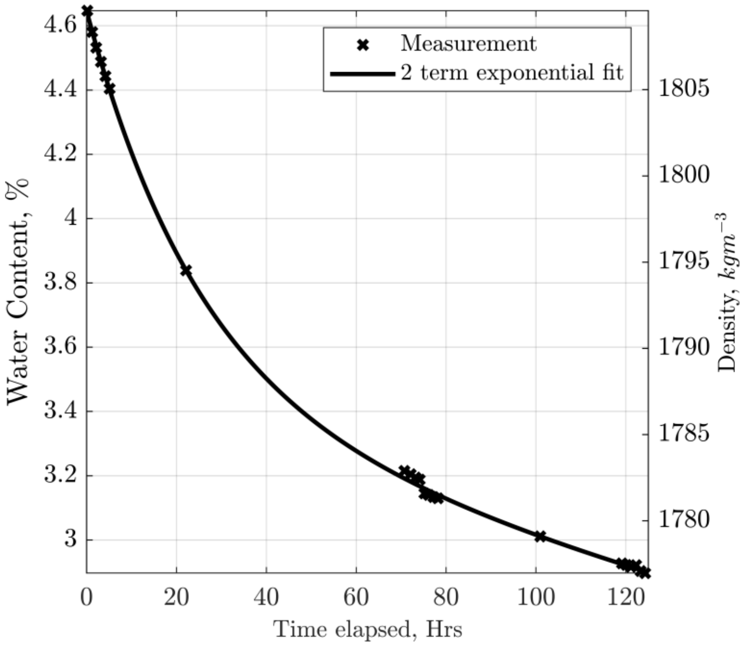

Figure 3-6 – Graph showing the change in moisture content of the reference block as a function of time. The trend follows an exponential decay of form $y = Ae^{Bx} + Ce^{Dx}$.

A two-term exponential curve of the form $y = Ae^{Bx} + Ce^{Dx}$ was fitted to Figure 3-6 using the Levenberg-Marquart algorithm. The coefficients, A, B, C, and D are 0.08056, -1.896, 3.146, and -0.06828 respectively. Note that there is no constant term; this is because as time tends towards infinity, the water content must tend towards 0. From this, an empirical equation for the moisture content is established:

$$w = Ae^{Bt} + Ce^{Dt} + (w_0 - A - C) \tag{3-16}$$

$$w = 0.08056e^{-1.896t} + 3.146e^{-0.06828t} + (w_0 - 3.2311) \tag{3-17}$$

where w_0 is initial water content of the concrete as a percentage of the mass of the concrete blocks and t is the drying time in hours. The empirical equation 3-17 has no explicit consideration of the temperature, humidity or airflow in the local environment around the block. In this sense it is a bespoke fit, unique to this scenario. To generate a general equation, one would need to know: the porosity, the aggregate size, the temperature, humidity, airflow, salinity of the material,

The S_{21} transmission through the block and the S_{11} resonance have been measured periodically as the concrete block dries. The block was left for several days to simulate the natural drying of the material. During this time, the probes were left in place to reduce error. The resonance modes were observed in the S_{11} measurements but were heavily influenced by noise, thus were discarded. The S_{21} measurements show a gradual change in the modal frequencies as well as the amplitude of the signal as the concrete block dries. This would indicate that there is also a gradual change in the permittivity of the material.

Using all the S_{21} measurements, the permittivity is extracted for each measurement via equation 3-4. The loss tangent, tan(δ), can also be estimated using the S_{21} measurements by calculating the Q values associated with the cutoff trough:

$$\tan(\delta) = \frac{1}{Q} = \frac{\Delta \mathrm{f}_{3\mathrm{dB}}}{f_c} \qquad \textbf{3-18}$$

where f_c is the frequency of the null and Δf_{3dB} is the 3dB bandwidth of said null. Recall that the error in frequency used in equation 3-10 is the 3dB width of the trough. The fractional error in frequency is therefore also the loss tangent.

The frequency range of 0.1Ghz to 0.155GHz has been identified as containing the first cutoff frequency. In Figure 3-7 a select few of the measurements are shown. The cutoff frequency troughs are seen to migrate very slightly around 0.14-0.15GHz. This would indicate that there is little change in the material permittivity.

For each measurement, the minima are identified and the corresponding cutoff frequency extracted. The cutoff frequencies are used in equation 3-4 to produce an estimate of the real part of the complex relative dielectric. Due to the sparsity of the frequency collection in the S_{21} measurements, the dielectric approximations were seen to oscillate between two values. Therefore, to improve the quality of the dielectric approximation the S_{21} spectrum is upsampled via zero padding. The extracted values for the relative permittivity are presented in Figure 3-8 as a function of moisture content, showing that there is a gradual increase in material permittivity with respect to moisture content. To provide more insight, the uncertainty associated with the extracted values is calculated and included as error bars. The error bars are not sufficient to draw a meaningful line of best fit between the datapoints. Therefore, one has not been included.

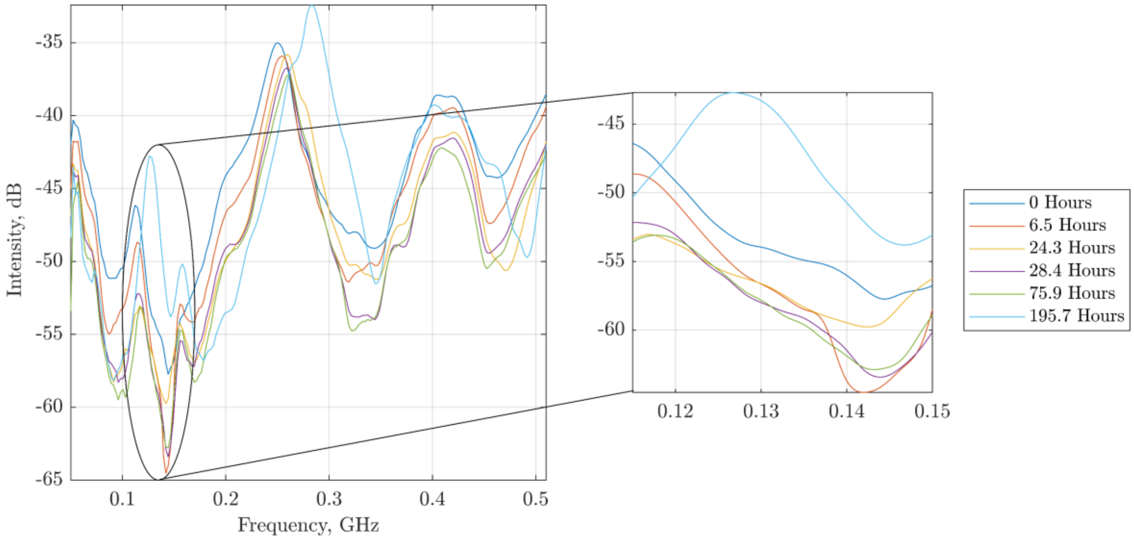

Figure 3-7 – A select few of the spectra taken as the block dries. The cutoff frequency nulls are shown to become more distinct and migrate slightly as the block dries. This indicates that the loss tangent is decreasing.

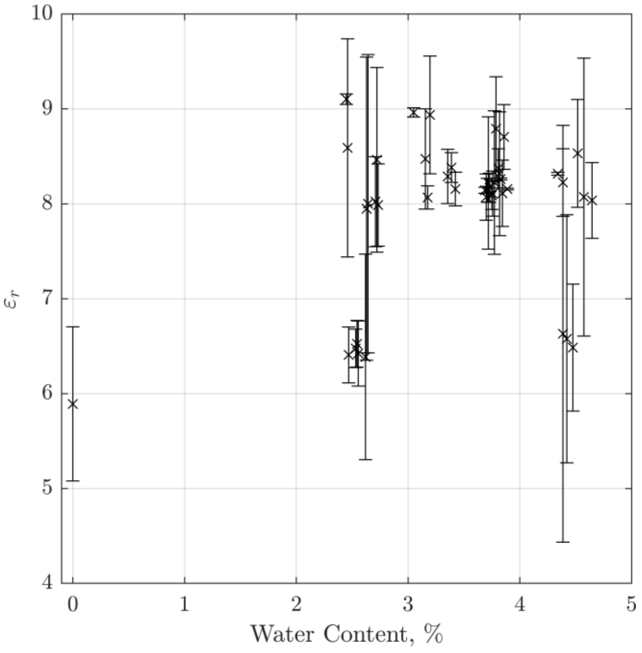

Figure 3-8 – Relative permittivity with respect to moisture content. The values for ε_r, and their associated error bars indicate that there is no obvious trend between sequential measurements.

The Q values of the measurements are presented in Figure 3-9 and are quite disparate. One would expect the Q values to increase as the block dries, as this would correspond with a decreasing loss tangent. However, this is not the case for these measurements. In fact, if you squint hard enough, you could claim the opposite. The wide spread of values make it difficult to reliably infer information about the loss tangent, and hence the conductivity of the material. For a cut off frequency $F_{c_u} \pm \frac{\Delta \mathrm{f}_{3\mathrm{dB}}}{2}$, the Q values can be interpreted as analogous to the fractional uncertainty in cut off frequency. Since the fractional uncertainty in thickness is negligible (0.3%) when compared to the cut off frequency, equation 3-10 can be simplified and rewritten in terms of the loss tangent:

$$\varepsilon_r - 1 = \left(\frac{uc}{8h_{guide}}\right)^2 F_{c_u}^{-2} \tag{3-19}$$

$$\frac{\Delta(\varepsilon_r - 1)}{\varepsilon_r - 1} = \frac{\Delta\mathrm{\varepsilon_r}}{\varepsilon_r - 1} = \frac{2\Delta F_{c_u}}{F_{c_u}} \tag{3-20}$$

$$\frac{\Delta\mathrm{\varepsilon_r}}{\varepsilon_r - 1} = \tan(\delta) \tag{3-21}$$

This is what is illustrated in Figure 3-9. The variation in Q value corresponds to the variation in uncertainty associated with the relative permittivity shown in Figure 3-8.

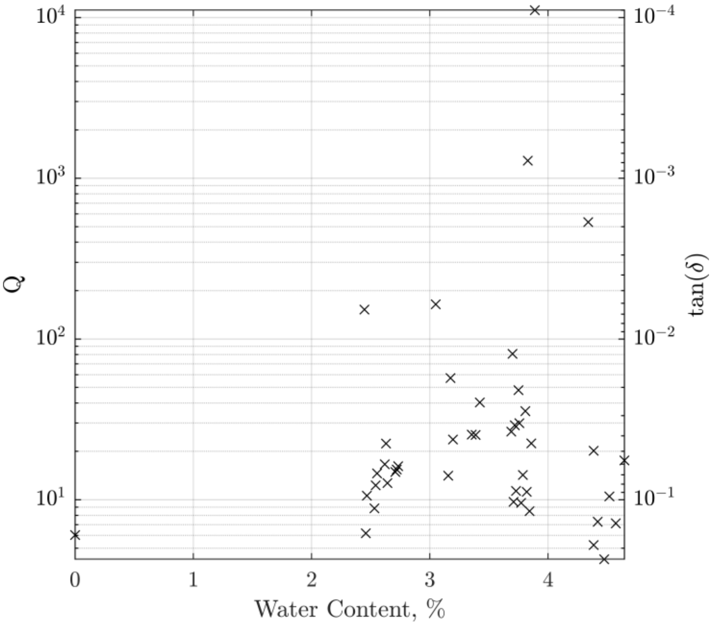

Figure 3-9 – Q values for the TE$_1$ modal cutoff frequency trough as a function of moisture content. Ideally, the Q value would increase as the block dried however, that is not the case here. The disparate nature of the Q values makes it difficult to infer any meaningful information concerning the conductivity of the material.

There is a notable lack of measurements below 2% water content. This is due primarily to time constraints. Unfortunately, this means that the curve fitting performed for Figure 3-8 should be taken with some scepticism.

In summary, treating the concrete block as a slab waveguide and using the cutoff frequencies to extract values of the permittivity for the block produces sensible numbers for the permittivity, albeit with disparate values for Q. The values for relative permittivity range from 5.9 to 9 as water is added. This trend of increasing permittivity is in agreement with other literature, although the lack of measurements with less than 2% water content causes some concern with regards to the reliability of the curve fitting.

3.4 Rapid Nicholson-Ross-Weir Method

Since the metric presented in the previous section is best suited to low frequency narrowband measurements centred on specific frequencies, a different approach should be taken.

As mentioned in Chapter 3.1, the Nicolson-Ross-Weir method is a well-established technique for explicitly defining the permittivity and permeability of a material sample. The NRW method is well suited for wideband measurements, so therefore it is an appropriate technique to extract information about the concrete's relative permittivity, permeability, and dielectric loss.

Despite the NRW technique usually using comparatively small samples, it was decided that a full-sized concrete block should be used. The rationale behind this is two-fold: a small sample is less representative of the whole concrete batch, and the smaller a sample becomes, the less homogeneous it gets. With this in mind reducing the size the concrete sample would no longer be representative of the batch.

3.4.1 Theoretical Model

The general form of the technique, as described by Nicolson and Ross, relates the reflection coefficient of a material to its characteristic impedance, and from there equates measured values of S_{11} and S_{21} directly to the material properties.

Consider a slab dielectric sample illuminated by some input signal, shown in Figure 3-10. There is some input signal, E_{In}, that then traverses a material of a specific thickness, d, before being ejected out the other side as E_{Out}. Throughout this traversal, energy is reflected at each material boundary. This leads to reflections both inside and outside the material.

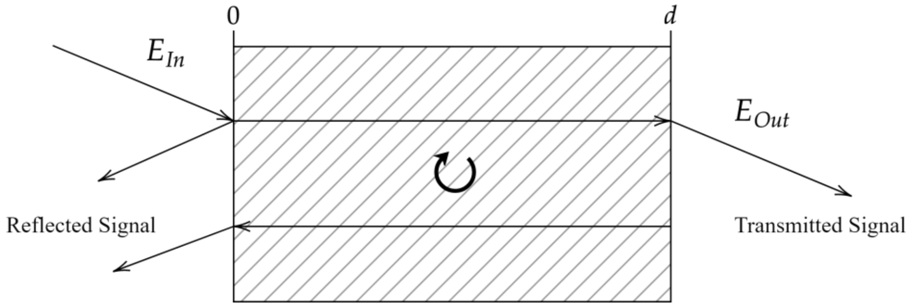

Figure 3-10 – Illustration of the internal reflections due to transmission through a slab dielectric of thickness d.

When an EM wave passes from one medium to another, the reflection coefficient, Γ, can be defined in terms of the impedance mismatch between the two media:

$$\Gamma(\varepsilon_1, \varepsilon_2, \mu_1, \mu_2) = \frac{Z_2(\varepsilon_2, \mu_2) - Z_1(\varepsilon_1, \mu_1)}{Z_2(\varepsilon_2, \mu_2) + Z_1(\varepsilon_1, \mu_1)} \quad \textbf{3-22}$$

In equation 3-22, Z_1 and Z_2 refer to the characteristic impedances of the two media. Rearranging the equation gives the reflection coefficient in terms of the relative permeability and permittivity, μ_r and ε_r respectively.

$$\Gamma(\varepsilon, \mu) = \frac{\sqrt{\frac{\mu_r}{\varepsilon_r}} - 1}{\sqrt{\frac{\mu_r}{\varepsilon_r}} + 1} \quad \textbf{3-23}$$

$$\sqrt{\frac{\mu_r}{\varepsilon_r}} = \frac{1 + \Gamma}{1 - \Gamma} \quad \textbf{3-24}$$

Following Figure 3-10, the scattering coefficients for the reflected signal S_{11}, and the transmitted signal S_{21} can be defined in terms of the transmission function, $z = e^{-\gamma d}$ [104]:

$$\mathrm{S}_{21} = \frac{(1-\Gamma^2)z}{1+\Gamma^2 z^2} \tag{3-25}$$

$$\mathrm{S}_{11} = \frac{(1-z^2)\Gamma}{1+\Gamma^2 z^2} \tag{3-26}$$

Where γ is the complex propagation constant, defined as $\gamma(f) = \alpha(f) + i\beta(f)$. The propagation term has been described extensively in the literature [52,57,58,105] and a derivation for which has been included in appendix A.1.

At this stage, a couple of additional variables are introduced, both in order to make the following equations syntactically simpler and to comply with conventional norms:

$$A = S_{21} + S_{11} \tag{3-27}$$

$$B = S_{21} - S_{11} \tag{3-28}$$

From equations 3-25 and 3-26, the transmission function, z, can be equated to the measured scattering parameters, rather than as an exponential:

$$\mathrm{z} = \mathrm{e}^{-\gamma \mathrm{d}} = \frac{A-\Gamma}{1-A\Gamma} \tag{3-29}$$

and the reflection coefficient as:

$$\Gamma = \chi \pm \sqrt{\chi^2 - 1} \tag{3-30}$$

where χ is defined as:

$$\chi = \frac{1-\mathrm{AB}}{\mathrm{A}-\mathrm{B}} \tag{3-31}$$

Plugging the reflection coefficient into the transmission function allows for the explicit calculation of the material properties as follows:

$$\gamma = \frac{-\ln\left(\frac{A-\Gamma}{1-A\Gamma}\right)}{d} \tag{3-32}$$

For a coaxial line, equation 3-32 can be rearranged to give the material properties, however, for a rectangular waveguide, the propagation term is constrained by the waveguide boundaries. It is therefore also constrained by the cut-off frequency of the mode. Derived in Appendix A.2 and taking the same syntax style as Weir and Morrow [69,70], the following equation is defined:

$$\frac{1}{\Lambda^2} = \left(\frac{\varepsilon_r \mu_r}{\lambda^2} - \frac{1}{\lambda_c^2}\right) = \left(\frac{i \ln\left(\frac{A - \Gamma}{1 - A\Gamma}\right)}{2\pi d}\right)^2 \qquad \textbf{3-33}$$

The terms λ and λ_c represent the free space frequency of interest and the cutoff wavelength in the material. Note that both these wavelengths are independent of the actual material properties, so no assumption about the material needs to be made.

From equation 3-33, the relative permeability and relative permittivity of the waveguide material are:

$$\mu_r = \frac{1 + \Gamma}{\Lambda(1 - \Gamma)\sqrt{\frac{1}{\lambda^2} - \frac{1}{\lambda_c^2}}} \qquad \textbf{3-34}$$

$$\varepsilon_r = \frac{\lambda^2}{\mu_r}\left(\frac{1}{\Lambda^2} + \frac{1}{\lambda_c^2}\right) \qquad \textbf{3-35}$$

It is well known that the NRW method is algebraically unstable at low intensities. In particular as S_{11} tends to 0, χ tends to ∞, and by extension so does the reflection coefficient. Following the non-iterative solution to this problem presented by Boughriet *et al* an interim set of properties for the material are established:

$$\mu_{r_{eff}} = \left(\frac{1 + \Gamma}{1 - \Gamma}\right)\frac{\lambda_g}{\Lambda} \qquad \textbf{3-36}$$

$$\varepsilon_{r_{eff}} = \left(\frac{1 - \Gamma}{1 + \Gamma}\right)\frac{\lambda_g}{\Lambda} \qquad \textbf{3-37}$$

From this, the actual properties of the material are established as:

$$\mu_r = \mu_{r_{eff}} \qquad \textbf{3-38}$$

$$\varepsilon_r = \left(1 - \left(\frac{\lambda}{\lambda_c}\right)^2\right)\varepsilon_{r_{eff}} + \left(\frac{\lambda}{\lambda_c}\right)^2 \frac{1}{\mu_{r_{eff}}} \qquad \textbf{3-39}$$

The parameter λ_g is used to represent the wavelength in an empty guide:

$$\lambda_g = \left(\frac{1}{\lambda^2} - \frac{1}{\lambda_c^2}\right)^{-\frac{1}{2}} \qquad \textbf{3-40}$$

In a non-magnetic material $\mu_r = 1$ therefore, the following generalised equation for the interim permittivity can be established:

$$\varepsilon_{r_{eff}} = \left(\frac{1-\Gamma}{1+\Gamma}\right)^{q-1} \left(\frac{\lambda_g}{\Lambda}\right)^{q+1} \qquad \textbf{3-41}$$

This is the key finding of Boughriet *et al's* original paper, as it encompasses the original NRW approach ($q = 0$), the non-iterative solution ($q = 1$), and the so called Stuchly method ($q = -1$) [106].

As a final theoretical note, since γ depends on a complex logarithm, it has an infinite number of roots. Luukkonen *et al* [83] solved this issue by writing the logarithm in an iterative fashion whereby $\ln(e^{\gamma d}) = \ln(Ae^{i\phi}) = \ln(A) + i\phi$. The argument of the exponential is obtained via an iterative approach:

$$\phi_N = \phi_0 + \sum_{a=1}^{N} \arg\left(\frac{e^{\gamma_a d}}{e^{\gamma_{a-1} d}}\right) \qquad \textbf{3-42}$$

Combining this with equation 3-39 gives a solution to the NRW problem that is non-iterative, and has a specific root at each frequency of interest.

3.4.2 Experimental Work

Using the same measurement setup as Figure 3-1, with a dry block and the same coaxial probes, a calibrated measurement over the frequency range of 50MHz to 12GHz was undertaken, this time for both S_{11} and S_{21}.

Figure 3-11 shows the received intensity for both configurations. This shows three interesting phenomena.

1. The S_{11} measurement intensity is close to 0dB. This implies near total reflection at low frequencies. This is problematic as this implies that the relative wave impendence is infinite.

2. As one may expect, the S_{21} measurement intensity is smaller than the S_{11} intensity. This is problematic, since the reflection coefficient and each subsequent variable, will be dominated almost entirely by the S_{11} component. At the lower frequencies, there is an approximate -35dB difference between the intensities. At the higher frequencies, this difference grows to -80dB. This corresponds to the S_{21} intensity being less than 2% of the S_{11} intensity.
3. The noise floor is visible above 6GHz in the S_{21} intensity. Unfortunately, this limits the usable data. However, since the primary frequencies of interest are less than 6GHz, this does not pose much of a problem.

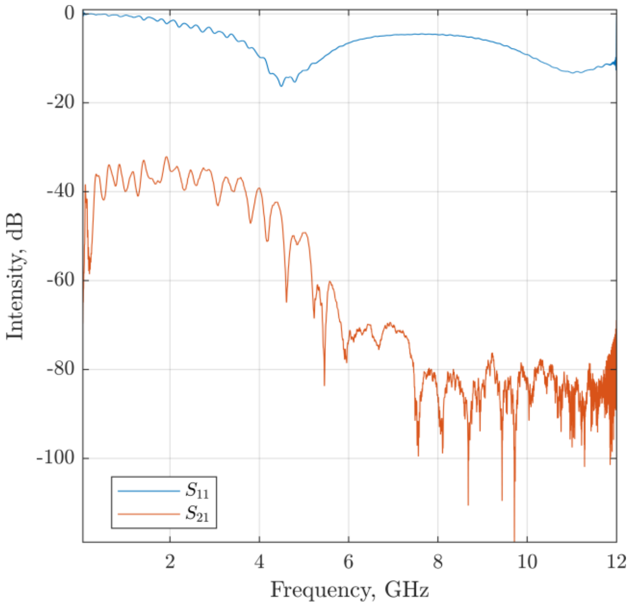

Figure 3-11 – Intensity of S_{11} and S_{21}. The system has been calibrated such that the cable propagation has been accounted for. At low frequencies, the difference between S_{11} and S_{21} is approximately -35dB. This dips to an approximate -80dB at higher frequencies.

Since the noise floor is visible above 6GHz, higher frequency data is discarded. From equations 3-27 and 3-28, the A and B terms are approximately related by $A \approx -B$. Plotting A and B shows this quite clearly:

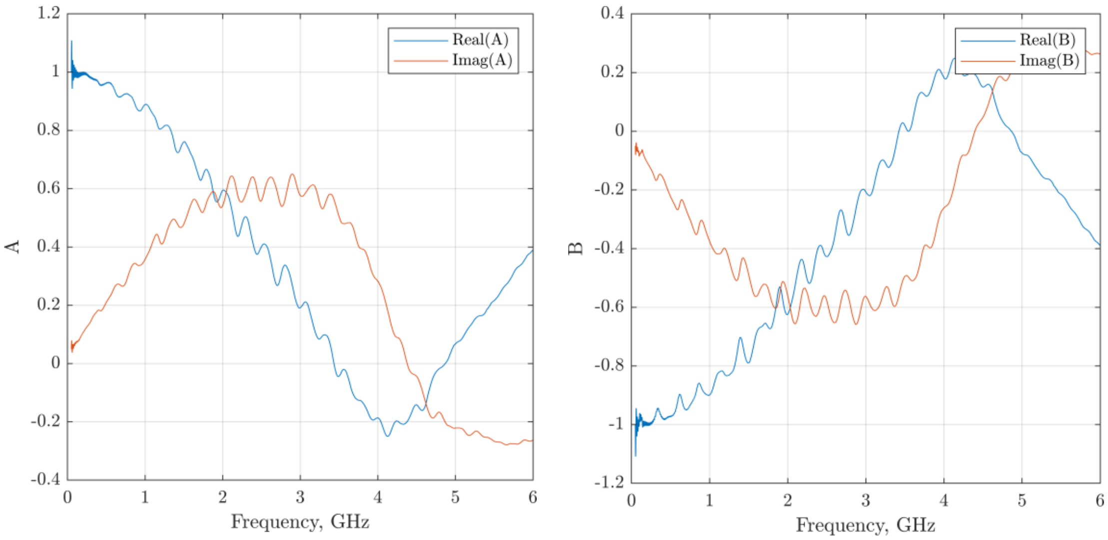

a) b)

Figure 3-12 – The interim parameters *A* and *B*, obtained from equations 3-27 and 3-28. The *A* parameter (a) is the negative of the *B* parameter (b).

The implication here is that there is, visually, little dependence upon the transmission measurement. As remarked in [83], as $S_{21} \rightarrow 0$, the angle in equation 3-42 becomes extremely sensitive to noise, and difficult to reliably extract. This poses a reliability problem for the entire approach.

The TE cutoff wavelengths were calculated using equation A-52 and known dimensions for the block. Since the cutoff wavelengths are independent of the material properties, there is no requirement that any prior assumption about the refractive index be made. However, to use equation 3-41 the material must be non-magnetic. This is a safe assumption for the dry non-reinforced concrete being used.

Plotting the real component of the relative permittivity, via equation 3-39, shows that there is an instability in the extraction process, leading to a variation in the extracted relative permittivity between 4 and 6. There is a greater instability at frequencies less than 1GHz. This is due to a small mismatch between the probes and the material. The problem is further exacerbated by the fact that the reflection coefficient is approximately 1 at the low frequencies.

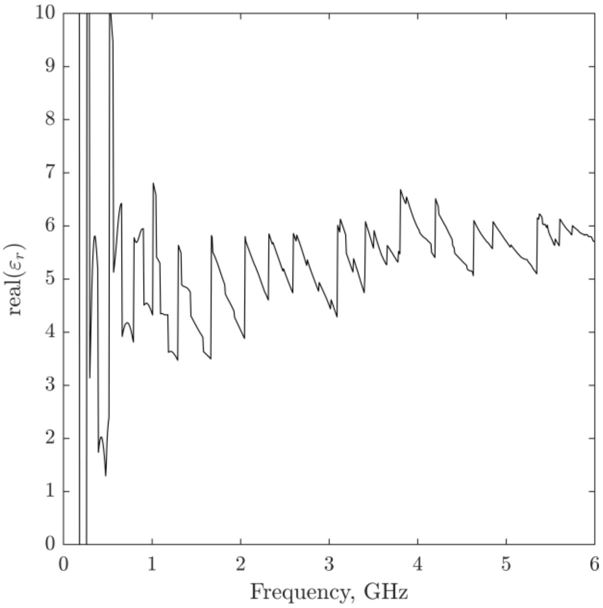

Figure 3-13 – Real component of the permittivity obtained via equation 3-39. There is a fair amount of uncertainty surrounding the extraction, due in part to the numerical instability arising from the small values of S_{21}. Realistically, the permittivity is somewhere between 4 and 6.

The spread of relative permittivity corresponds to a spread of refractive indices between 2 and 2.45. This is in agreement with the relative permittivity extracted via the cutoff frequency approach used previously, however not hugely precise.

Plotting the imaginary component of the relative permittivity highlights some additional problems. Figure 3-14 shows that the imaginary component of the relative permittivity exhibits the same low frequency instability as its real component. In addition, the imaginary component becomes negative at several points. This indicates that the material is experiencing a gain. Considering that the material is passive, this gain is physically infeasible.

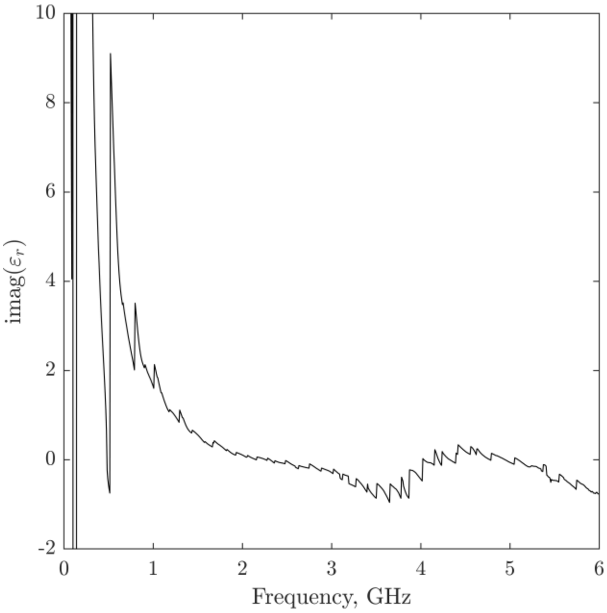

Figure 3-14 – Imaginary component of the relative permittivity. In some sense, this is a reassuring plot, as it indicates that the material is low loss. However, it is problematic since the material is passive. I.e. the imaginary component should be greater than 0.

Considering that the material appears to experience a gain, and the relative permittivity values are unstable, this implementation of the NRW method is not sufficient to give a workable measure of the material properties at the frequencies of interest. It is rather unfortunate that this doesn't give a sensible answer for the material properties, however it is sufficient to show that the real component of the dielectric is roughly constant across the wideband measurement, and in agreement with the previous methodology.

Originally the experiment was designed in the hopes of developing a less constrained NRW method, using a much larger waveguide than normal. Ideally, what should have been done was to use a smaller sample of material, in a closed loop. This would have increased the S_{21} transmission signal strength, subsequently reducing errors, at the expense of reducing the representitiveness of the sample with respect to the full concrete batch. Since the goal of this process was to obtain a reference measurement by which to compare later experimental results, using a small sample that is not representative of the material as a whole is not meaningful, so was not used.

3.5 TWR Trihedral measurement

Given that the NRW method fails to give a sensible result for complex relative permittivity, and the cutoff frequency analysis produces a value that is only representative around 0.2GHz, to get an estimate of the permittivity that is usable at a greater frequency, a different approach must be taken.

With a goal of quantifying the effects of introducing a wall into a radar measurement over the frequency range of interest (1GHz to 6GHz), an intuitive approach is to measure the effect on a single well-defined reference target. Ergo, a small experimental campaign was undertaken. This consisted of a series of single pulse measurements of a large 60cm trihedral both with no intervening wall and situated behind a one block thick concrete wall. The trihedral was placed on a polystyrene plinth with the point of the trihedral 71cm above ground. This is within half a centimetre of the height of the antennas. In addition the direct distance from the left and right antennas to the trihedral was 264.9cm and 264.6cm. From these measurements, the trihedral was deduced to be approximately the same height and directly in front of the radar antennas.

To isolate the trihedral signature, corresponding background measurements were also taken. These take the form of 1) a background measurement where there is no target of interest, 2) a measurement with a single trihedral shown in Figure 3-15, 3) a measurement with a small wall (and no trihedral) and finally 4) a measurement with the small wall and trihedral re-added to the scene. From these four measurements, both an unobscured and obscured measurement for the trihedral can be extracted. The wall signature can also be extracted. The coherent subtraction arrangement is shown in Figure 3-16.

a) b)

Figure 3-15 – a) unobscured and b) obscured trihedral placed a distance of 2.648m from the antennas. The height of the trihedral is 0.705m.

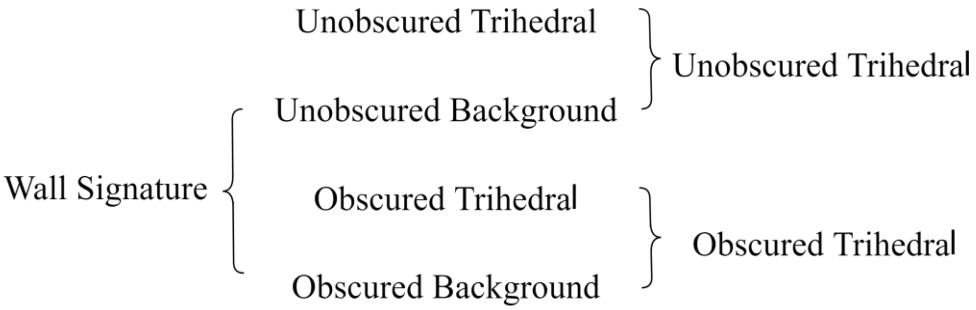

Figure 3-16 – Measurement diagram for the isolation of a trihedral signature obscured by an attenuating wall. Four separate measurements were taken; by coherently subtracting sets of measurements, individual targets can be isolated.

The subtracted images are used to provide a direct comparison between attenuated and non-attenuated scattering. This provides both an estimation of the attenuation term and the refractive index of the wall material. Figure 3-17 illustrates the attenuating properties of the concrete material. As a general observation, the received signal intensity for the attenuated measurement is seen to decrease with increasing frequency, whereas the unobscured measurement is broadly constant.

There is an approximate drop in signal intensity of 5dB at 1GHz, this intensity difference increases to approximately 20dB as the frequency increases to 6GHz.

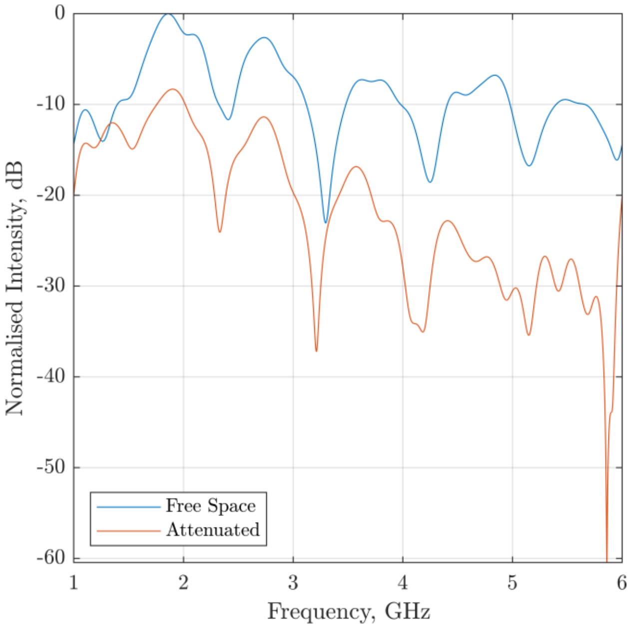

Figure 3-17 – Comparison between the spectral intensity for unobscured and obscured measurements of the trihedral. The obscured signal is seen to decrease in intensity, whereas the unobscured intensity is broadly unchanging over the bandwidth. The sharp rise in intensity for the attenuated signal at 6GHz is a consequence of the circular nature of the FFT algorithm.

To extract an accurate measure of the actual attenuation, it is important to account for the energy lost due to reflections from the wall itself. This involves calculating the power reflection coefficient via the Fresnel equations. Therefore, the refractive index of the material must first be established.

Figure 3-18 shows a time domain comparison between the unobscured and obscured measurements. There is an approximate 10dB drop in returned signal strength and a 0.1177m down range shift, $\Delta R_{trihedral}$, between the return signals. This down range shift is due to the decreased velocity of the EM waves as they propagate through the material. Using equation 3-43, the refractive index of the material can be established by relating the measured shift to the thickness of the material. It is important to note that this is an approximation of the refractive index, since this function is only applicable in the time domain, therefore the frequency dependence of the refractive index [67,70,90] are neglected. That said, non-reinforced concrete does not exhibit significant variation in refractive index [59, p.12,67,107] with respect to frequencies greater than 1GHz.

Equation 3-43 defines the refractive index of the material as being dependent upon the down range shift of the target, $\Delta R_{trihedral}$, and the thickness of the wall, δ, as a ratio between a delayed range, and a non-delayed range.

$$n = \frac{\Delta R_{trihedral} + \delta}{\delta} \qquad \textbf{3-43}$$

From this, it should be clear that to use the shift in target position as a means to extract the refractive index, the thickness of the wall must be known a-priori. Recalling from Figure 3-2 that the mean thickness of the wall is 96.6mm, this provides a refractive index between $1.95 > n > 2.6$. The ranges of values reflect the uncertainty associated with the 3dB width of the responses.

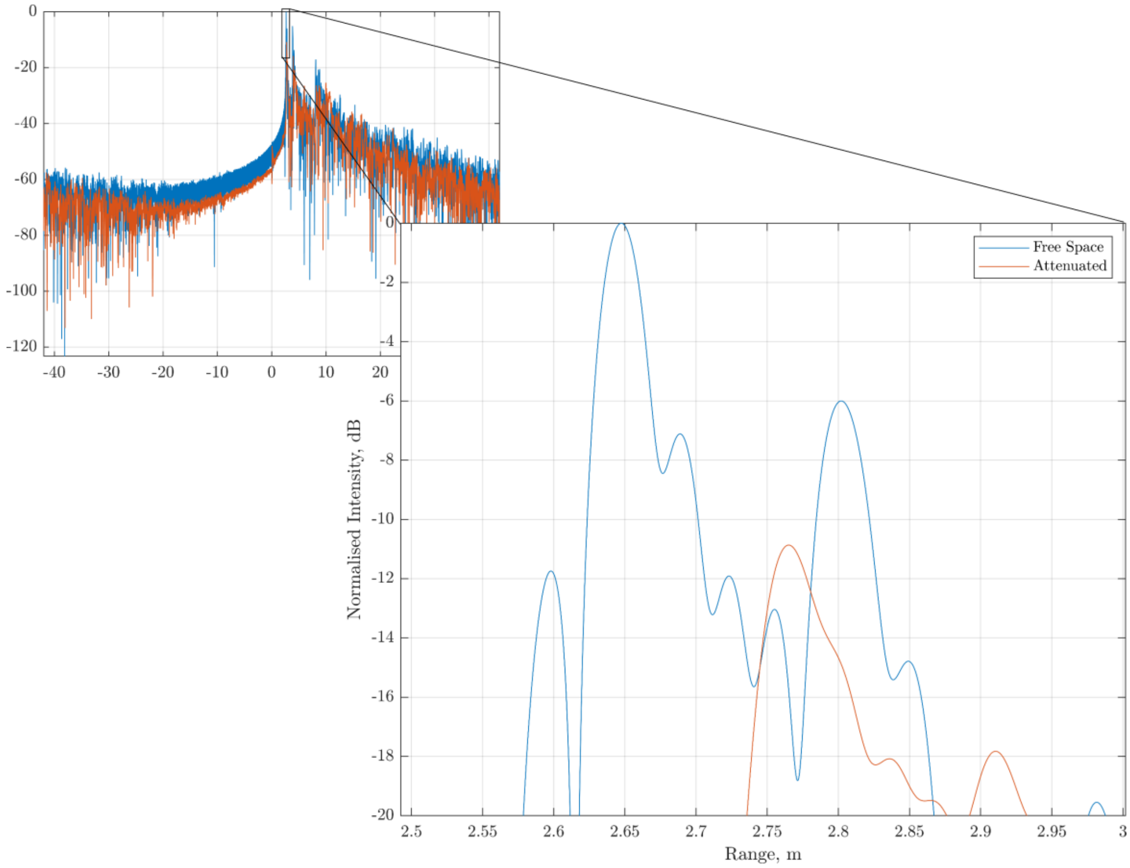

Figure 3-18 – Direct comparison between unobscured and through-wall measurements of a trihedral. The down range shift observed between the two measurements is a direct consequence of the decreased speed of the EM waves as they pass through the wall material.

The value for n can be further refined by averaging multiple measurements. For the 5 repeat measurements taken of this trihedral, the uncertainty in the refractive index can be reduced by a factor of approximately $\sqrt{5}$. For the 5 measurements taken, the 3dB width uncertainty is broadly very similar between measurements and is as follows:

Table 1 – Peak ranges and 3dB width for non-obscured and obscured trihedral for 5 consecutive independent measurements. On a millimetre scale, the peak ranges do not change between measurements, while the 3dB width changes on a minor level. Note that values have been rounded to the nearest mm, since that is the accuracy on the antenna positioning.

	NON-OBSCURED (m)			**OBSCURED (m)**		
	3dB 1	3dB 2	Mean Range	3dB 1	3dB 2	Mean Range
1	2.633	2.662	2.648	2.747	2.792	2.770
2	2.633	2.662	2.648	2.748	2.790	2.769
3	2.633	2.662	2.648	2.748	2.790	2.769
4	2.633	2.662	2.648	2.748	2.791	2.770
5	2.633	2.662	2.648	2.748	2.791	2.770

From Table 1, the mean range to the non-obscured trihedral is 2.648 ± 0.006 and the mean range to the obscured trihedral is 2.770 ± 0.010. Plugging values for the ranges and uncertainties into equation 3-43 yields:

$$n = \frac{(2.770 \pm 0.010 - 2.648 \pm 0.006) + 0.0966 \pm 3.22 \times 10^{-4}}{0.0966 \pm 3.22 \times 10^{-4}} \tag{3-44}$$

$$n = \frac{(0.122 \pm 0.012) + 0.0966 \pm 3.22 \times 10^{-4}}{0.0966 \pm 3.22 \times 10^{-4}} \tag{3-45}$$

$$n = 2.263 \pm 0.124 = 2.263 \pm 5.50\% \tag{3-46}$$

The uncertainty associated with the wall thickness is two orders of magnitude less than the uncertainty associated with ΔR. Since it is so much smaller, it has little effect on the uncertainty in n and is hidden by rounding.

Considering the uncertainty associated with the refractive index, reducing the bandwidth in order to extract the refractive index at specific frequencies would constitute a significant uncertainty. For example, reducing the bandwidth to 1GHz would result in a 27.5% uncertainty in n. Going forward, it is more useful to use a more precisely known parameter, and assume it is constant across the bandwidth.

To extract the attenuation term from the peak intensities of the two responses, the Fresnel Reflection Coefficients must be calculated. For a given angle of incidence, θ_i and an angle of transmission, θ_t, the reflection coefficients are:

$$R_s = \left|\frac{n_1 \cos(\theta_i) - n_2 \cos(\theta_t)}{n_1 \cos(\theta_i) + n_2 \cos(\theta_t)}\right|^2 \tag{3-47}$$

$$R_p = \left|\frac{n_2 \cos(\theta_i) - n_1 \cos(\theta_t)}{n_2 \cos(\theta_i) + n_1 \cos(\theta_t)}\right|^2 \tag{3-48}$$

Where R_s and R_p refer to the power reflection coefficients for s and p polarisations respectively. Since both antennas are pointing directly at the trihedral, the cosine terms can be neglected. Additionally, since the refractive index of air is approximately 1 [108] This simplifies the equations to:

$$R_s = \left|\frac{1 - n}{1 + n}\right|^2 \tag{3-49}$$

$$R_p = \left|\frac{n - 1}{n + 1}\right|^2 \tag{3-50}$$

In this context, n refers to the refractive index of the wall. Since there is some uncertainty in n, there is also an uncertainty in the reflection coefficients:

$$R_s = R_p = \left|\frac{1 - 2.263 \pm 0.124}{1 + 2.263 \pm 0.124}\right|^2 \tag{3-51}$$

$$R_s = R_p = 0.150 \pm 0.012 = 0.150 \pm 7.778\% \tag{3-52}$$

Now consider the trihedral. For the non-obscured case, the received power is proportional to the transmitted power, $P_{r_{air}} \propto P_t \sigma$. For the obscured case, the received power depends upon both the transmitted power and the power reflection coefficients. Ignoring multipath, the power received from the obscured trihedral consists of four boundaries, as seen in Figure 3-19. The received power is therefore dependent upon the 4th power of the transmission coefficient:

$$P_{r_{wall}} + L\delta \propto T^4 P_t \sigma \tag{3-53}$$

Where P_t is the transmitted power, $T = 1 - R_s$, is the power transmission coefficient, L is the dielectric loss per unit length associated with travelling through the wall, δ represents the wall thickness, and σ is the power reflection coefficient for the trihedral. Since the trihedral is a metallic retroreflector orientated properly, $\sigma \approx 1$.

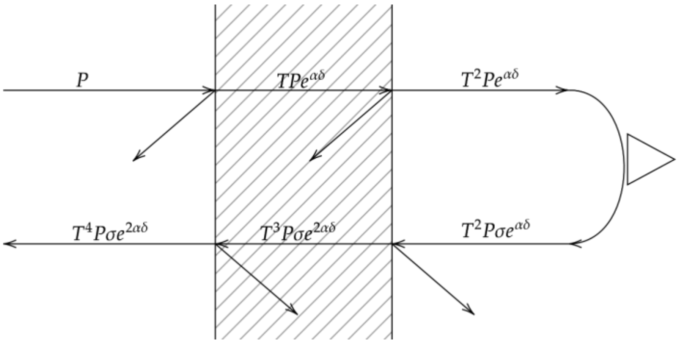

Figure 3-19 – Diagram illustrating how the received power from a through-wall reflection of a trihedral is calculated for a power transmission term $T = 1 - R$.

Since the antenna gain, direct range, and wavelength are the same between obscured and non-obscured measurements, the received power for both cases share the same constant of proportionality, K [109]. In short, the received power for the through-wall measurement is a decreased version of the air measurement.

From equation 3-53, the transmitted power for both measurements can be equated:

$$\frac{(P_{r_{wall}} + L\delta)}{T^4\sigma} = KP_t = \frac{P_{r_{air}}}{\sigma} \tag{3-54}$$

$$\frac{(P_{r_{wall}} + L\delta)}{T^4} = P_{r_{air}} \tag{3-55}$$

Rearranging equation 3-55, gives an explicit equation for the loss per unit length associated with travelling through the wall:

$$L = \frac{(T^4 P_{r_{air}} - P_{r_{wall}})}{\delta} \tag{3-56}$$

Plotting this function shows that as frequency increases, the loss also increases. There are periodic increases in the loss, which correspond with the decreases in measured intensity shown in Figure 3-17:

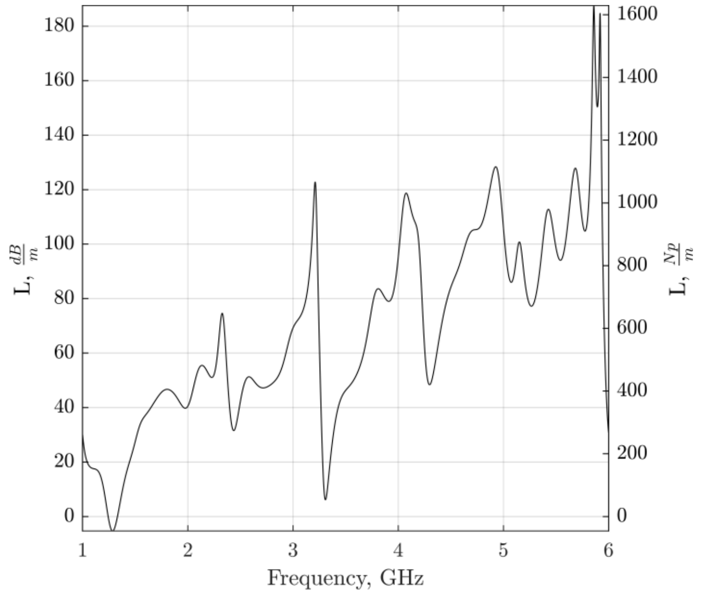

Figure 3-20 – Two-way loss per metre due to passing through the wall. The periodic decrease in loss lines up with the periodic decrease in received signal, for both obscured and non-obscured measurements.

With regards to measurement uncertainty in L, uncertainty in $P_{r_{air}}$ and $P_{r_{wall}}$ are very small, as is the uncertainty in wall thickness. Therefore, the uncertainty in L is dominated by the uncertainty of T. Since $T = 0.85 \pm 0.012$, the uncertainty in L is approximately 5.65%.

The loss function, L, can be considered to be encoding the attenuation term, therefore L can be equated to the exponential decrease in power due to the attenuation:

$$P_{r_{wall}} = KT^4 P_t \sigma e^{2\alpha\delta} \qquad \textbf{3-57}$$

Recall that $KP_t\sigma = P_{r_{air}}$, substituting and rearranging equation 3-57 provides an explicit equation for the attenuation term α:

$$\alpha = \frac{\ln\left(\frac{P_{r_{wall}}}{T^4 P_{r_{air}}}\right)}{2\delta} \tag{3-58}$$

Dimensional analysis of equation 3-58 reveals that it has units m^{-1}. This is in agreement with the standard transmission line equation for α given in Appendix A.1.

Plotting α shows that it follows the same trend as L, albeit negative. This negativity shows that, as one might expect, the wave is experiencing a loss in energy as it propagates through the material. It is also worth remembering that this value for the attenuation hinges on the value of refractive index obtained via equation 3-43. While literature would indicate that the refractive index is constant across the bandwidth, the frequency distributions for L and α should be taken with a grain of salt.

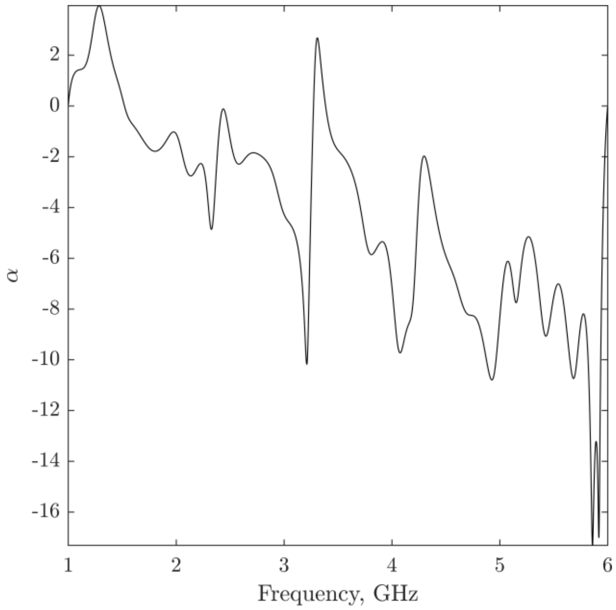

Figure 3-21 – Plot of the attenuation constant α as a function of frequency. Since α is negative, this constitutes a loss in received power as the wave propagates through the material.

A few questions arise from Figure 3-21, most notably why does it seem to indicate that the transmission through the wall experiences a gain at certain frequencies?

To answer this question, recall that the non-obscured power has been modulated by a factor of T^4 to account for the loss due to reflection. T^4 is roughly 0.5, so the non-obscured power has been essentially halved. Plotting the two powers shows that the supposed gain is due to the characteristic nulls in the spectra not aligning between measurements.

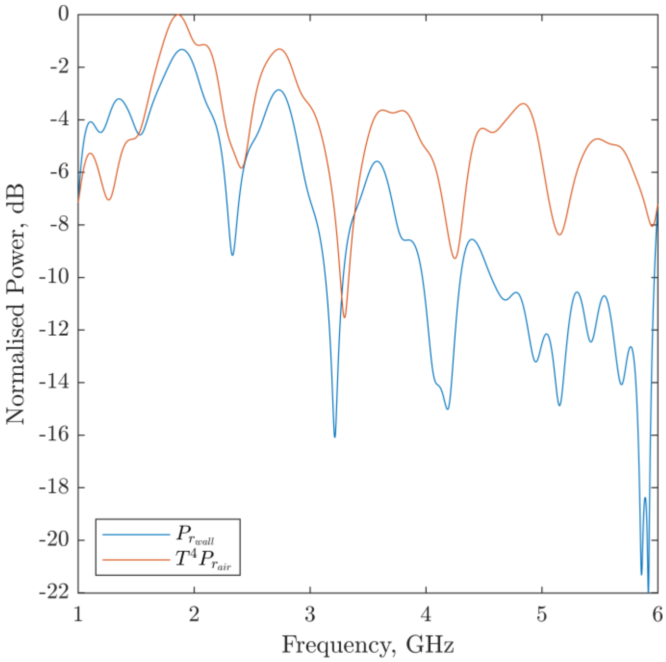

Figure 3-22 – Modulated frequency response for the obscured and non-obscured measurements. This figure shows that, when modulated for the transmission coefficient, the misalignment between nulls is sufficient to constitute a supposed gain.

The low frequency gain is due to multiple factors. The most obvious option is that the refractive index, and by extension T, is not representative at the low frequencies. Secondly, due to the low frequency, waves are diffracting around the top edge of the wall, leading to more energy reaching the trihedral, consequently leading to a larger received power. Neither of these options are contained within the framework leading to equation 3-58, and as such the low frequency values for α should be ignored.

Finally, there is the question of measurement uncertainty with regards to α. Recall from equation 3-58 that α is dependent upon a logarithm and the thickness of the material. Following the standard equations for error propagation [103], the uncertainty associated with α is:

$$\Delta\alpha = \sqrt{\left(\frac{\partial\alpha}{\partial T}\Delta T\right)^2 + \left(\frac{\partial\alpha}{\partial\delta}\Delta\delta\right)^2} \qquad \textbf{3-59}$$

$$\Delta\alpha = \sqrt{\left(\frac{2}{T\delta}\Delta T\right)^2 + \left(-\frac{\ln\left(\frac{P_{r_{wall}}}{T^4 P_{r_{air}}}\right)}{2\delta^2}\Delta\delta\right)^2} \qquad \textbf{3-60}$$

where ΔT and $\Delta\delta$ represent the measurement uncertainty in their respective variables. Since $P_{r_{wall}}$ and $P_{r_{air}}$ change as a function of frequency, the uncertainty in α is also going to change as a function of frequency. The latter part of equation 3-60 can be substituted for α, whcih simplifies the equation into something much more manageable:

$$\Delta\alpha = \sqrt{\left(\frac{2}{T\delta}\Delta T\right)^2 + \left(\frac{\alpha}{\delta}\Delta\delta\right)^2} \qquad \textbf{3-61}$$

Figure 3-23 shows α with superimposed upper and lower bounds. While there is an observed negative trend, since the model for α does not consider multipath, shadows, interference patterns, or other radar phenomenology outside of the idealised case, the uncertainty associated with α is not sufficient to draw a meaningful trend line.

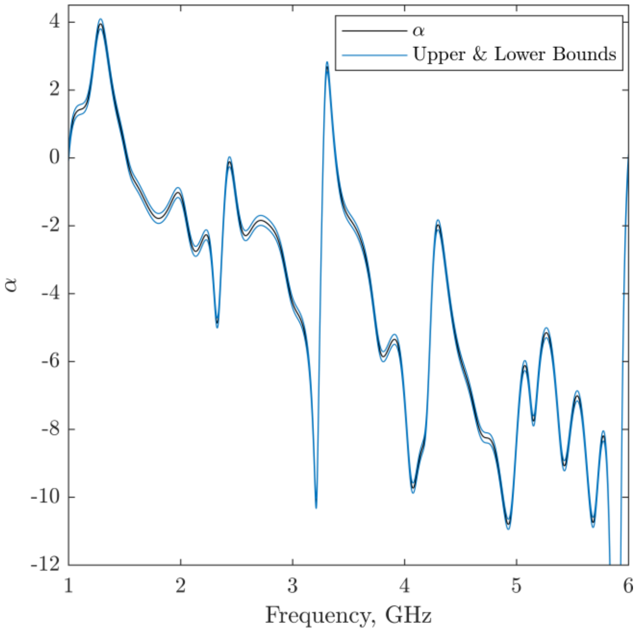

Figure 3-23 – Comparable plot to Error! Reference source not found. **showing the attenuation coefficient $\alpha \pm \Delta\alpha$. The uncertainty in α is on order of 3%, albeit it changes with frequency. The error bars are not sufficient to draw a meaningful line of best fit for the concrete attenuation.**

From Appendix A.1, the attenuation coefficient is dependent upon the material permittivity, permeability, conductivity, and the propagation frequency. For a non-magnetic material, the conductivity of such a material can be obtained from known material permittivity and frequency:

$$\sigma = \omega\varepsilon\sqrt{\left(\frac{2\alpha^2}{\omega^2\mu\varepsilon}\right)^2 + \frac{4\alpha^2}{\omega^2\mu\varepsilon}} \qquad \textbf{3-62}$$

$$\sigma = 2\varepsilon\alpha\sqrt{\frac{\alpha^2}{\omega^2\mu^2\varepsilon^2} + \frac{1}{\mu\varepsilon}} \qquad \textbf{3-63}$$

Since the material is assumed to be non-magnetic, the permeability is equal to that of free-space. Additionally, the permittivity of the material is $n^2\varepsilon_0$.

This can be further simplified by noting that $\frac{1}{\mu\varepsilon} = \frac{c^2}{n^2}$. This is convenient not only because it eliminates a requirement that the material be non-magnetic, but because the speed of light in a vacuum is an exact value, thus eliminating a minor source of uncertainty:

$$\sigma = 2n\varepsilon_0\alpha c\sqrt{\left(\frac{\alpha c}{\omega n}\right)^2 + 1} \tag{3-64}$$

Since the material is largely experiencing a loss, the conductivity should be positive. Therefore, the negative root of equation 3-63 is used. Figure 3-24 shows that the conductivity follows a similar linear growth as the attenuation term. This is to be expected, since the interior of the square root is approximately equal to 1. Therefore, the conductivity is approximately proportional to α.

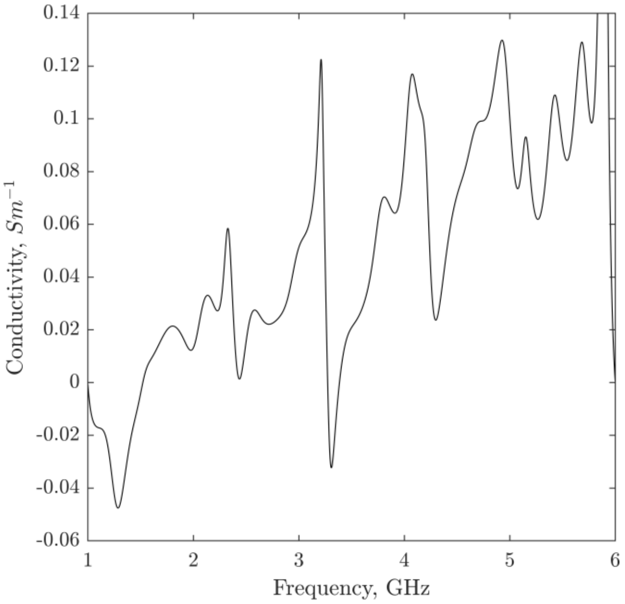

Figure 3-24 – Conductivity extracted from the attenuation coefficient via equation 3-62. There is a gradual increase from 10^{-2} S/m to 10^{-1} S/m as the frequency increases. The sharp increase in conductivity as 1GHz is due to the circular nature of the Fourier Transform.

With regards to propagating errors, the same approach as for the attenuation is used[6]:

$$\Delta\sigma = \sqrt{\left(\frac{\partial\sigma}{\partial\alpha}\Delta\alpha\right)^2 + \left(\frac{\partial\sigma}{\partial n}\Delta n\right)^2} \tag{3-65}$$

The partial derivatives are obtained via the product rule:

---

[6] There is some measurement uncertainty associated with ω. However, these uncertainties are insignificant when compared to the uncertainty associated with α and n.

$$\frac{\partial\sigma}{\partial\alpha} = 2c\varepsilon_0 n\left(\left(\frac{\alpha c}{\omega n}\right)^2 + 1\right)^{\frac{1}{2}} + \frac{2\alpha^2 c^3 \varepsilon_0}{\omega^2 n}\left(\left(\frac{\alpha c}{\omega n}\right)^2 + 1\right)^{\frac{-1}{2}} \qquad \textbf{3-66}$$

$$\frac{\partial\sigma}{\partial n} = 2c\varepsilon_0 \alpha\left(\left(\frac{\alpha c}{\omega n}\right)^2 + 1\right)^{\frac{1}{2}} - \frac{2\alpha^3 c^3 \varepsilon_0}{\omega^2 n^2}\left(\left(\frac{\alpha c}{\omega n}\right)^2 + 1\right)^{\frac{-1}{2}} \qquad \textbf{3-67}$$

The value for Δn is 0.124, and the value for $\Delta\alpha$ is obtained from equation 3-61. Putting this together gives an uncertainty associated with the conductivity on order of 1% to 3%. Plotting the conductivity with included error bars shows a final distribution for the material conductivity. As with the material attenuation, the error bars are not sufficient to draw a meaningful line of best fit.

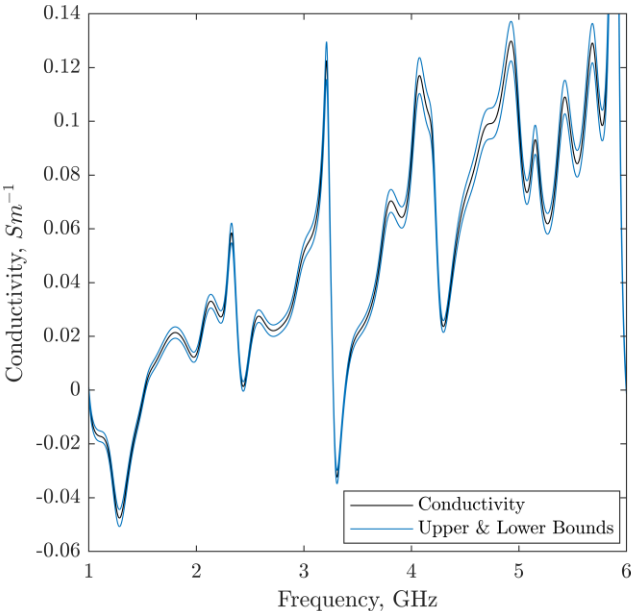

Figure 3-25 – Plot of the material conductivity, $\sigma \pm \Delta\sigma$, against frequency. Blue lines representing the upper and lower bounds of conductivity have been added to the plot. While there is a gradual positive trend in conductivity as the frequency increases, the error bars are insufficient to draw a meaningful line of best fit.

In summary, based on two quasi-monostatic trihedral radar measurements, one obscured, and one not, the representative refractive index and conductivity have been extracted over a frequency range of 1GHz to 6GHz. The conductivity behaves as expected, increasing with frequency, although there is a small gain at frequencies less than 1.5GHz. This is due to diffraction around the top of the wall and due to an interference pattern established between the retroreflector and the wall.

3.6 Discussion

This chapter focuses primarily on non-SAR based approaches to establish an independent validation measurement for the refractive index of the concrete wall material. To this end, three different approaches are taken.

Firstly, a novel analysis of the cutoff frequency arising from treating the concrete block as a slab dielectric waveguide was undertaken. This is an approach best suited to narrowband low frequency measurements. For this reason, it has not yet been implemented with respect to concrete. In this method, two probes are inserted into a concrete block; chosen to be representative of the concrete batch from which a wall is built. From the slab waveguide cutoff frequencies, the relative permittivity is directly extracted as 5.89±27% for dry concrete, increasing following a cubic polynomial as water is introduced. Since the material is assumed to be non-magnetic $\varepsilon_r = \varepsilon_r \mu_r$. This means that the refractive index is $\sqrt{\varepsilon_r} = 2.43 \pm 13.5\%$. Therefore, the refractive index obtained from this method ranges from 2.23 to 2.57.

Secondly, a NRW approach was undertaken in order to obtain a wideband metric for n. This involves measuring both the complex reflection and transmission via the same two probes. From this, the real component of the relative permittivity was extracted as being somewhere between 4 and 6. This corresponds to a refractive index between 2 and $\sqrt{6}$. Unfortunately, the complex component of the relative permittivity oscillates around zero. This means that either the material is completely lossless, or the approach has failed.

Finally, a set of single pulse radar measurements were taken of a trihedral before and after a wall was build. This approach is both mathematically simpler than the two prior approaches but also more representative of what values would be expected from a SAR measurement. From this approach, the refractive index of the material is 2.263±5.50% and therefore ranges from 2.138 to 2.318.

All three measurements agree with each other, at least as far as the refractive index goes, as illustrated with Figure 3-26. The trihedral based approach is the most precise, therefore the result from this method is used going forward.

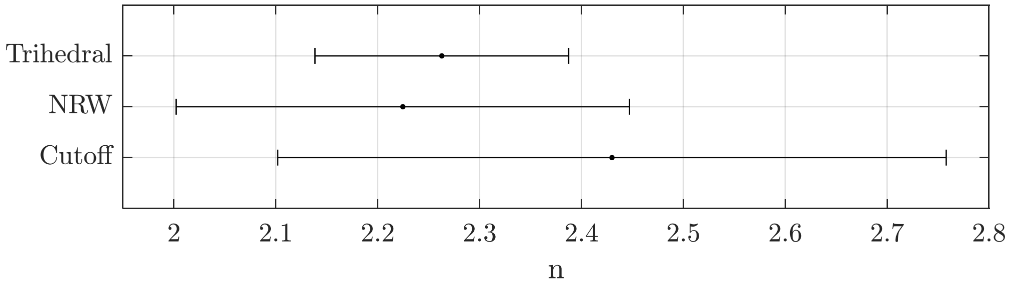

Figure 3-26 – Associated error bars obtained from all three different methods. All three methods are in agreement; with the trihedral based method giving the most precise measurement of the refractive index.

To put all this into context, the refractive index of this concrete batch is well within the $\sqrt{2}$ to 3 range of established values obtained from a literature survey for dry non-reinforced concrete. This indicates that any consequential effect, such as defocusing, will also be comparable to other works. From a radar perspective, one could interpret these results as meaning that any obscured target will appear roughly 22cm down range of its true location.

With regards to the dielectric loss, in some sense all three approaches yield information about the loss. The cutoff frequency analysis provides information in terms of the Q value, the NRW approach explicitly calculates the complex component to permittivity, and the trihedral based approach yields information relating the received power directly to the dielectric loss of the wall.

Firstly, the cutoff frequency analysis was performed at multiple different moisture contents. In agreement with Soutsos *et al* [67], McGraw [86], and others [102,110], and disagreement with Chung *et al* [76], the addition of moisture increased the relative permittivity of the material. However, the Q values for each moisture content did not form an obvious trend. Therefore, it is difficult to make an authoritative statement about the attenuation. One possible reason for this lack of trend is due to the material drying in a non-linear way. For example, different parts of the material had different saturations of water. Another potential cause is small motion in the probes, causing a slight air gap between the material and the probe.

Secondly, the NRW approach shows that the material appears to be lossless, with the exception of the low frequency components. This is in disagreement with the current literature [67,86,102,111]. Given the phase instability arising from $S_{11} \gg S_{21}$, the phase of ε_r is unstable. For this reason, it is more likely that the complex component of ε_r is erroneous, rather than showing a real physical trend. To correct this, the thickness of the block should be decreased.

Finally, the trihedral based approach shows that a target obscured by a wall will indeed be dimmer than one not obscured. By far the more significant contributor to this effect is the additional reflections the wall introduces; approximately half the energy is reflected away. Once one accounts for the reflected energy, the attenuation due to the wall is extracted via a comparison of the adjusted trihedral scattering. This approach has shown that the attenuation term decreases, and hence the conductivity of the material increases with frequency. This is in agreement with the literature, and disagreement with the NRW approach. There is a small gain observed at low frequencies, the current hypothesis being that this is caused by two factors. The first is diffraction around the top of the wall leading to an increased power being received. The second factor is that the refractive index, and by extension the power reflection coefficient is greater at the lower frequencies. This would cause an overcompensation of the received power, leading to a gain.

The uncertainty associated with the refractive index is not negligible. However, much of the established literature does not explicitly include error bars on their measurements, so it is difficult to say if this degree of uncertainty is unusual.

4 2D Non-Invasive Method

4.1 Introduction

This chapter focuses primarily on a bistatic method for extracting the refractive index of a large concrete wall present in a SAR scene. This differs from the in-situ methods presented in the previous chapter, as it does not require direct interaction with the concrete itself and allows for the direct formulation of a SAR image. From the point of view of a surveillance platform, this would decrease both the risk to the personnel and the risk of detection when compared to the probe-based methods.

This chapter is organised as follows: first a review of the remote methods for extracting the material properties for a wall is undertaken. In this context, the term ‘remote’ denotes a measurement modality where background measurements are not strictly necessary, and the entire radar system is on one side of the wall. Under this limitation, deconstructing the wall, or actively placing an antenna on each side, is disallowed. Secondly, the framework for an asymmetric bistatic SAR collection is established. This is used as the basis for extracting the refractive index and thickness from the wall. Following this is a simulation-based analysis of the sensitivity of the extraction process to erroneous assumptions concerning the SAR geometry and wall structure. Finally, the approach is proved to work using three experimental measurements, one with the bistatic trajectory parallel to the wall, one with the trajectory at a slight angle, and finally one with the presence of additional clutter.

Under the condition that one cannot simply walk up to the wall and measure the thickness, then to extract the refractive index of the material remotely, one also needs to obtain the thickness of the material remotely. For a SAR collection, the effective length of the wall changes as a function of look angle, therefore the combination of the thickness and refractive index can be recast as a simultaneous equation. This leads into the two main ways of extracting both properties of the wall: the first, and most common, is to use a known reference target behind the wall, the second option is to use a bistatic scenario, relating the range separation between front and back face reflections.

4.1.1 Target Based Optimisation

As the name implies, this category of wall parameter estimation involves the usage of one or more reference targets, usually a retroreflector, to obtain some information about the effect of the wall on the point spread function of said target.

Typically, this problem has been posed as how to obtain the best quality image in TWR. For example Wang and Amin [112–114], and later Ahmad *et al* [115,116], propose a beamformer containing a consideration for the refraction. They note that small errors in assumed parameters contribute to a compromised beamformer, and hence a defocused image. Specifically, they note that errors in thickness constitute a scaling term, whereas errors in the refractive index express themselves as both a scaling term and a phase error. In a later paper, Ahmad *et al* devised an autofocus approach to estimate the wall properties, and as such improve the quality of their beamformer [117]. This autofocusing approach iterates through different assumptions about the wall material, assessing the resultant image quality each time. In this case, they note that conventional contrast metrics, such as summing the image intensity, do not achieve a sufficient accuracy. Rather they look at the image kurtosis and skew, both of which can be affected by additional clutter in the imagery. In addition, they recommend that one modulate the brightness of the image to increase contrast beforehand.

While Ahmad *et al* proved the theoretical basis for the technique; they did not demonstrate it experimentally. An autofocus technique was successfully used experimentally by Dehmollaian and Sarabandi in 2008 [118]. Since, there has been a litany of similar papers published. Chen and Chen [119] note that since defocusing only occurs in cross-range, the entire focusing mechanism can be accelerated by only considering one cross-range slice. Jin *et al* [120] further accelerated the process by noting that the electrical length of the wall is independent of the actual points of refraction.

While these approaches are steadily becoming more and more complex, they rarely show experimental work, focusing primarily on simulation. This is due, in part, to such optimisation approaches reacting sensitively to unwanted clutter [120,121]. With this in mind, it may be preferable, in some scenarios, to eliminate clutter entirely, via gating or other such methods, and only focus on the wall itself. For example, Solimene *et al* [121] proposed a lightweight wave inversion method to match the scattered field to a theoretical slab dielectric, although they achieved less accurate results with the introduction of clutter, despite gating.

More recently, Solimene *et al* utilised a Multiple Input Multiple Output (MIMO) scenario [122,123] in conjunction with the material transmission coefficient to estimate the wave number, and by extension the material properties as they vary with frequency. While this MIMO technique does allow for a robust generalised formulation, the explicit requirement for a multistatic measurement scenario drives both cost and practicality. As such, a simpler geometry may be preferred.

Similar to the NRW method, a direct measurement of the material reflectivity can be used to estimate the refractive index of an obscuring wall, without having to approach it. Naturally, such an approach would require careful calibration of the radar system, and a solid understanding of the geometry of the measurement. Alternatively, one could make a reference measurement of a well-known reflector at the same time as the wall measurement. Aftanas *et al* [124] used a conveniently placed metal plate, of which they assumed 100% of the incident radiation was reflected. From this, they estimated the reflectivity of the test material as a ratio between the measured signal and the reference signal. This has since become a common method for extracting permittivity values [125–127]. In principle, this operates on the same principle as the S_{11} only probe-based approaches detailed in the previous chapter. As such, there is a precedent for the technique, however on its own it does not give information about the thickness of the wall material. To obtain the thickness the time delay between front and back faces of the wall is used.

All of these methods are somewhat problematic from an implementation perspective: a known and constant reference target is not something that will be readily available in many cases. Additionally, if one were to base the extraction on an optimisation of a focusing metric, then one runs the risk of conflating different sources of defocusing and overcompensating the value of permittivity. It will be shown in Section 5 that kurtosis is sufficient to extract both the refractive index and thickness of an unknown wall in a simulated scenario for both planar and volumetric simulations. However, it is not sufficient to obtain the properties when applied to physical measurements. This is due to the inability to completely remove the wall signature from the imagery and the conflation of multiple point spread functions in a cluttered environment.

The complex reflection measurements require both extremely good calibration and prior knowledge of the impulse response from the wall, or a serendipitous metal plate placed next to the wall. This is problematic for a number of reasons: firstly, the metal plate must be placed as close to the wall as possible, to mitigate discrepancies due to the spherical loss of energy. Secondly, one assumes that the reference measurement is a scaled version of the wall measurement. This is not the case, as a metal plate will behave specularly, whereas a wall will have some element of diffusity in its reflection.

That is not to say that there are no benefits to these approaches. The autofocusing approaches inherently create a highly focused image, thus saving time and effort further down the road. The reflectivity approaches, since they obtain a complex value for reflectivity, can obtain information about the loss tangent of the material, and the frequency evolution of the parameters. However, this does not offset the immense implementation hurdles that would be present in a real-world scenario, specifically, clutter and movement behind the wall.

4.1.2 Bistatic Methods

The autofocus papers work on the idea that the effective electrical length of the obscuring wall changes as a function of look angle. It follows that if one could force a change in look angle and record the effective length of the wall directly, then one could infer the refractive index and thickness of the wall without the need for an additional target. An intuitive way to evaluate the effective electrical length of a wall is to look at the time difference between front and back face reflections in a SAR collection. Unfortunately, in monostatic SAR this time difference will never change, since the geometric relationship between the antennas and the point of reflection is constant.

Thankfully, this is not the case in certain bistatic and multistatic measurements. If the bistatic baseline changes as a function of aperture position, this would force a change in look angle, and hence the effective electrical length of the wall.

In 2011, Protiva, Mrkvica, and Macháč demonstrated experimentally [100,128] that two divergent antennas would produce a sufficient time delay between faces such that the refractive index and thickness of a concrete wall could be extracted. They used a bistatic approach whereby each antenna is moving directly away from each other. This keeps the point of reflection for both faces in the same place, while still forcing a change in the angle of incidence. This approach significantly simplifies the mathematical model for refraction that must be implemented and is used somewhat effectively in the few papers that implement it [99,129–131]. Furthermore, Protiva *et al* showed that by making a relative measurement between the front and back faces of the wall, they remove the need for a prior calibration of the radar system. However, they still required a background measurement in order to remove the direct coupling between the antennas due to a small standoff distance, D.

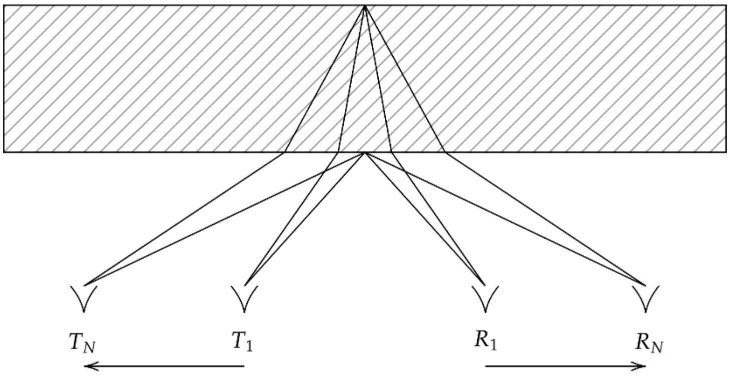

Figure 4-1 – Illustration of the Common Midpoint Processing (CMP) model for bistatic wall reflections. The transmitting and receiving antennas move symmetrically away from some central axis, meaning that the points of reflection do not change.

This technique requires accurate estimations of the range thus makes use of various super-resolution algorithms. The Estimation of Signal Parameters via Rotational Invariance Technique (ESPRIT) and the Multiple Signal Classification (MUSIC) algorithm are both used to estimate the range to a greater accuracy than the resolution would normally allow [132–135]. Potentially this enables the use of a smaller signal bandwidth, beneficial for practical through-wall radar where the higher frequencies are significantly attenuated. However, there are considerations to be made when implementing super-resolution algorithms, namely that in through-wall scenarios the front and back-face responses are often coherent, requiring additional pre-processing to decorrelate the scatterers [132]. Neither ESPRIT nor MUSIC provide information about the point spread function (PSF) of the scatterers without further post-processing and they have degraded performance at lower signal-to-noise ratios [133]. In addition, super-resolution is not a requirement if the front and back faces can be resolved properly in the first instance. Therefore, if the wall is sufficiently dry, and a large enough bandwidth can be transmitted, then super-resolution is not required. This is an important benefit of the approach demonstrated within this Section, as it significantly simplifies the processing chain and allows for additional clutter to be present without affecting the imaging performance, since both MUSIC [133] and ESPRIT [136] require knowledge of the number of dominant scatterers in the scene in order to work effectively.

From the description of the bistatic approaches arise a few key questions that have yet to be answered:

1. How accurate does the antenna positioning need to be?
2. What happens if the wall is not parallel to the antenna path?
3. What is the effect of clutter?
4. What effect does the inhomogeneity of the material have?

Due to the similarities between TWR and GPR, it should not be surprising that analogous techniques exist in GPR. Typically using common midpoint processing (CMP), these papers focus primarily on extracting information about sedimentary materials [137], and in some cases paving slabs [138,139]. Among these papers, there is a specific drive to evaluate water content, be it as groundwater, or direct water analysis [140,141].

The main benefit of these bistatic methods is that there is no requirement for any additional target or reference measurement. However, there are three main issues: firstly, CMP is not space efficient, thus in a cramped space, it may be of limited use. Secondly, since the point of reflection never moves, the values extracted are only representative of the small area around the midpoint, and not the wall as a whole. Finally, since the antennas are moving apart symmetrically, there is no azimuthal resolution obtainable from the bistatic collection, thus the collection cannot be used to form a SAR image with appreciable cross range resolution.

To alleviate these issues, the point of reflection for both the front and back faces of the wall should migrate. To do this, one needs an asymmetric collection geometry [41,142].

There is one final limitation to this bistatic approach that cannot be alleviated with an asymmetric geometry. No information about the complex reflectivity of the material is obtained and, as such, the dielectric loss is unattainable. Thajudeen and Hoorfar [143] recently attempted to combine the bistatic methods described here with the reflectometry methods described earlier. They did this by forming a multistatic system constituting both bistatic and monostatic components. To obtain the loss tangent of the material, they use monostatic multipath signals arising from internal reflection inside the wall.

The main concern here is those multipath signals arising from internal reflections are very dim compared to other signals. Taking a representative value of refractive index of 2.5 and normal incidence, the reflection coefficient is approximately 0.2. This would mean that the 3rd reflection would have an amplitude less than 3% of the first reflected signal. This would be equivalent to a -30dB difference before accounting for additional effects, such as attenuation or diffuse scattering. While this is by no means an insurmountable limitation, it does limit the current applicability of the approach to clutter free environments.

As mentioned, the prior art with regards to non-invasively extracting the material properties is, in general, quite contrived, either requiring that an object be present behind the wall [114,117,118,120,144], the wall measurement being accompanied by a reference measurement [124,138,145,146], or the measurements being conducted in a specific fashion [99,100,128–131,143]. The aim of this section is to develop and test a model for extracting the refractive index and thickness of a pre-built wall in the presence of clutter, without the need for additional measurements. To do this, the bistatic CMP method is evolved into a general solution requiring that the two antennas can be placed in any orientation in front of the wall. From an implementation perspective, a general framework would allow for a wider range of aspect angles on any given target, and a greater spatial efficiency. From a theoretical perspective, a migrating point of reflection produces an estimation of the wall properties that is not limited to a single patch of material and allows for measurements with appreciable cross range resolution.

4.2 Theoretical Model

With the goal of extracting the refractive index from a dielectric slab, a model for the electromagnetic propagation through the dielectric is required. Consider a bistatic radar configuration characterised by a transmitting antenna located at $\boldsymbol{T} = [T_x, T_y, T_z]$ and a independent receiving antenna at position $\boldsymbol{R} = [R_x, R_y, R_z]$. The separation between the two antennas is defined by the vector $\boldsymbol{V} = \boldsymbol{R} - \boldsymbol{T}$. A uniform dielectric slab of thickness δ and infinite extent in the xz plane is introduced a distance D from the transmitting antenna.

Figure 4-2 shows the horizontal component of a transmitted ray reflecting off of the front and back faces of the slab. The ray travels from the transmitting antenna and is received at the receiving antenna.

The refraction in the horizontal plane is treated independently to the refraction in the vertical plane. Under this assumption, the model is easily extendable to 3D. Consequently, this model allows for the antennas to be placed in any three-dimensional configuration, thus the ray need not be symmetric. This improves the usability of the technique when compared to the symmetric examples [99,100,128,129].

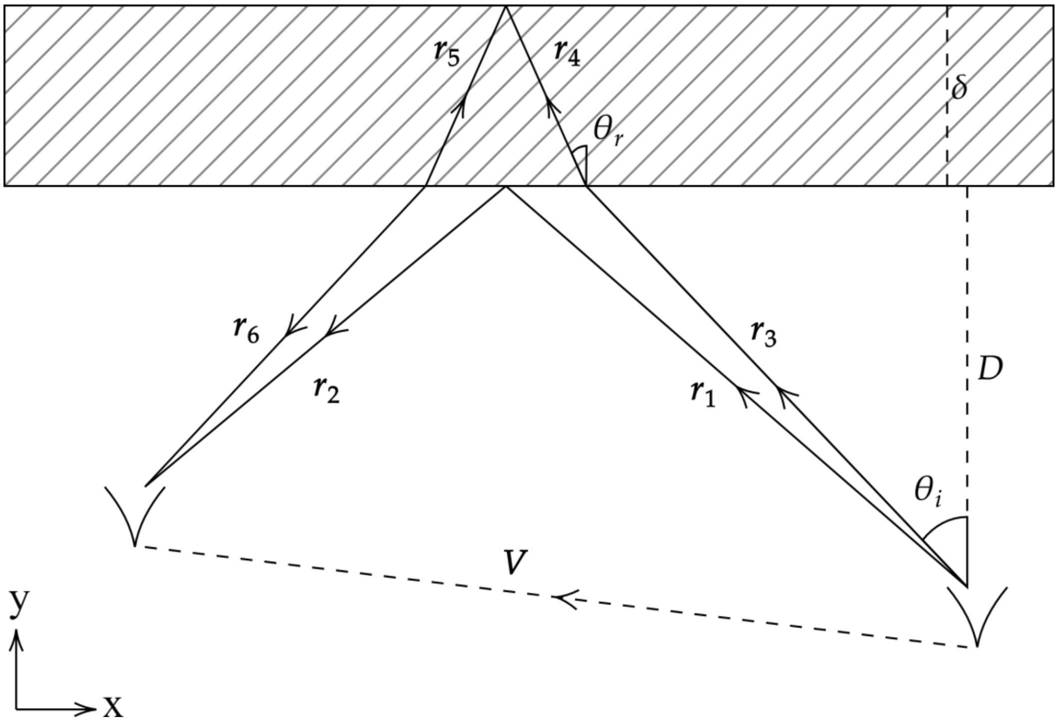

Figure 4-2 Bistatic ray tracing model for the reflection from the front and back face of a dielectric slab. While this image shows only a top-down two-dimensional view, the same model can be applied in the yz plane.

The range corresponding to the front face reflection is equal to the sum of the range from the transmitter to the point of reflection and from the point of reflection to the receiver. If the reflection is assumed to be specular then the total range can be written as:

$$R_{Front} = |\boldsymbol{r_1}| + |\boldsymbol{r_2}| \qquad \textbf{4-1}$$

Where $\boldsymbol{r_1}$ is the vector ray from the transmitter to the point of reflection and $\boldsymbol{r_2}$ is the ray from the point of reflection to the receiving antenna. Intuitively, this range can be found by calculating the point of reflection. However, equation 4-1 can also be solved by applying the Pythagoras Formula, this gives an equation for the range that is independent of where the reflection actually occurs:

$$R_{Front}(\boldsymbol{V}, \delta) = \sqrt{V_x^2 + \left(2D - V_y\right)^2 + V_z^2} \qquad \textbf{4-2}$$

Where V_x, V_y and V_z are the x, y and z components of the vector $\boldsymbol{V}$. D is the standoff range from transmitter to wall. Similarly, the range to the back face reflection can also be written in terms of its vector components:

$$R_{Back} = |\boldsymbol{r}_3| + |\boldsymbol{r}_4| + |\boldsymbol{r}_5| + |\boldsymbol{r}_6| \tag{4-3}$$

Via trigonometry, the magnitudes of all the components are defined by the angle of incidence, θ_i, the angle of refraction, θ_r, and the standoff distance, *D*. For the horizontal case, the magnitudes are given as follows:

$$|\boldsymbol{r}_3| = \frac{D}{\cos(\theta_i)} \tag{4-4}$$

$$|\boldsymbol{r}_4| = |\boldsymbol{r}_5| = \frac{n\delta}{\cos(\theta_r)} \tag{4-5}$$

$$|\boldsymbol{r}_6| = \frac{D - V_y}{\cos(\theta_i)} \tag{4-6}$$

In equation 4-5 the factor *n* is introduced to account for the decreased velocity of the electromagnetic wave inside the dielectric. This gives a total horizontal range and total vertical range as:

$$R_{Back\,H}(D, \boldsymbol{V}, n, \delta) = \frac{2D - V_y}{\cos(\theta_i)} + \frac{2n\delta}{\cos(\theta_r)} \tag{4-7}$$

$$R_{Back\,V}(D, \boldsymbol{V}, n, \delta) = \frac{2D - V_y}{\cos(\vartheta_i)} + \frac{2n\delta}{\cos(\vartheta_r)} \tag{4-8}$$

Here, ϑ is used to represent the vertical component of the path, while θ is used to represent the horizontal component. The total three-dimensional range can be established from equations 4-7 and 4-8. Therefore, finding the total range for a given bistatic radar geometry and wall material is rather an exercise in finding the angle of incidence.

Using the horizontal component $R_{Back\,H}$ as an example, since the vector $\boldsymbol{V}$ is a known variable, a relationship between θ_i and the component of $\boldsymbol{V}$ parallel to the wall can be established.

$$V_x = \left(2D - V_y\right)\tan(\theta_i) + 2\delta\tan\left(\theta_r\right) \tag{4-9}$$

In Equation 4-9, one can substitute the angle of refraction for the angle of incidence via Snell's Law. This leads to the deceptively benign looking boundary condition:

$$V_x = \left(2D - V_y\right)\tan(\theta_i) + 2\delta\tan\left(sin^{-1}\left(\frac{sin(\theta_i)}{n}\right)\right) \qquad \textbf{4-10}$$

From equation 4-10, it should be clear that as θ_i tends towards $\pm\frac{\pi}{2}$, the separation between the antennas must tend towards infinity to catch the specular reflection. In addition, from equation 4-8 it is clear that a similar expression hold true for the vertical component of the ray:

$$V_z = \left(2D - V_y\right)\tan(\vartheta_i) + 2\delta\tan\left(sin^{-1}\left(\frac{sin(\vartheta_i)}{n}\right)\right) \qquad \textbf{4-11}$$

Attempting to simplify the above equations via trigonometric identities proves fruitless, rather a Taylor Expansion of 4-10 around $a = 0$ provides an approximation as $F(x) = \sum_{m=0}^{M}\frac{\frac{d^m F(a)}{dx^m}(x-a)^m}{m!}$:

$$\begin{aligned} V_x \approx \left(2D - V_y + \frac{2\delta}{n}\right)\theta_i + \left(\frac{2D - V_y}{3} + \frac{2\delta}{n}\left(\frac{1}{2n^2} - \frac{1}{6}\right)\right)\theta_i^3 \\ + \left(\frac{4D - 2V_y}{15} + \frac{2\delta}{n}\left(-\frac{1}{4n^2} + \frac{3}{8n^3} + \frac{1}{120}\right)\right)\theta_i^5 \end{aligned} \qquad \textbf{4-12}$$

While it is true that the Taylor series, and in fact all forms of series expansion, is only exact for an infinitely long series, for realistic values of $\boldsymbol{V}$, D, δ, and n, the 5th order approximation given in equation 4-12 provides a good approximation within the limits $-1 < \theta_i < 1$ radians. Higher order expansions provide a better approximation[7] as the angle of incidence tends towards $\pm\frac{\pi}{2}$ and $\tan(\theta_i)$ tends towards infinite. However, this is not a general solution and obtaining the angle of incidence from the expanded equation requires obtaining the roots of the high order polynomial generated as part of the expansion.

---

[7] The Taylor series expansion of $\tan(x)$ is only valid in the region containing the expansion variable, a. I.e. the expansion of trigonometric identities do not repeat per 2π rotation. While this is problematic for a general equation, in practice the range of θ_i is constrained to $-\frac{\pi}{2} \leq \theta_i \leq \frac{\pi}{2}$ and as such the expansion variable a should also be constrained to $-\frac{\pi}{2} \leq a \leq \frac{\pi}{2}$.

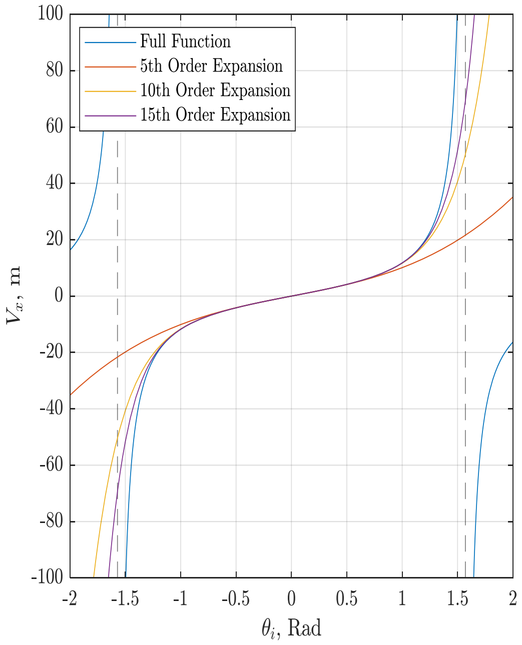

Figure 4-3 – Comparison between the full expression (4-9) and various orders of Taylor series centred around $a = 0$. While none of the expansions provide a good approximation as the function tends towards $\pm\frac{\pi}{2}$, the higher order approximations provide a more robust approximation at higher incident angles.

Since the function is monotonic within the region of $-\frac{\pi}{2} \leq \theta_i \leq \frac{\pi}{2}$, there is only one valid solution to Equation 4-9. As such, the problem of calculating θ_i can be pitched as an optimisation problem. I.e. minimising an objective function vis:

$$V_x - (2D - V_y)\tan(\theta_i) - 2\delta\tan(\theta_r) = 0 \tag{4-13}$$

The main benefit of this approach over the expansion and substitution approach illustrated thus far is a direct control over the attained precision and a greater reliability for high incident angles.

To do this minimisation, a recursive approach is taken. By rearranging Equation 4-9, an expression for the angle of incidence is obtained:

$$\theta_{i_q}(D, \boldsymbol{V}, n, \delta) = \tan^{-1}\left(V_x - \frac{2\delta\tan\left(\theta_{r_{q-1}}\right)}{2D - V_y}\right) \tag{4-14}$$

Where q is an integer number of iterations. As before, the angle of refraction is obtained through Snell's Law and a similar expression exists for the vertical component:

$$\vartheta_{i_q}(D, \boldsymbol{V}, n, \delta) = \tan^{-1}\left(V_z - \frac{2\delta \tan\left(\vartheta_{r_{q-1}}\right)}{2D - V_y}\right) \qquad \textbf{4-15}$$

By iterating through $q = 1,2,3 \ldots q_n$ and choosing a reasonable starting position, E.g. $\theta_{i_0} = 0$, the function converges towards a stable value for the angle of incidence. In effect, this finds the angle of incidence that minimises the total range. Whilst not as robust as a least squares regression, it is substantially faster. This becomes relevant in sections 5 and 7.

To further accelerate the optimisation, a moving average window is applied. In this way, the next value for θ_{i_q} is the mean of a window of previous iterations.

4.3 Extraction Methodology

To find the wall parameters, n and δ, it is necessary to fit this model to the data. This is done by minimising the discrepancy between the model and measured data, through means of an objective function.

4.3.1 Phase History

First, the bistatic $m \times p$ phase history data is generated, either through measurement or through simulation, where m and p are the number of frequency and aperture samples respectively.

At this stage, windowing functions are applied. The specific function and its weighting are dependent upon the quality of the data. For example, in [41] a Chebyshev window [147] is applied. Typically, with measured data, a pre-emphasis filter is also applied to maximise the received bandwidth, and thus giving the finest attainable resolution. The final stage of pre-processing uses equation 4-2. For a frequency, f, and a bistatic antenna configuration, A, the phase history, $\mathcal{P}(f, A)$, is corrected such that the front face of the wall appears at 0m range. This is done by multiplying $\mathcal{P}$ by a unitless phase ramp:

$$\mathcal{P}_{corrected}(f, A) = \mathcal{P}(f, A) \times e^{\frac{i2\pi f}{c} R_{Front}(A)} \tag{4-16}$$

This implies that the back face of the wall will appear at a range equal to the separation between the two faces:

$$\Delta R(n, \delta, D, \boldsymbol{V}) = R_{Back}(n, \delta, D, \boldsymbol{V}) - R_{Front}(D, \boldsymbol{V}) \tag{4-17}$$

The benefit of this is twofold. Firstly, it allows for any object in front of the wall, and hence shifted to a negative range, to be easily discounted. Secondly, it provides a convenient metric by which equation 4-2 can be evaluated for errors.

4.3.2 Range Profile Formation

After the pre-processing stages, the phase history data is converted into the time domain via a zero padded Fourier transform. The per pulse time domain representation of the phase history is referred to as the range profiles, $\hat{\mathcal{P}}(t, A)$. It has the same units (W) as the phase history. Under the Nyquist-Shannon criterion [2, pp.76–77,148,149] a complex band limited time domain signal can be completely recreated from discrete measurements if it is sampled at B samples per second, where B represents the bandwidth of the signal. Under these conditions, the range profile data, $\mathcal{F}[\mathcal{P}(f, A)]$, can be accurately interpolated at any time interval. From this, an unambiguous range, under which the system will not experience aliasing, is defined as $\frac{v}{2\Delta f}$, where Δf is the frequency step size (s^{-1}) and v is the signal propagation velocity (ms^{-1}).

Recall from Chapter 2.3, for an unmodulated signal the bandwidth is reciprocal to its time domain equivalent, i.e. $B\Delta t = 1$, increasing the bandwidth reduces the spread in time of the signal, Δt. From peak to null, the time difference is $\frac{\Delta t}{2}$, this gives the range resolution in meters from peak to null as:

$$R_{res}(v) = \frac{v}{2B} \tag{4-18}$$

Since $v < c$, the decreased velocity of the propagating EM wave inside a dielectric leads directly to finer range resolution when compared to free space. This is a major benefit to TWR and is the working principle of the so-called “Virtual Bandwidth SAR” [150,151]

For a given padded frequency domain signal, $\mathcal{P}(f,A) \in \mathbb{C}$, and a time domain equivalent, $\hat{\mathcal{P}}(t,A) = \mathcal{F}[\mathcal{P}(f,A)]$, the range profile value at range bin $M \in \mathbb{Z}$ must be determined. First, note that both $\mathcal{P}$ and $\hat{\mathcal{P}}$ are discrete datasets of equal length, $\mathcal{B}$, I.e. they both have the same finite number of elements. Following Gorham [152], the range bins are distributed evenly between $-\frac{\mathcal{B}}{2} \leq M \leq \frac{\mathcal{B}}{2}$. Given that the extremis of the range profile represented by $\hat{\mathcal{P}}(t,A)$ is given by the unambiguous range $\frac{v}{2\Delta f}$, the range at each bin is:

$$R_{bin}(M,v,\Delta f) = \frac{2v}{2\Delta f}\left(\frac{M-1}{\mathcal{B}-1}\right) - \frac{v}{2\Delta f} \qquad \textbf{4-19}$$

This is a normalised array between $-\frac{v}{2\Delta f} \leq R_{bin} \leq \frac{v}{2\Delta f}$ with bins equidistant between the limits. The fraction $\frac{M-1}{\mathcal{B}-1}$ controls the position in the array, with the unambiguous range controlling the scope.

4.3.2.1 Calculation of the Standoff Distance

The range profiles provide the Euclidean distance from the transmitting antenna to all the points of reflection in the scene and back to the receiving antenna for each bistatic antenna configuration in the SAR measurement. Given a known bistatic baseline, $\boldsymbol{V}$, the standoff distance from the transmitting antenna to the wall, D can be explicitly calculated via equation 4-2.

4.3.3 Defining the Objective Function and Upper and Lower Bounds

The objective function used to calculate the material properties calculates the sum of the intensities, ρ, of the range profile data at each antenna position in the bistatic collection, where ρ is the range profile intensity at $\frac{\Delta R(n,\delta,D,\boldsymbol{V})}{2}$. This intensity is found by interpolating the complex range profile data onto the query point.

$$F(n,\delta) = -\sum_{w=1}^{p}\left|\rho\left(\frac{[R_{Back}(n,\delta,D_w,\boldsymbol{V}_w) - R_{Front}(D_w,\boldsymbol{V}_w)]}{2},\boldsymbol{V}_w\right)\right| + \xi(n,\delta) \qquad \textbf{4-20}$$

$$F(n,\delta) = -\sum_{w=1}^{p} \left| \rho\left(\frac{\Delta R(n,\delta,D_w,\boldsymbol{V}_w)}{2}\right) \right| + \xi(n,\delta) \qquad \textbf{4-21}$$

A penalty term, $\xi(n,\delta)$, is introduced dependent upon the refractive index n and the material thickness, δ. This is so that the objective function becomes large when physically unreasonable properties are evaluated.

By summing over all positions, the objective function will cope with clutter that is only bright for part of the collection, since these will produce a worse fit than a consistently bright signature. Since the standoff distance D and the bistatic baseline vector $\boldsymbol{V}$ are known parameters, the objective function $F(n,\delta)$ can be minimised via a two-dimensional search algorithm.

The methodology for extracting the material properties is as follows: first, the ground truth positions of the antennas are established with respect to the wall. This includes the separation between the antennas, the height of both antennas, and the standoff distance to the wall. Next upper and lower bounds for n and δ are established. These bounds construct the penalty term, $\xi(n.\delta)$, that causes the objective function to increase substantially when the solver strays outside of the region of interest.

$$\xi(n,\delta) = \begin{cases} |n+1|^{30} & n_{lower} > n > n_{upper} \\ |\delta+1|^{30} & \delta_{lower} > \delta > \delta_{upper} \\ 0 & Otherwise \end{cases} \qquad \textbf{4-22}$$

The penalty term increases the further the solver travels outside of the allowed search space. This increase is in order to guarantee that a negative gradient, and thus the optimal direction for the minimisation routine, is in the direction pointing back towards the allowed search space.

To find the global minima of $F(n,\delta)$, a multistart conjugate gradient approach is incorporated. Given a random starting position $\boldsymbol{S_0} = [n_0, \delta_0]$ within the search space and the bounds defined by $\xi(n,\delta)$, the objective function is first minimised in the δ dimension. This provides a new interim position, $[n_0, \delta_1]$. In a two-dimensional optimisation, a one-dimensional minimum in the search space corresponds either a two-dimensional local minimum or a valley, at which point the optimal decision is to transition to the other variable. For this reason, the minimisation is then repeated in the n dimension, obtaining $\boldsymbol{S}_1 = [n_1, \delta_1]$. By iterating through $\boldsymbol{S_1}, \boldsymbol{S_2}, \boldsymbol{S_3} \ldots \boldsymbol{S_n}$, a two-dimensional local minimum is obtained. The global minimum is obtained by repeating this process for 500 different starting positions, from which a final minimum is extracted. This extracted minimum corresponds to the best fit for n and δ to the measured data.

4.3.3.1 Upper and Lower Bounds

This is based on both physical observations and an initial interpretation of the time domain data. The refractive index, n, cannot be less than 1, this leads to the logical boundary conditions that the wall thickness, δ, cannot be greater than the measured separation between the front and back face reflections, $\Delta R(n, \delta, D, \boldsymbol{V})$, and cannot be less than 0. An upper limit associated with the refractive index is obtained via prior knowledge that the material under test is concrete. For non-reinforced concrete, the material is non-magnetic and the relative permittivity has been reported as between 2 and 9 [59,67,90,99–101]. This gives a range of refractive indices between $\sqrt{2}$ and 3. In order to be encompassing, the limits chosen for the thickness and refractive index are broader than what is required. The upper and lower bounds used herein are $1 \leq n \leq 4$ and $0\text{m} \leq \delta \leq 0.3\text{m}$, this is a sufficiently range to include the known parameters obtained in Section 3.

4.3.3.2 Initial Sampling to Accelerate the Optimisation

To perform each of the one-dimensional minimisations required for the extraction of n and δ, Golden Section Search is implemented. In order to reduce the computation time an initial sampling of the search space is made. The objective function $F(n, \delta)$ is evaluated over a 100 by 100 grid covering the entire bounded search space, this grid is then interpolated at any position (n, δ) to quickly calculate $F(n, \delta)$. This reduces the number of computations of $F(n, \delta)$ speeding up the computation time of the solver at the expense of approximately 10^{-8}W accuracy.

4.3.4 Golden Section Search Algorithm

The goal of all minimisation routines, regardless of their complexity, is to obtain a value S that minimises the function $f(x)$. For a simple function, S can be obtained via differentiation, however, in more complex non-linear functions, it is often easier to iterate over the search space, x, until a reasonable minimum is found. Such is the guiding principle behind Golden Section Search [153, pp.384–386].

Consider the generic function $f(x)$, with a minimum, $x = S$. Illustrated in Figure 4-4.

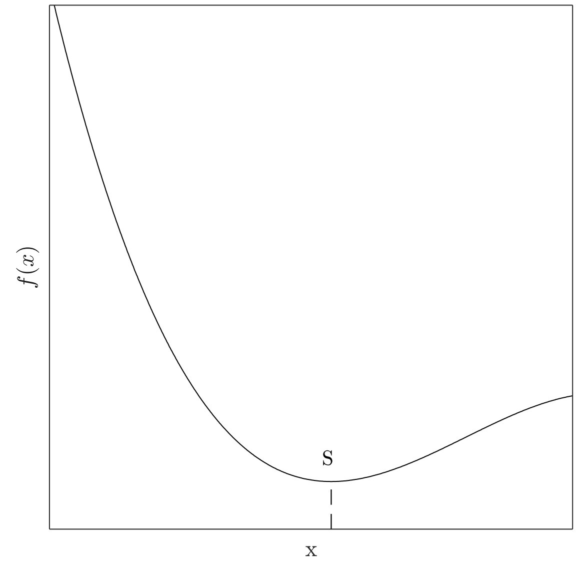

Figure 4-4 - Diagram of the generic function $f(x)$ with a minimum at $x = S$.

To find an initial approximation of S, the function is first bound. This involves calculating a region where the minimum is known to exist. To do this, an initial starting point x_0 is introduced. From x_0 the function is evaluated at x_1, where $x_1 = hx_0$. When $f(x_0) > f(x_1)$ then S is in the direction h. Repeating this process for $x_2, x_3, x_4 \dots x_n$ until the function finally increases provides an upper and lower bound on S such that $x_a < S < x_b$. In order to improve the speed of the optimisation, h is often increased by a constant factor [153, p.384] each iteration, this is so that the upper and lower bounds are found quickly. The implementation employed within this thesis uses $h = 0.001$ growing at a rate of 1.2.

Intuitively, this process can be repeated, making h successively smaller, until an appropriate tolerance is reached. However, this involves unnecessary computational work. The Golden Section Search algorithm uses a conceptually similar telescoping method; however, the function is only evaluated once per iteration. Consider the bound search space illustrated in Figure 4-5. The function $f(x)$ is evaluated at the points $x_a + R\Delta x$ and $x_b - R\Delta x$, where $\Delta x = |x_b - x_a|$. The telescoping mechanism is refined by redefining x_a and x_b as $x_a{}'$ and $x_b{}'$, depending on the function. The constant R is chosen such that the entire search space is at some point within the telescope.

If $f(x_b - R\Delta x) > f(x_a + R\Delta x)$ then one can conclude that the minima lies within $x_b - R\Delta x$ and x_b . Therefore x_a' is defined as $x_b - R\Delta x$ and x_b' remains constant. Similarly, if $f(x_a + R\Delta x) > f(x_b - R\Delta x)$ then $x_a' = x_a$ and $x_b' = x_a + R\Delta x$.

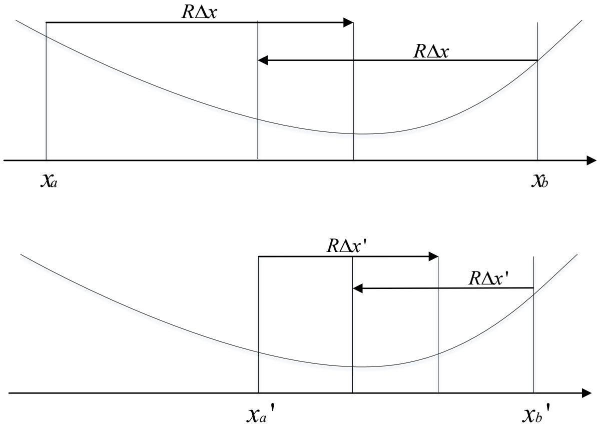

Figure 4-5 - Diagram of the telescoping mechanism utilised in Golden Section Search. The function is evaluated at the points $x_a + R\Delta x$ and $x_b - R\Delta x$ to choose a new set of bounds, x_a' and x_b'.

This telescoping method relies on the value of R being constant throughout. In such an instance, the value of R can be calculated by describing the width of the telescope, $(x_a + R\Delta x) - (x_b - R\Delta x)$ for both versions:

$$2R\Delta x - \Delta x = (x_a + R\Delta x) - (x_b - R\Delta x) \qquad \textbf{4-23}$$

$$2R\Delta x' - \Delta x' = (x_a' + R\Delta x') - (x_b' - R\Delta x') \qquad \textbf{4-24}$$

Since there should not be any region of the search space not potentially covered by the telescope, a further restriction on R can be placed. Namely that:

$$2R\Delta x - \Delta x = \Delta x' - R\Delta x' \qquad \textbf{4-25}$$

This equation implies that the telescoping is continuous [153, pp.384–386] and each subsequent iteration of the optimisation only requires one evaluation of the objective function. This can be further refined by substituting $\Delta x' = R\Delta x$. This produces:

$$2R\Delta x - \Delta x = \mathrm{R}\Delta \mathrm{x} - R^2\Delta x \tag{4-26}$$

$$2R - 1 = \mathrm{R} - R^2 \tag{4-27}$$

$$R^2 + R - 1 = 0 \tag{4-28}$$

The solution to this polynomial is the golden ratio, or more specifically, the conjugate of the golden ratio,

$$R = \frac{\sqrt{5} - 1}{2} = \phi - 1 = 0.6180 \ldots \tag{4-29}$$

In summary, the Golden Section Search minimisation routine utilises a telescoping method, converging at a rate of $R = 0.618 \ldots$, to accurately extract a local minimum from a generic function. The benefit of this approach is that, barring the first iteration, each subsequent iteration only requires one evaluation of the function. It is therefore well suited for complex and costly functions.

Since the optimisation converges at a rate of R, a predefined tolerance can be rewritten in terms of the number of iterations. The relation between the number of iterations and a tolerance Δs is:

$$\Delta x R^N = \Delta \mathrm{s} \tag{4-30}$$

10 iterations are enough to achieve a less than 1% tolerance. As will be shown in Section 4.6, this is significantly less than other sources of error. This was considered a good compromise between speed and accuracy.

4.3.4.1 Extension to Global Optimisation

The Golden Section Search Algorithm finds a local minimum, without any consideration for multiple local minima. Consequently, the algorithm is limited in its use for noisy and nonlinear functions. To extend the algorithm to a global optimisation, it is necessary to compute multiple local minima, $S_l \in x$, from which the global minimum can be extracted, via $S_g = \min(S_l)$.

For non-trivial problems, i.e. problems that require optimisation, there is no explicit way to determine the global minimum of the function [153, p.382]. As such, global optimisation generally requires multiple iterations, and lends itself well to a so-called *multistart* approach. The general form of a multistart algorithm is as follows:

```
While True:
    Generate random start position $x_0 \in x$
    Extract local minimum using minimisation routine, $S_l = g(x_o)$
    If $S_l < S_g$:
        $S_g = S_l$
        $k = k + 1$
    If stop criterion is met: end
```

Algorithm 4-1 - Generic multistart global optimisation routine.

From this, it should be clear that, allowed to run ad infinitum, a global minimum will be found. However, such a thing is impractical. As such, there is the question of how many iterations, k, are required to attribute a reasonable confidence to S_g. Following Lagaris and Tsoulos [154], the extent of the search space covered is a ratio between the index of the current iteration and the total number of iterations that fall within a predefined sub-space, $x' \in x$.

Let k' denote the number of iterations that terminate within x'. The ratio between k and k' denotes the coverage of the search space. As k tends towards infinity, the coverage, C, tends towards $\frac{x\prime}{x}$. I.e. for $x = Nx'$, $C \to \frac{1}{N}$. The variance of C is used to define the stopping criterion. The multistart operation is permitted to stop when no new global minimum has been found and $\sigma^2(C) < W\sigma^2(C_{last})$, where C_{last} is the coverage when the most recent global minimum was found. The variable W is used as a tuning factor to compromise between speed ($W = 1$) and completeness ($W = 0$).

The algorithm for multistart global optimisation can therefore be redefined as:

```
While $\sigma^2(C_n) \geq W\sigma^2(C_{n-1})$:
    Generate random start position $x_0 \in x$
    Extract local minima using minimisation routine, $S_l = g(x_o)$
    $k = k + 1$
    If $S_l \in x'$:
        $k' = k' + 1$
        If $S_l < S_g$:
            $S_g = S_l$
            $C_n = \sigma^2\left(\frac{k'}{k}\right)$
```

Algorithm 4-2– Multistart global optimisation routine containing a defined stopping criterion.

This definition of a stopping criterion is referred to as the Double Box criterion, so called due to the need for two predefined sets. It should be obvious then, that this stopping metric is ill suited for non-constrained optimisation.

Bayesian stopping criterions are also popular; however, such approaches require a prior assumption about the distribution to be applicable with Bayes' Theorem [155]. They are therefore unsuitable for applications where there is no prior knowledge.

Figure 4-6 shows a flow chart diagram of the pre-processing steps.

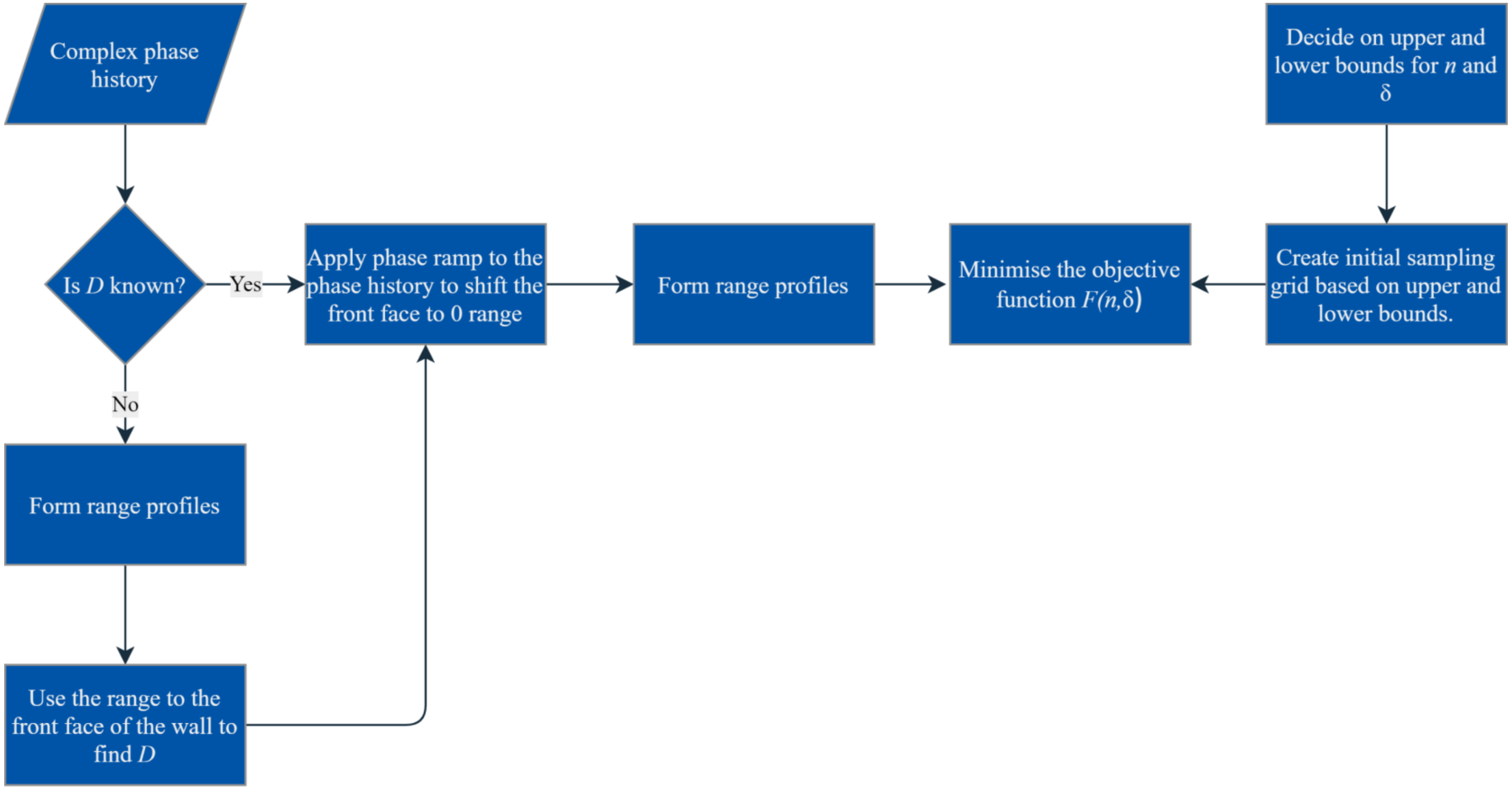

Figure 4-6 – Flow diagram of the extraction method. It shows the initialisation needed to create the objective function, as well as the optimisation routine. The optimisation is a two-dimensional Golden Section Search routine, treating n and δ independently.

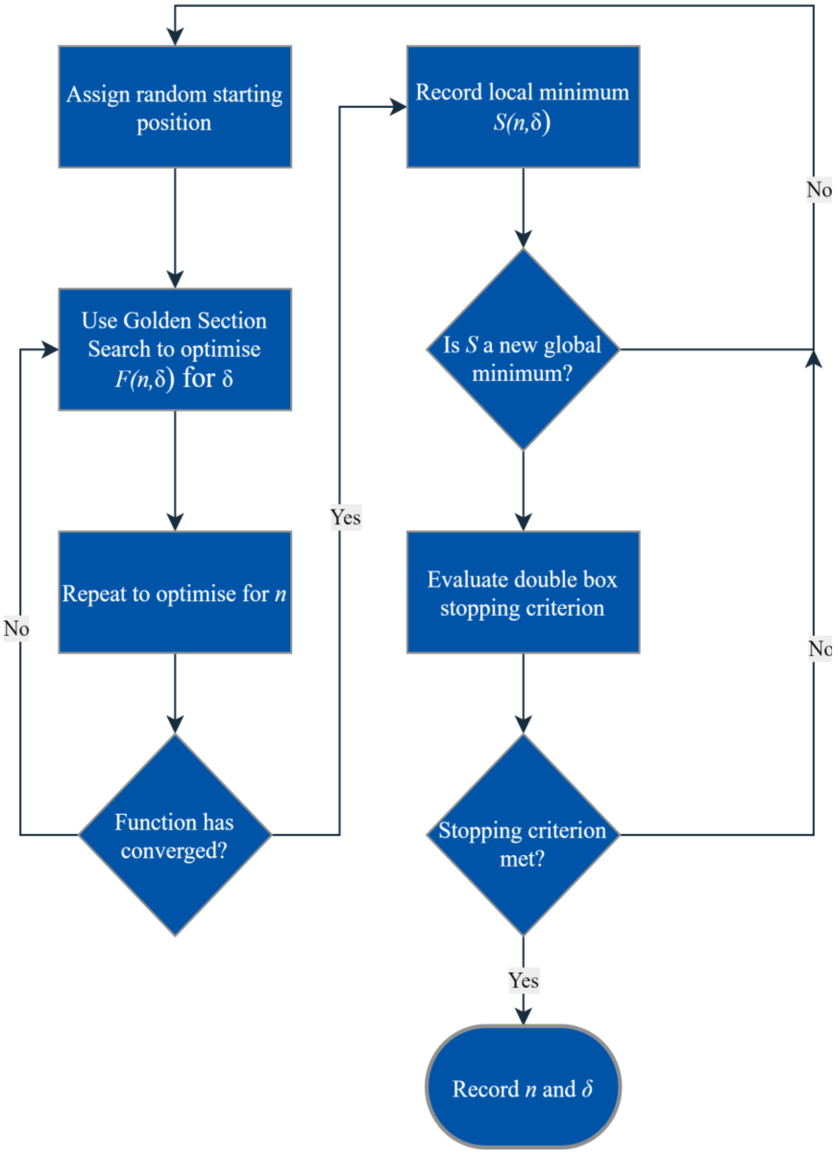

Figure 4-7 – Flowchart detailing the multistart two-dimensional Golden Section Search algorithm described in Sections 4.3.4 and 4.3.4.1 for finding the global minimum of equation 4-21.

4.4 Generalisation for Multi-Layer Walls

Similar to the previous single layer implementation discussed in Chapter 4, a multi-layer parameter extraction is characterised by two bistatic antennas separated by the baseline vector, $\boldsymbol{V} = \boldsymbol{R} - \boldsymbol{T} = [V_x, V_y, V_z]$, and a wall structure of L layers offset a distance D. This illustration is shown in Figure 4-8.

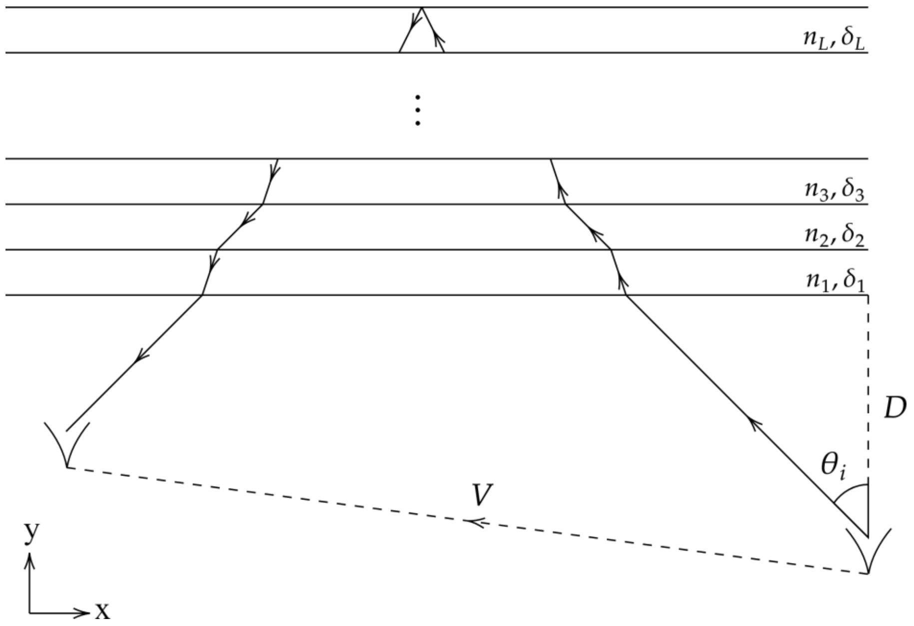

Figure 4-8 – Specular propagation through L layers of material, each of different thickness and refractive index.

Recall from Chapter 4.2, for a single layer of material, the angle of incidence in both the horizontal and vertical planes is obtained via rewriting ***V*** in terms of the angle of incidence and angle of refraction.

$$V_x = \left(2D - V_y\right)\tan(\theta_i) + 2\sum_{l}^{L} \delta_l \tan\left(\theta_{r_l}\right) \tag{4-31}$$

$$V_z = \left(2D - V_y\right)\tan(\vartheta_i) + 2\sum_{l}^{L} \delta_l \tan\left(\vartheta_{r_l}\right) \tag{4-32}$$

From Snell's Law, the angle of refraction for a specific layer is dependent upon the angle of the previous layer:

$$\theta_{l+1} = \sin^{-1}\left(\frac{n_l}{n_{l+1}}\sin(\theta_l)\right) \tag{4-33}$$

Rearranging equations 4-31 and 4-32 yields the generalised forms of equations 4-14 and 4-15:

$$\theta_i = \tan^{-1}\left(\frac{V_x - 2\sum_l^L \delta_l \tan\left(\theta_{r_l}\right)}{2D - V_y}\right) \tag{4-34}$$

$$\vartheta_i = \tan^{-1}\left(\frac{V_z - 2\sum_l^L \delta_l \tan\left(\vartheta_{r_l}\right)}{2D - V_y}\right) \qquad \textbf{4-35}$$

From these equations, it is clear that in order to calculate the angle of incidence, the thickness and refractive index for each layer must be known.

To extract the refractive index and thickness of each layer from a single measurement, for example, via a focusing based approach, requires a $2L$ dimensional optimisation. Doing so is both slow and prone to errors. A more efficient implementation is to use the range profile data. Since the refracted range to each layer boundary is dependent only upon the layers preceding it, the first layer parameters can be extracted without any consideration for the rest of the structure. The second layer properties are then extracted by including the first layer properties in the model. This continues for the third layer and so on. In this way, the thickness and refractive index for each layer are obtained. This iterative approach reframes the $2L$ dimensional optimisation as L 2-dimensional optimisations.

There is a major issue with this approach, however. An incorrect pair of parameters for the first layer will propagate through till+ the end of the optimisation, consequently affecting the extraction accuracy for each subquery layer. In short, lack of accuracy and precision due to ground-truth positioning errors will become exaggerated as more layers are added.

For practical reasons, alongside reasons regarding the parameter uncertainty that will be established in Chapter 4.6, a multi-layered structure is not considered within this thesis.

4.5 Simulation Methodology

In this section, simulations are used to estimate the dependence of each variable on the extraction methodology.

To model the received radar signal at each antenna position, the received EM pulse is treated as a sum of the contributions from all the different scatterers, τ_{total}, with return signal strength A, and additional white Gaussian noise, φ:

$$P(f,\varepsilon,\mu,\sigma) = \sum_{\tau=1}^{\tau_{\text{total}}} A_\tau e^{\gamma(f,\varepsilon,\mu,\sigma)R_\tau} + \varphi \qquad \textbf{4-36}$$

Where γ is the so-called propagation constant [58, p.139], a complex expression containing a consideration for both the phase term and the attenuation term. Derivations for the propagation constant are readily available in the literature, however different notation conventions are used with regards to the material conductivity, for this reason a derivation for γ has been included in appendix A.1. The propagation is dependent upon: the angular frequency, $\omega = 2\pi f$, the conductivity of the material, σ, the permittivity, ε, and the permeability, μ.

$$\gamma(f,\varepsilon,\mu,\sigma) = \alpha(f,\varepsilon,\mu,\sigma) - i\beta(f,\varepsilon,\mu,\sigma) \qquad \textbf{4-37}$$

$$\alpha(f,\varepsilon,\mu,\sigma) = \pm\sqrt{\frac{\omega^2\mu\varepsilon\left(\sqrt{1+\frac{\sigma^2}{\omega^2\varepsilon^2}}-1\right)}{2}} \qquad \textbf{4-38}$$

$$\beta(f,\varepsilon,\mu,\sigma) = \pm\sqrt{\frac{\omega^2\mu\varepsilon\left(\sqrt{1+\frac{\sigma^2}{\omega^2\varepsilon^2}}+1\right)}{2}} \qquad \textbf{4-39}$$

It is possible, depending on the established framework, to derive a complex permittivity, permeability, and refractive index. Due to this it is common to refer to complex material properties when discussing dielectric materials. To justify real values of the material properties, a derivation for equations 4-37, 4-38, and 4-39 is given in appendix A.1. While the permittivity and the permeability both affect the attenuation, the conductivity, and the frequency are the main components. The propagation frequency is usually known ahead of time; however, the conductivity varies from material to material.

It can be shown that, for a transverse propagating wave, the refractive index of the material is a ratio between the phase terms, β and β_0:

$$n(f,\varepsilon,\mu,\sigma) = \frac{c}{v} = \frac{\beta}{\beta_0} \qquad \textbf{4-40}$$

Therefore, the refractive index is also affected by the conductivity of the material, vis:

$$n(f,\varepsilon,\mu,\sigma) = \frac{\beta}{\beta_0} = \sqrt{\frac{\varepsilon\mu}{2\varepsilon_0\mu_0}\left(\sqrt{1+\frac{\sigma^2}{\omega^2\varepsilon^2}}+1\right)} \qquad \textbf{4-41}$$

$$\beta(f,n) = n\beta_0(f) \qquad \textbf{4-42}$$

For a conductive material, $\left(\frac{\sigma}{\omega\varepsilon}\right)^2 \gg 1$ whereas for an insulative material, $\left(\frac{\sigma}{\omega\varepsilon}\right)^2 \ll 1$, therefore for a dielectric:

$$\frac{c}{v} < n < \sqrt{\frac{\sigma\mu}{2\omega}}c \qquad \textbf{4-43}$$

For non-reinforced concrete, the conductivity is small, ~10^{-2} S/m [156–158], therefore the conductivity does not constitute a significant contributing factor to the refractive index. This is shown in Figure 4-9, where for nominal material properties (f =1GHz - 5GHz, $\mu = \mu_0$, $\varepsilon = 5\varepsilon_0$), the refractive index is calculated for a range of different conductivities. Below a conductivity of 10^{-1} S/m the material acts as an insulator, thus the conductivity does not play a significant role. Assuming a constant permittivity and permeability, at low conductivities, the frequency also does not contribute to the refractive index. This is because, the comparatively small-scale change in frequency does not offset the very small conductivity.

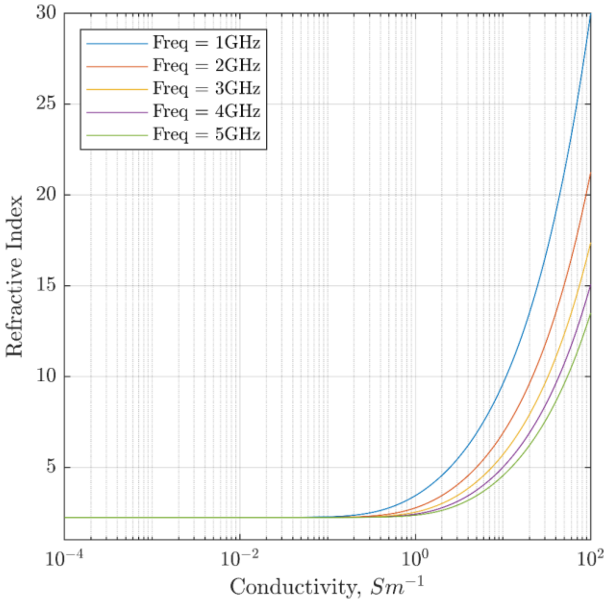

Figure 4-9 – Plot of refractive index against conductivity following Equation 4-41. Below 10^{-1} S/m, the conductivity does not have a significant impact on the refractive index.

Given that $\gamma(f, \varepsilon, \mu, \sigma)$ is dependent upon the material properties, to simulate a wall, the front and back face reflections need to be treated separately. Neglecting multipath, for the two specular reflections given from a single layer wall, denoted by layer 0 for the front face and layer 1 for the back face, the phase history is modelled as:

$$P(f, D, \boldsymbol{V}, \delta, n) = A_0 e^{\gamma_0(|\boldsymbol{r_1}|+|\boldsymbol{r_2}|)} + A_1 e^{\gamma_0(|\boldsymbol{r_3}|+|\boldsymbol{r_6}|)+\gamma_1(|\boldsymbol{r_4}|+|\boldsymbol{r_5}|)} + \varphi \qquad \textbf{4-44}$$

For non-conductive materials, such as dry concrete, the attenuation term, equation 4-38, is 0. For this reason, the propagation constant γ is only dependent upon the phase term, $\beta(f, n)$, and consequently, equation 4-44 is dependent upon n rather than ε and μ.

The γ_1 term is calculated from the wall material properties, whereas the γ_0 term is for air. The delay due to the refraction is inherently contained within γ_1, thus there is no need to explicitly include modulation of the range to the back face of the wall. The variables A_0 and A_1 represent the amplitude of the received signal from the front face and back face respectively. They are 1 and 0.5 respectively. The noise term φ is independent of the wall material, bistatic geometry, and frequency. It will be examined Section 4.6.2.

4.6 Sensitivity to Errors

The following discussion of error sensitivity is based on the following simulation, onto which errors are added step wise.

A bistatic geometry consisting of a moving transmitter and a fixed stationary receiving antenna is shown in Figure 4-10. A wall, modelled as an infinite slab in elevation and cross range, has been introduced to the scene 5m down range from the transmitting antenna. The wall thickness is 0.1m and its refractive index is 2.5. The phase history is generated via equation 4-44 and converted into the range profiles shown in Figure 4-11. As the moving antenna moves across the aperture, and away from the stationary antenna, the bistatic range is seen to increase. The opposite trend would be observed if the antennas were moving closer together. Due to interference between the two range profile signatures, there is a very small ($\sim 10^{-4}$m) difference between the signature range and its true range for both the front face and back face signatures. This is a small enough error that it can easily be overshadowed by rounding errors in P, however is sufficient to cause errors in the extracted results, even for simulations with no deliberately introduced errors.

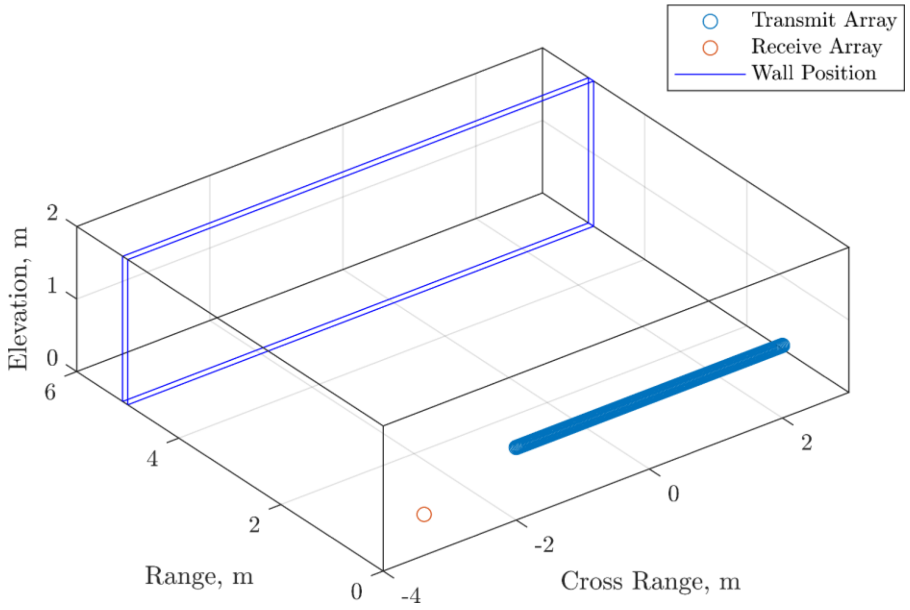

Figure 4-10 – Simulated antenna configuration. Showing the transmitting and receiving antenna positions with respect to a wall. The receiving antenna is fixed at coordinate [-3,0.5,0.2] whilst the transmitting antenna ranges from [-2,0,1] to [2,0,1]. The wall is modelled as an infinite slab of thickness 0.1m at a distance of 5m from the transmitting antenna.

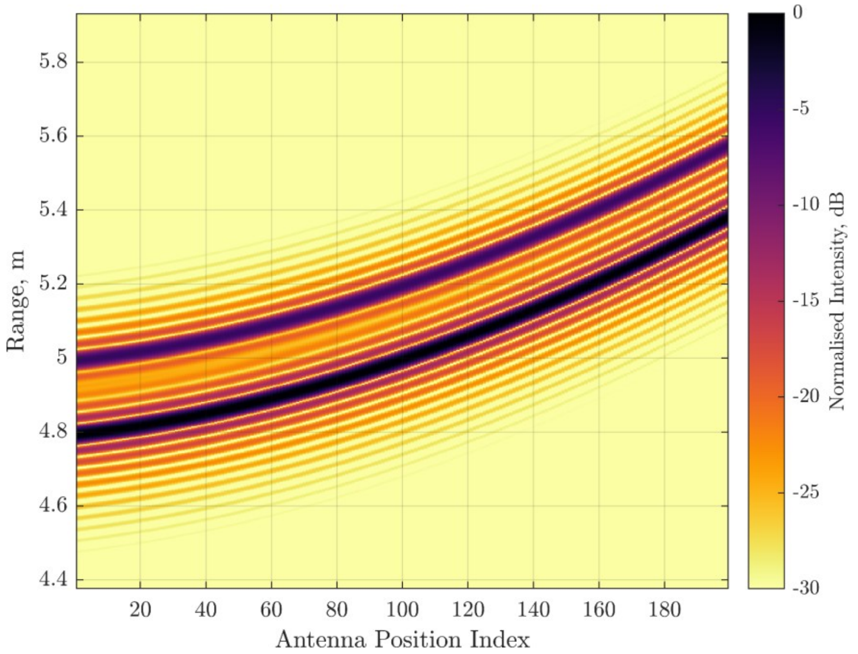

Figure 4-11 – Simulated range profile obtained by a Fourier transform of the raw phase history obtained from the measurement geometry shown in Figure 4-10. As the transmitter moves from its starting position across the aperture, it moves further from the receiving antenna. Therefore, the range to the wall is seen to increase.

4.6.1 Positional Errors

Positional errors refer to discrepancies between the assumed and true geometry of the wall with respect to the antennas, either as an error in the antenna positioning or in the wall positioning. The uncertainty in geometry can be split into two categories: random errors, due to motion and the like, and systematic errors, due to inaccurate ground truth measurements. The two sources of error are treated separately, as, unlike systematic errors, one would expect repeat measurements of random errors to regress towards the mean.

4.6.1.1 Random Errors

The random positional errors that occur on a ground based SAR system are predominantly small-scale motion errors due to flex and wobble of the SAR rig and is approximately independent for each pulse. Modelling this error as a Gaussian distribution, the effect of this motion error is directly investigated. By introducing a random 3-Dimensional offset to each antenna position, the motion error in the system can be characterised by a standard deviation, σ_{motion}.

Table 2 – Mean and standard deviation on extracted parameters following an error introduced in V on a per pulse basis.

σ_{motion} (m)	$\bar{n}$	$\bar{\delta}$, mm	σ_n	σ_δ, mm
0	2.50	100.12	0.02	0.80
10^{-4}	2.50	100.14	0.02	0.76
10^{-3}	2.50	100.13	0.04	1.71
10^{-2}	2.59	99.15	0.44	15.10
10^{-1}	2.44	149.20	1.37	85.23
1	2.19	135.70	1.34	81.02

From this table, it is shown that random motion error introduced to the moving antenna produces a decrease in precision for the extracted parameters. Motion error on order of a mm is sufficient to extract the wall properties, more than that however, and the algorithm becomes imprecise. Plotting the parameter standard deviation against the motion error (Figure 4-12) shows that the effect follows noticeable polynomial distribution on a logarithmic scale.

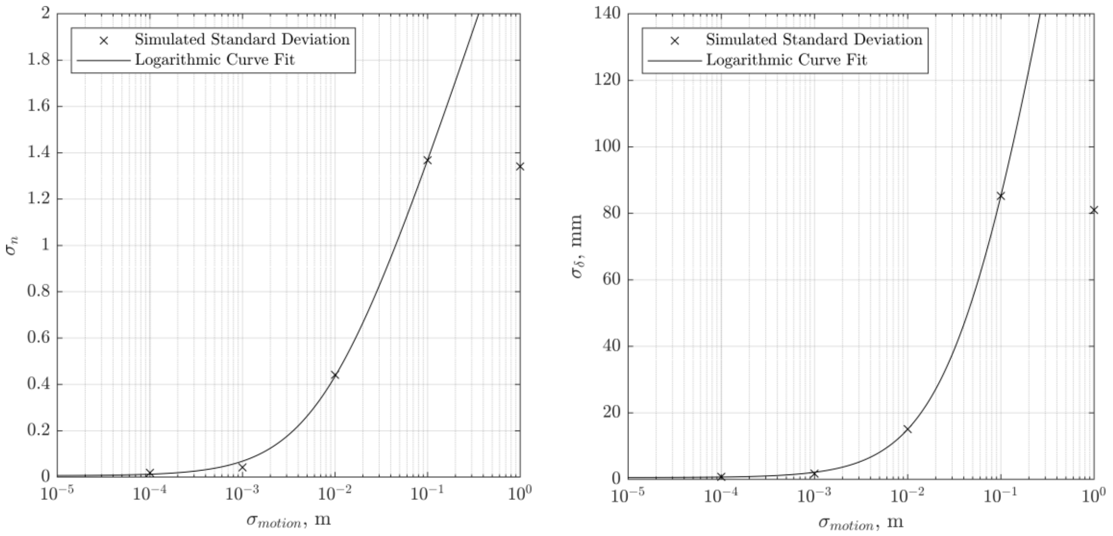

a) b)

Figure 4-12 – Plot of standard deviation as a function of introduced motion error for a) refractive index, and b) thickness. The plots show that the precision follows a logarithmic trend and that motion errors under a standard deviation of 1mm is sufficient to precisely extract the material properties.

Since the datapoints follow a noticeable polynomial trend, a logarithmic curve fit is employed. The logarithmic curve fit follows the function $y = A\ln(x + B) + C$. For the refractive index, A, B, and C are 0.52, 7.8×10^{-3}, and 2.52 respectively. For the thickness, A, B, and C are 72.52, 0.045, and 225.2 respectively.

Due to the requirement that there be little motion error, the moving antenna should either be fixed to a rigid frame or be sufficiently slow moving. For the GBSAR system used in the experimental component of this chapter, the maximum motion error is observed to be on order of 0.5cm. Modelling the motion error as a simple sinusoid, the root mean square error is 3.5mm. This corresponds to $\sigma_n = 0.20$ and $\sigma_\delta = 5.94$mm.

It is worth noting that reducing the size of the bound search space would also reduce the standard deviation on both parameters. This is an artificial effect due to solutions bunching up at the extremes of the search space, therefore, to minimise the effect the search space was made far larger than is strictly necessary. That said, this effect is still present to some degree, hence the outliers at $\sigma_{motion} = 1$m.

4.6.1.2 Systematic Errors

In addition to the random error discussed thus far, there are also systematic errors in the motion. These derive from underlying inaccuracies in the actual positioning of the SAR system with respect to the wall. For example, the wall may be further away than first thought, or it could potentially be at an angle with respect to the antenna trajectory.

There are:

- Propagation delays due to the radar components. For example, propagation along microwave cables.
- Inaccuracies in $\boldsymbol{V}$
- An unknown or changing distance to the wall, D.

Propagation delays due to internal components do not change as a function of antenna position or scene content. It follows then, that the range difference between front and back wall faces remains unaffected.

Inaccuracies in the bistatic baseline vector, $\boldsymbol{V}$, are far more problematic, as a known baseline vector is inherent to the entire process. $\boldsymbol{V}$ will change as a function of antenna position, however, if the motion of the moving antenna is known, then $\boldsymbol{V}$ can be explicitly calculated from an initial baseline. It will be shown in Chapter 4.8 that $\boldsymbol{V}$ can be recovered from an analysis of the front face scattering. However, for now, assume that there is some uncertainty with the measurement.

Similarly, the standoff distance, D, is also a required parameter. Potentially, D may also change as a function of antenna position. For the linear SAR trajectory used herein, this would imply that the wall is at an angle with respect to the SAR motion. As with $\boldsymbol{V}$, the standoff distance can be calculated via an analysis of the front face scattering.

To examine the effect of an erroneous baseline vector, a Gaussian distributed error is added to the initial antenna positions. Modelled as a 3-Dimensional normal distribution with mean 0 and standard deviation $\sigma_{\boldsymbol{V}}$, this error is added to 200 repeat simulations following the geometry outlined in Figure 4-10, the results of which are shown in Table 3

Table 3 – Mean and standard deviation on extracted parameters following a systematic error introduced in the first pulse.

σ_V (m)	$\bar{n}$	$\bar{\delta}$, mm	σ_n	σ_δ, mm
0	2.50	100.17	0.02	0.81
$\mathbf{10^{-4}}$	2.49	100.22	0.02	0.79
$\mathbf{10^{-3}}$	2.50	100.18	0.03	1.62
$\mathbf{10^{-2}}$	2.56	99.45	0.30	14.52
$\mathbf{10^{-1}}$	2.76	91.05	1.23	53.03
1	2.09	135.96	1.23	86.39

From Table 3 it is apparent that introducing a systematic error in the antenna positioning is not an issue on a millimetric scale but is problematic for positioning uncertainties greater than 1cm.

As before, the uncertainty in the extracted parameters follows a polynomial distribution on a logarithmic scale. Therefore, the same curve, $y = A\ln(\mathrm{x} + \mathrm{B}) + C$, is fitted. Shown in Figure 4-14, the fitted curve follows all but the last datapoint. For errors introduced in the positioning of the first pulse, A, B, and C are equal to 0.65, 0.02, and 2.62 for refractive index and 24.19, 0.01, and 105.80 for thickness.

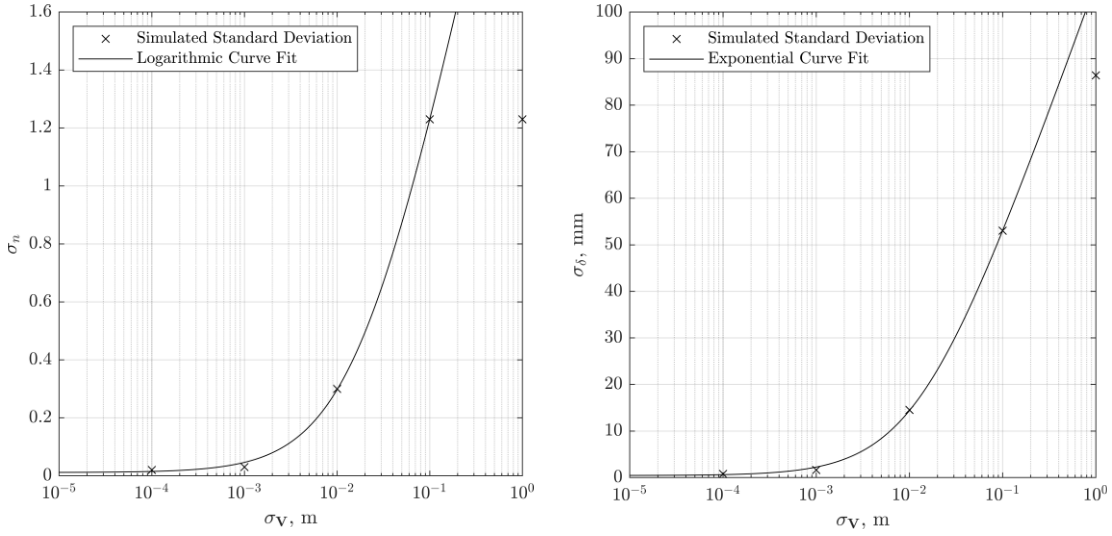

a) b)

Figure 4-13 – Plot of standard deviation as a function of introduced systematic error in the bistatic baseline for a) refractive index, and b) thickness. From this it is clear that antenna position errors under a standard deviation of 1mm is sufficient to precisely extract the material properties.

The same approach is followed to investigate the effect of an inaccurate standoff distance. 200 repeat simulations are carried out, each introducing a Gaussian distributed error in D with standard deviation σ_D. This is presented in Table 4. Since it is a Euclidean range being altered, this is not dissimilar to altering the y component of $\boldsymbol{V}$.

Table 4 - Mean and standard deviation on extracted parameters following an error introduced in D.

σ_D (m)	$\bar{n}$	$\bar{\delta}$, mm	σ_n	σ_δ, mm
0	2.50	100.12	0.02	0.80
10^{-4}	2.50	100.12	0.02	0.81
10^{-3}	2.50	100.26	0.07	2.87
10^{-2}	2.65	99.99	0.66	23.31
10^{-1}	2.23	148.50	1.38	86.40
1	2.31	127.50	1.38	81.13

From this table, it is deduced that standard deviations above a millimetre scale introduce a significant uncertainty, in line with the uncertainty arising from motion errors, as shown in Table 2. This is to be expected, as a changing standoff distance is analogous to a changing antenna position. This similarity is illustrated in Figure 4-14 wherein it is shown that the standard deviation on the extracted parameters follows the same logarithmic curve as Figure 4-12.

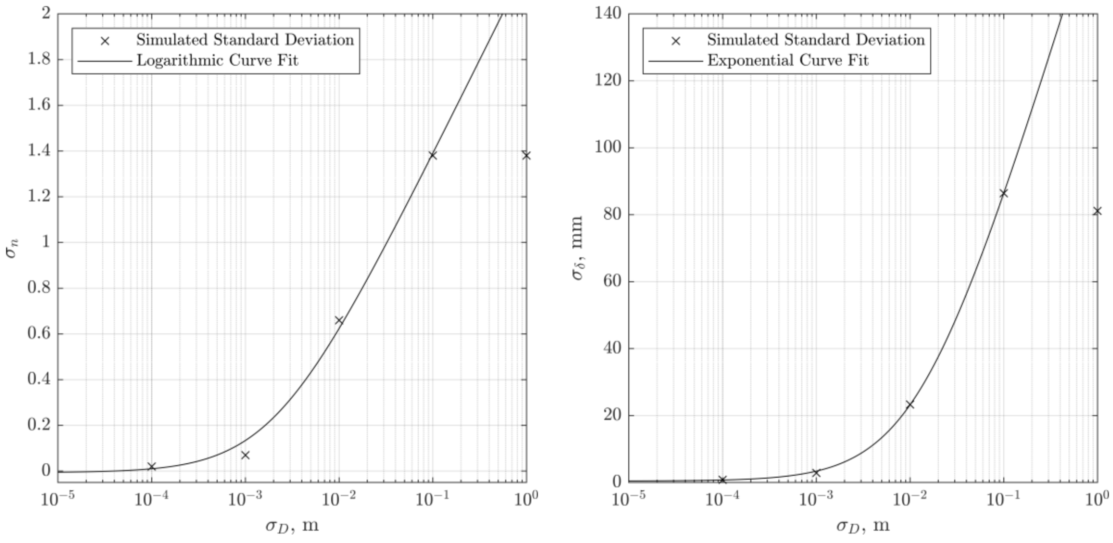

a) b)

Figure 4-14 – Plot of standard deviation on extracted parameters as a function of random errors introduced to the standoff distance for a) refractive index, and b) thickness. The plots show that although the curves follow a logarithmic trend, the standoff distance has a greater effect than $\boldsymbol{V}$.

The curve fitting follows the same format as Figure 4-12. For the refractive index: $A = 0.36$, $B = 2.1 \times 10^{-3}$, and C =2.21. For the thickness: $A = 39.59$, $B = 0.01$, and $C = 172.8$. From this, it is clear that errors in the standoff distance have a greater effect on the final extraction of thickness than errors in the bistatic baseline, $\boldsymbol{V}$. This is a trend that is also subtly observed with respect to the refractive index.

But, what about a linearly changing D? I.e. the SAR rail being at some erroneous angle with respect to the wall.

Note that a changing standoff distance can be approached in two ways, either as the rail moving towards the wall, or as the wall moving towards the rail. In this sense, a linear change in standoff distance can be re-cast as a consequence of a linear change in $\boldsymbol{V}$. This is a key benefit of the asymmetric approach, namely the wall need not be parallel to the SAR system.

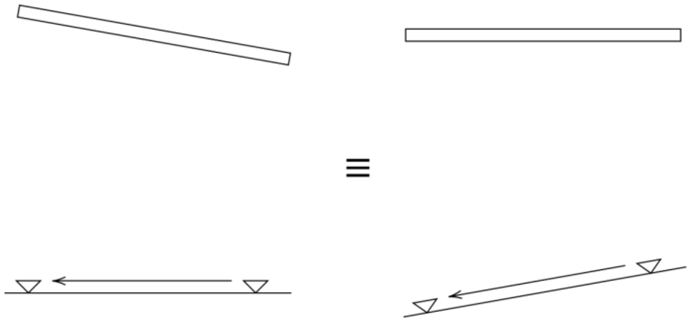

Figure 4-15 – Visual illustration that a linear change in standoff distance can be expressed as a linear change in the down range component of $\boldsymbol{V}$.

This is simulated via rotating the SAR trajectory around the z axis. Again, the errors introduced follow a Gaussian distribution with mean 0 and standard deviation $\sigma_{\angle}$.

Table 5 - Mean and standard deviation on extracted parameters following an error introduced in the angle of the SAR rail with respect to the wall.

$\boldsymbol{\sigma_{\angle}}$ (rad)	$\boldsymbol{\overline{n}}$	$\boldsymbol{\overline{\delta}}$, mm	$\boldsymbol{\sigma_n}$	$\boldsymbol{\sigma_\delta}$, mm
0	2.50	100.12	0.02	0.80
$\mathbf{10^{-4}}$	2.51	99.49	0.06	2.28
$\mathbf{10^{-3}}$	3.14	83.30	0.66	18.16
$\mathbf{10^{-2}}$	3.03	108.43	1.23	61.78
$\mathbf{10^{-1}}$	2.21	126.15	1.44	68.65
1	2.48	144.79	1.33	73.24

From Table 5 it is clear that the angle of the SAR motion with respect to the wall must be precisely known for the extracted wall properties to have any significant meaning. An uncertainty in the angle on order of 0.1° ($\sim 10^{-3}$ radians) would incur an uncertainty associated with the refractive index of approximately 25%.

As before, the standard deviation associated with both extracted parameters follows an approximate logarithmic curve $A\log(x+B)+C$ that is most appropriate for smaller values. In this case, $A = 0.48$, $B = 7.5 \times 10^{-4}$, and C =3.47 for refractive index and 25.76, 1.02×10^{-3}, 177.9 respectively for thickness. Figure 4-16 shows that these fitted curves are most appropriate for smaller numbers. The trend appears to break down for angle errors above 0.01 radians (0.57 degrees).

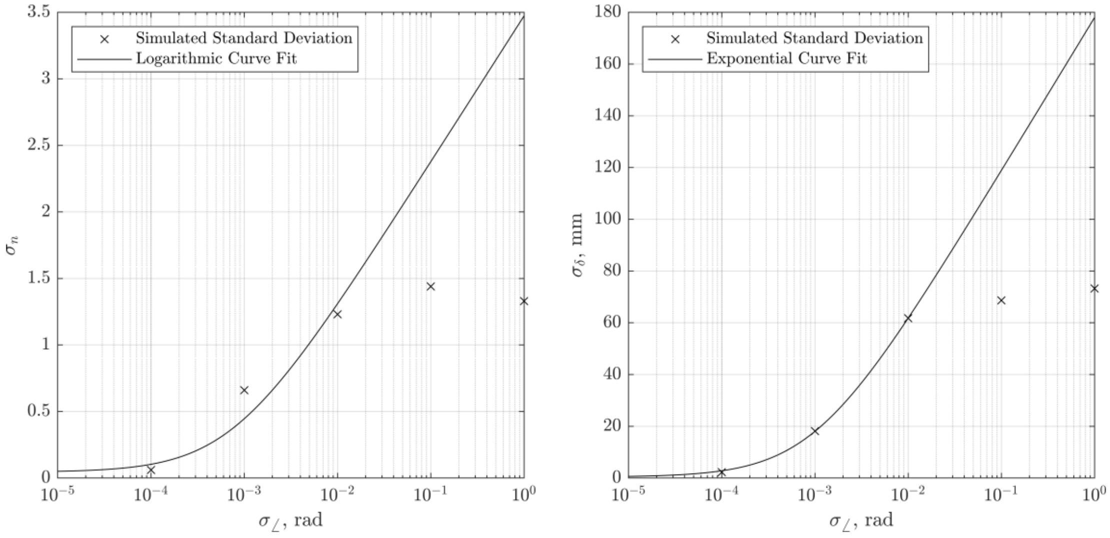

a) b)

Figure 4-16 – Plot of standard deviation on extracted parameters as a function of random errors introduced to the angle of the SAR rail with respect to the wall for a) refractive index, and b) thickness. Angle errors above 10^{-2} radians are shown to cause the parameter estimation to break down.

4.6.2 Noise

Noise is an inherent property in physical EM measurements, due to thermal radiation, interference, atmospheric electrostatics, and the cosmic microwave background. Due to the complexity of the interactions between all these different sources, radar noise is typically considered to have a random amplitude and phase, following a complex white Gaussian distribution with mean of 0.

By modulating the standard deviation of the distribution, the effect of said noise is directly investigated. This is done by varying the SNR and re-simulating the data then running the extraction algorithm detailed in 4.3:

$$\mathrm{SNR} = \frac{\max|\mathcal{P}|}{\sigma_{noise}} \qquad \textbf{4-45}$$

For various signal to noise levels, the simulated data shown in Figure 4-11 is generated and fed into the parameter extraction algorithm. This is then repeated 100 times, to give a reasonable approximation of the uncertainty in n and δ.

Table 6 – Extraction results from simulated data, given additive noise.

SNR (dB)	$\bar{n}$	$\bar{\delta}$, mm	σ_n	σ_δ, mm
-20	2.61	97.71	0.40	13.20
0	2.51	99.93	0.10	3.84
20	2.50	100.21	0.03	1.42
40	2.50	100.15	0.02	0.88
60	2.49	100.21	0.02	0.78
80	2.50	100.19	0.02	0.82
∞	2.50	100.17	0.02	0.81

The standard deviation for both parameters is seen to decrease as the SNR increases, this would imply that the extraction methodology is more precise when using higher SNR data. The accuracy, however, does not change significantly with the addition of noise. This makes sense since the mean of the additive noise is 0. Plotting the standard deviation, for both n and δ, as a function of SNR reveals that the precision follows an exponential decay of the form $Y = Ae^{Bx} + C$ where $A = 0.076$, $B = -0.080$, and $C = 0.019$ with respect to refractive index, and $A = 3.07$ and $B = -0.070$, and $C = 0.73$ with respect to thickness. From Figure 4-17, the exponential nature of the decay means that a SNR below 0 is problematic. However, for more reasonable noise floors ($\mathrm{SNR} \geq 40\mathrm{dB}$) there is little effect on the extracted parameter accuracy or precision, and as such noise is not a significant cause for concern.

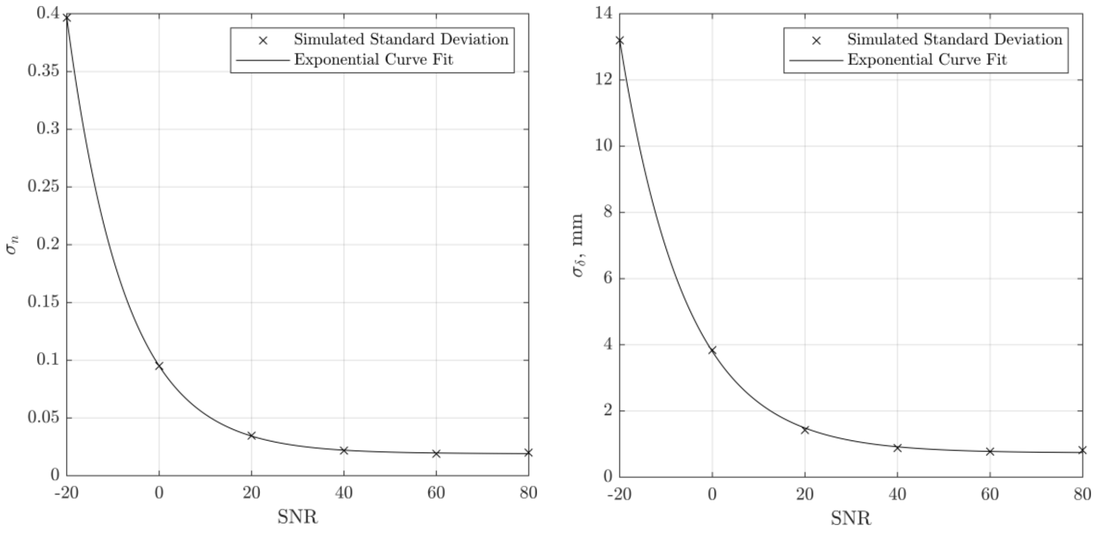

a) b)

Figure 4-17 – Plot of the standard deviation of the extraction methodology as a function of SNR for both a) refractive index, and b) thickness. The plots show that the precision follows an exponential decay.

4.6.3 Material Inhomogeneity

The concrete wall material has, broadly speaking, two metrics for homogeneity. The first being the material mix, and the second being the surface roughness. The former contributes toward a spatially variant refractive index, while the later contributes toward a variant wall thickness and disrupts specular scattering.

4.6.3.1 Inhomogeneous Material Mixture

As mentioned in Chapter 3.2, concrete can be considered a mixture of a homogeneous (at the wavelengths of interest) host material and an inhomogeneous perturbation material. Following Maxwell-Garnett [95], it is not possible to extract either the properties of the host material or the perturbation material without first knowing the mixing ratios used in manufacture.

This perturbation material is, by definition, spatially variant. It is therefore important that a large section of the wall is considered, in order to obtain an effective set of properties that are representative of the entire structure.

4.6.3.2 Inhomogeneous Material Surface

The roughness of a surface, from the point of view of an EM wave, is generally considered in terms of the phase change between the extremes of the material depth. Consider a material whose surface undulates with a RMS[8] error of Δh, illustrated in Figure 4-18.

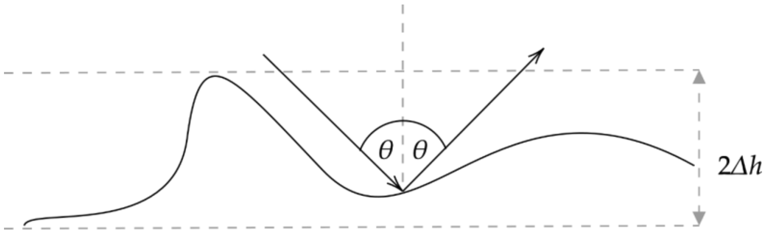

Figure 4-18 – Example reflection from a rough surface characterised by a height offset of Δh.

For two propagating waves with angle θ interacting with the material, offset by Δh, there is a difference in path length. From this difference in path length, there arises a phase change between the two waves. Illustrated in Figure 4-19, the phase difference due to the height difference is dependent upon the wavelength, and the incident angle:

$$\Delta\phi = \frac{4\pi f}{c} d = \frac{4\pi\Delta h cos(\theta)}{\lambda} \qquad \textbf{4-46}$$

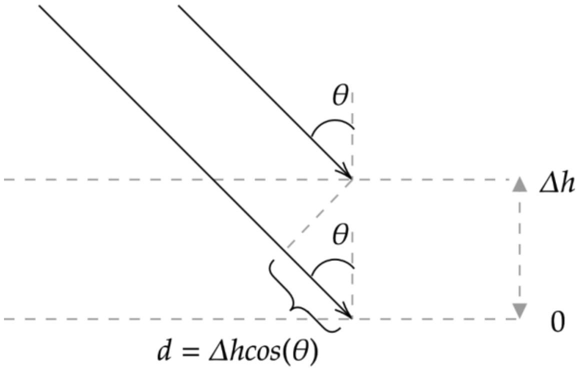

Figure 4-19 – Illustration of the path length difference arising due to a depth offset of Δh.

---

[8] The root mean square (RMS) error is used as a metric for the entire surface of interest. As such, Δh is also representative of the entire surface.

Equation 4-46 can be rewritten to find the height offset needed to satisfy an upper limit on $\Delta\phi$:

$$\Delta h \leq \frac{\Delta\phi\lambda}{4\pi\cos(\theta)} \qquad \textbf{4-47}$$

Thus, the only remaining question is what is an acceptable phase change? A widespread metric is the Rayleigh Criterion [159,160], $\frac{\pi}{2}$, this gives a max height difference of $\frac{\lambda}{8}$ for normal incidence. An alternate metric, the Fraunhofer Criterion [33,160], uses a phase change of $\frac{\pi}{8}$, giving a height of $\frac{\lambda}{32}$ for normal incidence. The range of possible incident angles ranges from -90 to +90 degrees. Normal incidence therefore represents the minimum height variation required to satisfy equation 4-47.

At the 6GHz upper limit for these wall measurements, the free-space wavelength corresponds to approximately 5cm. However, given that propagating wavefronts are compressed within a dielectric, the interior wavelength (taking a representative value of $n = 2.5$) is 2cm. This implies that for a wall material to be sufficiently rough as to cause an issue, the RMS error on block thickness must be greater than 2.5mm. Given that the surface roughness of the wall is estimated as 0.322mm the wall is assumed to be smooth with respect to the 1GHz to 6GHz frequency band of interest. For this reason, the reflection from the wall surface is assumed to be specular for both the front and back faces.

While the reflection from the wall is specular, it is unclear if a small change in the surface is sufficient to cause an inaccuracy with regards to the extraction of the material properties. To emulate a small depth differences at the point of reflection, a normally distributed random range offset between $-\Delta hcos(\theta_i)$ and $\Delta hcos(\theta_i)$ is added to the simulations. This random range offset constitutes a random phase offset. In this regard, adding a rough surface is not dissimilar to adding noise.

Similar to Table 6, a comparison of the effectiveness of the extraction methodology under different surface roughnesses is presented in Table 7.

Table 7 – Comparison of the effectiveness of the extraction methodology under different surface roughness's, defined by a standard deviation σ_h.

σ_h, m	$\bar{n}$	$\bar{\delta}$, mm	σ_n	σ_δ, mm
$\mathbf{0}$	2.50	100.19	0.02	0.74
$\mathbf{10^{-4}}$	2.50	100.12	0.02	0.71
$\mathbf{10^{-3}}$	2.50	100.12	0.02	0.99
$\mathbf{10^{-2}}$	2.52	99.56	0.12	4.87
$\mathbf{10^{-1}}$	2.66	110.04	1.02	44.00
1	1.93	144.79	1.26	71.83

The surface roughness of the material does not have a significant impact on the parameter extraction for material perturbations on a scale less that 1cm. The measured surface roughness of the concrete is 0.322mm, this is further justification that the wall acts as a specular reflector.

Recall via Figure 3-2, the standard deviation of block thickness is 0.322mm. The expected laboratory error due to surface roughness associated with the bistatic measurements presented in Chapter 4.7 is therefore negligible.

In this instance, the curve fit coefficients: A, B, and C are 5.67, 0.52, and 3.77 for the refractive index and 383.1, 0.83, and 70.37 for thickness.

To summarise, systematic errors, such as an erroneous antenna positioning, have a much greater impact on the precision of the asymmetric parameter extraction than random errors, such as noise. It is therefore important that the antenna geometry with respect to the wall be known very precisely in order to minimise the uncertainty associated with the extracted parameters.

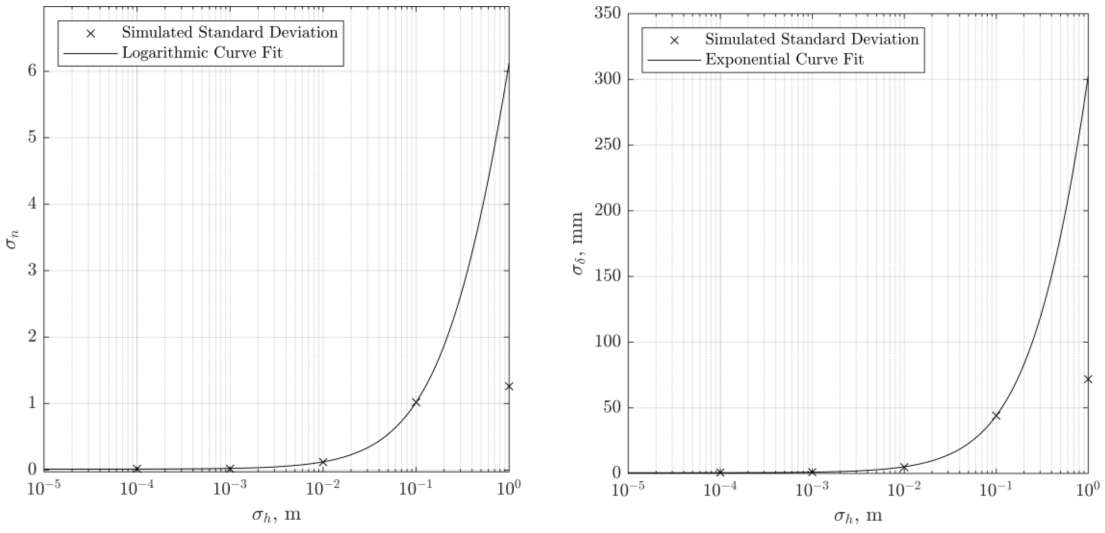

a) b)

Figure 4-20 – Plot of the standard deviation of the extraction methodology as a function of surface roughness for both a) refractive index, and b) thickness. The plots show that surfaces with a standard deviation less than 1cm cause a negligible effect.

4.6.4 Clutter

The proposed bistatic method for extracting wall properties is resistant to clutter, as clutter follows a different azimuthal evolution than the wall structure. However, the range profile signatures of the wall may still be distorted by interference from different scatterers. As such, range gating is often employed. However, range gating is limited in that clutter near or inside the wall cannot be effectively gated. Clutter near to the wall signature is the only clutter that is particularly worrying, so range gating is of limited use. However, as will be shown in Chapter 6, a two-dimensional synthetic aperture allows for height discrimination, thus allowing for clutter to be removed based on its height. This allows for the elimination of ground-based clutter and multipath signatures, such as the wall-floor dihedral.

4.7 Initial Lab Testing

An initial evaluation of the technique was undertaken using a simple bistatic geometry similar to Figure 4-10. In this case, a moving antenna is mounted to a linear motorised rail as a stop-start style of SAR. The other antenna is placed on a polystyrene plinth angled towards the centre of the wall. The wall was built 1.29m high at a distance of 4.09m. This is illustrated in Figure 4-21. The exact bistatic vector, $\boldsymbol{V}$, was obtained via measuring the initial antenna separation and adding an offset for each pulse based on the step size of the moving antenna. In this case that step size is 2cm in the along track direction.

176 radar measurements were taken over a frequency range of 1GHz to 6GHz using a Keysight N5245B PNA-X network analyser and a pair of A-Info LB-10180-NF broadband horn antennas. This gives a theoretical free space range resolution of 3cm, although, as will be seen, the actual achieved resolution is much coarser. The 3dB beamwidth for both antennas ranges from 33 to 61 degrees over the frequency range of interest [161]. The ground-based antenna was orientated such that the aperture pointed at the centre of the wall structure, shown in Figure 4-21. The point of reflection does not therefore travel outside of the 3dB beamwidth of either antenna. The points of reflection on the back face of the wall is similarly always withing the beamwidth.

For cluttered measurements, with objects immediately behind the wall, the clutter is likewise within both antenna beamwidths. From Section 4.6.3.2, the material surface roughness does not have a significant impact on the extraction of the material properties, therefore the brightest return signal in the measured range profile is assumed to correspond to the specular reflection from the wall surface.

Since only a relative measurement between the front and back face signatures is required, there is no need for a prior calibration of the radar system [128].

In this initial block of experimental work, two subtly different antenna trajectories are used: the first is with a rail parallel to the wall, the second is with a rail rotated slightly to an angle of 11^0 with respect to the wall. In both cases, the ground-based antenna was not moved. The motivation behind the rotation was both to demonstrate the flexibility of the extraction methodology, and to better focus the antenna beam pattern on the centre of the wall.

Figure 4-21 – Photograph of the measurement setup. One antenna is placed on a polystyrene plinth facing towards the centre of the wall. The other antenna traverses a linear trajectory at a constant height.

4.7.1 Parallel Moving Antenna

In this scenario, the moving antenna is parallel to the wall. The moving antenna is at a vertical height above ground of 0.873m and the detached antenna has a height of 0.234m. This roughly corresponds to a reflection height of 0.55m, close to the centre height of the wall.

From the measurement data, the range profiles are generated via a zero padded Fourier Transform, showing that the back face of the wall is an approximate 10dB dimmer than the front face. In addition, the 3dB width of the front face signature is 5cm, while the 3dB width of the back-face signature is on order of 9cm. The degraded resolution for the front face reflection is due to a Hamming window being applied to the data. It was noted that the back face reflection was obscured by the sidelobe structure of the front face reflection, therefore a window weighting was applied in order to reduce the sidelobes of the front face signal, thus making the back face signal more distinct.

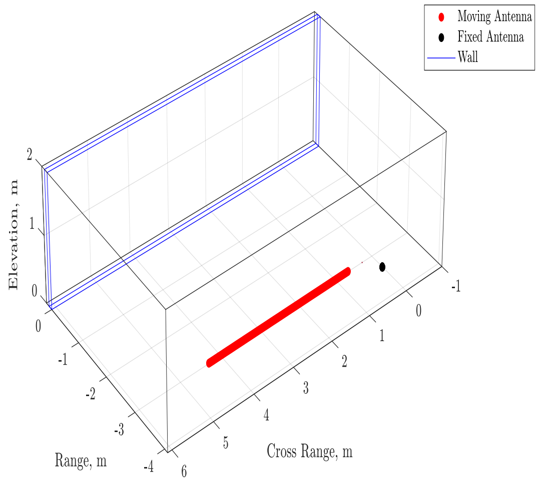

Figure 4-22 – Geometry for the first of the initial measurements. The moving antenna is parallel to the wall.

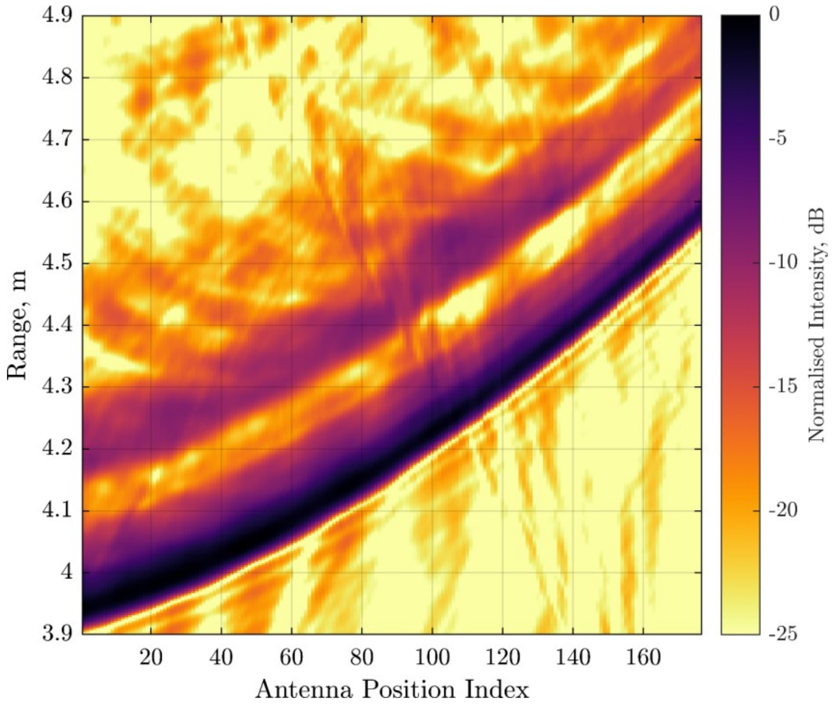

Figure 4-23 – TWR range profile for a 1GHz to 6GHz frequency range and a parallel antenna motion. The back face of the wall is approximately 10dB dimmer than the front face.

Applying the phase ramp ascribed in equation 4-16 provides the corrected range profile for input into the extraction method. The same trends between front and back faces are observed, I.e. the separation between faces follows the same trend.

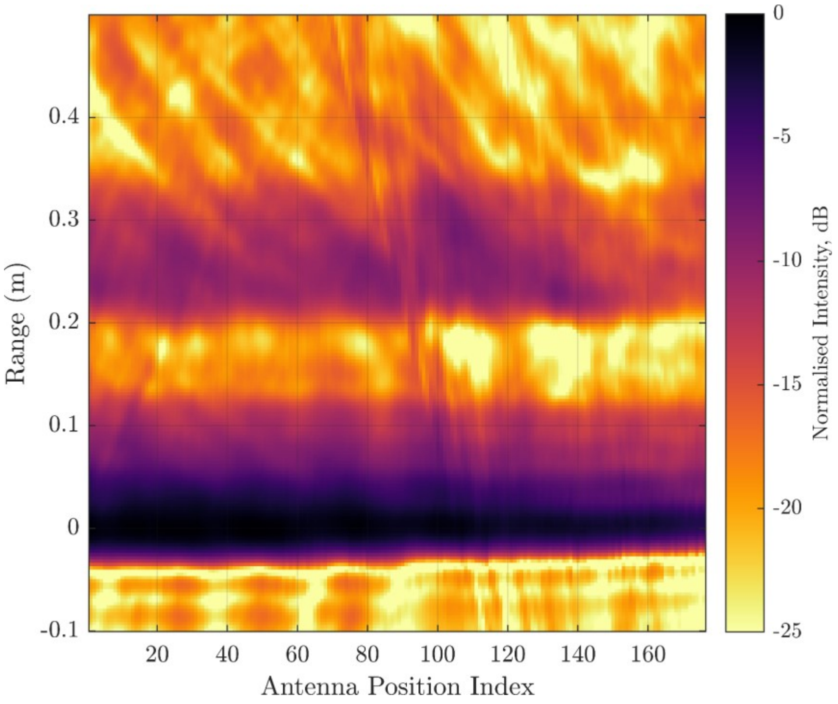

Figure 4-24 – Corrected range profile obtained via applying the phase ramp established in equation 4-16.

Substituting this corrected range profile into equation 4-21 gives a set of parameters for this wall. The extracted value for refractive index is 2.46 and the thickness is 91mm. Both these values are outside the errorbars ascribed to the parameters in Chapter 3.

The front and back faces are distinct in range at -25dB. Therefore, gating can be used to isolate the individual signatures, from which the frequency spectra for each face can be extracted. Gating the front face signature as between -0.1m and 0.15m, and the back face signature between 0.15m and 0.4m gives the frequency response illustrated in Figure 4-25. Since, the gain of the antennas is not known as a function of frequency, it is difficult to make a definitive statement about the absolute response. However, since the signatures were gathered in the same way, using the same antennas, a direct comparison is possible. The spectrum for the back face is consistently dimmer than the front face, with a practical upper limit of 4GHz. The resolution one would expect for a bandwidth of 3GHz is 10cm, lining up roughly with the observed resolution for the back face signature. In addition, the frequency response for both the front and back face signatures does not change significantly with antenna position.

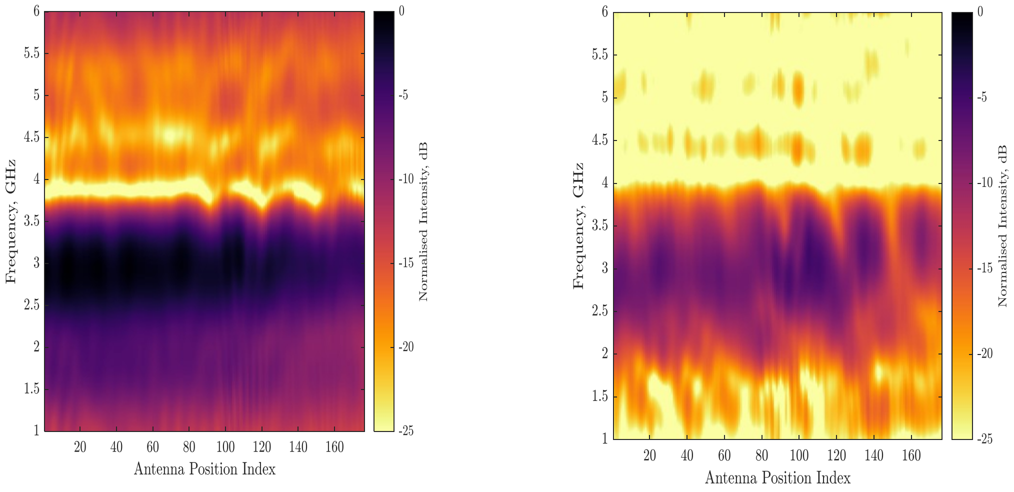

a)

b)

Figure 4-25 – Frequency responses for the a) front and b) back faces of the wall, obtained via a Fourier transform of the gated range profile data. The back face is consistently dimmer that the front, with an effective upper limit of 4GHz.

Comparing the frequency response for the 1st pulse shows the same phenomena as Figure 3-17, albeit reversed. The back face response is shifted to a higher frequency in a similar way to Figure 3-17. In addition, there are characteristic dips in frequency above 4GHz for both measurements, however, in the back face signature they are much more pronounced. This is due to the shallower angle of incidence and a shorter wavelength giving rise to a more specular reflection.

There are small fluctuations visible in Figure 4-25 as a function of antenna position. Since the point of reflection for both the front and back faces lies entirely within the 3dB beamwidth of the antennas, this is not due to the antenna beam pattern. Instead, the periodic fluctuations in intensity correspond, roughly, to the along track extent of the concrete block, 215mm. This means that the fluctuations are due to the structure of the wall, arising from small discontinuities between adjacent blocks.

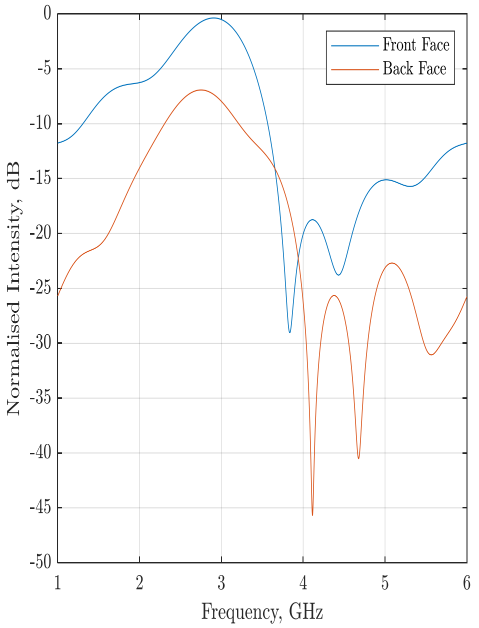

Figure 4-26 – Comparison between the frequency responses for the front and back face of the wall. There are characteristic troughs above 4GHz in both signatures. However, the back face produces much sharper dips. This is due to a more specular reflection from the back face.

4.7.2 Angled Moving Antenna

Similarly to the previous section, the heights of both antennas are 0.873m and 0.234m respectively. Again, the point of reflection is roughly the middle height of the wall. This time, however, the SAR rail has been rotated slightly towards the wall. The angle of this rotation has been measured to be 11.17^0 via measuring the distance from wall to rail at each extrema of the aperture and combining the difference with a known rail length. The assumed geometry is represented in Figure 4-27.

The range profiles were formed using the same method, producing the plot shown in Figure 4-28, showing the same properties as the parallel measurement. However, the range change is less than the parallel measurement. This is due to the moving antenna moving towards the wall.

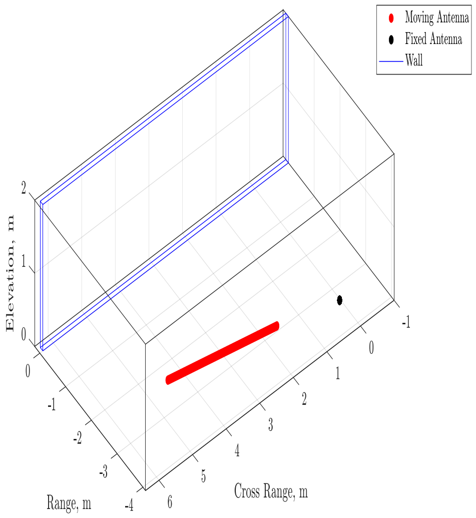

Figure 4-27 – Geometry for the second of the initial measurements. The moving antenna is at an angle of 11.17^0 with respect to the wall.

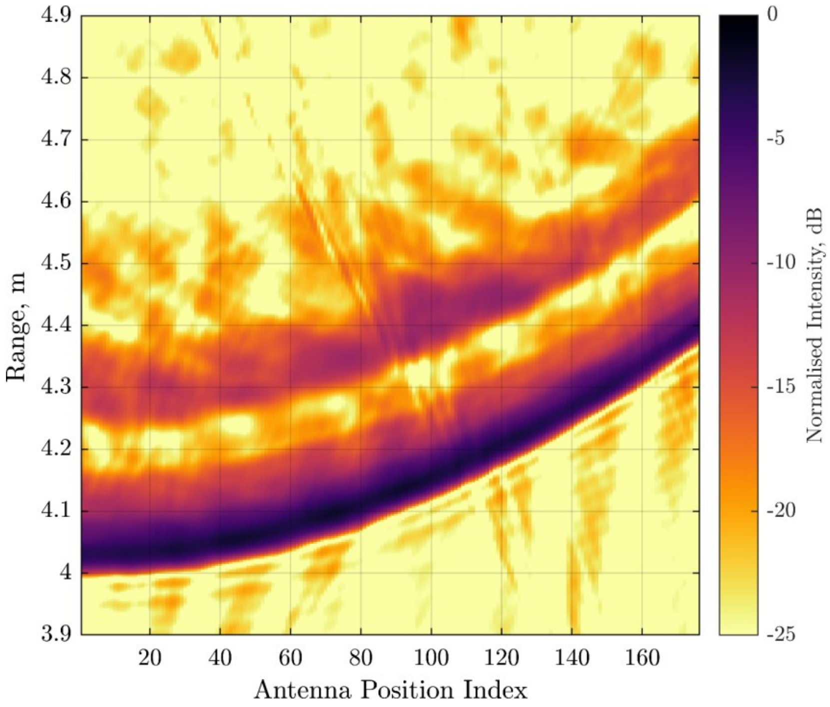

Figure 4-28 – TWR range profile for the angled measurements. Similar to the parallel measurements, the back face of the wall is approximately 10dB dimmer than the front face.

Again, applying the phase ramp produces a plot showing the range separation between front and back faces.

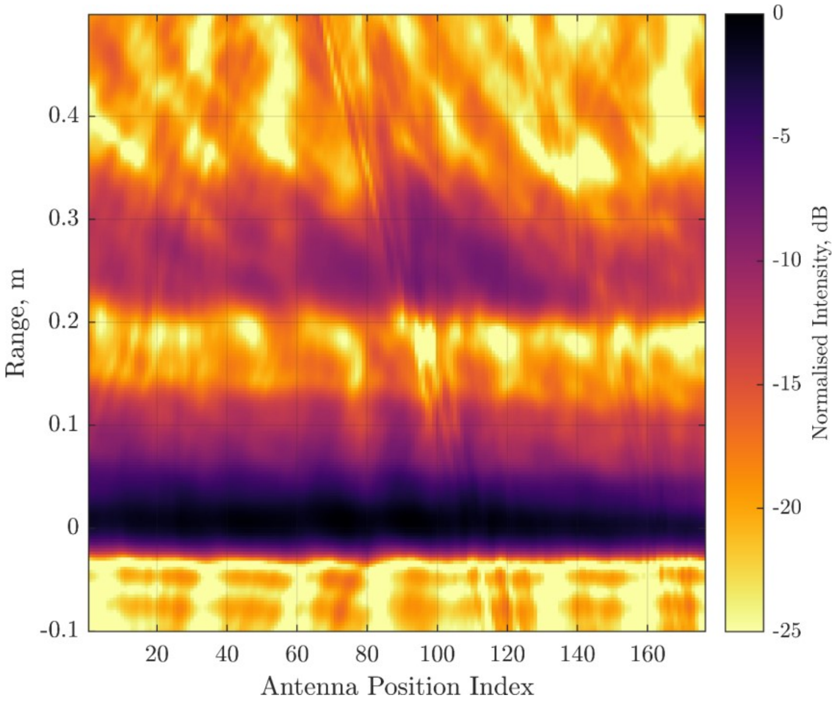

Figure 4-29 – Corrected range profile for the angled measurements. This looks extremely similar to Figure 4-24, implying that the material properties have not changed between measurements.

Given that the corrected range profiles are extremely similar between parallel and angled measurements the material properties should also be very similar. This is indeed true. For the angled measurement, $n = 2.33$, and $\delta = 96\text{mm}$.

The same frequency behaviour as the previous measurement is also observed. There is still a distinct drop in intensity at slightly less than 4GHz. There are still the same periodic fluctuations in intensity every 27cm. Therefore, the frequency response of the individual signatures is predominantly a consequence of the material structure, rather than the geometry of the collection

4.7.3 Cluttered Measurements

In addition to the angled measurements, some clutter was introduced behind the wall. This was to evaluate the clutter rejection properties of the proposed algorithm. This clutter takes the form of an archetypal office, complete with desk, chair, and computer. In addition to the afore mentioned office paraphernalia, two metal barrels and a metal case were introduced in order to provide a strong, consistent reflection that can easily be identified in subsequent imagery.

Figure 4-30 – Side on view of the additional clutter. This image shows a small metal sphere placed in front of the wall.

Figure 4-31 – Additional clutter consisting of a desk, chair, computer, metal briefcase, and two empty metal barrels placed immediately behind the wall.

The geometry for this cluttered measurement is the same as the angled measurement discussed previously, as is the frequency band used for the measurement. The angular diversity and spatial resolution are therefore comparable.

Plotting the range profile clearly shows that the clutter is clustered to one side. This corresponds with the extremes of the aperture, which makes sense given that the clutter is situated towards the centre of the wall.

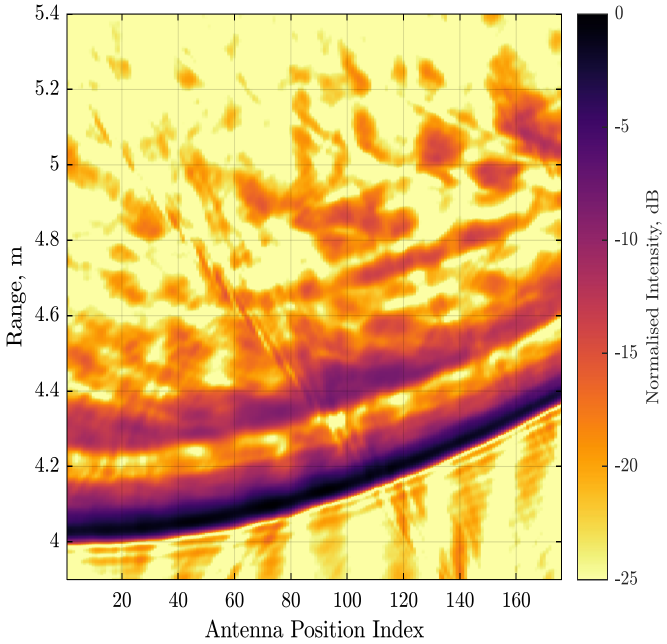

Figure 4-32 – Range profile for the cluttered measurement. The clutter is visible behind the back face of the wall on the right-hand side of the image. This area corresponds to the limits of the aperture.

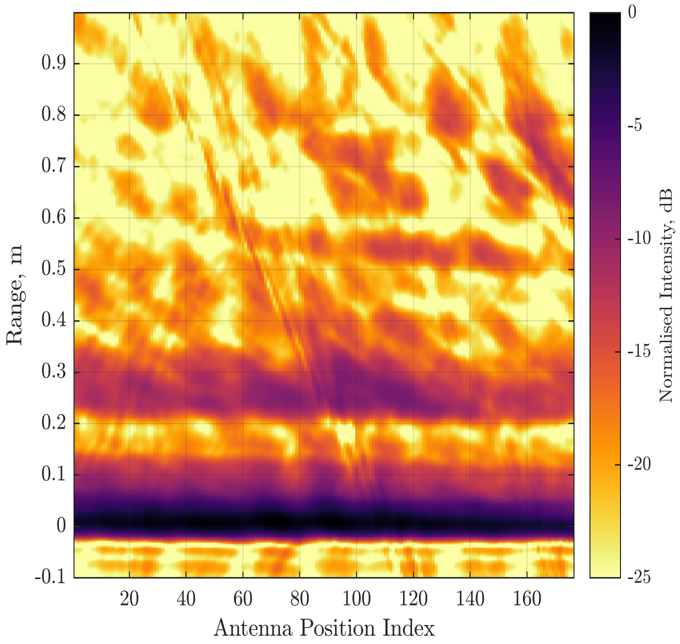

Figure 4-33 – Corrected range profile for the cluttered measurement.

For this measurement, the extracted values for n and δ are the same as the non-cluttered measurement, at least to a precision of three significant figures. This indicates that the addition of clutter did not have a significant effect on the extraction process, and that the algorithm can be safely deployed in scenes where there is a not inconsiderable amount of clutter. However, some questions do remain, namely why did the parallel measurement discussed in Chapter 4.7.1 not work?

The hypothesis as to why the parallel measurement produced a set of values outside of experimental error bars is that the original ground-truth antenna coordinates were incorrect. Therefore, a solution to refine the antenna positioning needs to be found. This would be beneficial in practical scenarios where the exact orientation and position of the wall are not known beforehand.

4.8 Ground-Truth Refinement

As mentioned in the previous section, the extraction method is sensitive to inaccuracies in the assumed positioning of the antennas with respect to the wall. Since the scale of these errors compound, it is necessary to devise a mechanism to refine the ground-truth antenna positions using the measured data.

Under the assumption that the front face of the wall acts as a constant specular reflector, one can use it as a well-known reference target via equation 4-2. With this in mind, the goal is to correctly identify each variable in the equation.

4.8.1 Assumptions

To build up the mathematical model on which to base the refinement method, the following assumptions are made about the antenna positions throughout the bistatic SAR collection:

- There are two antennas $\boldsymbol{T}$ and $\boldsymbol{R}$. At position vectors $\boldsymbol{T} = [T_x, T_y, T_z]$ and $\boldsymbol{R} = [R_x, R_y, R_z]$. Where $\boldsymbol{R}$ is constant.
- The coordinate system is derived from the starting position of the collection. I.e. the first position along the synthetic aperture corresponds to $\boldsymbol{T_1} = [0,0,T_z]$.
- The wall acts as a constant specular reflector of infinite extent in the xz plane.
- The spacing between the w sequential pulses is a known value, s.
- There is a constant down-range shift in the range profile data, CL. This is due to the additional path length needed for the electromagnetic waves to travel from the antennas to the VNA and through the internal electronics. Since neither the microwave cabling nor the VNA changes throughout the SAR measurement, CL is invariant with respect to the bistatic antenna positions.

Since the height of the both antennas are known, as is the travel between pulses, the parameters that need to be extracted are:

- the separation between the antennas for the first pulse of the collection, δX, and δY. Given the angle of the rail with respect to the wall, the bistatic baseline vector $\boldsymbol{V}$ is calculated for each antenna position in the SAR measurement.

  $$\boldsymbol{V}_k(\phi, s, k, \delta X, \delta Y, \delta Z) = (k-1)s[\sin(\phi), \cos(\phi), 0] + [\delta X, \delta Y, \delta Z]. \quad \textbf{4-48}$$

  δZ is the known height difference between the transmitter and receiver, $\delta Z = R_z - T_z$. $k = 1,2,3 \ldots w$.

- The distance, D, to the wall at the first pulse position.
- The angle of the rail with respect to the wall, ϕ.
- The delay due to the cables and VNA, CL.

There are 6 unknown variables. This can be reduced to 5 dimensions by assuming that the height of the receiving antenna is known. It can be further reduced to 4 dimensions by using the cross-talk signature in conjunction with the antenna coordinates to calculate the cable length. However, the cross-talk signature is not as well defined in the time domain as the wall signature, as such is not as useful in this context.

4.8.2 Optimisation Approach

The optimisation approach requires that the ranges corresponding to the front face reflection and the dihedral multipath reflection be compared to the measured data, M, in the time domain for each of the w number of bistatic antenna positions constituting the SAR measurement. Conceptually, this is similar to prominent point autofocus [5, pp.268–270], however, it is pitched as a means to obtain the initial starting point of the SAR collection, rather than a pulse-by-pulse position.

This is done for a minimum of 5 different pulse positions (one for each dimension). Therefore, the pulse positions relative to each other must be either recalculated or taken from earlier in the image formation process. Since the coordinate system is derived from the start of the collection, the antenna positions can be calculated from the angle of the rail with respect to the wall, ϕ, and the step size between sequential measurements.

For a given set of parameters, the range to the front face of the wall can be expressed as, $R_{Front}(\phi, \delta X, \delta Y, D, CL) = R_{Front}(\boldsymbol{X})$. CL represents a constant linear shift down-range and $\boldsymbol{X}$ represents the optimisation vector. The goal of the optimisation is to find $\boldsymbol{X}$ such that the total difference between the measured and predicted range is minimised. This is a standard least squares optimisation. The solution vector $\boldsymbol{S}$ is given by:

$$\boldsymbol{S} = \operatorname{argmin}\left[\sum (R_{Front}(\boldsymbol{X}) - M_{Front})^2\right] \quad \textbf{4-49}$$

This corresponds to the best agreement between theory and measured data. Where M_{Front} corresponds to the measured range to the front face of the wall.

This optimisation can be done in exactly the same way as that described in Section 4.3. However, since the front face of the wall is, in general, much brighter and more consistent across the SAR aperture, the range can be extracted by evaluating the maximum intensity of the range profile via $M_{Front}(k) = \text{argmax}\left[\hat{\mathcal{P}}(f, A_k)\right]$ for $k = 1,2,3 \dots w$.

Implementing this optimisation on the measurement data does refine the antenna coordinates, however, there is some variety in the extracted parameters. This is to be expected, since it is a discrete dataset, with a random initial starting vector. To avoid this sort of variation, a multistart functionality is taken whereby the minimisation is repeated 10000 times with new initial guesses of $\boldsymbol{X}$ within the constrained search space. The algorithm used to evaluate equation 4-49 is constrained minimisation using Sequential Quadratic Programming (SQP) [162, chap.4] as it has been observed to produce stable solutions for the ground-truth antenna positions. SQP is a standard optimisation algorithm implemented as part of the Matlab's Global Optimisation Toolbox. The limits on the constrained search space are derived from estimated measurement tolerances from the initial measurement of the antenna positions. The uncertainty associated with each parameter is as follows: the standoff distance D is ± 5cm, the initial antenna separation δX and δY is ± 1cm, the angle of the SAR rail is ± 0.2 radians, the cable length CL is ± 4cm. These uncertainties are combined with the measured parameters to provide upper and lower limits on each parameter.

4.9 Final Extraction of Parameters

Implementing this ground truth refinement on the parallel trajectory measurement shows slight disagreement between the assumed trajectory and the obtained trajectory. In particular, the standoff distance is approximately 4cm less than measured. There is little difference in angle, or the bistatic vector.

Finally, there is the question of how precise this is. By evaluating the standard deviation of the ground-truth refinement procedure over 200 iterations a standard deviation for each parameter is obtained. These standard deviations are then fed back into the sensitivity analysis performed in Chapter 4.6 to obtain a final uncertainty for the extracted parameters. The ground-truth refinement operation does not obtain the SNR, an estimate of the per-pulse SAR motion error, or the material surface roughness. It has been shown in Chapter 4.6 that errors due to noise and roughness are negligible when compared to systematic errors, so this is not an issue. The motion error associated with the SAR system has been estimated to cause

From Table 9 it is clear that the extracted values for refractive index and thickness agree completely with those obtained in Chapter 3. This is true regardless of clutter or the angle of the SAR collection with respect to the wall. Furthermore, the addition of clutter has not significantly affected the extraction accuracy, i.e. the extracted parameters are nearly identical to the non-cluttered measurement.

Table 8 shows an estimate of the uncertainty associated with each parameter, and the associated uncertainty in wall parameters. The measurement uncertainty associated with the refractive index is at least 0.23 and at most 0.41. Since the down range component of the antenna offset is equivalent to an erroneous D, it is difficult to obtain an exact value for the uncertainty associated with each parameter. The uncertainty associated with the refractive index is at least 0.23 and less than 0.41. A reasonable estimation of the uncertainty is the mean value, 0.32. The same is true for the wall thickness, it lies between 6.28mm and 14.36mm. Taking the mean as representative of the uncertainty associated with the extracted thickness, an uncertainty of 10.32mm is obtained. This equates to an approximate uncertainty of 14% and 10% for the extracted refractive index and thickness respectively. It is worth noting that this is a 1σ errorbar, therefore one would expect 68% of any repeated measurements to agree. 95% of repeat measurements would fall within a 28% and 20% range for each parameter.

From Table 9 it is clear that the extracted values for refractive index and thickness agree completely with those obtained in Chapter 3. This is true regardless of clutter or the angle of the SAR collection with respect to the wall. Furthermore, the addition of clutter has not significantly affected the extraction accuracy, i.e. the extracted parameters are nearly identical to the non-cluttered measurement.

Table 8 – Estimated uncertainty on the antenna positioning with respect to the wall and the associated uncertainty in wall parameters.

PARAMETER	GROUND-TRUTH σ	σ_n	σ_δ, mm
STANDOFF DISTANCE, D	0.002 m	0.23	6.16
ANTENNA OFFSET	0.0035 m	0.13	6.28
ANGLE	5.93×10^{-5} Rad	0.05	1.92

Table 9 – Final extracted parameters for all three measurements after the ground-truth refinement.

MEASUREMENT	n	δ, mm
PARALLEL	2.11	100
ANGLED	2.28	106
ANGLED WITH CLUTTER	2.29	105

4.10 Discussion

In this chapter a non-invasive remote sensing approach to extracting both the wall thickness and refractive index from a single asymmetric bistatic SAR measurement is developed. This has been demonstrated both experimentally and via simulations.

A key novelty with this methodology is the generalised nature of the bistatic SAR geometry. This allows for much greater versatility with regards to the collection geometry when compared to the prior art [99,100,128–131]. As will be shown in Chapter 6 this allows for both the formation of SAR imagery, and the extension into a generalised three-dimensional collection geometry.

Another point of novelty is the addition of clutter to the measurement area. Clutter is avoided in the literature, primarily because including clutter in a focusing based optimisation, as will be shown in Chapter 5, is problematic, and including it in the bistatic CMP approaches would make the typically implemented super-resolution algorithms that much more difficult. It has been shown in this chapter, that the addition of clutter behind the wall has no significant impact on the accuracy of the wall parameter extraction when using an asymmetric geometry.

With regards to technical limitations, the discussed approach is designed to only obtain the material thickness and refractive index, not the material conductivity. While methods to obtain the conductivity in conjunction with the other properties do exist [143], they require a more complex measurement geometry. A second limitation is that the back-face of the wall must be distinguishable from the front-face signature. i.e. the resolution must be fine enough to differentiate between the two signatures. For the concrete blocks used in this study, with a refractive index of approximately 2.3, and a thickness of approximately 100mm, the resolution must be finer than 230mm. Using $\frac{c}{2B}$ results in a bandwidth requirement of 0.65GHz. This is readily achievable, even in a through-wall scenario.

As part of the chapter, simulations are used to evaluate the sensitivity of the bistatic extraction method to inaccuracies in the assumed antenna positioning. The outcome of these simulations reveals that the extraction methodology is extremely sensitive to errors in the ground-truth positioning of the antennas with respect to the wall. This culminates in a large ($\Delta n = 14\%$, $\Delta \delta = 10\%$) uncertainty associated with the extracted values. Since the extracted refractive index and thickness, for all three measurements, are in agreement with the measured values obtained in Chapter 3 one must conclude that the asymmetric bistatic approach works. That said, the large uncertainty limits the applicability of the approach, especially when there is a large degree of motion error, and or positional uncertainty with regards to the radar platform. It is worth noting that these uncertainties are decoupled from the system resolution, so increasing the signal bandwidth or employing a super-resolution algorithm would not alleviate them. It should also be noted that this has been achieved without the need for either a background measurement or the need to calibrate the radar system.

To obtain the antenna positions with respect to the wall, or refine an initial measurement, a least-squares based optimisation routine has been developed. This new method leverages the change is range to the front face of the wall as a means to obtain both the bistatic antenna coordinates and the distance to the wall directly from the measured data. This approach does not estimate, on a pulse-by-pulse basis, the motion errors inherent to the SAR motion, rather it calculates the initial position of the SAR system. For this reason, it is not applicable to as a form of motion compensation. The method relies on a changing range to the front face of the wall at each antenna position. It is, therefore, not applicable to monostatic SAR.

5 Refraction Compensation for 2D and 3D Images

This chapter focuses on methods to use the extracted values for thickness and refractive index for improving both the spatial accuracy and point spread functions of any resultant through-wall SAR image. This chapter primarily gives examples in two-dimensional imagery; however, it is possible to apply to volumetric imagery without major modifications.

5.1.1 Through-Wall Image Formation

A large proportion of published TWR work is, by necessity, near-field. Therefore, to achieve high quality imagery, either Backprojection or the Matched Filter Algorithm can be used.

Derived from the Matched Filter Algorithm, the Backprojection Algorithm operates by calculating, via interpolation, the total received signal at any given Cartesian coordinate [152]. In principle, Backprojection can be applied to any coordinate frame, for example polar coordinates [163]; however, Cartesian is the most common.

For any given Cartesian coordinate, $\boldsymbol{P}$, the Euclidean bistatic range, R_{pix}, from the transmitting and receiving antennas, with vector coordinates $\boldsymbol{T}$ and $\boldsymbol{R}$ respectively, is calculated, (Figure 5-1). This range is then interpolated onto the complex range profile data, ρ, to ascribe a complex return signal with that coordinate. A sum of the contribution from each pulse produces the total complex return signal corresponding to that pixel.

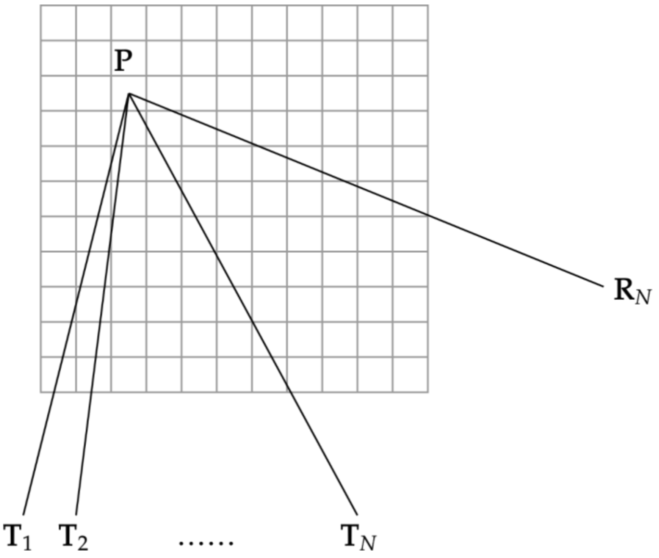

Figure 5-1 – Diagram of a generic bistatic SAR collection in relation to an imaging grid. The position vectors, *T*, *R*, and *P* are used to calculate the bistatic range to the pixel.

For free space ($n = 1$) the Backprojection Algorithm to produce an image, I, is:

$$R_{pix} = \frac{(|\boldsymbol{P} - \boldsymbol{T}| + |\boldsymbol{P} - \boldsymbol{R}|)}{2} \tag{5-1}$$

$$I(\boldsymbol{P}) = \sum_{N=1}^{p} \rho_N\left(R_{Pix_N}\right) \times e^{\frac{i4\pi\bar{f}}{c}R_{pix_N}} \tag{5-2}$$

The phase correction term exists as a focusing term utilising a matched filter for an isotropic point scatterer at range R_{pix} [152]. It is therefore mathematically equivalent to be rewritten as a matched filter modulation of the raw range profile data:

$$\rho'(m,f) = \rho(m,f) \times e^{\frac{i4\pi f}{c}R_{bin}(m)} \tag{5-3}$$

Since the R_{bin} is calculated using c, the matched filter also uses c. This modification accelerates the Backprojection Algorithm, since the exponential need only be calculated once.

$$I(\boldsymbol{P}) = \sum_{N=1}^{p} \rho'_N(R_{pix}) \tag{5-4}$$

Repeating this process for each coordinate in the image builds up an area where the range profile data constructively interferes. This area corresponds to a scatterers location in space, thus highlighting the scatters location in the image. The iterative nature of this process is illustrated below:

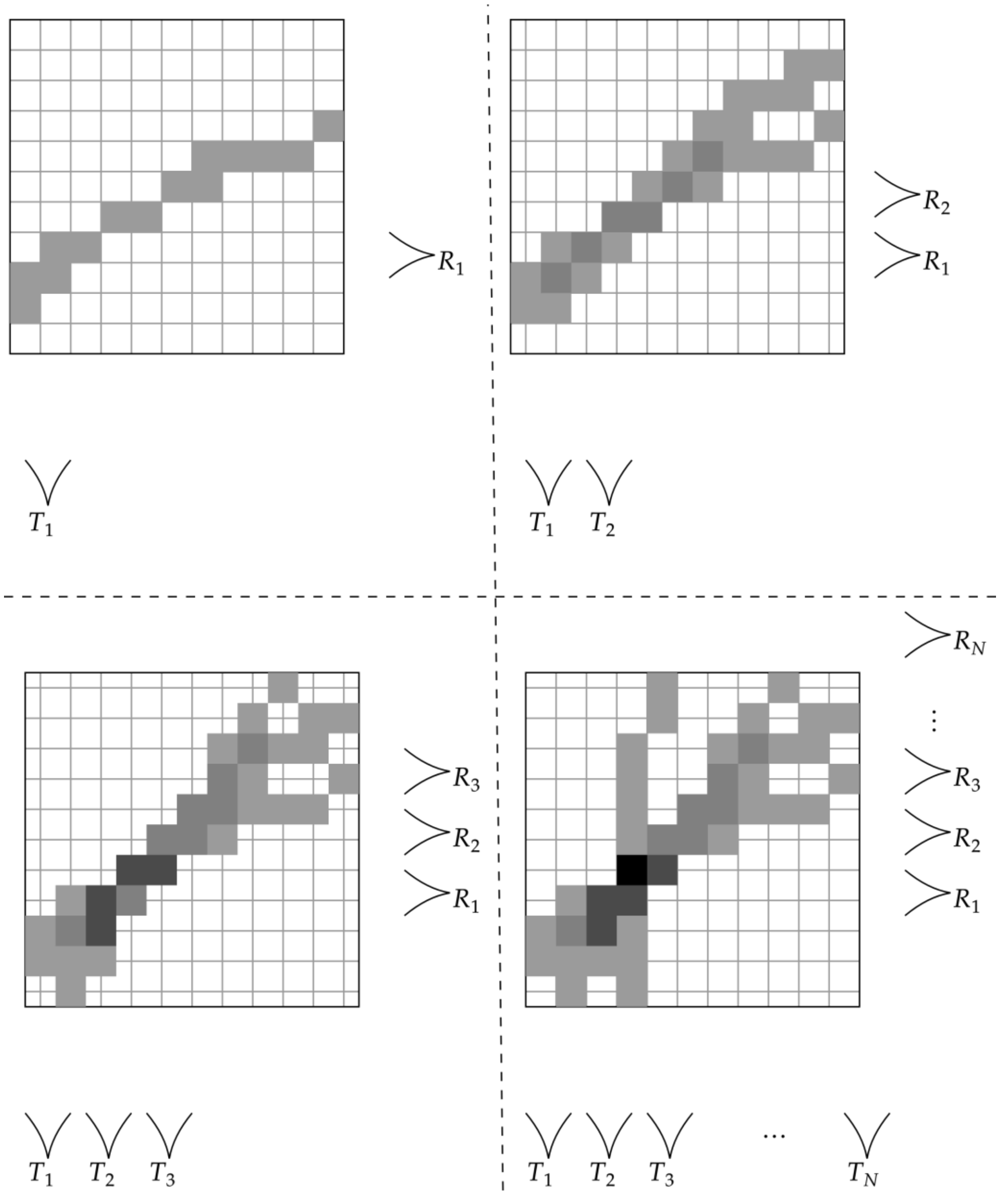

Figure 5-2 – Illustration of Backprojection. As more pulses are added to the image, the areas where the range profile data constructively interferes become more prominent, thus highlighting a scatterers location.

In a TWR scenario, the direct path denoted by equation 5-1 no longer denotes the actual path taken by the propagating EM wave due to the refraction through the wall and the decreased velocity of propagation. This culminates in an appreciable down range shift in the range profile data that is not accounted for in the standard Backprojection algorithm.

In effect, each scatterer behind the wall is shifted down range from its true location in the image. To compensate for this delay, either the range to the pixel, or the matched filter argument needs to be adjusted. The latter is achieved via calculating the Green's function for the structure. The former is achieved via direct calculation of the path length.

5.1.2 Mitigation Techniques

Mitigating the effect of wall refraction in TWR falls into two main categories: subtraction, and compensation. The goal of a subtraction technique is simple: to remove the bright wall signatures from the SAR imagery. By contrast, the goal of the compensation is to correct for the wall delay inherent to TWR.

With regards to subtraction, if one knows the exact electric field scattered off the wall, then, barring noise, it can be cleanly subtracted from the measured data. By far the easiest way to obtain a good metric for the scattered wall field, $\boldsymbol{E}_{wall}$, is to perform a background measurement, before any targets have been introduced. This is, for practical reasons, not ideal. In addition, as the wall shadows the area behind it, a direct background subtraction is therefore not perfect. As such, various algorithms have been introduced to either remove or explicitly calculate $\boldsymbol{E}_{wall}$.

Dehmollaian *et al* proposed a form of differential SAR [164] that aims to reconstruct the complex phase history of a SAR measurement, without the constant wall signature. In essence, they perform a detrending operation by calculating the difference in phase history between sequential pulses. If the wall signature extends across the entire aperture, then, in a monostatic collection, it can be approximated as a constant term, i.e. $\Delta\boldsymbol{E}_{wall} = 0$. Therefore, the difference between sequential pulses contains information about targets only.

While this approach is useful, it is by no means ideal. For example, the approach fails for non-constant wall signatures, e.g. bistatic measurements. The same limitations are present in the spatial filtering approach proposed by Yoon and Amin [165]. In general, there is little work concerning removal of wall signatures in bistatic and multistatic modalities, although it should be noted that in cross-polar measurements, the approximate flat plate response of the wall disappears [61].

In the far-field regime, the angle of incidence does not vary significantly from target to target, therefore wall compensation can be approximated by a single linear shift of $n\delta$, where n is the refractive index and δ is the thickness of the wall material. In the near-field regime, the angle of incidence can vary significantly between targets, therefore the correction term needs to vary as a function of angle. Near-field wall compensation can be achieved via an explicit calculation of the refracted path through the wall material [41,166] or, more commonly, via the calculation of the Green's function associated with the structure [8,167–172].

Correcting via calculation of the refracted path makes more intuitive sense and is mathematically simpler than calculating Green's function. However, it is a computationally intensive approach. On the other hand, calculating the transmission through the wall material is less computationally expensive, but more mathematically involved. Neglecting attenuation, both approaches will produce the same output image, and integrate nicely with the existing Backprojection Algorithm.

5.2 Implementation

Unlike [113,114,118–120], the method proposed in Chapter 4.3 does not inherently produce a compensated SAR image. Therefore, the image correction needs to be applied after the fact. In the Backprojection Algorithm, this is done by calculating the refracted range to each pixel in the image.

Given known properties for the wall, a compensation can be applied during the image formation process. Figure 5-3 shows the 3 different paths available in a two-dimensional Through-Wall SAR image. The image is split into 3 distinct layers. Layer 0 hosts both antennas, Layer 1 is the wall material, and Layer 2 is the material on the far side of the wall.

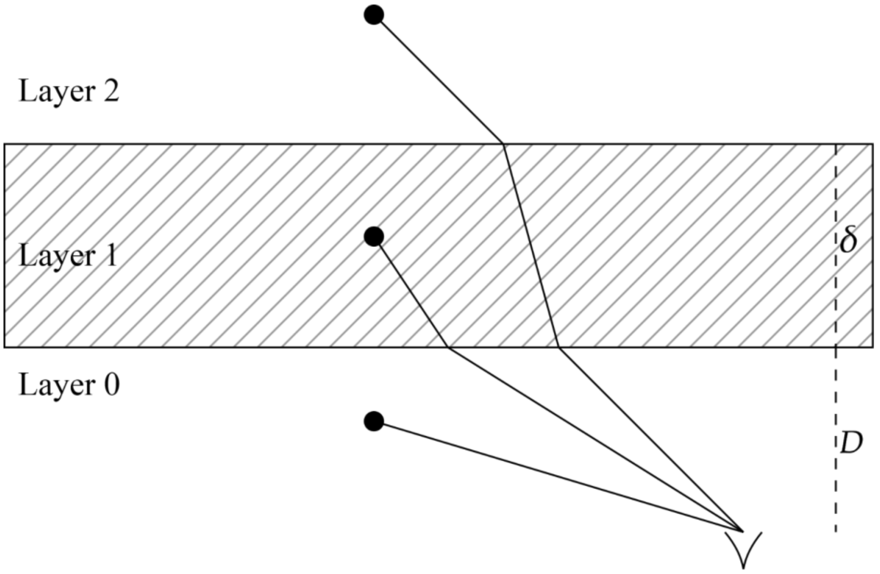

Figure 5-3 – Diagram showing the different refraction paths that would occur in a two dimensional Through-Wall SAR image. Layer 0 contains no refraction; Layer 1 contains a two-layer refraction problem whereas Layer 2 contains a 3-layer refraction problem.

For a pixel with position vector $\boldsymbol{P} = [P_x, P_y, P_z]$, the path length is calculated in much the same way as R_{back}. However, since the reflection need not be specular, the outgoing and incoming components of the range, R_{Pixel}, can be calculated separately.

For an antenna located at position vector $\boldsymbol{A} = [A_x, A_y, A_z]$, finding R_{Pixel} requires that the angle of incidence be calculated for both the horizontal and vertical planes. For any pixel in Layer 0 ($P_y < D$), this is trivial. However, for a pixel in Layers 1 or 2, the same iteration method as equation 4-14 is employed. The goal is to calculate the angle of incidence, from which the refracted range is easy to calculate.

5.2.1.1 Pixel Inside Wall

For a pixel in Layer 1 ($D < P_y < D + \delta$), the ray from the antenna to the pixel is refracted once. The separation in the x and z dimensions can therefore be described as:

$$\Delta X = P_x - A_x = D\tan(\theta_i) + (\Delta Y - D)\tan(\theta_r) \qquad \textbf{5-5}$$

$$\Delta Z = P_z - A_z = D\tan(\vartheta_i) + (\Delta Y - D)\tan(\vartheta_r) \qquad \textbf{5-6}$$

Where $\Delta Y = P_y - A_y$. This gives rise to the equations describing the angle of incidence in both the horizontal and vertical planes.

$$\theta_{i_q} = \tan^{-1}\left(\frac{\Delta X - (\Delta Y - D)\tan\left(\theta_{r_{q-1}}\right)}{\mathrm{D}}\right) \quad \textbf{5-7}$$

$$\vartheta_{i_q} = \tan^{-1}\left(\frac{\Delta Z - (\Delta Y - D)\tan\left(\vartheta_{r_{q-1}}\right)}{\mathrm{D}}\right) \quad \textbf{5-8}$$

Where the angle of refraction is related to the angle of incidence via Snell's Law. This iteration works in the same way as equation 4-14. However, to accelerate the process, the starting angle is set as the solution for the previous pixel. This is because there is little angular variation between adjacent pixels, thus the solution for the previous pixel is a good approximation for the solution to the current pixel.

5.2.1.2 Pixel Behind Single Layer

For a pixel in layer 2 ($P_y > D + \delta$), the ray is refracted twice: once going into the wall material and once going out of the material. This leads to a 3-layer problem, constrained by:

$$\Delta X = P_x - A_x = (\Delta Y - \delta)\tan(\theta_i) + \delta\tan(\theta_r) \quad \textbf{5-9}$$

$$\Delta Z = P_z - A_z = (\Delta Y - \delta)\tan(\vartheta_i) + \delta\tan(\vartheta_r) \quad \textbf{5-10}$$

Note that the term D has disappeared, or rather it is contained within the term $\Delta Y - \delta$. Rearranging these two equations gives an angle of incidence that follows a similar trend to the interior solutions.

$$\theta_{i_q} = \tan^{-1}\left(\frac{\Delta X - \delta\tan\left(\theta_{r_{q-1}}\right)}{\Delta\mathrm{Y} - \delta}\right) \quad \textbf{5-11}$$

$$\vartheta_{i_q} = \tan^{-1}\left(\frac{\Delta Z - \delta\tan\left(\vartheta_{r_{q-1}}\right)}{\Delta\mathrm{Y} - \delta}\right) \quad \textbf{5-12}$$

From these systems of equations, one can correct for refraction for any pixel in a three-dimensional volumetric image for any of the laboratory measurements presented in this body of work.

5.2.1.3 Pixel Behind Arbitrary Number of Layers

Given the equations 5-11 and 5-12 include terms for the interior components of the wall independent of the exterior medium, the equations can be generalised for $l > 1$ layers. This results in:

$$\theta_{i_q} = \tan^{-1}\left(\frac{\Delta X - \sum_{l=1}^{L}\delta_l \tan\left(\theta_{l_{q-1}}\right)}{\Delta Y - \sum_{l=1}^{L}\delta_l}\right) \qquad \textbf{5-13}$$

$$\vartheta_{i_q} = \tan^{-1}\left(\frac{\Delta Z - \sum_{l=1}^{L}\delta_l \tan\left(\theta_{l_{q-1}}\right)}{\Delta Y - \sum_{l=1}^{L}\delta_l}\right) \qquad \textbf{5-14}$$

Where θ_l is the angle of refraction for that specific layer, given by iterating through Snell's Law for each layer:

$$\theta_{l+1} = \sin^{-1}\left(\frac{n_l}{n_{l+1}}\sin(\theta_l)\right) \qquad \textbf{5-15}$$

While not shown experimentally within this body of work, this is nonetheless an important generalisation. One could generalise this further by setting $\delta_{l=0} = 0$. This would allow the same pair of equations to be valid for all layers. However, doing so is both contrived and unintuitive and as such the equations have been left as is.

Including these corrections in the SAR imaging process modulates the range to each pixel in the image in accordance with the refracted path length. Additionally, since each component of the path is obtained, the decreased velocity of the propagation inside the wall is easy to account for. The impact of this correction is a distortion in R_{Pix} as a function of position. This shifts each scatterer behind the wall closer towards the mean antenna position. This correction is illustrated in Figure 5-4 where a direct comparison is made between corrected and non-corrected images. In addition to the target shift, there is a minor improvement in focusing quality. The point spread function of the back face of the wall is compressed. This is because the wavelength inside the wall is shorter than outside; this corresponds to a finer resolution arising from the correction.

Figure 5-4 shows a direct comparison between corrected and non-corrected images generated using the bistatic simulation geometry shown in Figure 4-10. For this example a single point target has been introduced in the midpoint of the bistatic aperture a distance of 5.7m away from the antennas. A wall of thickness 0.1m and a refractive index of 2.5 has been introduced between the antennas and target, a distance of 5m away.

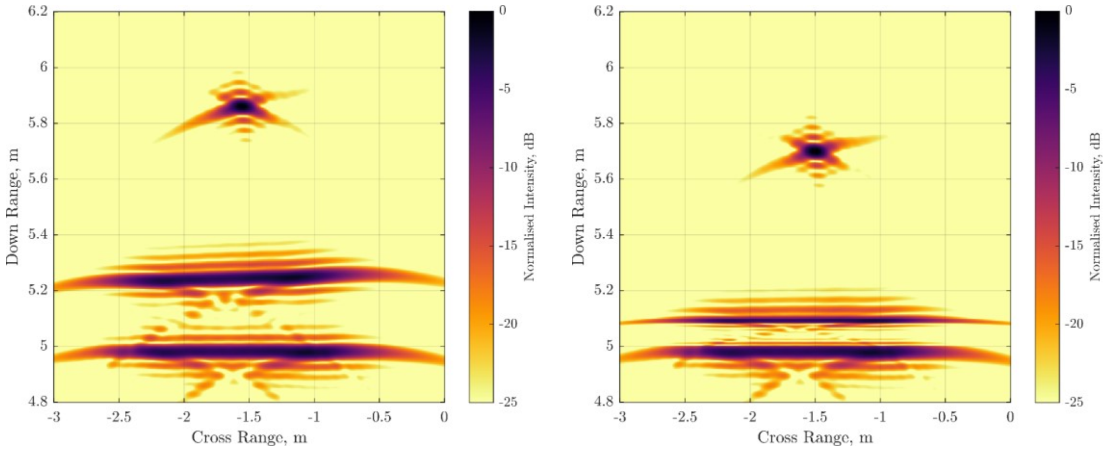

a) b)

Figure 5-4 – Comparison between a) non-corrected, and b) corrected SAR images of a single point target behind a wall generated from the simulation geometry shown in Figure 4-10.

In the non-corrected case, the target appears further back than it should. It is also slightly defocused; this is due to the effective electrical length of the wall changing as the angle of the antenna with respect to the target changes. Increasing the assumed refractive index of the wall causes the target to pendulate around its true position. This is illustrated in Figure 5-5, wherein both too small and too large refractive indices cause the target to appear in the wrong location, and defocused. While the target is near-field, it is sufficiently far away that the target effectively maintains a fixed cross range position. While the defocusing is obvious for large errors, for smaller errors there is little visual difference in the image quality.

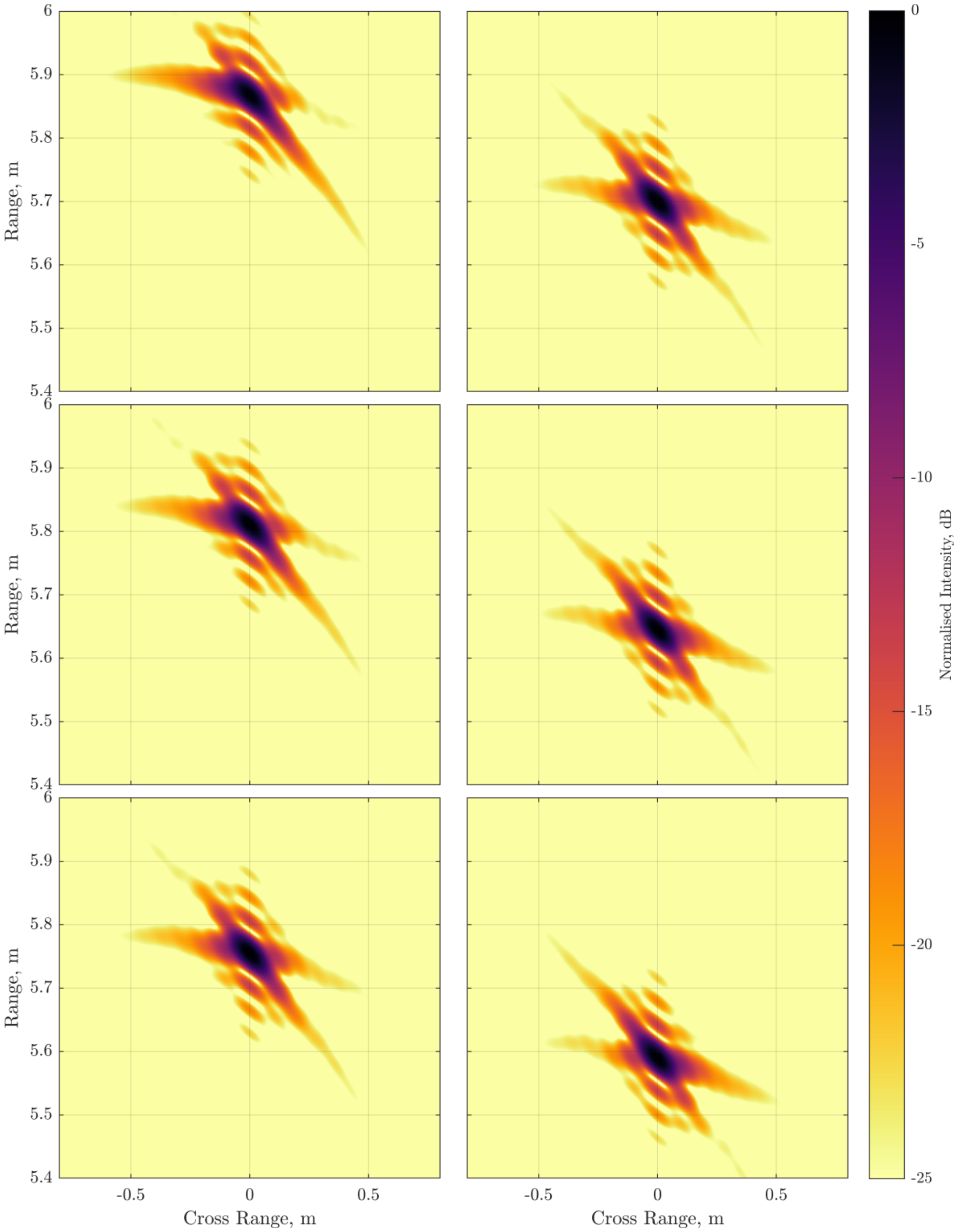

Figure 5-5 – Simulated bistatic SAR of a single target behind a wall of $n = 2.5$ and $\delta = 0.1$. Images formed using different assumptions about the wall refractive index. From top to bottom, the first column has $n = 1$, $n = 1.5$, and $n = 2$. The second column has $n = 2.5$, $n = 3$, and $n = 3.5$. Incorrect assumptions about n cause some degree of defocusing and a positional error.

5.3 Focusing Quality

Since there is little visual difference between images formed with small errors in assumed wall properties, a mathematical approach to evaluating image quality must be taken. To evaluate the focusing ability of this correction methodology, the same bistatic scenario is used. However, an error in wall parameters is deliberately introduced during the correction process. This is repeated several times, each time evaluating the image quality in the area immediately around the target. It is important to exclude the wall signature, as this will introduce a bias towards higher refractive indices due to the finer down range resolution.

Quality metrics for image processing is a broad field, with applications in many areas of science, but predominantly used in photography and computer graphics. Broadly speaking, image quality metrics fall into two main categories: metrics that require a comparison to an idealised image, and metrics working off of features in a single image [173]. Working from a reference image, so called full reference metrics, would require the presupposition that a correctly compensated image produces the highest quality. Full reference metrics are therefore not appropriate for this test.

In this section two feature-based metrics are used to evaluate the focusing quality of the image. The first is a simple evaluation of the maximum intensity of the image. The second method follows previous publications that use a standardised moment of the image [117,120].

5.3.1 Peak Intensity

Firstly, to assess the quality of the image, the peak brightness of the image as a function of wall parameters is used. For the specific case of a single isolated target in the image and a constant correct thickness, the brightest peak intensity corresponds to the correct value of refractive index. As will be shown, this is not true in a generalised sense. Figure 5-6 shows the distribution of peak intensities for 31 images with assumed refractive indices ranging from 1 to 3.5.

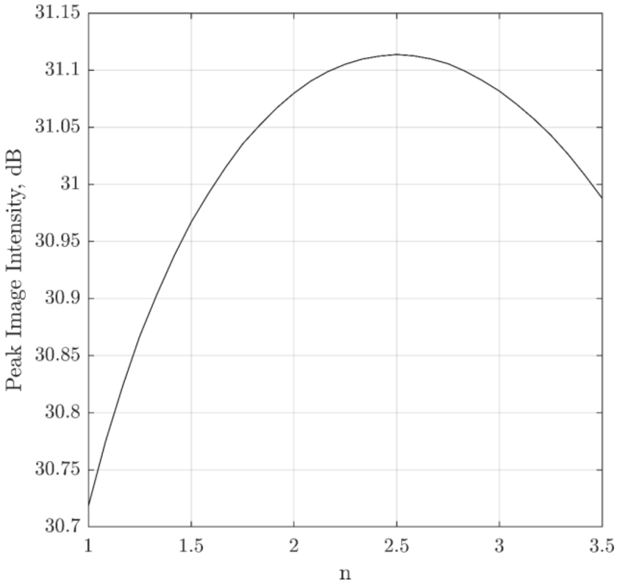

Figure 5-6 – Plot of the maximum intensity for images formed under different assumptions about n. For this plot, the assumed thickness matches the thickness used to simulate the data. Therefore, the maximum of this plot ($n = 2.5$) corresponds to the correct simulated wall properties.

From Figure 5-6, a correct assumption about the material properties leads to a higher peak intensity. However, since the difference between correct and incorrect images is in order of 0.4dB, using this as the basis for an optimisation routine would be challenging in either the presence of noise, or a more complex target. The same phenomenon is observed with regards to the material thickness, via Figure 5-7, wherein the highest peak intensity corresponds to a correct assumption about the material thickness (0.1m).

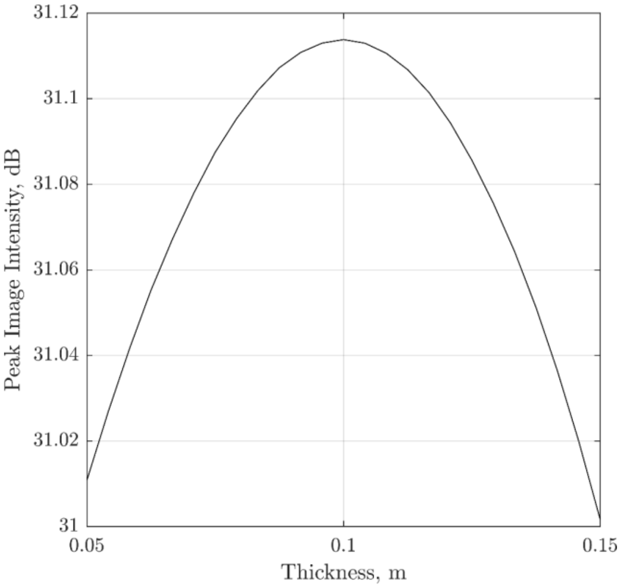

Figure 5-7 – Peak intensity of images formed under different assumptions about the wall thickness. The true value used in the raw data generation is 0.1m. The assumed refractive index (2.5) is correct.

Plotting a range of possible assumptions reveals that the maximum peak intensity, while a possible evaluation of the image quality, is not ideal. This is because, in this scenario where the target does not deviate significantly in cross range, there are multiple combinations of parameters that give the same electrical length. To differentiate between the possible solutions, either a new geometry must be chosen, or an extremely high pixel density must be used in the image formation, at which point the subtle cross range deviation can be observed. Figure 5-8 shows this phenomenon.

The maximum of the image, and hence the global maximum for all values of refractive index and thickness, does line up with the actual values used in the data generation ($n = 2.5$, $\delta = 0.1\text{m}$). However, the similarities between intensities render using the peak intensity of the image as a means to obtain the material properties quite suspect.

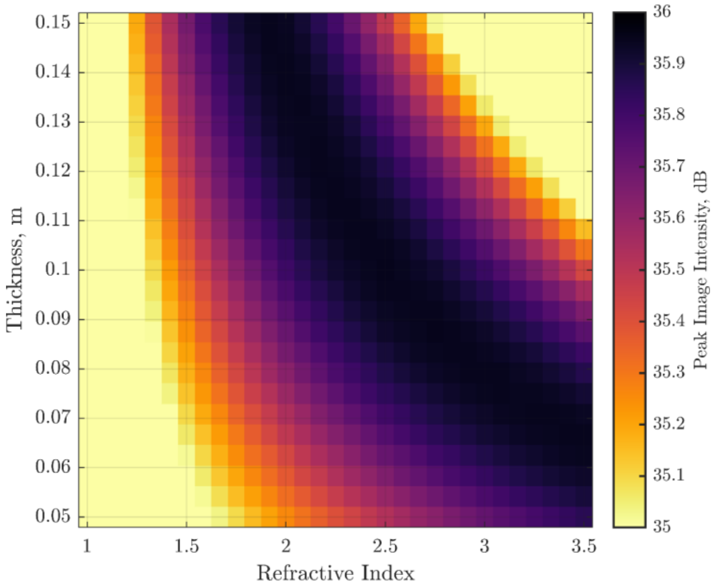

Figure 5-8 – maximum intensities of images formed under different assumptions about the material properties. The peak intensities follow a curving ridge along a trajectory where $n\delta$ is approximately constant.

5.3.2 Kurtosis

Previous publications have opted to use kurtosis as a metric to assess image focusing [117,120]. Kurtosis is the 4th power of the standardised moment of the image, I.

$$\mathrm{Kurt}(I) = \mathrm{E}\left(\left(\frac{I-\bar{I}}{\sigma}\right)^4\right) \tag{5-16}$$

where σ represents the standard deviation of an image consisting of L pixels and $\mathrm{E}(\cdot)$ is the expectation value. For a scenario where each pixel intensity is equally likely, the expected value is the mean value, therefore the kurtosis metric reduces to:

$$\mathrm{Kurt}(I) = \frac{\sum_{l=1}^{L}(I_l-\bar{I})^4}{L\sigma^4} \tag{5-17}$$

Intensity values less than one standard deviation from the mean do not contribute significantly to the kurtosis. Therefore, the only values that contribute significantly are those outside the main peak. In this way, kurtosis represents how outlier prone a distribution is; therefore, a smaller kurtosis corresponds to a better focused image.

Evaluating the kurtosis of the entire image shows that unlike [117,120] the kurtosis of the image does not reach a minima at the correct values of n and δ. This is because of the lower intensity components of the point spread function of the target. As the target moves towards the edge of the image, more and more of the side lobe structure is outside of the image extent, and thus does not contribute to the metric. This introduces a bias towards higher wall parameters. To avoid this, either the image extent must be made larger, or an intensity threshold must be applied.

From Figure 5-5, the majority of the visible defocusing is present within a -10dB intensity range. Applying a -10dB intensity threshold produces an image only containing the most significant components of the point spread function.

In the same fashion as Figure 5-6 and Figure 5-7, the negative kurtosis of the thresholded images is plotted along lines of constant refractive index (Figure 5-9) and thickness (Figure 5-10). From these figures, the negative of the kurtosis does reach a maximum at the correct assumptions concerning the wall properties. This means that including the correct properties in the image formation does indeed produce a more focused image. However, as with the peak image intensity metric, the difference between a correct and incorrect assumption is very slight. Additionally, in [117] there are periodic fluctuations in the kurtosis that are not observed here.

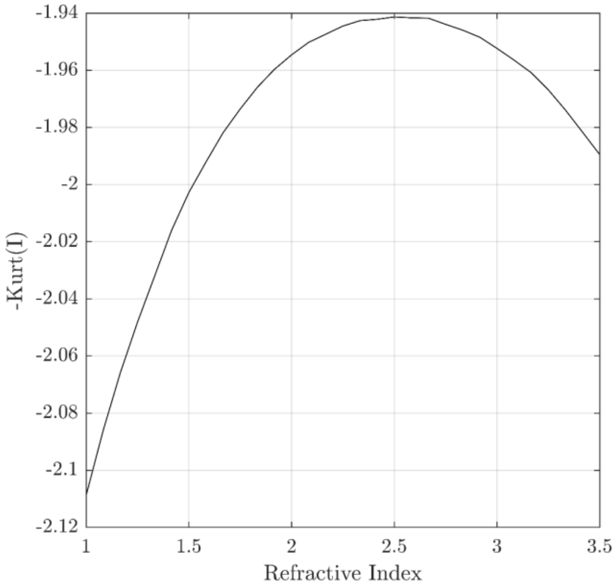

Figure 5-9 – Negative kurtosis of thresholded images as a function of refractive index. The maximum of this distribution, and hence the most focused image corresponds to the correct assumption of n.

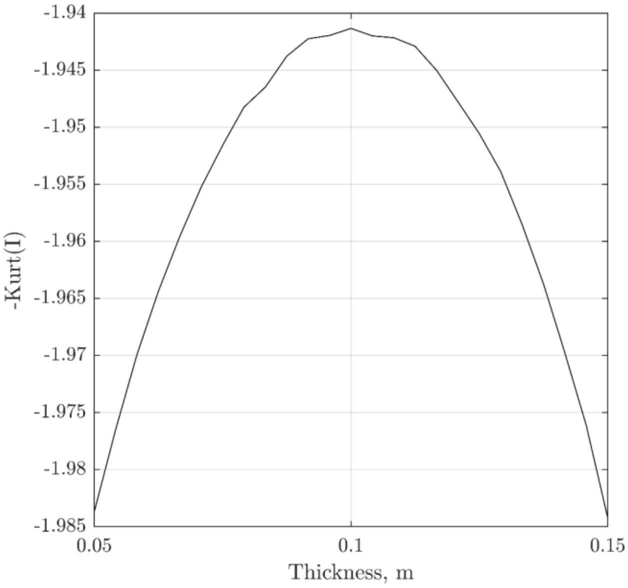

Figure 5-10 – Negative kurtosis as a function of assumed wall thickness. The maximum of this distribution corresponds to the correct assumption concerning the wall thickness.

Plotting the negative kurtosis when neither parameter is known produces a plot that is very similar to Figure 5-8:

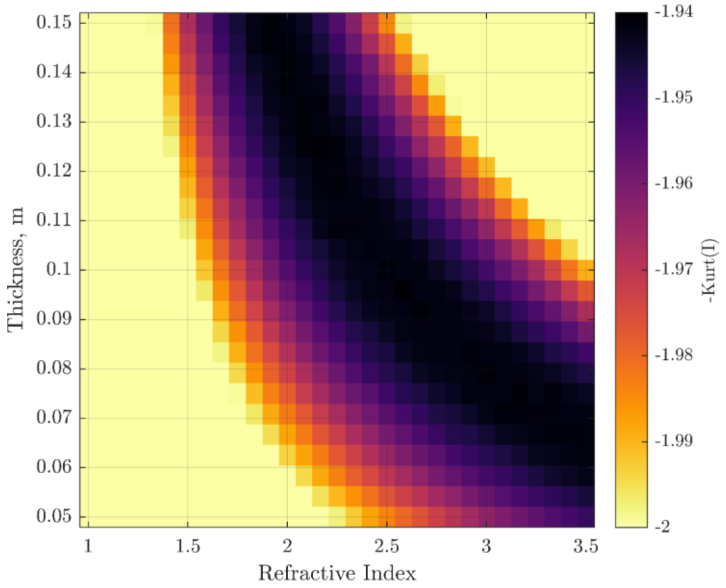

Figure 5-11 – Negative kurtosis of images formed under different assumptions about both n and δ. The shape of the curving ridge is due to the electrical length of the wall being constant along the ridge, giving rise to a similar focusing quality.

The maximum of the negative kurtosis is not exactly in agreement with the true wall values. It corresponds to 2.58 and 0.096m for n and δ respectively. This is attributed to an insufficient pixel density in the image formation, and a coarse sampling of wall properties in the test.

In summary, while statistical metrics for focusing quality do show that the most highly focused images are those formed under correct assumptions about the wall material, the difference between correct and incorrect assumptions is very slight (~2%).

5.4 Experimental Demonstration

In addition to the simulated images shown in Figure 5-4, a similar comparison is made using gathered laboratory data. Specifically, the cluttered measurements discussed in Chapter 4.7.3. A background subtraction has been performed in order to remove the wall signature as best as possible. It is not a perfect subtraction, as there is some small area of the front face still visible. This small perturbation is due to a change in the wall position, most likely a result of being knocked during the construction of the scene.

In the corrected image, the scatterers appear parallel to the wall and significantly closer. However, there is no obvious improvement in the focusing of the individual targets. This is due to the point spread function of the multiple scatterers interacting, and due to the distance of the antenna from the wall, implying that there is not sufficient variation in the angle of incidence from the direct path.

Finally, in image b), there is a very pronounced sidelobe distortion as it passes though the wall. This distortion is a direct consequence of applying this form of correction, as the speed of light is no longer assumed to be constant throughout the image.

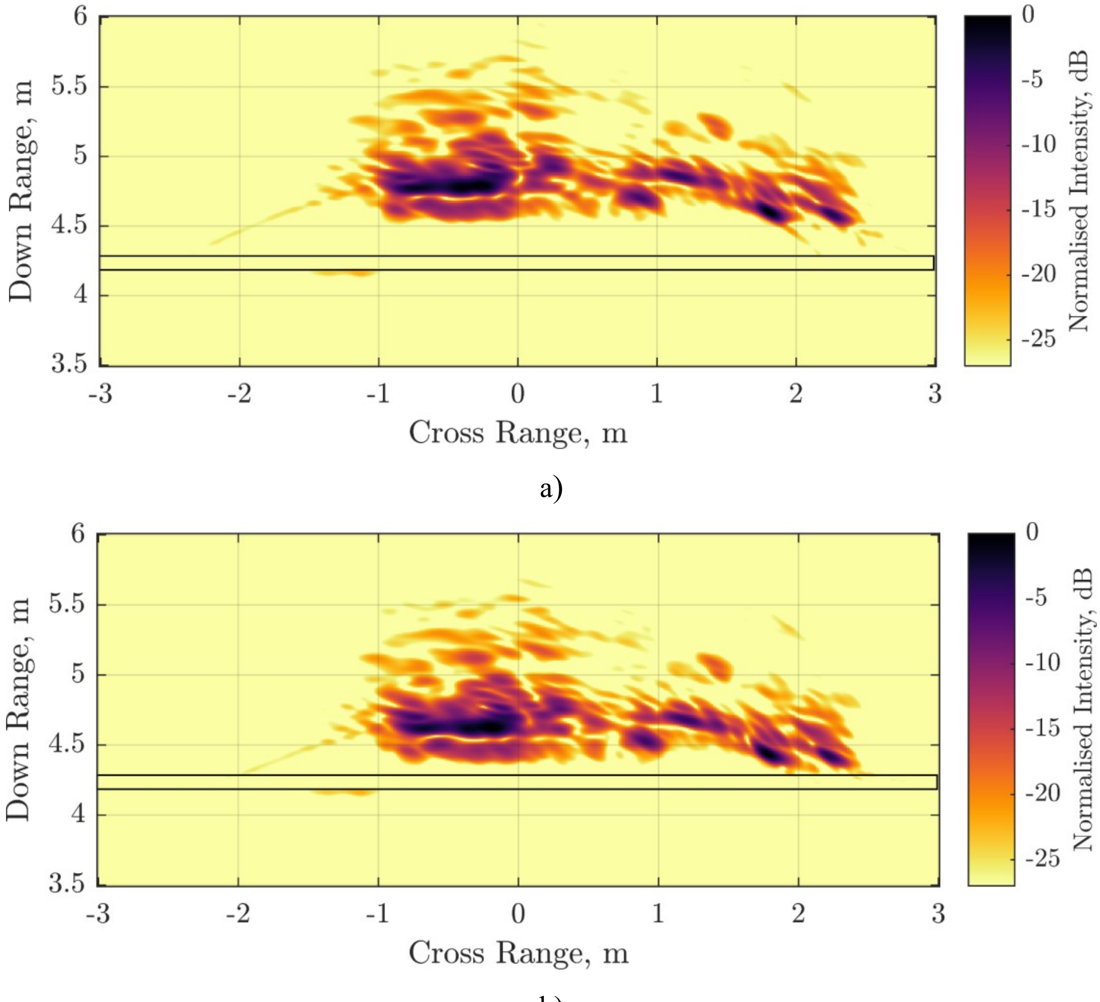

Figure 5-12 – Comparison between a) non-compensated and b) compensated imagery. The compensated imagery is seen to shift towards the wall. While subtle, there is also a small rotation of the image.

Plotting histograms of the pixel values for each image shows that there is no practical difference between the focusing quality of the two images. There is less than a 1% difference between the mean of both images. The same is true of the standard deviation.

This small change is due to the small angular difference between the refracted path and the equivalent free space path. In addition, the point spread function of each scatterer overlaps. As the correction is applied, the PSF of each scatterer gets sharper, but the scatterers move closer together and thus the ensemble becomes less distinct.

To produce a more obvious effect, without altering the wall properties, the radar system would have to be moved closer to the wall. This would generate a greater angular variation, and a greater degree of defocusing as well as obtaining finer cross range resolution, thus reducing the interference between scatterers.

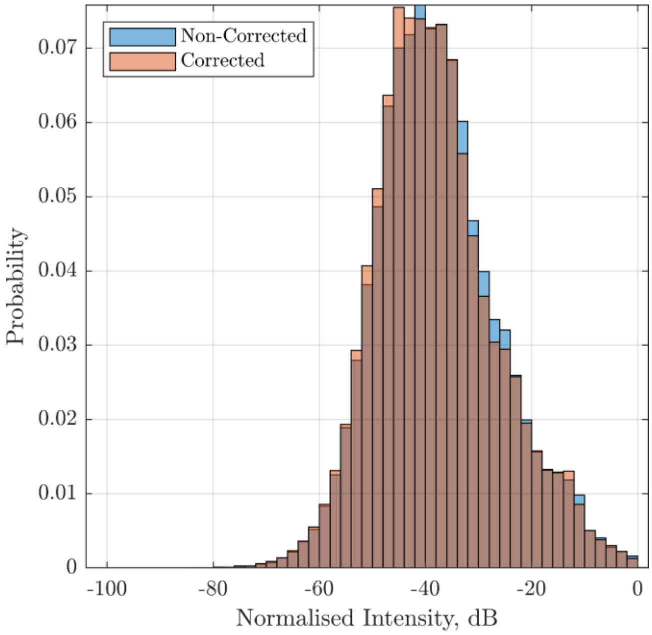

Figure 5-13 – Histograms of the pixel values for both the corrected and non-corrected images. The mean and standard deviation for both images is incredibly similar, meaning that the correction operation has had little effect on the focusing quality of the image.

Due to the extreme similarity between corrected and non-corrected imagery, the refocussing approaches commonly taken in the literature are unlikely to work for a heavily cluttered scene such as this.

This conclusion is reinforced when one examines the image intensity and kurtosis. In the same manner as Figure 5-8 and Figure 5-11, the negative kurtosis and peak image intensity was evaluated over a range of different thicknesses and refractive indices. Figure 5-14 shows the negative kurtosis for this scene, whereas Figure 5-15 shows the peak image intensity.

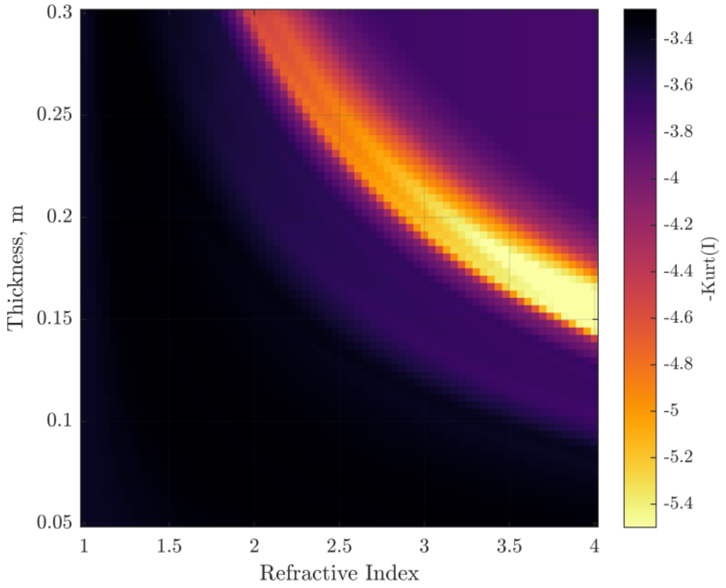

Figure 5-14 – Negative kurtosis for the SAR image shown in Figure 5-12 when corrected using different assumptions about the material properties.

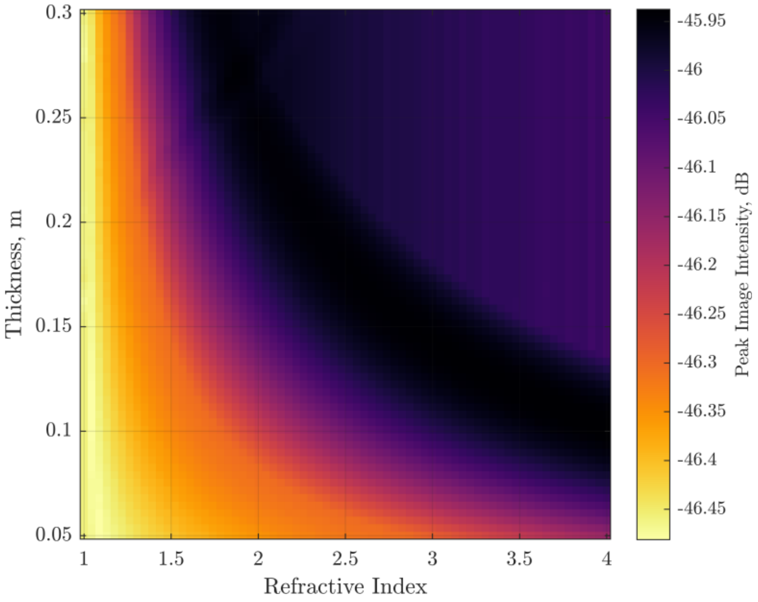

Figure 5-15 – Peak image intensity for the SAR image shown in Figure 5-12 when corrected using different assumptions about the material properties.

The image intensity shows that there is a global maximum corresponding to wall parameters of $n = 3.96$ and $\delta = 0.10$m. Meanwhile, the global maximum of the negative image kurtosis corresponds to $n = 1.26$ and $\delta = 0.29$m. These numbers are not in agreement with the extracted values from Chapters 3 and 4. The reasoning behind this is due to the byplay between the individual scatterers in the image. As the scale of the refraction correction becomes greater, the individual scatterers become closer together. This leads to greater constructive interference between the point spread functions of each scatterer, thus driving up the image maximum and introducing a bias in the focusing metrics towards higher refractive indices and thicknesses. This phenomenon was not observed in the simulated images because there was only one scatterer.

Since the scatterers are close to the wall, an assumed thickness and or refractive index that is larger than the actual value would be sufficient to shift some of the scatters inside the wall layer. As seen from Figure 5-4, this leads directly to finer down range resolution. This introduces a bias towards larger parameters. The dim band in Figure 5-14 is a sweet spot where the image has been shifted too far, yet the parameters are not large enough to include the scatterers as part of the wall structure.

From Figure 5-12, and the corresponding evaluation of the image quality, one must conclude that unlike the simulated point target, the best focusing quality does not correspond to the correct values of n and δ. That said, the image is better focused than its non-corrected counterpart.

5.5 Discussion

In this chapter, a ray tracing method for correcting the refraction in a through-wall radar image is introduced. Unlike the more popular correction approaches, this method does not calculate the transmission function through the material and is, mathematically, much simpler. The counter point is that it is computationally intensive, due to the iterative nature of the solver. This can be alleviated via effective parallelisation, either on the computer CPU or GPU [174].

The bistatic simulations have shown that there is a small focusing improvement between corrected and non-corrected imagery. This phenomenon has been widely reported in literature, both as simulations [112,113,117,120,171] and as experimental demonstrations [118,168,175,176] using retroreflectors. In agreement with this literature, there is little change in focusing quality for reasonably accurate estimations of the wall parameters. This is in some sense beneficial, as it means that slight inaccuracies in the bistatic extraction technique discussed in the previous chapter will not have a dramatic impact on the resultant image quality. However, on the other hand, it makes it very difficult to assess accuracy from an image perspective.

Finally, from the bistatic simulations, to effectively employ an image quality metric, a high pixel density is desired. An optimisation routine based around a focusing metric is therefore very computationally expensive. To alleviate this problem, a coarse image should be used to locate the target of interest, around which a finer sampled image should be formed. This would reduce the size of the image, thus reducing computational load.

However, the small difference between the corrected and non-corrected imagery shown in Figure 5-12 indicates that using such a metric as a means to extract meaningful information about the wall structure is untenable for complex and or cluttered scenes such as the one shown. In addition, one should remove the wall signature, either via gating or some other method, as this will introduce a bias towards higher refractive indices due to the correction method introducing finer range resolution.

6 Extension to 3D and Multistatic

6.1 Introduction

Thus far, a novel method for extracting the thickness and refractive index of an unknown wall using a bistatic SAR collection has been both discussed and successfully implemented using a two-dimensional collection geometry. In addition, a ray tracing based compensation method has also been discussed, using a novel framework that allows for generalisation to both two-dimensional and three-dimensional imagery in both bistatic and monostatic scenarios.

In this chapter, this is all brought together into a three-dimensional multistatic SAR collection; demonstrating both the wall parameter extraction, and the compensation method discussed in the previous chapter. Based on the exhaustive literature search performed throughout this work, this has not yet been achieved.

A three-dimensional through-wall multistatic image was simulated by Gennarelli *et al* in 2016 [177]. However, this was both passive and there was no consideration for refraction through the wall. Topographic representations are more common [41,177–179]; that said, given that signatures can move into or out of the focal plane during refraction compensation, these can be misleading. For example, a topogram may show a reduced PSF under refraction compensation, this could easily be due to the signature moving out of the focal plane rather than a true improvement in quality. It has been reported in [41] that refraction correction to a multistatic SAR image shows little to no improvement in focusing when compensated for. The question is then, is this a consequence of a topogram misrepresenting the data, or not?

Like the two-dimensional case presented in Chapter 4, three-dimensional refraction compensation requires knowledge of the material refractive index, thickness, and position with respect to the radar platform. The bistatic methodology already introduced can account for an arbitrary bistatic trajectory so long as both antennas are on the same side of the wall. It can therefore account for a two-dimensional bistatic aperture without additional modifications. It is, however, prone to the same sources of error, namely antenna positioning inaccuracies.

6.2 3D Ground Truth Estimation

Similarly to the front face reflection, the reflection from the dihedral is assumed to be entirely specular. However, since a dihedral is formed of two reflections, the points of specular reflection, $\boldsymbol{P_1}$ and $\boldsymbol{P_2}$ both need to be calculated. To this end, similar assumptions to Chapter 4.8 are made, namely:

- The bistatic measurement consists of two antennas, $\boldsymbol{T} = [T_x, T_y, T_z]$ and $\boldsymbol{R} = [R_x, R_y, R_z]$. The bistatic baseline between the two antennas is $\boldsymbol{R} - \boldsymbol{T} = [\delta X, \delta Y, \delta Z]$.
- The wall is a specularly reflecting flat surface along the X dimension a distance D from the transmitting antenna.
- The floor acts as a specular reflector and is flat at a height of $Z = 0$ perpendicular to the wall.
- There is a constant down range shift due to internal electronics, CL.
- The step size between sequential pulses is a known value.

The specular reflection from the front face of the wall is characterised using the same procedure as Chapter 4.8. However, the dihedral reflection is less intuitive. Consider the three dimensional bistatic geometry outlined in Figure 6-1 and Figure 6-2, where the specular points of reflection are mathematically described.

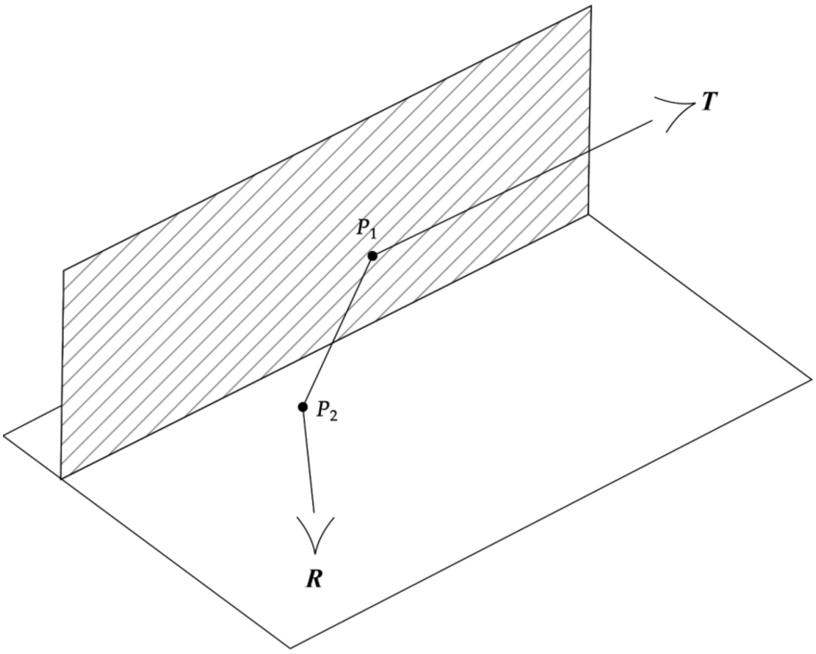

Figure 6-1 – Diagram of the three dimensional dihedral scattering that occurs in a bistatic regime. The points of reflection, P_1 and P_2 combine to give purely specular reflection.

The 3D visualisation of the dihedral shown in Figure 6-1 can be split into a top-down and a side-on projection. The top-down projection is similar to Figure 4-2, whereas the side-on projection is bounded by the height of the antennas and the distance to the wall.

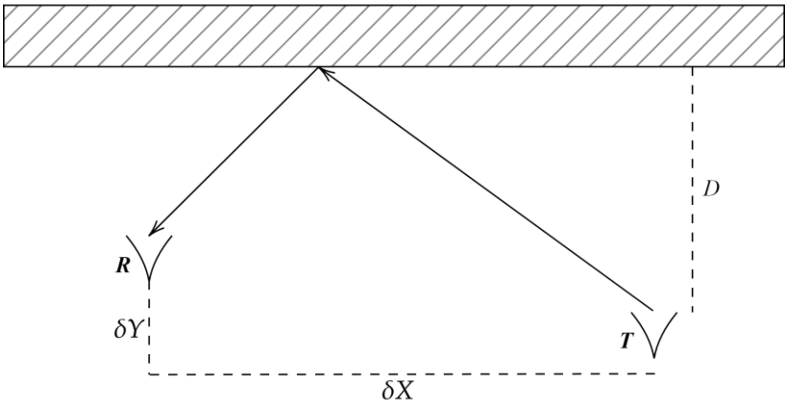

a)

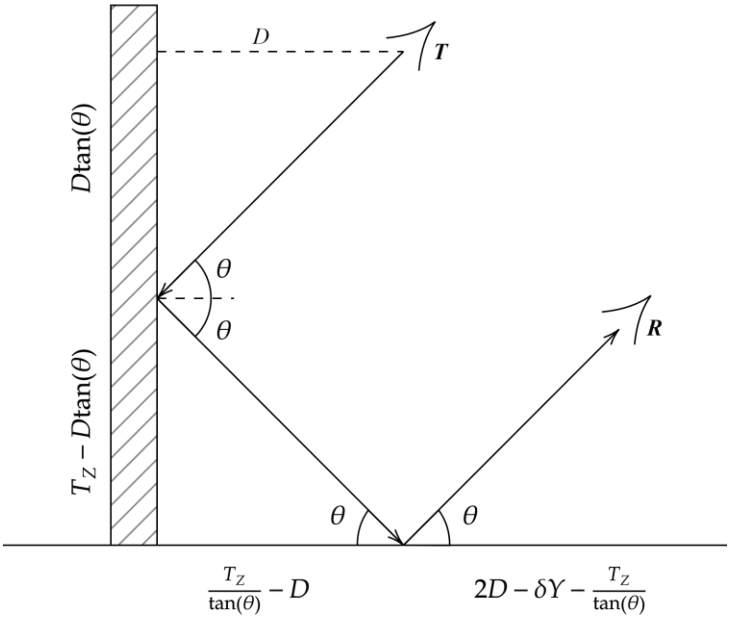

b)

Figure 6-2 – Projections of the 3D bistatic dihedral scattering. Shown as: a) top-down and b) side-on projections. These projections illustrate that since the scattering is bounded between the wall and floor, the reflection points can be found from the height of the two antennas and their separation.

From b), the equations for the specular reflections in the YZ plane can be used to calculate θ explicitly:

$$R_z = \tan(\theta)\left(2D - \delta Y - \frac{T_z}{\tan(\theta)}\right) \tag{6-1}$$

$$T_z + R_z = (2D - \delta Y)\tan(\theta) \tag{6-2}$$

$$\theta = \tan^{-1}\left(\frac{T_z + R_z}{2D - \delta Y}\right) \tag{6-3}$$

This gives the coordinates for the two specular reflections as:

$$\boldsymbol{P_1} = \begin{bmatrix} \frac{\delta X D}{2D - \delta Y} + T_x \\ D \\ T_z - D\left(\frac{T_z + R_z}{2D - \delta Y}\right) \end{bmatrix} \boldsymbol{P_2} = \begin{bmatrix} \frac{\delta X Z_1}{T_z + R_z} + T_x \\ 2D - T_z\left(\frac{2D - \delta Y}{T_z + R_z}\right) \\ 0 \end{bmatrix} \tag{6-4}$$

From the points of reflection, and the assumed transmitter and receiver locations, the bistatic range associated with the dihedral response is calculated thus:

$$R_{dihedral} = |\boldsymbol{P_1} - \boldsymbol{T}| + |\boldsymbol{P_2} - \boldsymbol{P_1}| + |\boldsymbol{P_2} - \boldsymbol{R}| \tag{6-5}$$

Including the dihedral response in the ground-truth refinement routine increases the reliability of the solver, since there is twice as much information to work from. The reason why the dihedral was not included in the previous ground-truth estimator was because it simply was not visible in the imagery. The reason for this, is that as the height of the antennas reduces, the dihedral range becomes similar to the direct specular reflection range. Therefore. for low height antenna measurements, the dihedral and the front face signature blend together in the range profile data. Since there is more variation in height in these measurements, the dihedral signature becomes distinct, and therefore should be used.

To find a set of ground-truth antenna positions that best fit the measured data, a non-linear least squares minimisation routine is used. As with the previous iteration, the unknown parameters are rewritten as a vector, $\boldsymbol{X} = [\phi, \delta X, \delta Y, D, CL]$. The objective function is formed using a least-squares approach separately for the front face and dihedral signature, this is so that weightings, w_f and w_d, can be applied to each component in order to express the confidence in that component. The solution, S, corresponds to the best fit between theory and measured data, given as:

$$S(\boldsymbol{X}) = \min \sum \left(w_f \left(R_{front}(\boldsymbol{X}) - M_{front} \right)^2 + w_d (R_{dihedral}(\boldsymbol{X}) - M_{dihedral})^2 \right) \tag{6-6}$$

6.3 Extraction Results

To prove that the wall parameter extraction discussed in Chapter 4 is extendable to three-dimensions, a large 3.5m by 1.5m 2D bistatic aperture was used to measure the bistatic range to a new wall. Over a frequency range of 1GHz to 6GHz, both monostatic and bistatic collections were performed, imaging a complex scene behind a 1.3m high wall, placed 3.64m from the aperture, shown in Figure 6-3.

Figure 6-3 – The 1.3m high concrete wall placed 3.6m from the SAR system. In addition to the wall structure, a metal sphere is place prominently in the scene. This is to aid image coregistration.

Figure 6-4 – Photograph of the scene constructed behind the wall. The scene is deliberately modelled after the scene used in Chapter 4.7.3.

An initial estimation of the wall properties, before any refinement of the antenna positions, was reported as $n = 2.04$ and $\delta = 110$mm [41]. As a reminder, the thickness and refractive index of the Cemex 1400 lightweight concrete aggregate blocks used throughout are 96.6mm and 2.26 respectively. As before, the precision at which the ground-truth antenna coordinates are reduced via application of the three-dimensional ground-truth refinement method discussed earlier.

This is demonstrated using two measurements. Firstly, background measurement including no additional targets other than those intrinsic to the lab space and the wall. Secondly, a scene is introduced consisting of two metal barrels, a desk and computer setup, a metal briefcase, and a bicycle. This scene was designed to emulate the scene used in the previous implementation shown in Chapter 4.

6.3.1 No Scene

In this no scene measurement, the only scatterers present in the environment are those associated with the wall, and those intrinsic to the laboratory space, i.e. roof lights and support crossbars. As such it approximates, as close as possible, an ideal environment.

The measurement was conducted using a 3.5m by 1.5m two-dimensional aperture segmented into 2.5cm square increments, resulting in 8601 pulses. Observing the range profile data for this measurement reveals that in addition to the wall signature and antenna cross-talk, there are multipath signatures generated via internal reflections inside the wall cavity and reflections off the lab space. This multipath is easy to remove via range gating, so does not affect the parameter extraction. It will however, as will be shown, be present in the volumetric SAR imagery. The range profile data is shown in Figure 6-5. This includes a zoomed in snippet of a select few pulses approximatly in the middle of the synthetic aperture. The range profile appears discontinuous due to multiple horizontal sweeps.

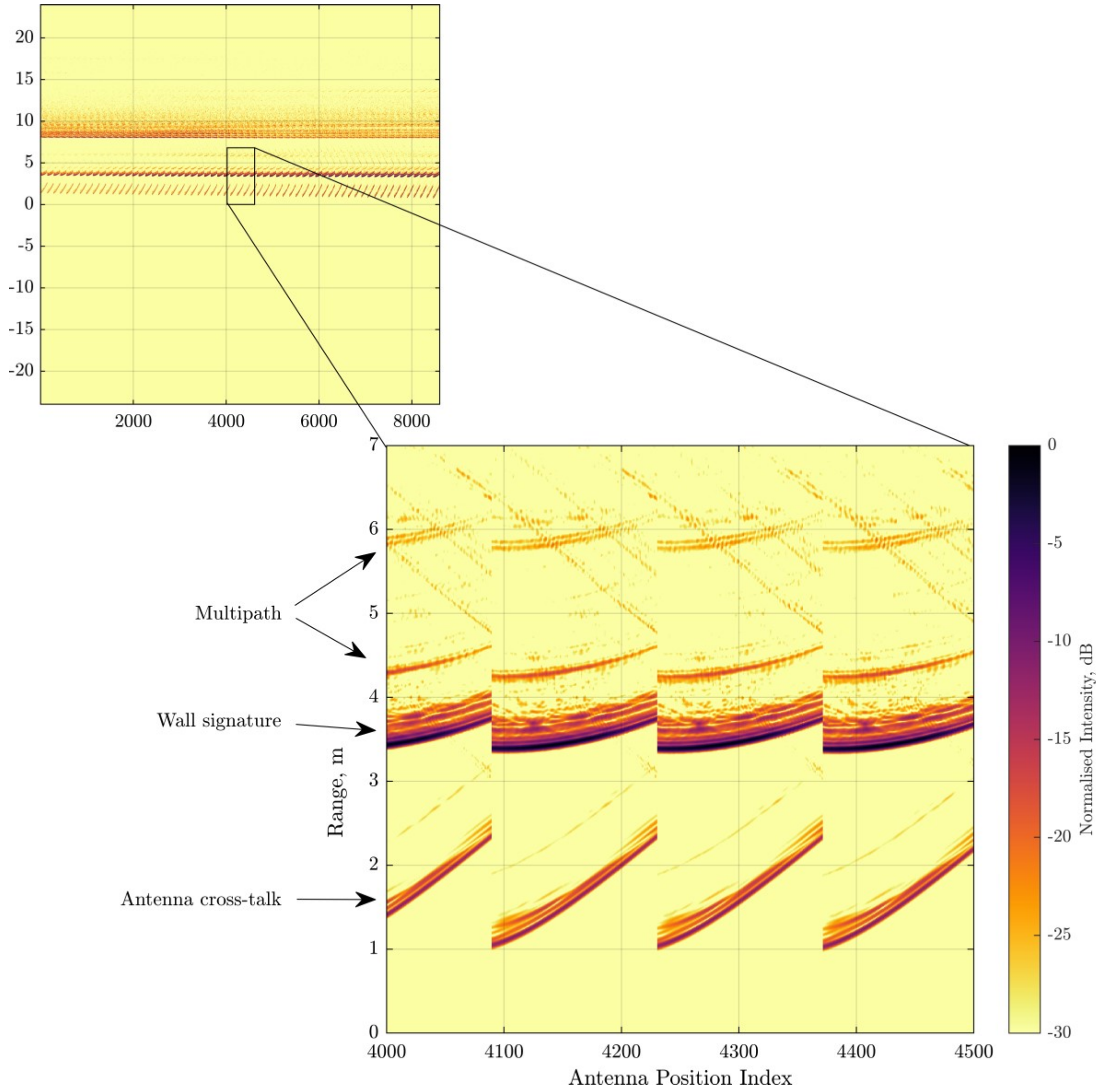

Figure 6-5 – Range profile for the wall shown in Figure 6-3. From the 8601 pulses, a 3.5m by 1.5m two-dimensional aperture is formed. In the region of interest (<5m) distinct signatures are visible in addition to the wall signature, most notably: the antenna cross-talk, and multipath signatures formed due to internal reflections.

While removing the multipath signatures and the antenna cross-talk is easily done via range gating, the same cannot be said for the individual components of the wall signature. Since the measurement is bistatic, the signatures appear further away as the antennas become more separated. As the point of specular reflection becomes closer to the ground, so to does the specular dihedral reflection, as shown in equation 6-4. This causes the range to the specular wall reflection and the dihedral to become closer. The same is true for the rear dihedral and the back face specular wall reflection. By considering one vertical segment of the two-dimensional aperture, chosen such that the horizontal component of $\boldsymbol{V}$ is greatest, the height evolution for each scatterer is obtained. This is illustrated in Figure 6-6 where the dihedral signatures are seen to merge with the direct wall reflections. Due to this merger introducing additional errors, the usable data is constrained to antenna heights above 1.8m. Unfortunately, this means that a little less than half the dataset is unusable.

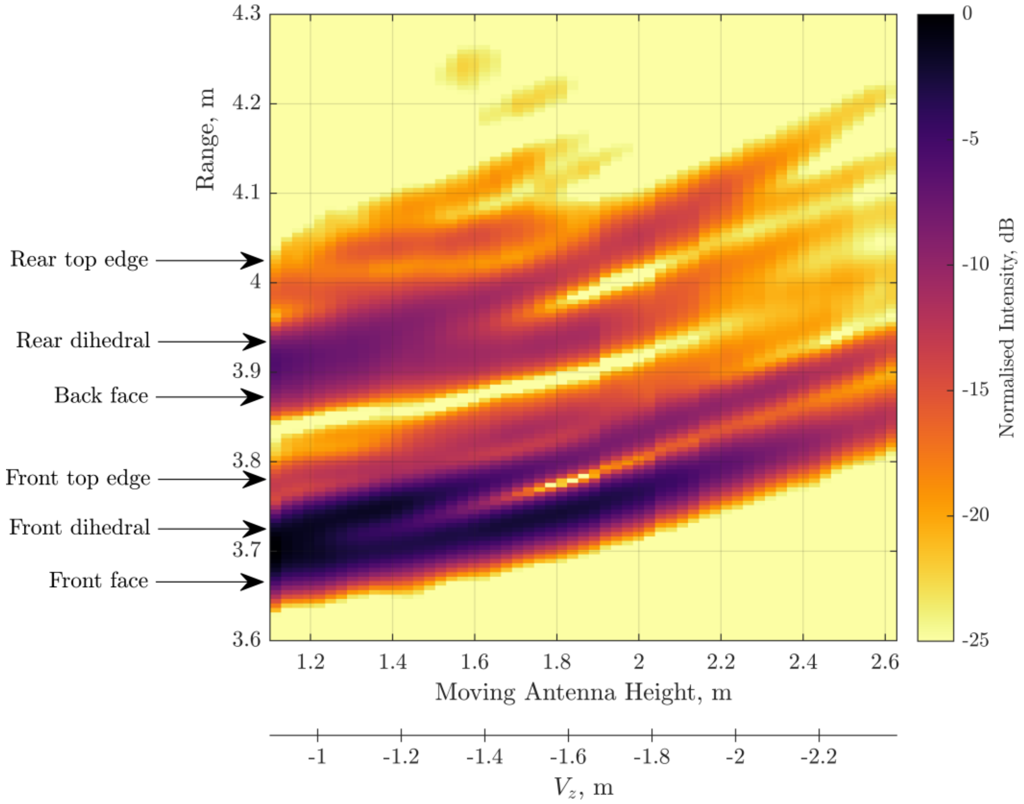

Figure 6-6 – Height evolution of the scatterers showing the range to each signature as a function of antenna height. As the antennas become closer in height, the dihedral signatures begin to merge with the specular wall reflection signatures. The back face is distinct only for heights greater than 1.8m. Heights below this will be prone to errors.

As the difference in elevation between the bistatic antennas becomes smaller, the intensity of the front and back face reflections becomes greater. This means that the objective function (equation 4-21) is more heavily influenced by lower elevations. One can remove this skew via normalisation. However, due to the geometry of the collection, a lower elevation corresponds to a point of reflection that is further away from the wall edges. This means that the lower elevations produce a signal that is more representative of the idealised mathematical model. As such, this skewness of the objective function is acknowledged and subsequently left alone.

For this scenario, the extracted wall parameters are 2.23 and 98.5mm for the refractive index and thickness respectively. This result has been generated using the ground-truth refinement approach discussed in Chapter 6.2, in conjunction with 4000 pulses.

As with the previous measurements discussed in Chapter 4, the uncertainty in the extracted wall parameters is 14% for the refractive index and 10% for the thickness. This agrees with both the previous measurements, and the trihedral validation performed in Chapter 3.

Including this result in the compensated image formation, discussed in the Chapter 5, results in small scale positional change. Figure 6-7 shows a direct comparison between compensated and non-compensated three-dimensional imagery. Given that the only object of any significance is the wall itself, there is not much change between the two images, with the exception of a new signature being introduced at 6m range. This new signature is due to the positional shift of image. In the non-corrected case, it falls outside of the image extent.

The multipath present in both images is not accounted for as part of the wall signature. While it is possible to account for the multipath via modelling the wall structure as multi-layer structure with each additional reflection constituting a new layer, doing so would cause any unrelated signatures to be over corrected. As such, since this dataset is going to be used in the formation of multistatic imagery, the multipath is not considered.

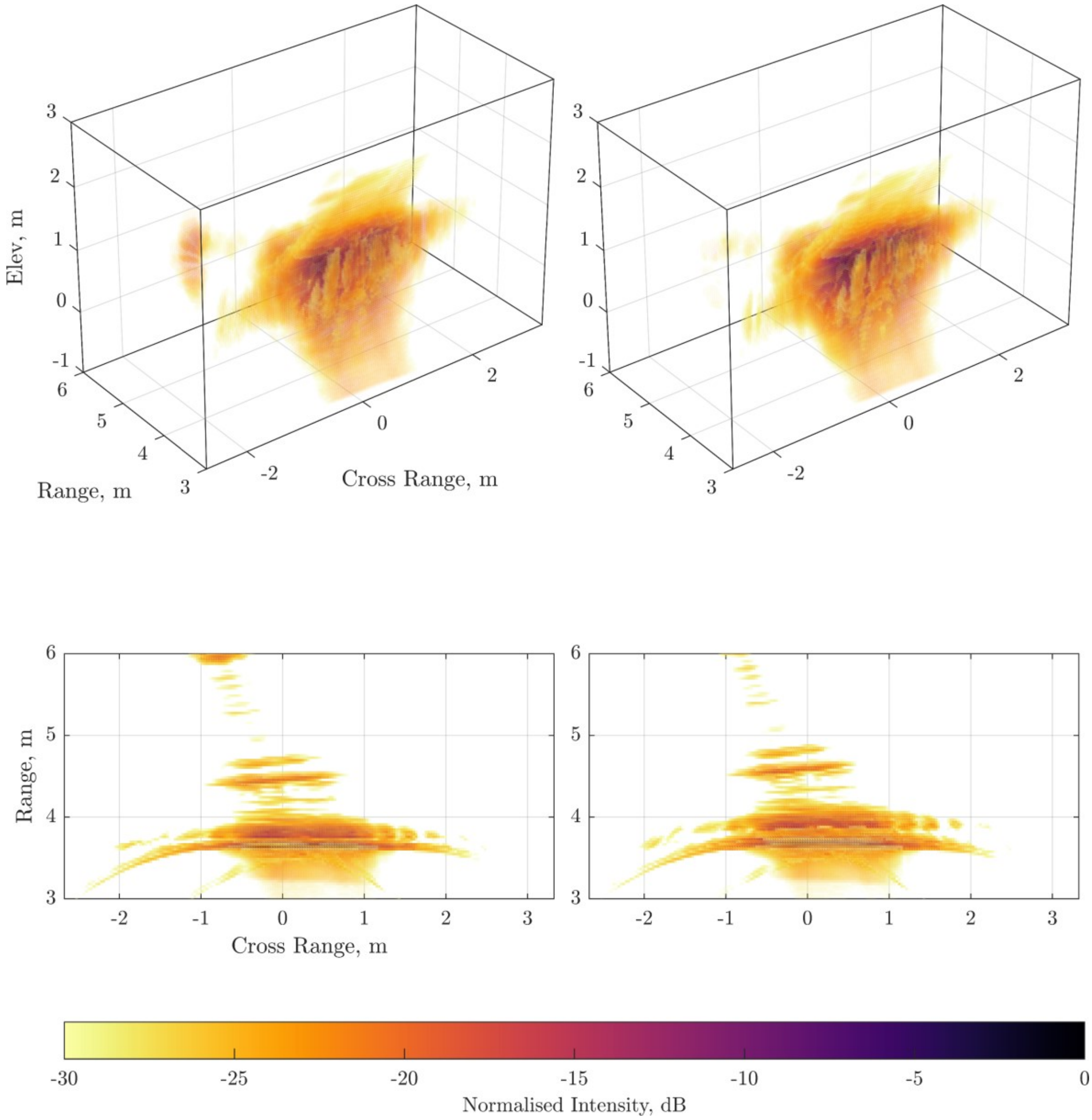

Figure 6-7 – Comparison between corrected (left) and non-corrected (right) for the three-dimensional dataset gathered in this section. Overall, there is not much difference between the corrected and non-corrected images. There is a small shift in the back-face wall position due to the correction, and a signature that was previously outside the bounds of the image is visible in the corrected case.

6.3.2 With Scene

The addition of the scene does not change the nature of the specular reflections from the wall. Nor does it change the relation of the antennas with respect to the wall. For this reason, the range profile data is broadly the same. The only difference between the two, is the additional scene. This similarity is illustrated in Figure 6-8.

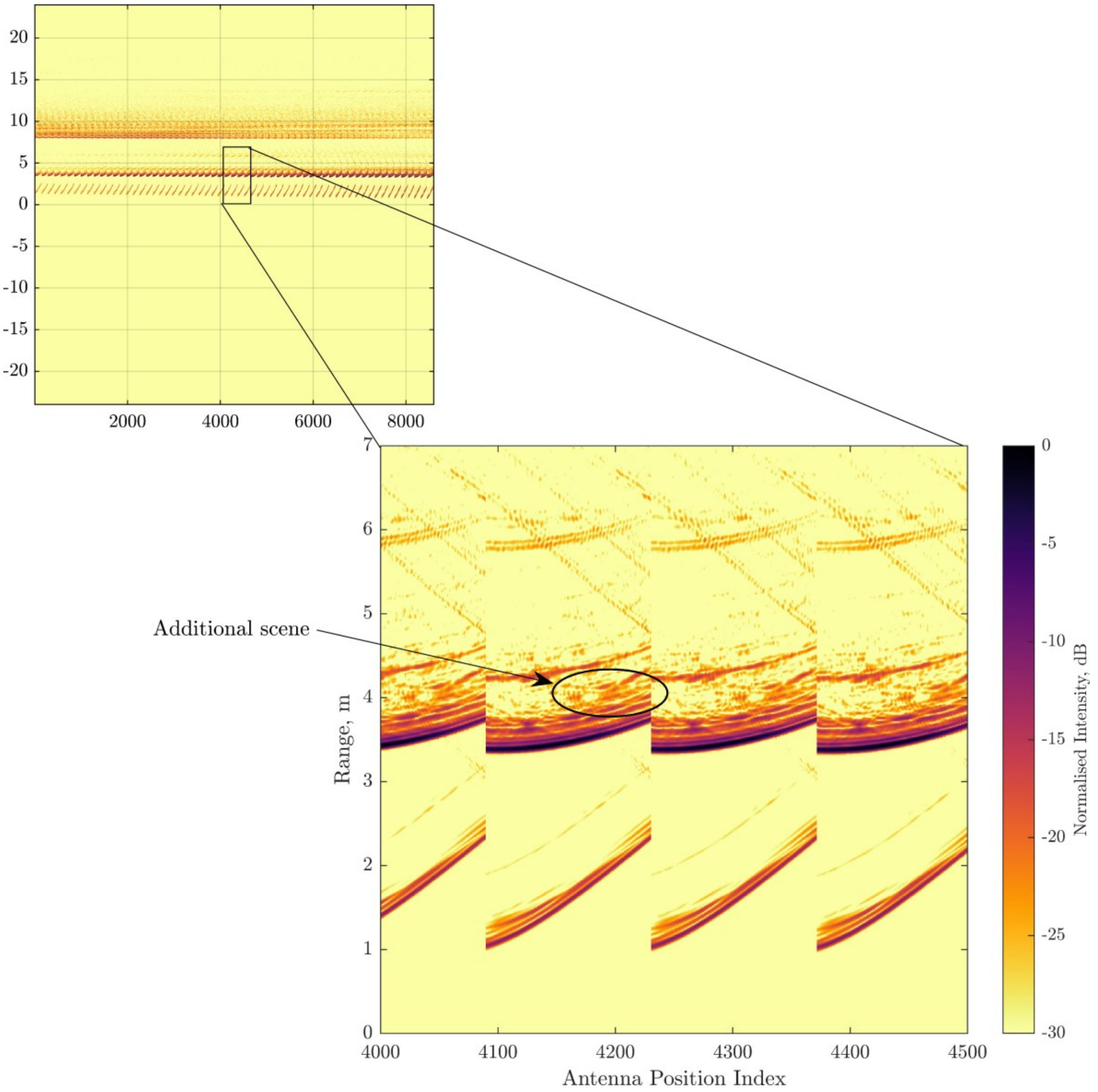

Figure 6-8 – Range profile for this measurement. In addition to the wall signature, cross-talk, and multipath, there is additional signatures associated with the scene. Since the scene is located predominantly in centre of the bistatic synthetic aperture and consists of multiple specular reflections, the scene is brightest when the antennas are furthest apart.

Similarly to the previous measurement, front and rear dihedral signatures are present in the range profile data. As before, these can be removed via truncation of the bistatic synthetic aperture. In addition to the dihedral and top edge signatures, there are signatures associated with the scene. However, since a majority of the scene exists below the point of specular reflection, as illustrated in Figure 6-9, it too can be removed via truncating the dataset.

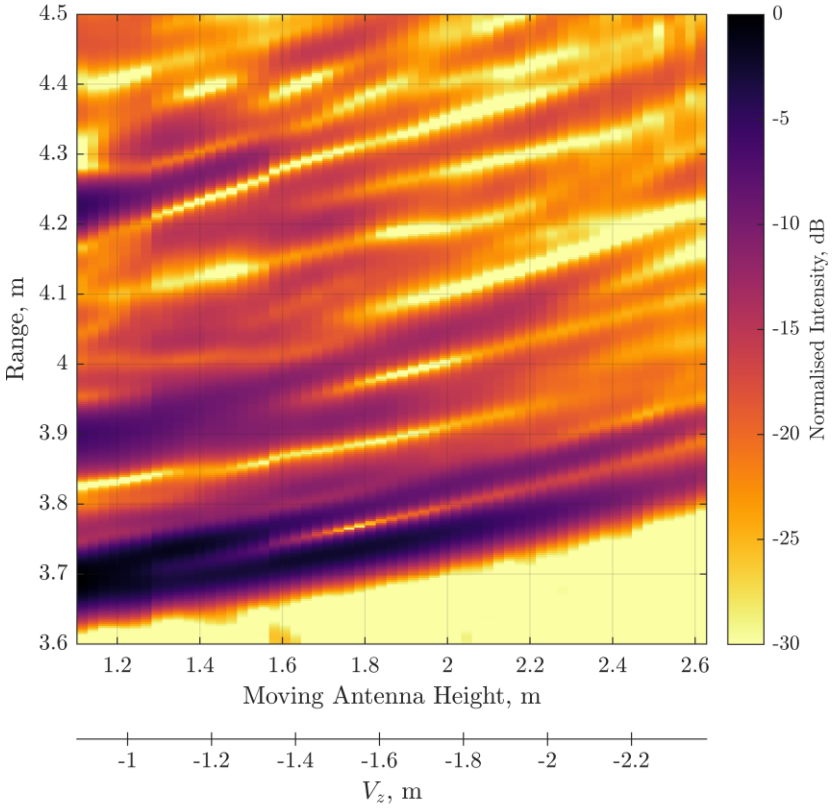

Figure 6-9 – Height evolution of the wall signature and scene. As with Figure 6-6, as the antennas become closer together, the wall and dihedral signatures merge. The scene is most prominent at lower antenna heights, therefore it can be removed via a combination of range gating and eliminating the lower antenna heights.

While the range profile has a higher mean intensity than the wall only measurement, the region of interest, between 3.6m and 4.1m, is of a similar intensity. For this reason, the extracted parameters will also be similar.

For this measurement, the extracted parameters are 2.31, and 95.0mm for refractive index and thickness respectively. This was obtained using the same antenna coordinates and sub-aperture as the wall only measurement. The uncertainty in this extraction is therefore of the same order, this being 0.32 and 9.5mm respectively.

As with Figure 6-7, there is a small positional shift between corrected and non-corrected imagery. However, unlike the previous example, there is a subtle rotation of the scene with respect to the wall. This is the same phenomenon as that shown in Figure 5-12 and is due to the asymmetry of the collection.

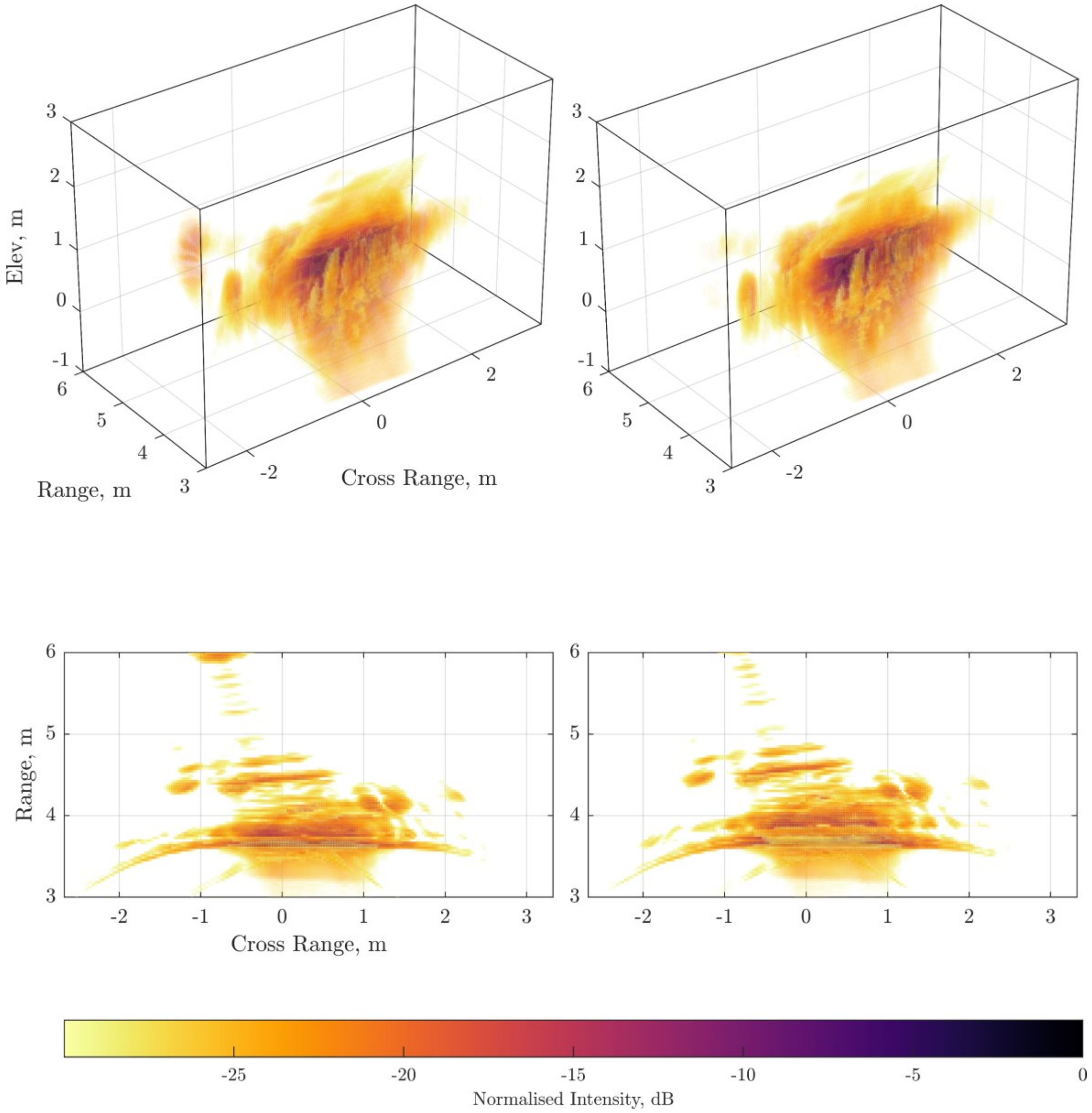

Figure 6-10 – Comparison between corrected (left) and non-corrected (right) for the wall and scene. As before, there is a positional shift of all the signatures behind the wall. In addition, there is a very subtle rotation of the scene due to the correction. However, there is no visible improvement in the focusing quality of the image.

While the difference in extracted parameters is small, to perform background subtraction, and subsequently compensate for the refraction, a single set of wall parameters must be used during the image formation. This is to ensure coherency between the two images. Since the wall material has not changed between measurements, the arithmetic mean is chosen to be representative of both datasets. This corresponds to a refractive index of 2.27 and a thickness of 96.8mm.

Figure 6-11 shows a three-dimensional comparison between corrected and non-corrected background subtracted imagery. In this image, the individual target signatures become clear. For example, both metal barrels are now distinct.

Evaluating the image kurtosis for both the corrected and non-corrected imagery via the procedure laid out in Chapter 5, reveals that the corrected image is quantifiably better focused. The negative kurtosis of the corrected image is -5.6, whereas the negative kurtosis for the non-corrected image is -6.3. However, since the presence of the desk causes interference and thus changes the received electric field from the wall, the wall itself cannot be removed entirely. This causes a bias in the evaluation of the kurtosis towards a more focused image when corrected.

On the other hand, evaluating the peak intensity of the images reveals that the non-corrected image is 0.2dB brighter than the corrected image. This would imply that the non-corrected image is better focused, in contrast to the evaluation performed in the previous chapter. That said, a 0.2dB difference is negligible when considering scene complexity and the interaction between the individual target PSFs.

To better evaluate the effect of the correction on individual targets, each target should be isolated. Implementing this isolation is difficult in this case, since the PSF of the targets overlap. For the same reason, one cannot remove the left-over wall signature via range gating, as this would impinge on the PSF of the desk.

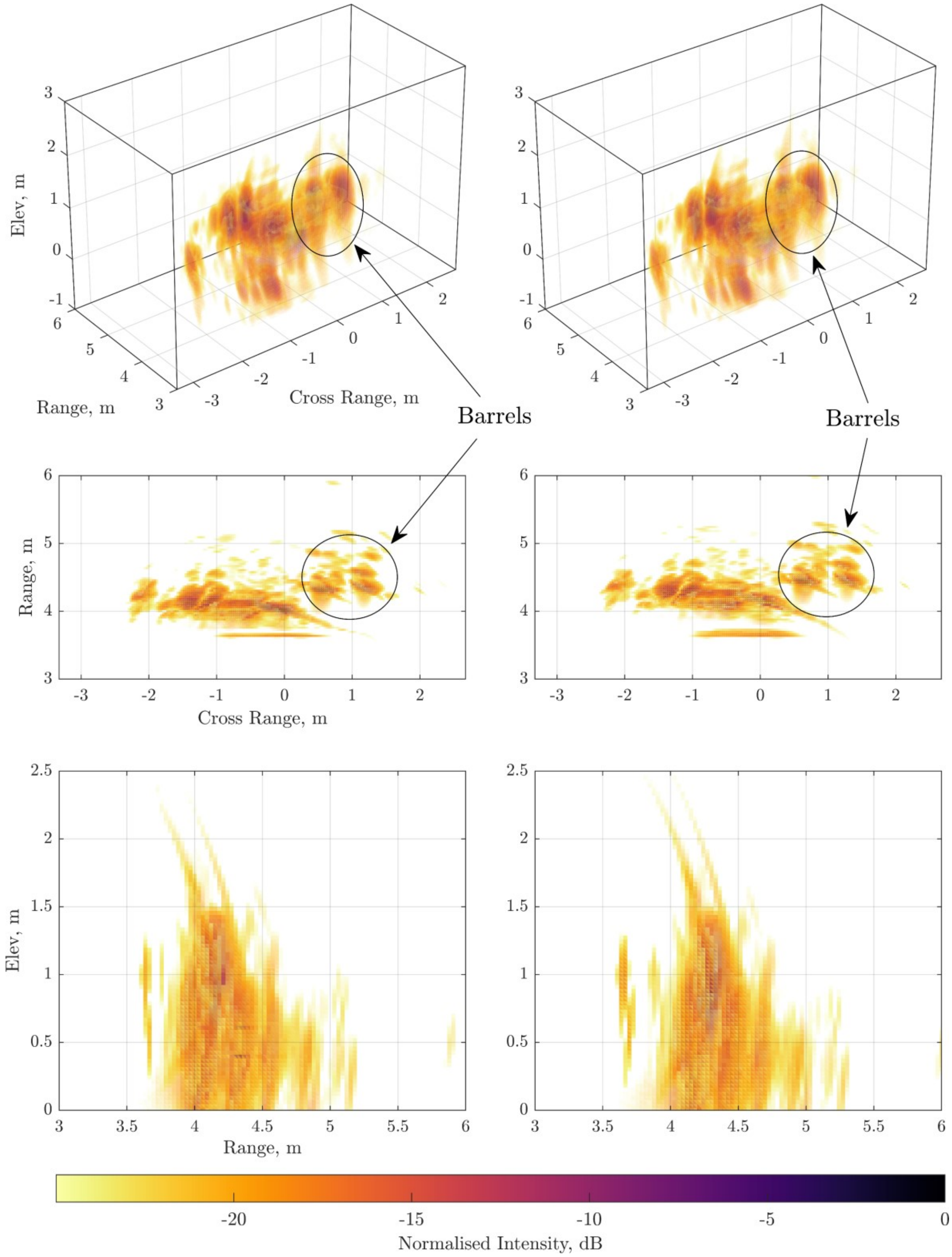

Figure 6-11 – Comparison of corrected (left) and non-corrected (right) for a coherent background subtraction of both datasets. There is little focusing change between the two images, as expected given the results shown in Chapter 5.

6.4 Multistatic Image Formation

Multistatic SAR is, as mentioned in Chapter 2.5, a collection type consisting of multiple transmitting and receiving antennas. Usually, this is done concurrently, taking great care to coordinate each antenna. This quickly becomes more and more complex, not to mention expensive, as more antennas are added. To both decrease the monetary cost and to decrease the system complexity, one can opt for a form of data fusion. If the scene of interest is static, then by the coherent addition of multiple time independent measurements, an equivalent multistatic image is obtained.

To achieve a high-fidelity multistatic SAR image, a bistatic SAR collection is fused with a monostatic SAR collection. This is to achieve the best of both worlds; the higher azimuthal resolution of the monostatic collection with the wall property extraction from the bistatic measurement. To do so coherently, the scatterers must be stable, and the antenna coordinates must be known to a high degree of accuracy. Since the antenna coordinates for the monostatic measurement are, at best, known to a precision of 1cm, coherent addition of bistatic and monostatic images results in misalignment errors.

A sub-optimal, but also less stringent, method of forming multistatic images is to simply add the magnitude of both bistatic and monostatic components together:

$$I_{Multi}^2 = |I_{Mono}|^2 + |I_{Bi}|^2 \qquad \textbf{6-7}$$

A consideration for TWR imagery is that the refraction through the wall material follows a different trajectory for monostatic and bistatic SAR collections. Therefore, to effectively add the images together, both must be independently corrected following the procedure outlined in the previous chapter. Leaving out this correction results in defocusing, as illustrated in Figure 6-12. Including the correction both improves focusing quality, and positional accuracy [41]. However, as shown in the previous chapter, this focusing improvement is slight.

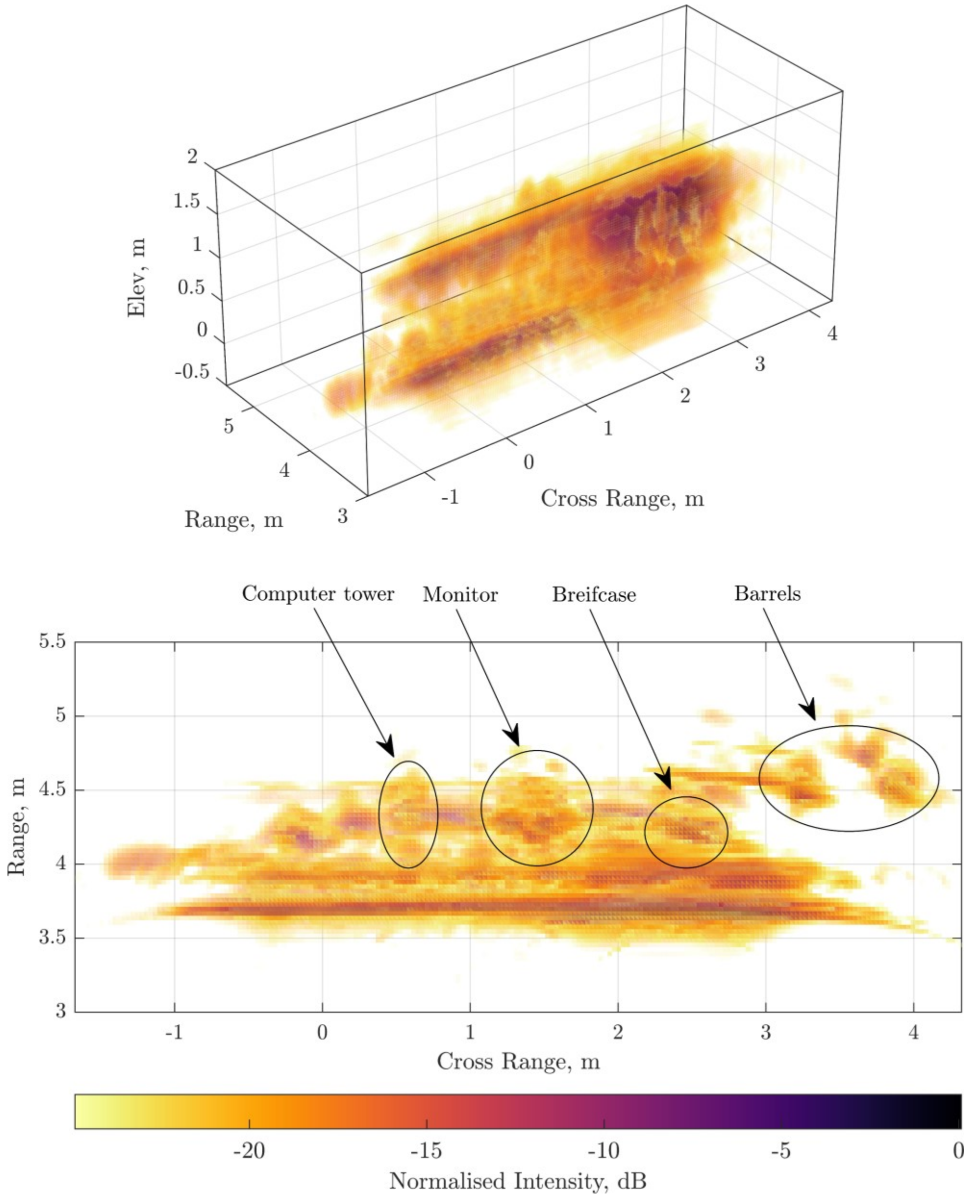

Figure 6-12 – Non-corrected multistatic SAR formed via incoherent addition of monostatic and bistatic images. Targets of interest are highlighted in the top-down representation. These include the computer monitor, tower, metal briefcase, and metal barrels.

The images are added together incoherently, this means that the areas of the image where the bistatic and monostatic images overlap will be brighter than areas where they do not. In practice, signatures only present in one image will be suppressed when evaluating the image as a whole. This is the reason why only half of the wall appears to be illuminated.

Since the monostatic and bistatic components follow different synthetic apertures, the correction to each constituent image needs to be performed separately. Using the same parameters to correct both the monostatic and bistatic components results in a more accurate image, and slightly more distinct signatures. Most notably, the computer monitor, and barrels are better focused in addition to the wall compression. Figure 6-13 shows a corrected multistatic image. Forming such an image, while novel and of higher quality, is time consuming, thus accelerating the image formation is desirable.

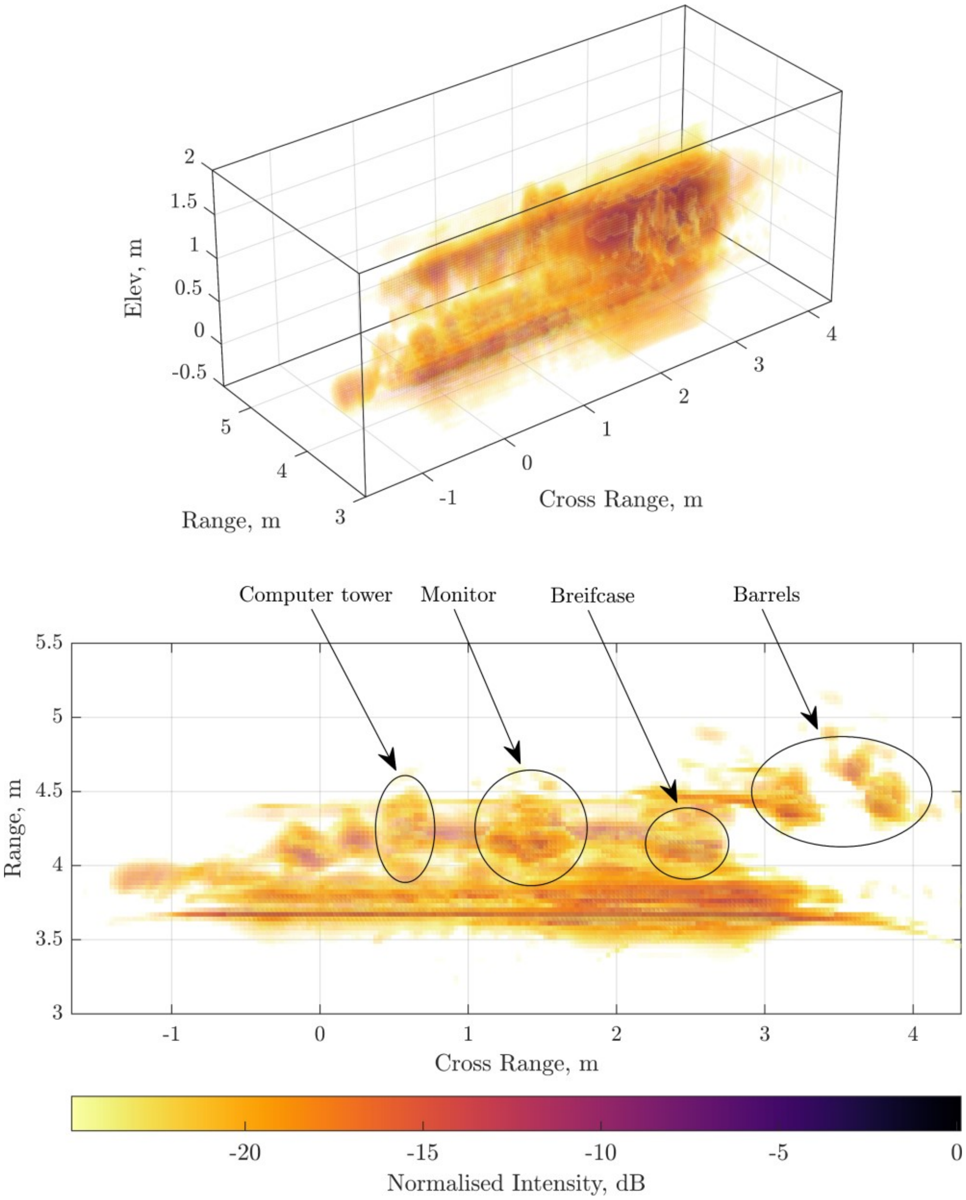

Figure 6-13 – Corrected 3D multistatic SAR. Both the monostatic and bistatic components were corrected for refraction using the extracted parameters in Chapters 6.3.1 and 6.3.2, leading to a more focused image. As before, a top down view is presented highlighting key features. While subtle, the barrels and monitor are both more distinct from the wall signature and better focused.

Removing the wall signature, via background subtraction, allows for a less biased evaluation of the image quality. Figure 6-14 and Figure 6-15 show the corrected and non-corrected cases. There is a very subtle improvement in the image quality for the corrected image. The reasoning for the improvement being small is two-fold. Firstly, the concrete wall is not sufficient to cause major defocusing in the first place, and secondly, the bistatic and monostatic components are not sufficiently different to cause the monostatic and bistatic signatures to appear visibly separated. A more divergent multistatic collection, such as one antenna trajectory being perpendicular to the other would result in a greater effect.

That said, the negative kurtosis of the corrected and non-corrected cases, -588 and -749 respectively, show that the multistatic imagery does indeed become more focused when compensated for the wall refraction.

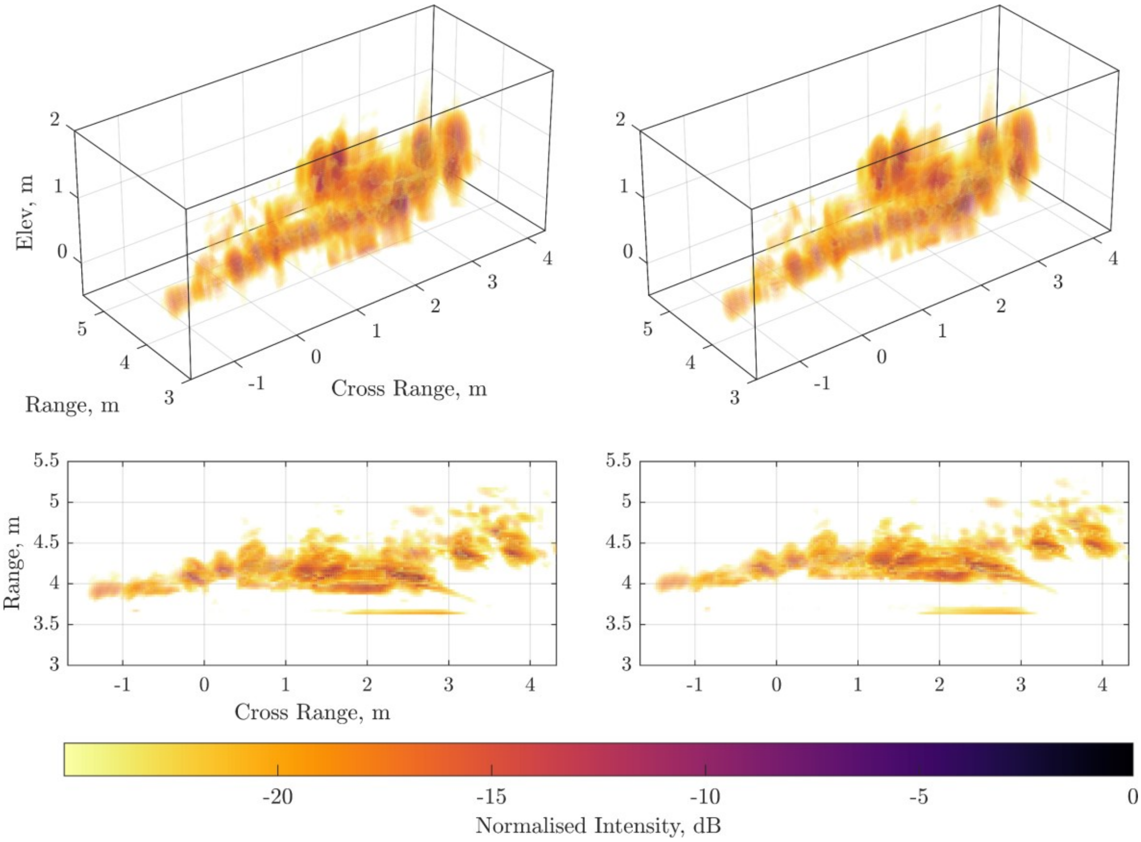

Figure 6-14 – Comparison between corrected (left) and non-corrected (right) for multistatic background subtracted imagery. While there is an improvement in the image quality, it is so small as to be unnoticeable without careful study of both images.

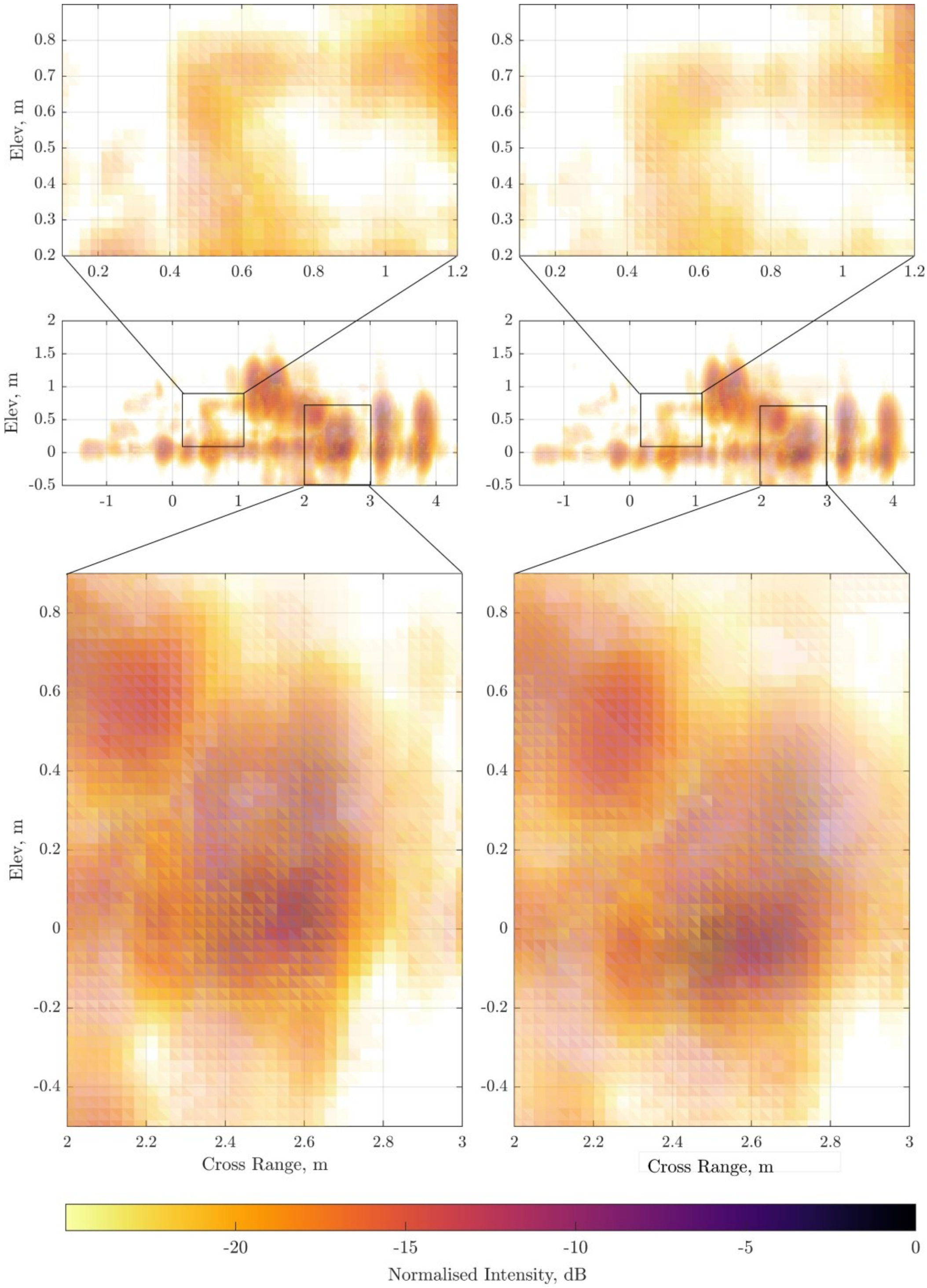

Figure 6-15 – XZ projection of the multistatic imagery showing that select targets do indeed improve in both intensity and focusing. The edge of the table especially becomes clearer in the corrected image (left) when compared to the non-corrected image (right).

6.5 Discussion

In this section, a natural evolution of the two-dimensional parameter extraction methodology is employed. This new approach has the benefit of further mitigating both clutter, and multipath effects via multiple radar heights. This height variation allows for the alleviation of dihedral and clutter signatures via judicious sub-aperture selection. Including this variation in the parameter extraction has yielded accurate results in agreement with both the planar implementation shown in Chapter 4 and the separate validation measurements shown in Chapter 3.

To put this into context with regards to the prior literature, most bistatic extraction processes are performed with the antennas extremely close to the wall in order to both maximise energy throughput and to avoid additional scattering phenomenology [99,100,128,131,143]. The work presented in this section shows that such positioning is unnecessary.

Given that the extracted parameters are in agreement with the known parameters, one must conclude that this bistatic three-dimensional approach fundamentally works. However, given the scale of the measurement uncertainty, derived from uncertainty in the antenna ground-truth coordinates, the precision of the approach leaves much to be desired. As stated in Chapter 4, finer parameter precision derives from a more precise knowledge of the antenna positioning. Mounting both antennas to a rigid frame would alleviate some of the concern. However, this does not fix issues relating to a non-parallel wall or uncertainty with regards to standoff distance and introduces practical limitations on measurement design.

This all feeds in towards fully volumetric refraction compensated SAR imagery. Two-dimensional compensation has been reported on in the past, as discussed in Chapter 5. Three-dimensional imagery, and in particular the volumetric style of image generated herein, is much rarer. Topographic representations [41,177,178] are more common, due in part to easier representation on paper, and a reduced computational cost. However, since signatures have the capacity to move both vertically and horizontally under refraction compensation, a topographic representation is insufficient to fairly evaluate the image focusing quality as signatures may travel into or out of the focal plane. This is not an issue if the three-dimensional SAR image is represented as a fully volumetric image.

Unfortunately, volumetric image formation, and more so full refraction compensation, is a computationally intensive endeavour. The time constraints associated with the data collection, parameter extraction, and volumetric image formation culminate in a long and time-consuming processing chain. As such this will be difficult to implement in a timely manner. As will be shown in Chapter 7, the image formation can be dramatically accelerated without significant loss in image quality. However, the raw data collection is still a limiting factor.

There is a slight improvement in the image focusing when comparing the bistatic corrected and non-corrected imagery. However, this improvement is not readily visible despite being numerically proven.

Future work should focus on more divergent multistatic geometries, where the effect of the differing propagation paths is more readily apparent. As shown, the single bistatic measurement is sufficient to extract the wall parameters. However, multiple bistatic measurements would only improve the precision, and provide a more meaningful multistatic image. A remotely controlled drone swarm would be of interest, as this would provide ample measurement geometries and potential for a more generalised multistatic collection. This would, however, require that the positioning of each drone be known extremely precisely.

7 Time constraints with 3D Image Formation

Unlike two-dimensional Backprojection, with a computational complexity of $O(N^3)$ [180] to form an $N \times N$ image from N projections, volumetric imaging has a computational complexity of $O(N^4)$. Therefore, it can take orders of magnitude longer to form a reasonably sampled volumetric image. To this end, methods to accelerate the image formation are desired.

Multiple faster implementations of Backprojection have been proposed, such as the well-established Fast Backprojection algorithms [180–183]. These algorithms rely on the symmetry of the Radon Transform. Under this approximation, half the image can be formed using half the number of projections, reducing the computational complexity from $O(N^3)$ to $O(N^2 \log_2 N)$ for two-dimensional imaging. However, given the algorithm's origin in tomography, they are best suited for spotlight SAR. The other general method for accelerating image formation is to leverage the massively parallelisable nature of Backprojection, splitting the process over several processing threads, either on the computer CPU [184,185] or GPU [174,185–189].

As mentioned in Chapter 4, sufficiently sampled time domain signals can be efficiently upsampled via zero padding in the frequency domain. While this notion is typically applied to one-dimensional signals, SAR images can be considered time domain signals. They can therefore be upsampled via zero padding in the spatial frequency domain [190–192].

Additionally, the sampling should be fine enough that the entire spatial-frequency support, f, for the image be contained within the frequency range given by equation 7-1.

$$F_{xyz} = \frac{c}{2\Delta P_{xyz}} \qquad \textbf{7-1}$$

Where F_{xyz} is the frequency range associated with the time domain pixel spacing ΔP_{xyz} in the respective dimension. If the spatial-frequency content is outside the range $-\frac{F_{xyz}}{2} \leq f \leq \frac{F_{xyz}}{2}$ then the data will begin to wrap around due to the circular nature of the Fourier Transform. This leads to sharp discontinuities between the measured dataset and the padded values, causing ringing. To avoid excessive ringing, El-Darymli *et al* [191,192] proposed that a window function be applied over the dataset. While this would reduce ringing, since this also reduces resolution, it is not ideal. In addition, the padding of wrapped spatial-frequency data introduces gaps. This leads to artefacts. Alternatively, one could increase the pixel density of the image, however, this requires additional computation that is ultimately unnecessary.

A better approach is to use a suitable reference shift to centre the support around zero frequency. This has the benefit of minimising the required initial sampling and eliminating the need for a circular shift of the dataset [191]. To achieve this reference shift, both conventional far field basebanding, and a novel spatially variant basebanding operation can be employed [193,194]. A basebanded signal is one where the transmitted signal has a near zero frequency component, as such the majority of the signal is contained within $0 \rightarrow B$ for a real signal and $-\frac{B}{2} \rightarrow \frac{B}{2}$ for a complex signal[9]. If done properly, the frequency extent given by equation 7-1 should be no larger than the signal bandwidth. In other words, to avoid wrapping, the pixel size should match the size of a resolution cell.

7.1 Conventional Basebanding

Conventional basebanding [193–195] acts as a de-ramping phase screen applied directly to the SAR image, with the aim of smoothing the phase of the image [194]. While often used in interferometry and coherent change detection to improve image coregistration through a reduction of interpolation errors, it has the additional benefit of centring the spatial-frequency support of the image around zero frequency.

Basebanding, both conventional and spatially variant, operates by multiplying the complex SAR image by a phase ramp, $\Phi_{ramp} \in \mathbb{C}$ of unit magnitude, i.e. $\left|\Phi_{\text{ramp}}\right| = 1$.

$$\Phi_{\text{ramp}} = e^{-\frac{i2\pi f_c}{c}\left(p_x B_{vec_x}\right)} \times e^{-\frac{i2\pi f_c}{c}\left(p_y B_{vec_y}\right)} \times e^{-\frac{i2\pi f_c}{c}\left(p_z B_{vec_z}\right)} \qquad \textbf{7-2}$$

$$\Phi_{\text{ramp}} = e^{-\frac{i2\pi f_c}{c}(\boldsymbol{P} \cdot \boldsymbol{B}_{vec})} \qquad \textbf{7-3}$$

---

[9] Since a complex signal exists within $\frac{-B}{2} \rightarrow \frac{B}{2}$, the maximum frequency component for a complex basebanded signal is half of that of a real signal. For this reason, the Shannon-Nyquist sampling rate for a complex signal is also half that of a real signal. This can be thought of as being due to a complex number encoding twice as much information as a real number.

Where f_c is the centre of the SAR frequency range, and c is the speed of light in a vacuum. The vector $\boldsymbol{P}$ is the vector position for each pixel in the SAR image (2-D or 3-D).

In conventional basebanding, the vector $\boldsymbol{B_{vec}}$ is the bistatic vector from the antennas to the scene centre. For a scene centre vector position, $\boldsymbol{S}$, the bistatic vector used in conventional basebanding is given by:

$$\boldsymbol{B_{vec}} = \frac{\boldsymbol{S}-\boldsymbol{T}}{|\boldsymbol{S}-\boldsymbol{T}|} + \frac{\boldsymbol{S}-\boldsymbol{R}}{|\boldsymbol{S}-\boldsymbol{R}|} \qquad \textbf{7-4}$$

Where $\boldsymbol{T}$ and $\boldsymbol{R}$ are the mean position vectors for the transmitting and receiving antennas respectively. Since a phase ramp in one domain is equivalent to a linear positional shift in the other domain, multiplying the complex SAR image by Φ_{ramp} is equivalent to shifting the frequency support along the vector $\boldsymbol{B_{vec}}$ by the centre frequency. Thus, the centre frequency is shifted to zero.

To illustrate the effect of basebanding on the image phase, a monostatic SAR image of speckle was generated. In speckled images, multiple scatterers exist within a single resolution cell and, as will become relevant in the next section, each scatterer has a different spatial-frequency support associated with it. Since phase associated with a low intensity pixel is not that meaningful, to get an appreciation for the full effect of the basebanding procedure, it is important that a large proportion of the image be populated, hence the speckle shown in Figure 7-1:

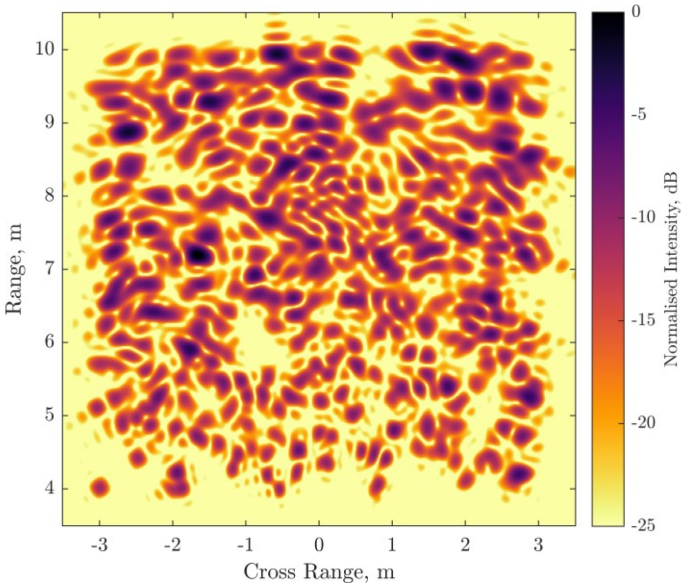

Figure 7-1 – Speckled SAR image. Speckle is used in this simulation because it exhibits a wide variety of spatial-frequency supports, while simultaneously populating much of the image.

In Figure 7-2, the non-basebanded image exhibits a greater phase gradient across the entire image when directly compared to the basebanded version. This is because the spatial-frequency support is further from the origin. As discussed in Chapter 4, a shift in one domain is equivalent to a phase ramp in the other domain. Therefore, since the non-basebanded dataset is shifted away from the origin, there exists a phase ramp in the image domain. This does not affect the intensity of the image, since the magnitude of the phase ramp is one, however it does affect the phase of the image. By moving the spatial-frequency support towards the origin, the phase ramp is reduced, producing the smoother phase seen in Figure 7-2d. This smoother phase makes complex interpolation more accurate, thus leading to more accurate image coregistration in interferometry and CCD.

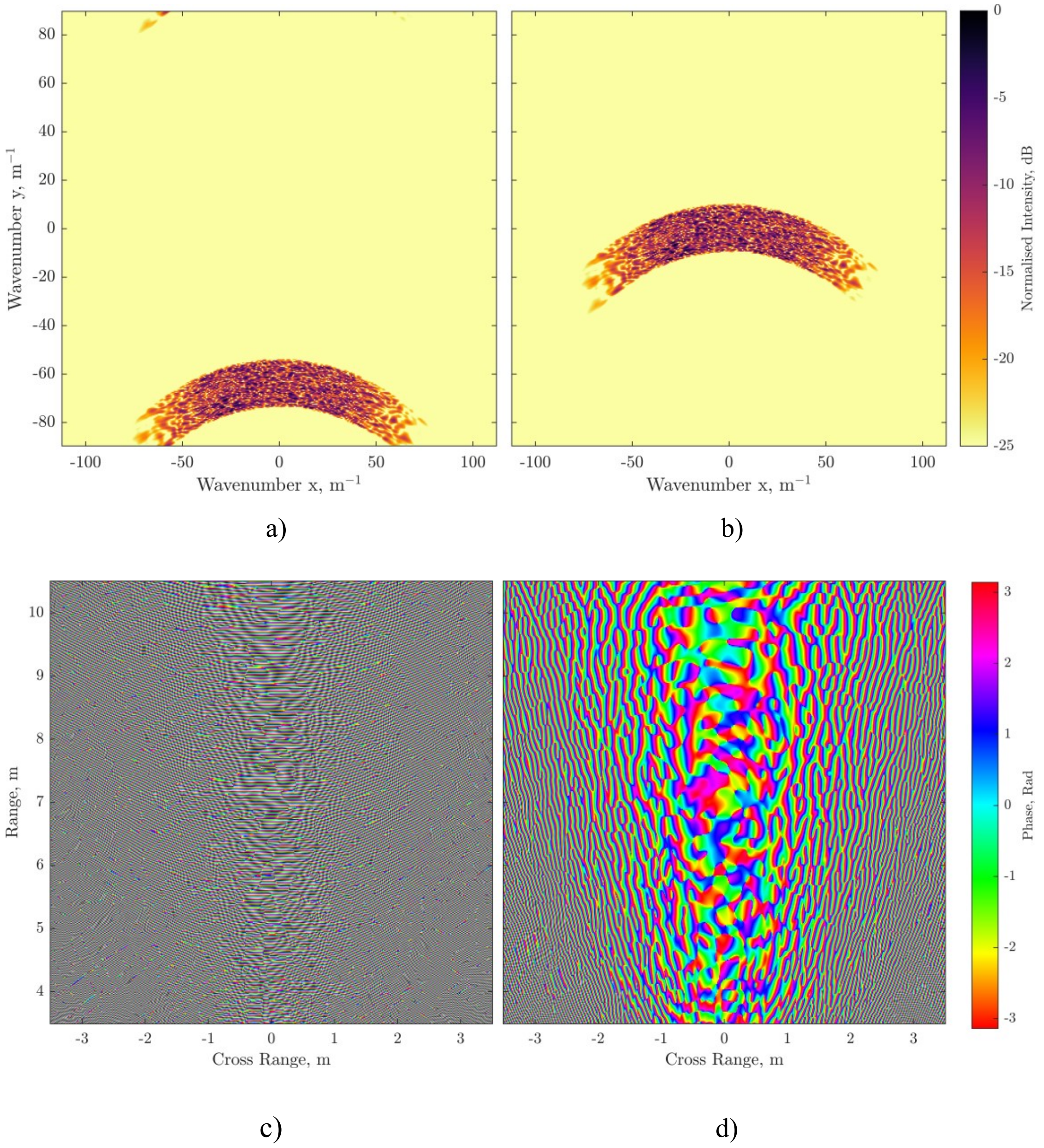

a) b)

c) d)

Figure 7-2 – Comparison of the spatial-frequency support, and phase for non-basebanded and conventionally basebanded images. a) non-basebanded spatial-frequency support, b) basebanded spatial-frequency support showing the support centred around zero frequency, c) non-basebanded phase (rad) showing a greater phase gradient across the image than d) the basebanded phase.

While the phase gradients are substantially reduced, especially in the central column, the extremes of the image still exhibit notable phase ramps. This is due to the near-field nature of the SAR image and the differing squint angle associated with each scatterer.

7.2 Spatially Variant Basebanding

Conventional basebanding makes an implicit assumption that the SAR image scene operates in the far field. This is because it assumes that the entire image support can be centred by shifting the entire support along the same vector. For SAR near-field measurements, where propagating wavefronts are significantly curved throughout the image, this is not the case, as the squint angle may change significantly between different patches in the image. This leads to different spatial-frequency support for each patch of image. This is further complicated by the limitation placed on GBSAR systems where the $\frac{W}{2}$ stripmap resolution may be unattainable due to a physical limitation on the size of obtainable aperture. The difference in SAR near-field image support is illustrated in Figure 7-3 by the near-field SAR image, and its corresponding spatial-frequency support. In order to clarify which support segment corresponds to which target, each target has been ascribed a different amplitude. As illustrated, each target produces its own spatial-frequency support and, due to the SAR near-field nature of the image, each support is rotated. This is to be expected, as a rotated time domain representation corresponds to an equally rotated frequency domain representation [2, pp.32–33].

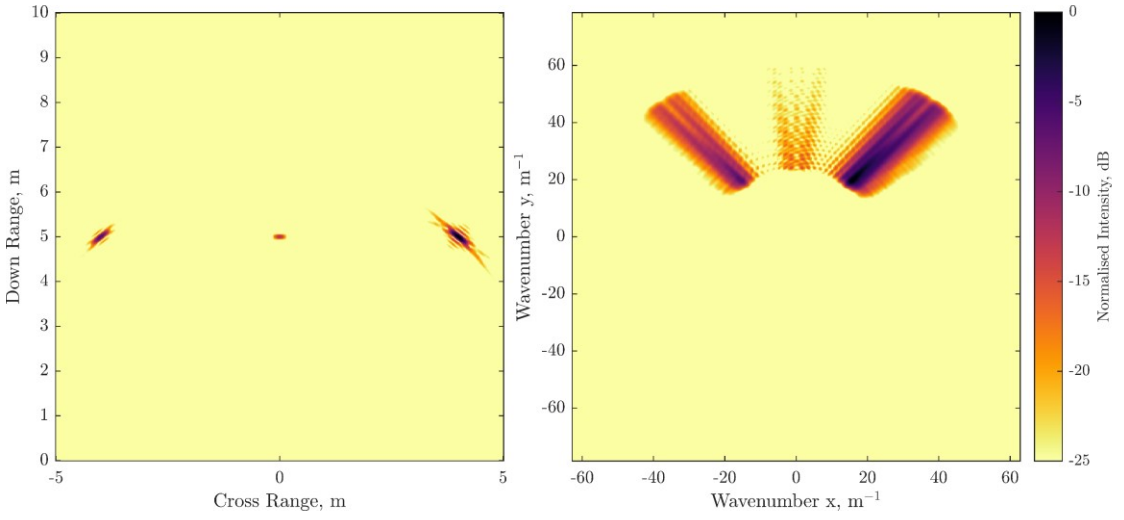

a) b)

Figure 7-3 – a) SAR near-field image of three targets, and b) the corresponding spatial-frequency support. Each target corresponds to its own support. For example, the leftmost target corresponds to the leftmost section of spatial-frequency support.

Spatially variant basebanding differs from the conventional form by varying the bistatic vector, $\boldsymbol{B_{vec}}$, at every point in the image. This variation allows the basebanding to operate in the SAR near-field wherein each pixel in the image exhibits a potentially significant difference in support.

For a bistatic SAR collection defined by an origin, a mean transmit vector position, $\overline{\boldsymbol{T}}$, a mean receive vector position, $\overline{\boldsymbol{R}}$, and a pixel position vector $\boldsymbol{P}$, it has been found [196] that the bistatic vector used in equation 7-3 should be:

$$\boldsymbol{B_{vec}} = \frac{2\overline{\boldsymbol{T}} - \boldsymbol{S} - \boldsymbol{P}}{|2\overline{\boldsymbol{T}} - \boldsymbol{S} - \boldsymbol{P}|} + \frac{2\overline{\boldsymbol{R}} - \boldsymbol{S} - \boldsymbol{P}}{|2\overline{\boldsymbol{R}} - \boldsymbol{S} - \boldsymbol{P}|} \tag{7-5}$$

This differs from equation 7-4 since $\boldsymbol{P}$ is a function of image position, not a fixed value.

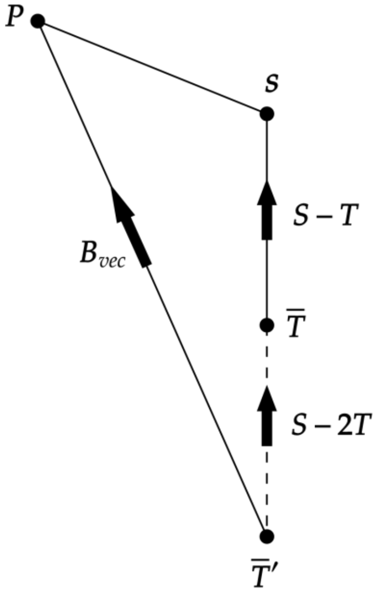

Figure 7-4 – Vector diagram illustrating the orientation of the antenna, $\boldsymbol{T}$ with respect to the pixel position $\boldsymbol{P}$. This configuration illustrates a monostatic scenario, where $\boldsymbol{R} = \boldsymbol{T}$.

Figure 7-4 illustrates the vector scenario from which equation *7-5* is derived whilst Algorithm 7-1 provides a pseudocode implementation.

```
Image has size [X, Y, Z]

# Basebanding Coarse Image.
Transmitter := Scene Centre – 2*mean(Transmit Array)
Receiver := Scene Centre – 2*mean(Receive Array)
Phase Constant := j*2*pi*mean(Frequency)/c
For I := 1:NPixels do
        Pixel Position := [$X_I$, $Y_I$, $Z_I$]
        Transmitter to Pixel := (Scene Centre – Pixel Position) + Transmitter
        Receiver to Pixel := (Scene Centre – Pixel Position) + Receiver
        Bistatic Vector := Transmitter to Pixel / abs(Transmitter to Pixel) +
                           Receiver to Pixel / abs(Receiver to Pixel)

        Phase Ramp := exp(Phase Constant * Pixel Position[x] * Bistatic Vector[x]) *
                      exp(Phase Constant * Pixel Position[y] * Bistatic Vector[y]) *
                      exp(Phase Constant * Pixel Position[z] * Bistatic Vector[z])
```

Algorithm 7-1 – Pseudocode for the spatially variant basebanding described in this section. For each pixel in an image of size X by Y by Z, calculate the dot product between the position vector of the pixel and the vector travelling from the antenna to the pixel. This dot product is then used in a phase ramp applied to said pixel.

Both the spatially variant and conventional basebanding algorithms can be applied to both planar and volumetric imagery without additional modifications. This is because neither algorithm makes any assumption about the z-coordinates of either the scene centre or of individual voxels.

The effect of this variation can be seen in Figure 7-5, where the phase screen applied to the image is seen to be differ significantly between the spatially variant and conventional versions of basebanding.

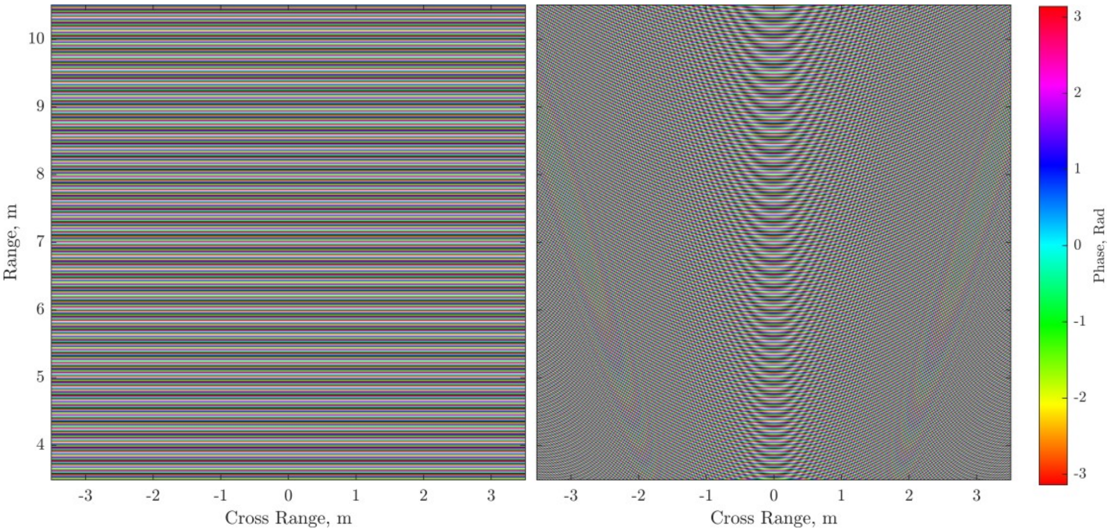

a) b)

Figure 7-5 – Comparison between the phase screen Φ_{ramp} for a) conventional basebanding and b) spatially variant basebanding.

The result of this variant phase screen is that the spatial-frequency support for each individual pixel is centred around zero frequency, as opposed to the global shift applied in the conventional case. Consequently, the image experiences a smaller phase ramp away from the central column. The spatial-frequency and the basebanded SAR image phase are shown in Figure 7-6a and Figure 7-6b respectively, in which this effect can be seen.

The spatial-frequency is noticeably more compressed than the conventional basebanding approach. This implies, via equation 7-1, that a coarser image sampling can be used in Backprojection while still avoiding wrapping.

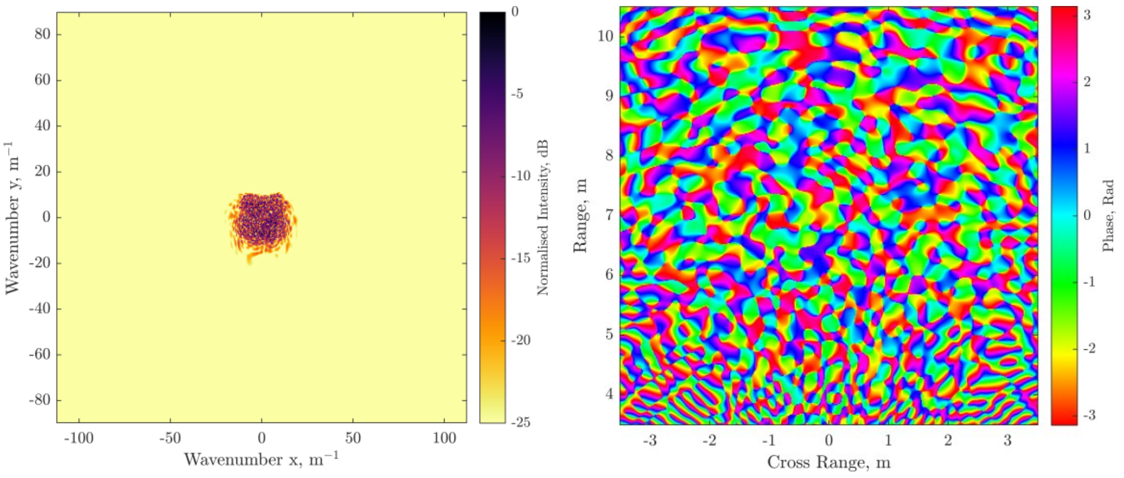

a) b)

Figure 7-6 – Spatial-frequency support (a) and corresponding image phase (b) after the image has undergone spatially variant basebanding. When compared to the original and conventionally basebanded datasets shown in Figure 7-2 the support is noticeably more compressed and the phase gradients are reduced, even at the edges of the image.

In summary, two forms of basebanding have been introduced. Both methods reduce the phase gradient of the SAR image. However, since the spatially variant form of basebanding does not require that the SAR image be exclusively far-field, it operates better when applied to near-field lab data.

7.3 Volumetric Upsampling.

To upsample a SAR image, be it two-dimensional or three-dimensional, the following procedure is performed: Firstly, a coarse SAR image is formed, secondly, this SAR image is basebanded and converted to the spatial-frequency domain via an inverse Fourier Transform[10]. The support is then symmetrically zero padded to a desired size. Finally, Fourier Transforming the padded spatial-frequency support results in a higher sampled image.

There are two hypotheses being tested here. Firstly, that this method is faster than standard Backprojection, and secondly, that spatially variant basebanding prior to the

---

[10] Matlab's implementation of the inverse Fast Fourier Transform algorithm includes a $\frac{1}{L}$ coefficient. By implementing an inverse transform first, the upsampled image will maintain the same energy content regardless of the desired sample rate.

upsampling reduces errors when compared to either no basebanding or conventional basebanding.

In this subsection, the proposed method for upsampling a volumetric image is introduced, following two example datasets:

1. A 21.5GHz to 50GHz measurement of a 20th scale T72 tank (Figure 7-7), using a 0.5m by 0.5m monostatic aperture.
2. A 1Ghz to 6GHz measurement of the concrete wall (Figure 7-12), using a 3.5m by 1.5m monostatic aperture.

The first example is used to establish the time benefits to the approach, whereas the second example is used in conjunction with the second hypothesis.

7.3.1 Tank Dataset

Although not an exact scale model, this miniature tank presents an interesting target consisting of multiple identifiable features. For example, the main gun is clearly visible in the SAR imagery.

In this measurement, a loaned PNA-X N5245B network analyser was used to generate an extreme wideband measurement covering 21.5GHz to 50GHz, for a total bandwidth of 28.5GHz. This gives a theoretical down range resolution of 5.3mm. At full scale, this would be equivalent to 10.6cm.

The tank was placed an approximate 50cm from the synthetic aperture. This gives, via equation 2-13, an approximate cross range resolution in both the horizontal and vertical planes of 4.2mm, scaling to 8.4cm. A photograph of the model tank is shown in Figure 7-7, wherein the tank is shown to be stacked on top of a polystyrene plinth. This was done to separate, in range, the target backscatter from any potential clutter and multipath effects.

Three metal ball bearings are used as pseudo-calibration targets. These balls show up cleanly in the SAR imagery and are used to estimate the true resolution of the measurement, via their 3dB width.

Figure 7-7 – The 20th scale T72 tank used to illustrate high frequency spatially variant basebanding. The tank is raised on a polystyrene plinth, this is in order to separate the backscatter from unwanted clutter and multipath signatures, and better centre the tank inside the aperture.

From the measurement data, a three-dimensional volumetric image of the tank is formed using standard Backprojection. This image is shown in Figure 7-8. Measuring the 3dB width of the spheres shown in the figure, the down range resolution is estimated at 1cm and the cross range and vertical resolution as 0.5cm and 1cm respectively.

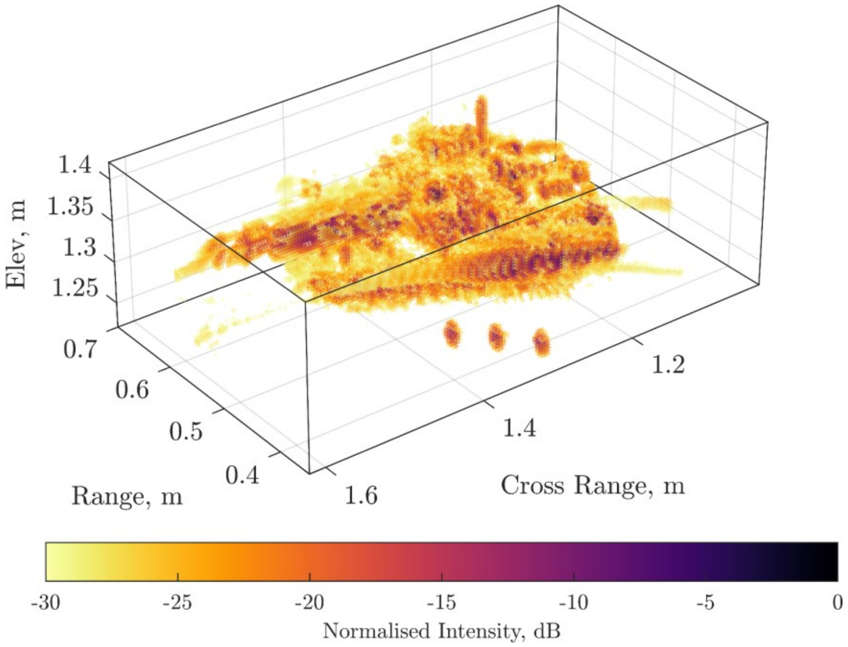

Figure 7-8 – Volumetric image of the miniature tank shown in Figure 7-7. Key features are the pronounced gun barrel, the antenna atop the tank, and the three spheres. From the 3dB width of the spheres, the resolution in range is estimated to be 1cm and the cross-range and vertical resolution as 0.5cm and 1cm respectively.

Key features of this image are the prominent scattering off the main gun, the small spheres, and the antenna mast visible at the top of the image. These will become useful points of comparison with the eventual upsampled image.

Plotting the spatial-frequency support for this image reveals that it is, in fact, under sampled. That is, there is wrapping occurring due to the unambiguous frequency extent being too small. However, this is not a fundamental limitation for this pixel size. As seen in Figure 7-9, spatially variant basebanding centres and compresses the spatial-frequency support, allowing for an unambiguous support.

There is the question of when it is decided that the initial pixel sampling is fine enough. Recall that each patch of the image has its own support associated with it. Each support is individually centred around the zeroth frequency. Therefore, the spatial-frequency extent of each support is independently defined by the frequency and azimuthal variation experienced by that section of image. In other words, to calculate the desired spatial-frequency extent (equation 7-1), one need look no further than the theoretical resolution of the patch.

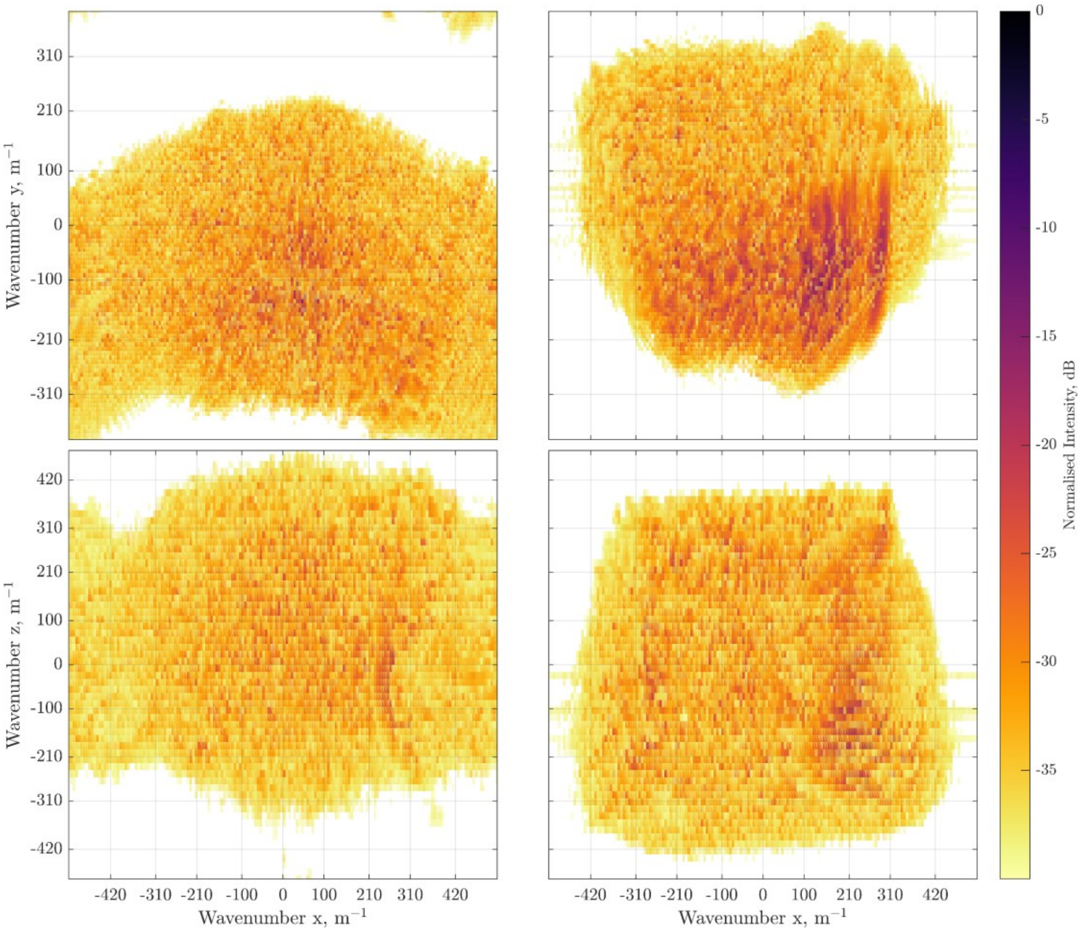

a) b)

Figure 7-9 - Comparison between the non-basebanded spatial-frequency support, column a) and the spatially variant basebanded support, column b). The basebanded support is noticeably more compact and better centred around the zeroth frequency.

Finally, the unambiguous spatial-frequency support is symmetrically zero-padded to any desired sample rate in the three spatial dimensions. Inversing the Fourier transform returns an accurately interpolated complex image of the specified sampling. From observation, this is more accurate than common image domain interpolation, such as linear and spline methods.

A good example is presented in Figure 7-10, wherein a coarsely sampled image is directly compared to an upsampled image of 64 times as many voxels. Effectively the two images took the same amount of time to form.

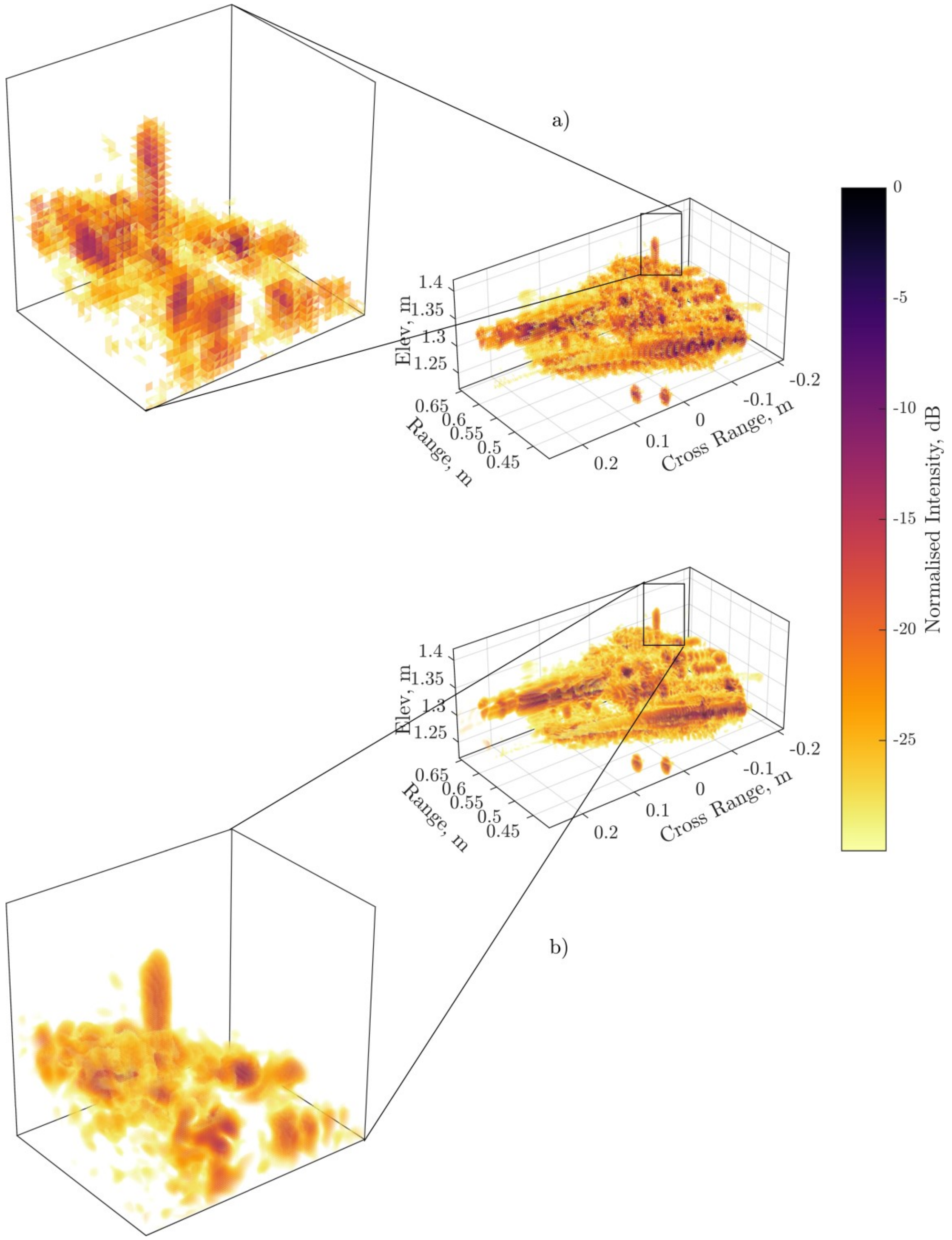

Figure 7-10 Comparison between a) the original coarse sampled tank and b) the upsampled version with four times as many voxels in each dimension, for a total of 64 times as many.

From equation 5-4, standard Backprojection loops over each voxel in the image P times. Therefore, the computational complexity of the function is $O(PN^3)$. The novel upsampling, with spatially variant basebanding, approach relies on a three-dimensional

Fast Fourier Transform of a coarse image followed by a second Fourier transform of the padded image support. The computational complexity of this approach is therefore $O(N^3\log(N)+\Xi^3N^3\log(\Xi N))$. Where Ξ is the upsampling factor. For small values of Ξ ($\Xi \ll$ N), the computational complexity is approximately $O\big(N^3\log(N)\,(1+\Xi^3)\big)$. Crucially, the performance of the upsampling method is independent of the number of pulses.

The actual under the hood implementations of Matlab functions are proprietary and encrypted, therefore a detailed theoretical evaluation of the performance is impossible. Thus, to evaluate the performance of the proposed approach, empirical evidence must be used.

The purpose of this upsampling is to reduce the computation time associated with forming volumetric SAR images. To this end, a direct comparison between standard Backprojection and this novel upsampling method has been carried out[11]. Figure 7-11 shows the time taken to form a $N\times N\times N$ image from 10201 pulses. As expected, the upsampling is significantly faster than forming a finely sampled image directly. In addition, the growth rates of the computation times differ. The standard Backprojection follows the well reported N^3 cubic curve, whereas the upsampled Backprojection follows a quadratic curve.

Best fit curves following $y=Ax^B+C$ have been included. For the standard Backprojection, the best fit given by $A=6.26\times10^{-9}$, $B=3.124$, and $C=0.046$. For upsampled Backprojection: $A=3.181\times10^{-7}$, $B=2.042$, and $C=0.066$.

---

[11] The tests were carried out using a parallelised Backprojection implementation written in Matlab. The used processors were two Intel Xeon Gold 12 core processors running without Hyperthreading.

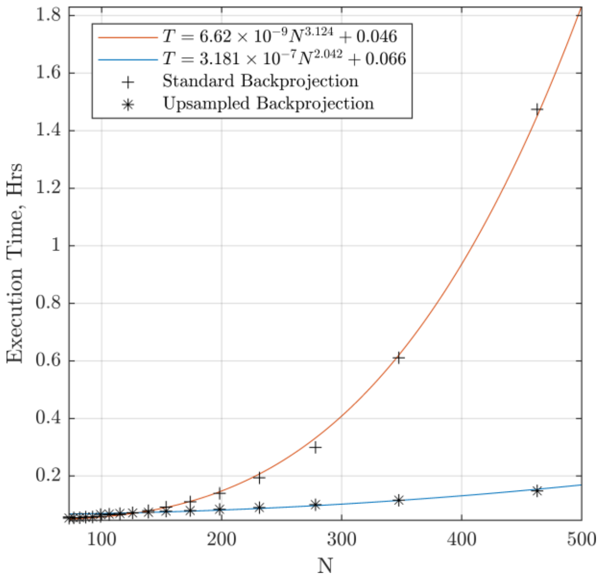

Figure 7-11 – Time taken to form a N by N by N 3D SAR image from 10201 pulses for standard backprojection and this novel upsampling method. Lines of best fit have been added, showing that standard Backprojection follows a cubic distribution, whereas the upsampling follows a square growth.

When $N \cong 10^2$ the execution times for both implementations are similar. This is because there is a minimum image size required for accurate upsampling. For this example, that prerequisite image size is in order of $N = 100$ in each dimension.

7.3.2 Through-Wall Dataset

The previous section focused primarily on establishing the upsampling method, and the time benefits gained from it. This subsection focuses primarily on where the basebanding and upsampling break down. It will be shown that introducing the approximate far field response of a wall reduces the effectiveness of the basebanding process, and that subsampling the original image introduces artefacting into any subsequent image.

First the wall in question is made of the same concrete material as the previous chapters, that being 1400 Cemex lightweight concrete aggregate. A similar scene, consisting of two metal barrels, a metal case, a desk, and monitor is also introduced, as shown in Figure 7-12 and Figure 7-13.

Figure 7-12 – Photograph of the scene behind the wall showing: two metal barrels, a metal case, a desk, computer tower, and monitor. The bicycle is only present in the monostatic measurements, and as such is not discussed.

Figure 7-13 – Side on view of the same scene, showing the proximity of each element to the wall. A metal sphere has been added in front of the wall to help calibrate different measurements.

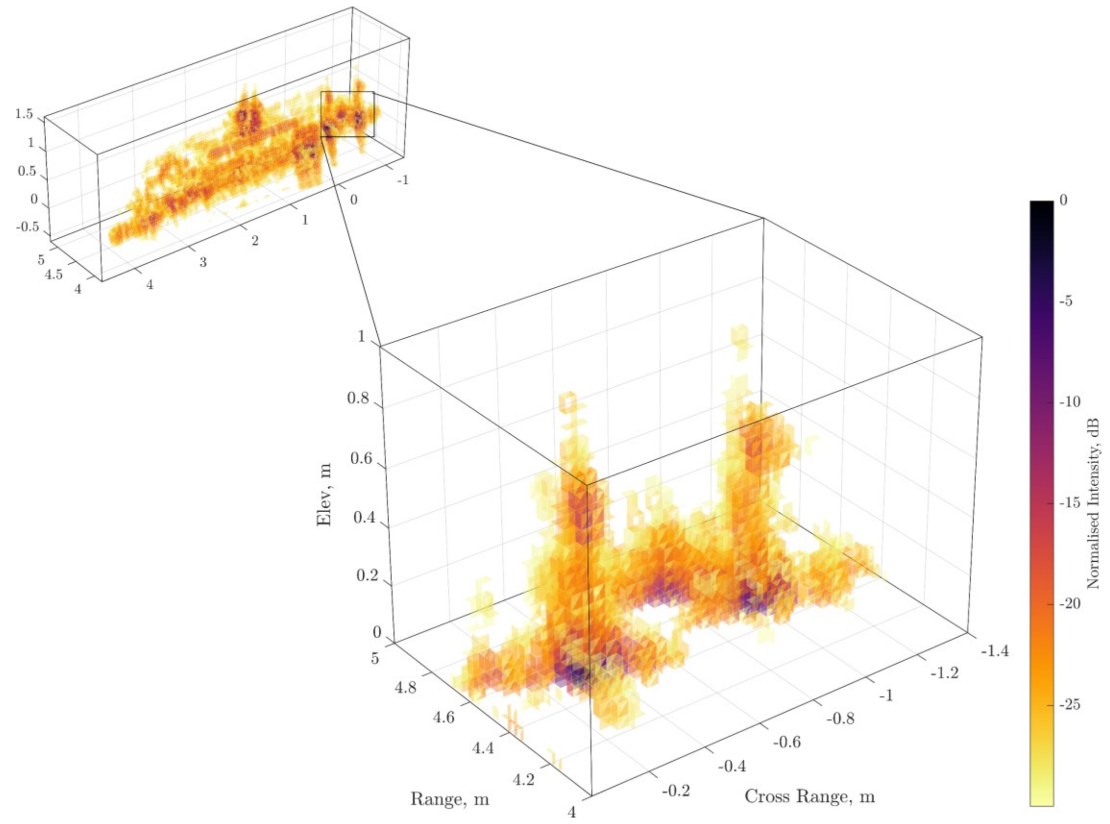

Figure 7-14 – Volumetric SAR image of the wall scene shown in Figure 7-12 and Figure 7-13. The wall signature has temporarily been removed via background subtraction. In this figure, the computer monitor and briefcase are both visible. However, the following visual analysis focuses primarily on the metal barrels, hence the isolated plot.

Figure 7-14 shows a volumetric rendering of the scene presented in Figure 7-12 and Figure 7-13. The two metal barrels are clearly visible, as is the computer monitor. The voxel spacing used in the image formation is enough to contain the entire frequency support without wrapping. However, as will become apparent, this is only once spatially variant basebanding has been applied.

Included in Figure 7-14 is a zoomed in plot of the two metal barrels. These have been chosen as useful reference targets due to the fact that they are easily identifiable, and somewhat separate from the other signatures. While the image fundamentally contains all the information, in accordance with the Nyquist-Shannon criterion, the coarse voxel sampling can lead to ambiguities with regards to the shape of individual targets. For example, it is difficult to differentiate between the target barrels and the multipath formed between them, without being able to rotate the volume.

This can be resolved by forming the image with a finer sampling rate, which is a lengthy process, or, as will be demonstrated, upsampling the coarse image.

Fourier transforming Figure 7-14 shows that without basebanding the dataset wraps around. If this occurs, then zero padding the dataset will result in multiple distinct supports. In Figure 7-15, this wrapping is clearly visible. This is due to the unambiguous spatial-frequency support not being sufficient to contain the non-basebanded data.

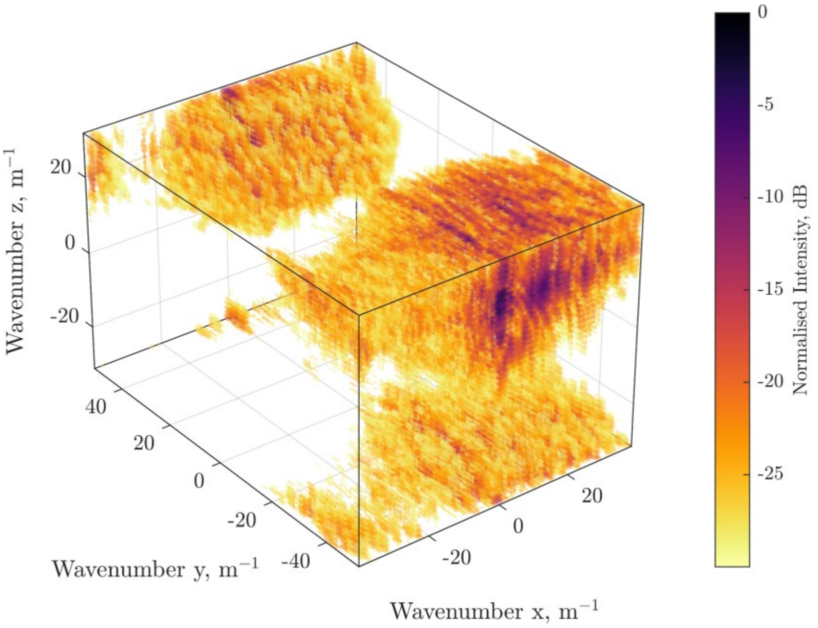

Figure 7-15 – Volumetric rendering of the spatial-frequency support associated with Figure 7-14. The unambiguous frequency extent is insufficient to contain the data without wrapping. The wrapped data does not appear continuous when zero padded.

The spatial-frequency support is not parallel to the Z plane. This is because the majority of the bright scatterers exist at a lower elevation than the antennas. This causes the majority of the received signal to originate below the antennas. This is better illustrated in two-dimensional projections of the spatial-frequency support, as shown in Figure 7-16.

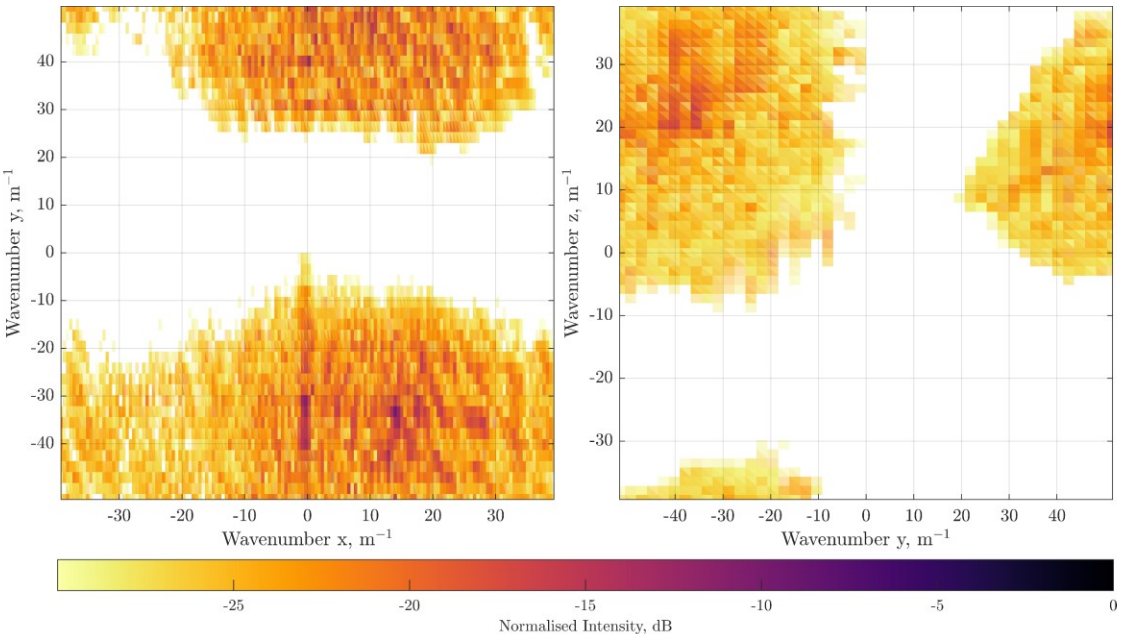

a) b)

Figure 7-16 - Top down (a) and side on (b) projections of the spatial-frequency support . The support can be seen to be wrapping around due to the frequency extent not being sufficiently large.

Symmetrically zero padding such a support results in significant artefacting. This is shown in Figure 7-17 where the same image has been upsampled by a factor of 4 in each dimension, resulting in 64 times as many voxels. While the number of voxels has increased, the actual image quality has degraded. This is because the Fourier Transform is circularly continuous. Without zero padding, the wrapped support would be evaluated as one continuous dataset. However, symmetrically zero padding the volume breaks this continuity. When the spatial-frequency support is converted back to the image domain, the disparate support patches each incoherently contribute towards the image. This is what gives rise to the artefacting shown in Figure 7-17 and why the spatial-frequency support for any image undergoing upsampling must be self-contained, at least within the dynamic range of the desired image.

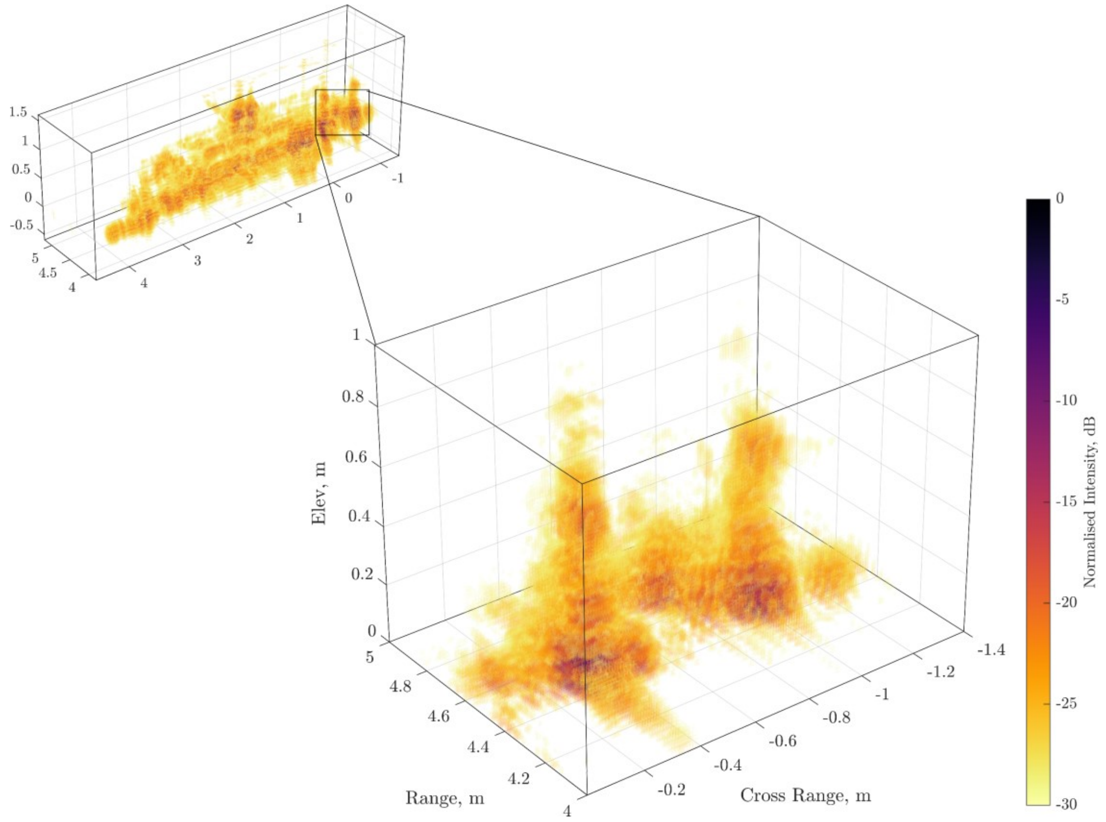

Figure 7-17 – The same two barrels as Figure 7-14. However, this image has been upsampled via symmetric zero padding by a factor of 4 in each dimension, for a total of 64 times as many voxels. While this results in a finer voxel sampling, naively padding a wrapped image results in significant artefacting.

When compared to an image formed using standard Backprojection, with the same voxel sampling, the deficiency in Figure 7-17 is visually obvious. An ideal image is shown in Figure 7-18. When compared to the image formed normally, the upsampled image is less focused and there is repetition of features.

To reduce the artefacting, the entire frequency support needs to be self-contained. To this end, it is necessary to baseband the image. To numerically evaluate the quality of the upsampled image, a direct comparison between it and a native image is necessary. The mean squared error (MSE) is a common metric. However, since in this case, the high intensity voxels are of primary interest and the lower intensity voxels would skew the MSE, a weighted implementation is used. For a native image formed using standard backprojection, I_n, and an upsampled image, I_u, the weighted MSE (WMSE) is:

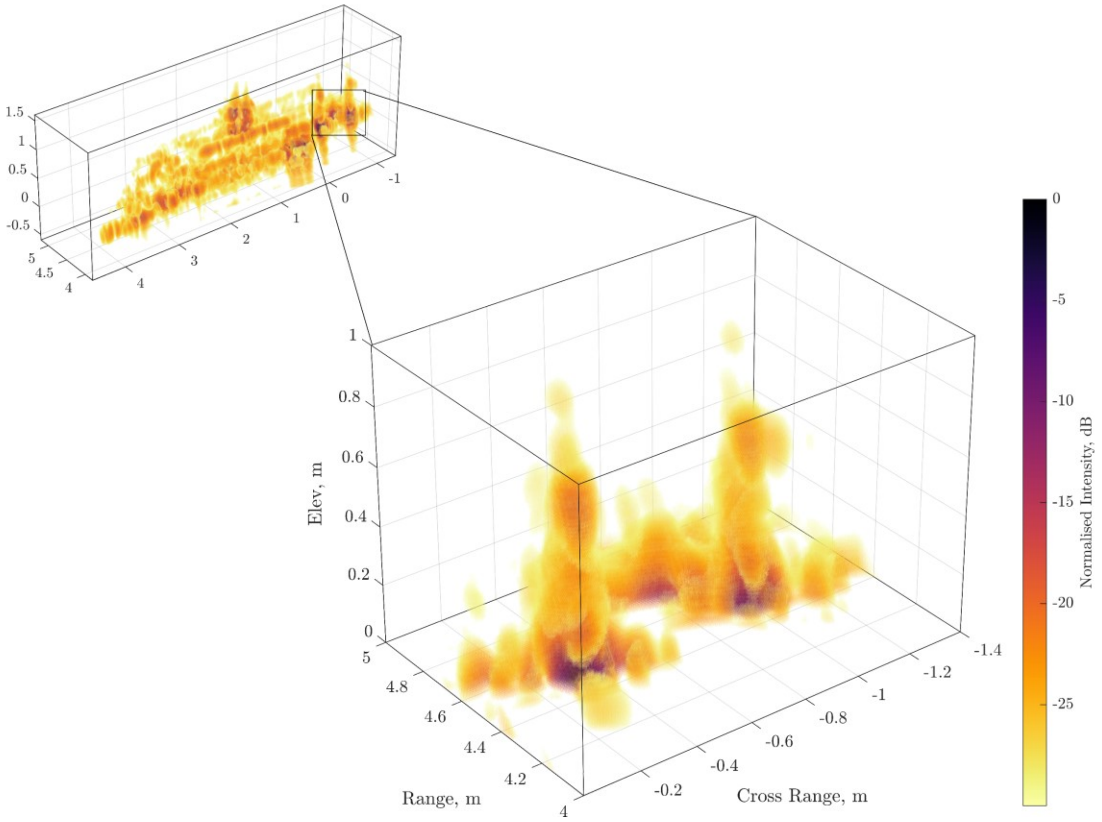

Figure 7-18 – Highly sampled image formed using standard Backprojection. Since this image is formed by explicitly calculating the intensity at each voxel, it is a gold standard by which to evaluate the upsampling process.

$$WMSE = \frac{\sum_{l=1}^{L} w_l \left(|I_{u_l}| - |I_{n_l}|\right)^2}{\sum_l^L w_l} \qquad \text{7-6}$$

$$w_l = \frac{|I_{n_l}| - \min(|I_n|)}{\max(|I_n|) - \min(|I_n|)} \qquad \text{7-7}$$

The weighting function w_l is normalised between 0 and 1, with the highest intensity voxel giving a weight of 1, and the lowest 0. In short, this makes the high intensity voxels contribute towards the WMSE more than the dimmer voxels.

For the non-basebanded case, the WMSE is $1.14 \times 10^{-4}\mathrm{Wm}^{-2}$. This is equivalent to a mean error of -39.4dB.

Figure 7-19 shows the volumetric spatial-frequency after it has undergone conventional basebanding. When compared to Figure 7-15, the support is noticeably more centralised around 0 frequency, thus reducing the phase ramps associated with the image. However, there is still some wrapping present, most notably in the x dimension. This leads to some artefacting still being present when the image is upsampled, albeit significantly reduced.

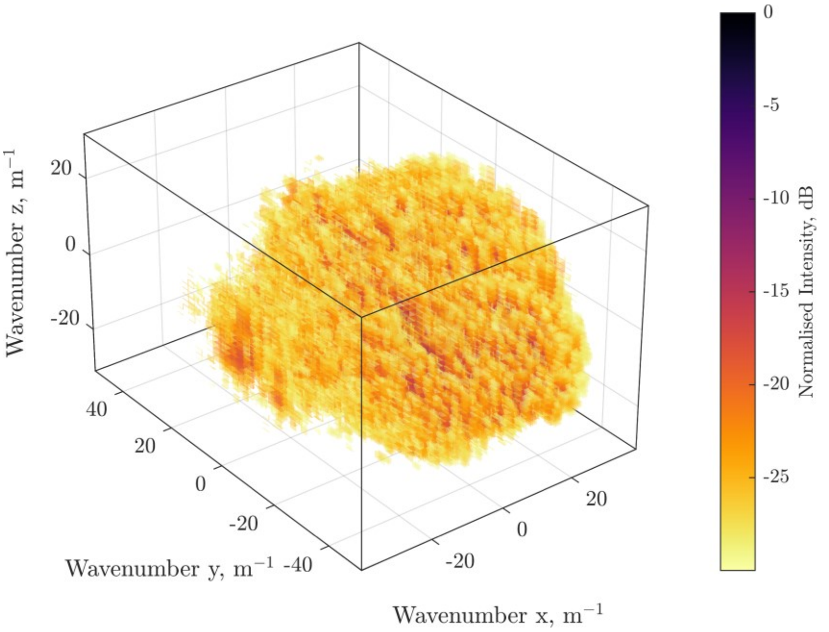

Figure 7-19 – The same support as Figure 7-15 after undergoing conventional basebanding. The support has shifted towards 0 frequency, thus reducing the phase ramps associated with the image and better centring the data. However, some wrapping is still present in the x dimension. This will, again, lead to artefacting, albeit reduced when compared to the non-basebanded case.

Figure 7-20 shows the same upsampled image, with the same two barrels as in Figure 7-17 after the image has undergone conventional basebanding. The image quality is significantly improved when compared to Figure 7-17. However, there is still some artefacting occurring due to the frequency support being suboptimal. When compared to the ideal image shown in Figure 7-18, the upsampled image shows repeating signatures in the cross-range dimension. As mentioned, this is because the spatial-frequency extent in the cross-range dimension is insufficient to contain the data without wrapping.

Using the WMSE metric, the basebanded image is shown to produce significantly less errors when upsampled. The WMSE for Figure 7-20 is $1.41 \times 10^{-5}\mathrm{Wm}^{-2}$ (-48.5dB). This is a substantial improvement over the non-basebanded case.

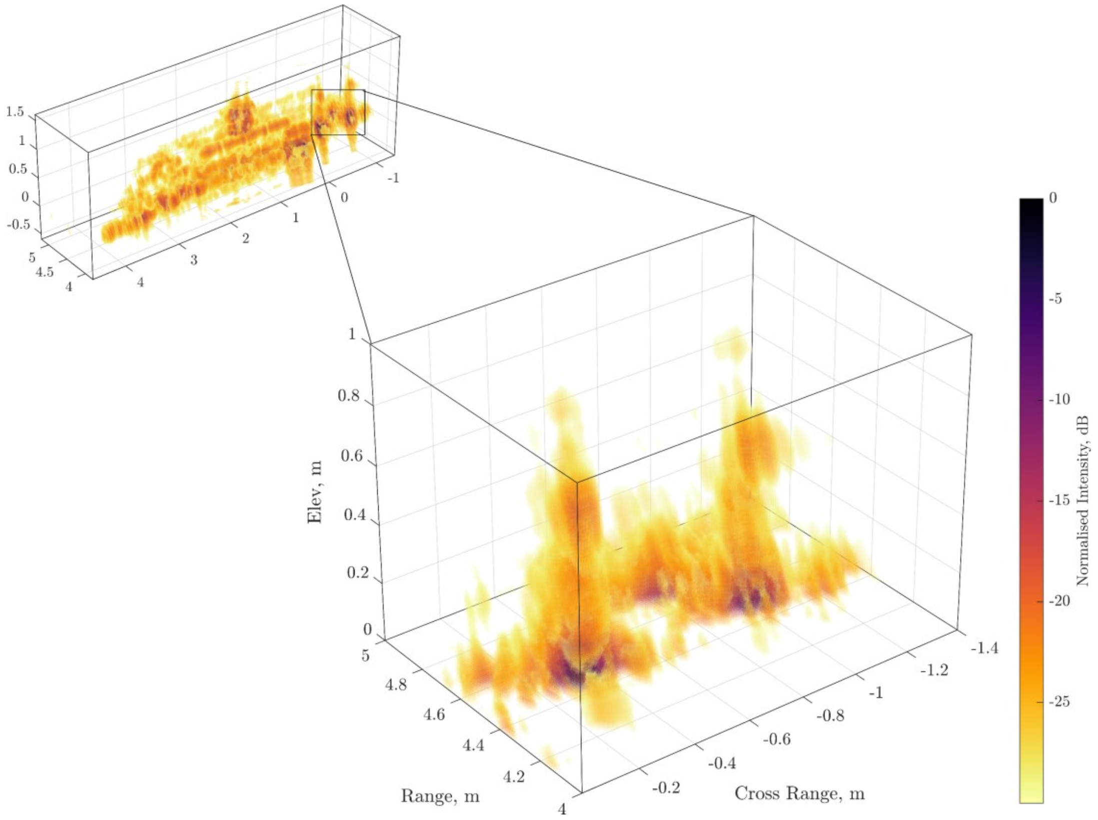

Figure 7-20 – Upsampled image after undergoing conventional basebanding. The artefacting is much reduced, leading to a better image. However, it is still not ideal.

As shown in Figure 7-6, the spatial-frequency support is compressed to a greater extent when using spatially variant basebanding. This is illustrated again in Figure 7-21, showing that volumetric spatial-frequency support is self-contained within the frequency range given by equation 7-1. This leads to a higher quality image when upsampled. Evaluating the WMSE for the spatially variant upsampling revels that the image quality is indeed better. For the spatially variant basebanded image, the WMSE is $1.14 \times 10^{-5}\ \mathrm{Wm}^{-2}$. This is equivalent to -49.4dB.

Naturally, one would produce a more accurate image when upsampling from a greater initial spatial-frequency coverage, i.e. reducing the ratio between coarse and upsampled images. However, there are diminishing returns. This is illustrated in Figure 7-23, whereby the WMSE is evaluated as a function of the spatial-frequency coverage.

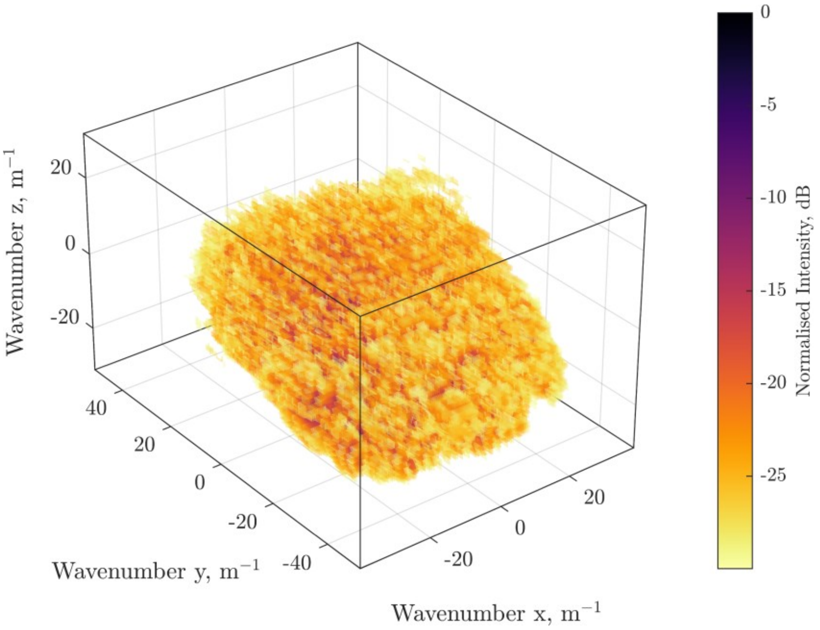

Figure 7-21 – Spatially variant basebanding spatial-frequency support for the SAR image shown in Figure 7-14. It is more compressed than either the original or conventionally basebanded images.

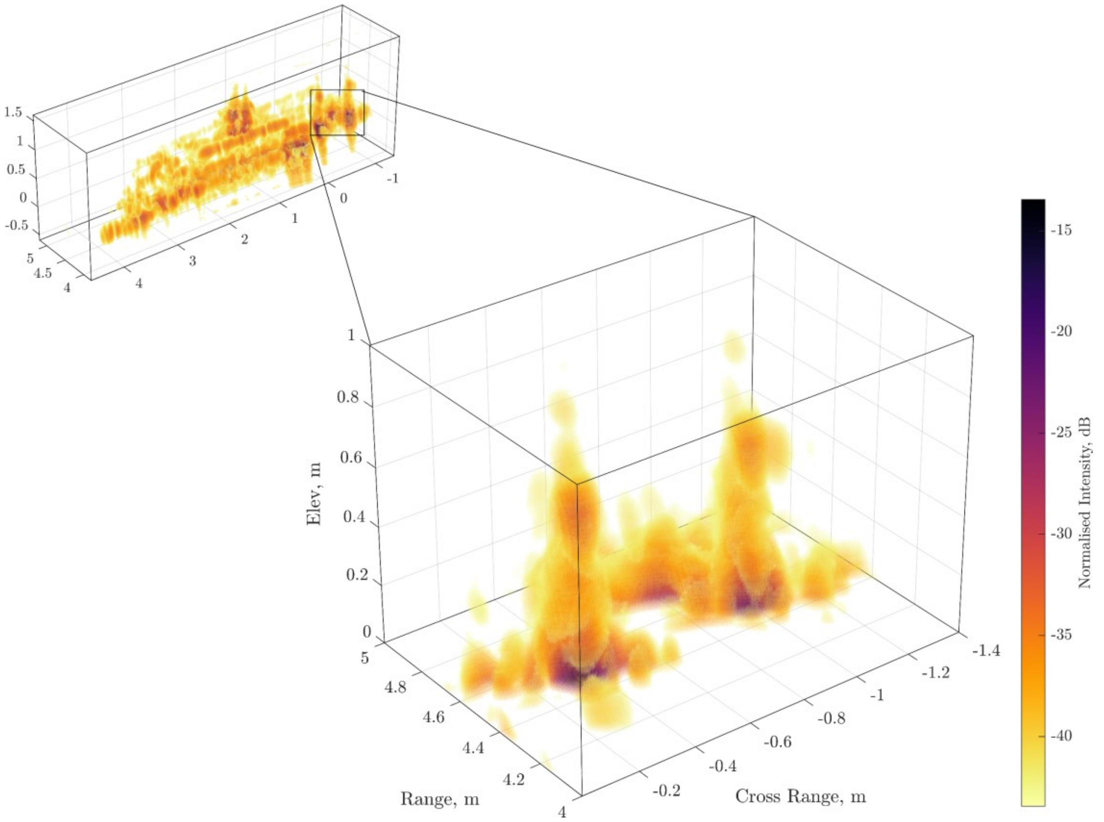

Figure 7-22 – Upsampled image after it has undergone spatially variant basebanding. The image quality is improved when compared to the other cases.

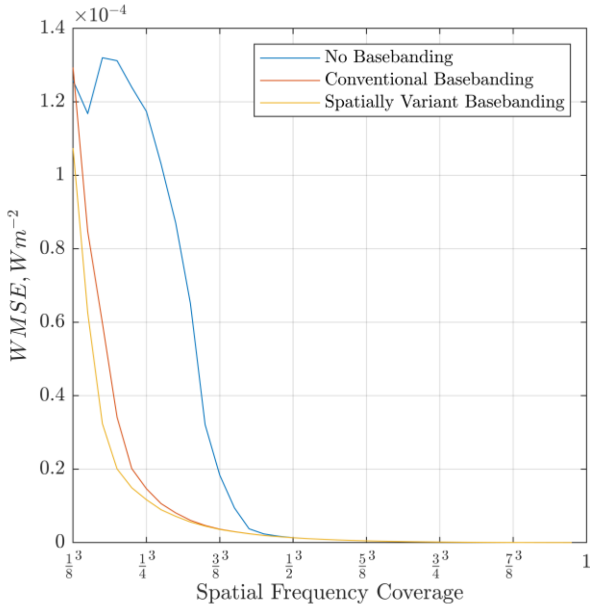

Figure 7-23 – WMSE expressed as a function of the ratio between initial and upsampled imagery. As one might expect, increasing the spatial-frequency coverage leads to a more accurate final image. However, this comes with increased computation time.

The uptick in the initial WMSE for the non-basebanded case is due to the initial sampling producing an unambiguous spatial-frequency that is smaller than the entire image support. As the unambiguous spatial-frequency extent increases, the non-basebanded dataset becomes discontinuous, leading to the artefacting observed in Figure 7-17. Since the basebanded cases are centred around the origin they at no point become discontinuous. For this reason, the same decrease in image quality is not observed.

The comparisons between non-basebanded, conventionally basebanded, and spatially variant basebanded upsampled images illustrate that to produce the highest quality image, with the smallest spatial-frequency extent; the original coarsely sampled dataset must first undergo spatially variant basebanding.

Therefore, the methodology for volumetric upsampling in the near-field is as follows: first generate a coarsely sampled image. Secondly, baseband this image using the spatially variant basebanding algorithm described. This basebanded time domain image is then converted into the frequency domain using a Fourier transform. The spatial-frequency support of the image can then be padded to an arbitrary length in each of the three spatial dimensions. Inverting the Fourier transform generates an image with a finer voxel sampling.

This process is illustrated in the flowchart shown in Figure 7-24.

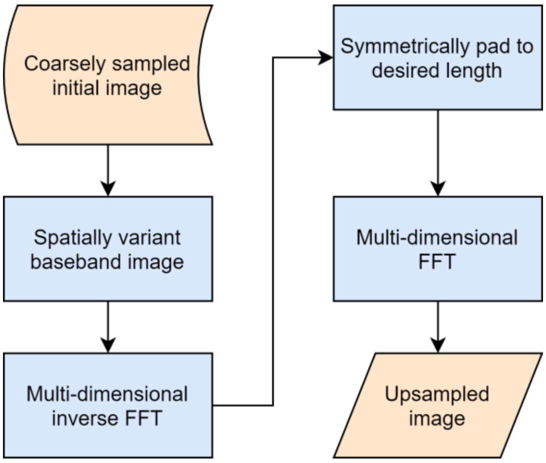

Figure 7-24 – Flowchart illustrating the proposed method for upsampling a volumetric (or 2D) image to an arbitrary sampling rate.

7.4 Through-Wall Considerations

The examples used thus far have not included a wall signature. This is because in monostatic SAR, a wall exhibits very little angular variation, since the point of reflection on the wall moves in lockstep with the antenna motion. In this way, it can be approximated as a SAR far field signature.

Figure 7-25 shows a volumetric monostatic SAR image of a single wall located 3.6m from the antenna. The strong reflection from the dihedral formed between the floor and wall shows up brighter than the direct spectral reflection from the face of the wall. The same is true for the edge boundary at the top of the wall. As such, there is some approachable vertical resolution.

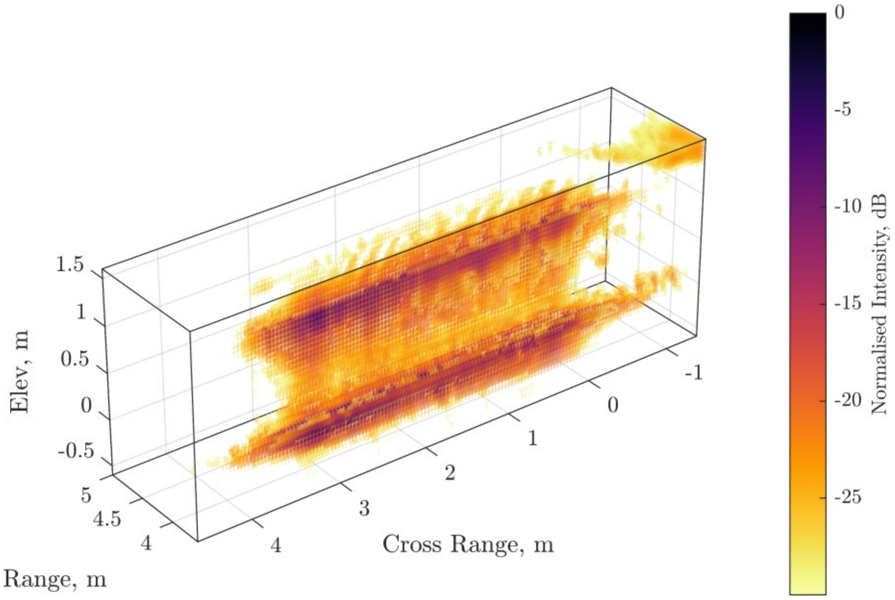

Figure 7-25 – Volumetric SAR image of a singular wall, located 3.6m from the antenna. The wall exhibits the RCS of a large flat plate. Consequently, it acts as a pseudo far field scatterer.

The spatial-frequency support for the wall illustrates that the wall exhibits very little horizontal angular variation. This is shown in Figure 7-26 in which the frequency support under the different forms of basebanding are directly compared.

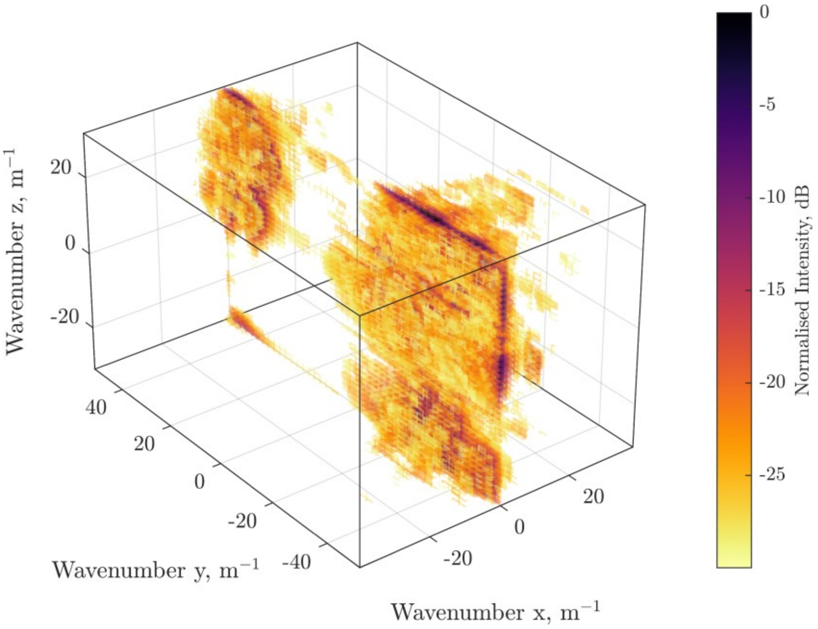

a)

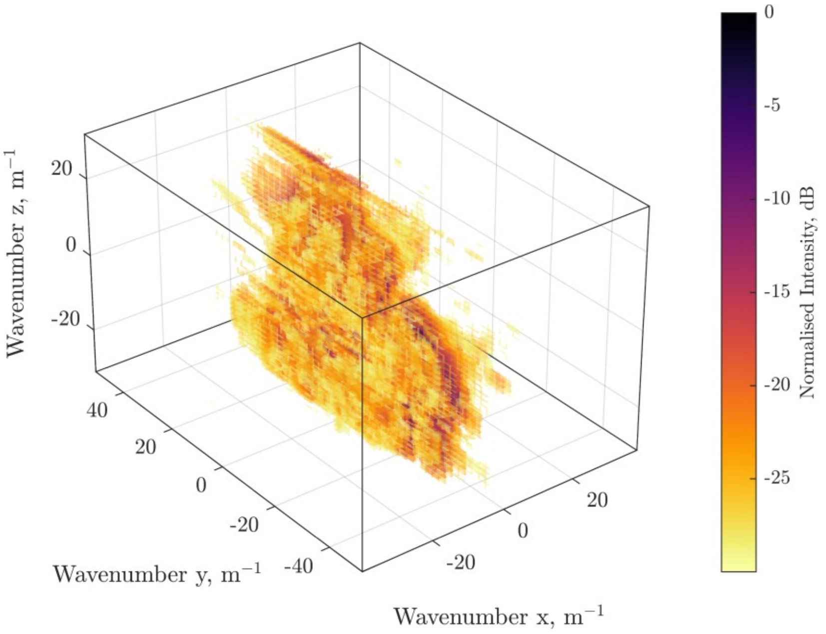

b)

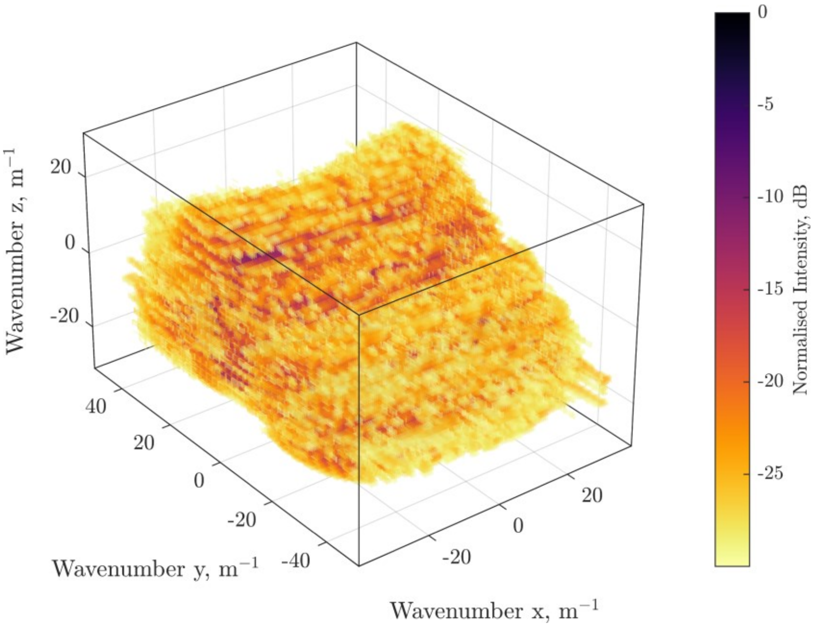

c)

Figure 7-26 – Comparison between the spatial-frequency support for the wall shown in Figure 7-25. Comparisons are given for: a) non-basebanded, b) conventionally basebanded, and c) spatially variant basebanding.

Figure 7-26 shows that while conventional basebanding operates as expected - shifting the entirety of the support whilst maintaining a similar shape - spatially variant basebanding leads to a distorting of the shape of the frequency support into something that is less optimal than the conventional basebanding. This is due to the wall signature being a far field signature and the basebanding phase screen treating it like a near-field signature. In essence, the spatially variant basebanding assumes that each area of the image has a different squint angle; however in the special case of a wall this is not true.

The basebanding procedure should be applicable over the entire image. As such, there is no solution to this problem without also developing a 'content aware' basebanding, one that is able to differentiate between targets and wall. Forming multiple sub-images, and basebanding each one would appear to be a way forward. However, to coherently combine each sub-image, the basebanding phase screen must be the same across each image.

An additional consideration, within the context of through-wall radar, is that applying the refraction corrections discussed in Chapter 5 compresses the wave-fronts inside the wall. This is because of the decreased speed of electromagnetic wave propagation. This wave-front compression leads to a finer range resolution within a wall-corrected image for any target inside the wall material, regardless of the actual nature of the scatterer.

As one might expect, an improvement in resolution implies a greater support in the frequency domain. However, it is important to note that the physical frequency of the radar transmission does not change; rather this is a scene dependant phenomenon.

For the case of the wall illustrated in Figure 7-25 this improvement in resolution manifests as a larger spatial-frequency extent in the f_y dimension. This is due to the wall being aligned perpendicularly. There is also a greater extent in the f_z dimension. That said, this is a small difference in comparison. This improvement in resolution and the corresponding growth of the support is illustrated in Figure 7-27.

To contain all the information, without wrapping, and thus enable the upsampling regime to operate, the down range frequency extent needs to be increased by a factor n. A plausible solution to this issue would be to make the basebanding refractive index dependent. In short, the speed of light in equation 7-3 would be modulated by the refractive index. However, this is by no means a major issue, as even doubling or tripling the sample rate along a single dimension is insignificant when greatly upsampling. As such, modulating the phase ramp is left as future work.

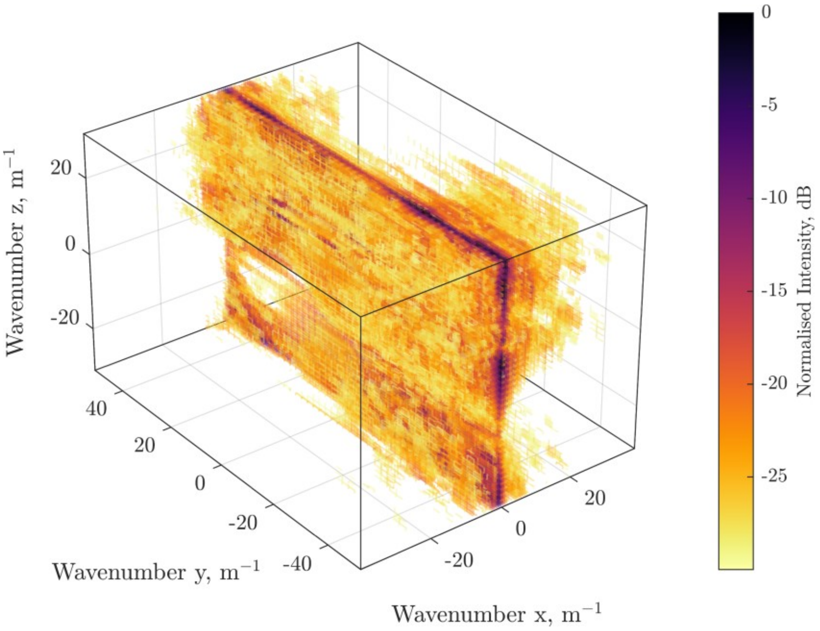

Figure 7-27 – Spatial-frequency support for the wall shown in Figure 7-25 after it has undergone the refraction compensation detailed previously.

In summary, for near-field imagery, spatially variant basebanding produces a more compact spatial-frequency support by applying a more robust phase screen to the image. This simultaneously reduces the phase gradient across the image, but also reduces the image sample rate required to unambiguously contain the entire image support. When upsampled, this produces a more accurate image. However, applying a near-field phase screen to a far field response distorts the spatial-frequency support. It should be noted that as the entire scenario becomes more far-field, the spatially variant baseband approximates conventional basebanding. Therefore, spatially variant basebanding is applicable in a far-field regime, just not in this case, where there is a far-field signature in a near-field regime.

7.5 Discussion

In this chapter, a novel near-field method of upsampling a three dimensional coarsely sampled image to a finer sample rate has been developed and tested. This approach differs from more conventional forms of upsampling, such as linear or cubic interpolation, by leveraging the properties of the Fourier transform to both rapidly and accurately interpolate SAR images. As one would expect, this is significantly faster than forming a finely sampled image normally [196].

Regarding image quality, previous implementations [191,192] have suggested that a suitable window function be applied to the image support post image formation. In this chapter, it has been shown that such a window is unnecessary. Accurate image upsampling is possible by ensuring that there is no wrapping in the image spatial-frequency support. To achieve this, with as little work as possible, a novel spatially variant basebanding procedure is introduced.

These claims have been proven using experimental data. Specifically, a 1/20th scale T72 tank [196], and a through-wall dataset, both gathered using angular variation in both the horizontal and vertical planes, thus allowing for volumetric imagery. This three dimensional aspect differentiates this block of work from its peers, which have focused primarily on two dimensional imagery [190–192] without the implementation of the near-field spatially variant basebanding..

The only complication to the spatially variant basebanding is that it breaks down when applied to far-field scattering behaviour in what would otherwise be a near-field image. In monostatic TWR, the point of specular reflection migrates across the face of the wall in lockstep with the antenna motion. This produces a response that has extremely coarse cross range resolution and is in effect a far field signal. This is not a use case explored in the prior literature, which has either worked with conventional basebanding, or with speckle [193–195]. Future works should aim to resolve this issue. However, this would require some mechanism by which to separate the wall signature entirely from other scatterers.

8 Conclusions

This chapter is laid out as follows: Firstly, a summary of the key points of the thesis is provided. Secondly, both technical and practical limitations to the parameter extraction process are given. This is followed by a recommendation for potential improvements and a discussion on the consequential effects on image quality. Finally, the thesis concludes by placing the thesis in the context of prior literature and giving recommendations for future work.

8.1 Summary

The thesis deals primarily with Through-Wall radar, a growing sub-field within the broader radar community. The primary issue facing TWR is electromagnetic refraction which causes a delay in the EM wave and an incorrect measurement of the distance to any obscured targets. The degree of this delay is dependent upon both the refractive index and the thickness of the wall in question, thus the question that this thesis aims to answer is this:

How does one safely and accurately determine the properties of an unknown, and in many cases unapproachable, wall whilst simultaneously obtaining usable SAR data?

With this question in mind, the thesis aims to develop a generalised methodology for remotely extracting the properties of an unknown obscuring wall, test this methodology in the presence of clutter and extend it to three-dimensions. Finally, the thesis aims to use the extracted parameters to compensate any subsequent SAR imagery.

With this in mind, the thesis has found that:

- **An asymmetric bistatic SAR geometry accurately extracts the refractive index and thickness of a wall. This is extendable to cluttered environments, and non-parallel wall trajectories without loss of accuracy.**
  Remotely extracting the refractive index and thickness from a wall is of interest to the TWR community, and to the wider EM communities. Conventional wisdom is to leverage convenient scatterers in the environment or use a symmetric bistatic configuration. By breaking this symmetry, the wall parameters can be accurately extracted while still maintaining appreciable cross range resolution. It has been found that for both non-cluttered and cluttered environments the extraction

process laid out in Chapter 4 and expanded upon in Chapter 6 accurately extracts both the refractive index and thickness of a concrete wall at a standoff distance much greater than the prior literature [99,100,128–131]. It has also been found that the proposed approach is very sensitive to small errors in the assumed antenna positions with respect to the wall.

- **Applying a compensation for refraction in the SAR imagery does not necessarily result in better image focusing.**
  It has been shown that the best image focusing, defined as the smallest kurtosis [117,120], does not necessarily align with the correct values for thickness and refractive index when the refraction compensation has been applied. This is because, when there are multiple signatures in the image, their individual PSFs can interfere, leading to a much more complex scenario. In addition, if the targets are too close to the wall, they can become conflated with the assumed wall position, thus the PSFs become compressed and the kurtosis is skewed towards greater assumed parameters. Ultimately, this means that a focusing metric should not be used when attempting to obtain the wall properties in a cluttered environment.
- **Volumetric multistatic image formation benefits from applied refraction compensation.**
  While image focusing may not improve, that is not to say that the image positional accuracy also does not. Rather, correct knowledge of the material properties is a necessity for multistatic image formation in order to obtain highly focused imagery. Previous implementations use topographic representations that can lead to misleading images when compensated. Extension to fully volumetric imaging shows that there is a significant improvement in image focusing independent of the focal plane.
- **SAR image formation, and in particular volumetric image formation, can be significantly accelerated via a spatially variant basebanding followed by zero padding.**
  The idea of zero-padding as a form of rapid interpolation is used frequently in range profile formation. It is rarely used directly on SAR images. Simply zero padding an image will result in artefacts unless the image spatial frequency

support is self-contained. To reduce the initial sample rate required to contain the support, a form of basebanding should first be applied to the image.

- **Spatially variant basebanding is sub-optimal when applied to a TWR scenario where there is a visible wall signature in the image.**
  Spatially variant basebanding is effective at both centring and compressing the image support. That is not to say it is ideal for every scenario. In a TWR the frequency extent of the image spatial frequency support appears to increase when spatially variant basebanding is applied to a wall. This is because a wall is essentially a far-field signature, i.e. there is little angular variation. Applying a near-field phase screen to a far-field signature results in an increase in the image spatial frequency extent.

8.2 Invasive Methods

Chapter 3 details three methods by which the permittivity, and by extension the refractive index, of a sample of concrete material was obtained. This was in order to provide an independent validation measurement for the bistatic parameter extraction detailed in Chapters 4 and 6.

The first approach is an analysis of the characteristic cut-off frequencies of a slab dielectric waveguide. From prior knowledge of the sample dimensions, the permittivity of the material is extracted. This is then converted into the material's refractive index. The approach found that the refractive index for a slab of concrete was 2.43 ± 13.5%. It is important to note that, while the uncertainty is significant, it does not invalidate the measurement. That said, since the approach relies on a distinct cutoff frequency, adding moisture makes extracting precise measurements of the material properties difficult.

In the pursuit of finer precision, the well-established Nicolson-Ross-Weir method [69,70,79–84,86]. was also employed. This involves rewriting the reflected and transmitted signals in terms of the material properties and the cutoff frequencies of the dielectric. It was decided that a larger sample of material would be more representative of the concrete batch. Unfortunately, due to a practical requirement for a strong transmitted signal, the NRW approach did not produce sensible, or indeed, physically plausible results for the material conductivity. That said, the measurement for the refractive index was in agreement with the previous method; between 2 and $\sqrt{6}$.

Finally, a series of single pulse radar measurements were taken of a trihedral. By comparing the measured range for non-obscured and obscured measurements, the refractive index for the concrete was calculated as $2.26 \pm 5.50\%$. This is the most precise of the three methods. What's more, by comparing the peak intensity of the trihedral in both measurements, the conductivity of the material was extracted. The conductivity was in agreement with the literature; increasing with frequency.

All three methods are in agreement, although the trihedral based approach provides the most precise measurement of the concrete refractive index. For concrete, it is recommended that as large a sample as possible be used. For this reason, future implementations of the NRW technique with respect to concrete should use as large a transmitting power as possible or limit themselves to a narrow low frequency bandwidth.

8.3 Bistatic Parameter Extraction

Chapters 4 and 6 discuss an asymmetric model for extracting the refractive index and thickness from a wall using bistatic synthetic aperture radar. This was achieved via a ray tracing approach which, given a specific radar geometry, will match the measured data to an estimated pair of parameters.

The approach is demonstrated using three laboratory measurements, a measurement with the SAR trajectory parallel to the wall, a measurement with the trajectory at a slight angle, and finally, one with the addition of clutter. All three measurements are in strong agreement with each other; thus, the asymmetric approach demonstrates strong clutter rejection properties and a versatility with regards to measurement geometry.

Analysis of the sensitivity of the estimation to incorrect assumptions concerning the position of the antennas has found that the method is imprecise ($\Delta n = 14\%, \Delta\delta = 10\%$). Having said that, the extracted parameters agree with those obtained via the invasive methods discussed in Chapter 3, thus one must conclude that the parameter extraction methodology fundamentally works and reject the null hypothesis.

In pursuit of finer measurement precision, a method for refining the antenna ground-truth positions with respect to the wall was developed. The method works by a nonlinear least squares optimisation between the measured and theoretical range to the front face of the wall. This is then used to refine the antenna coordinates. Conceptually, this is similar to Prominent Point Processing albeit working from range profile data rather than an image.

It should also be noted that these results were obtained without the need for any super-resolution algorithm. It has therefore been shown that the super-resolution typically employed by various bistatic methods [99,100,128–131] is unnecessary.

8.4 Effects on TWR Image Quality

In Chapter 5 a ray tracing method for compensating TWR SAR imagery for refraction is introduced. This works via the same general principle as the ray tracer developed in Chapter 4. By writing the cross-range displacement between antenna and pixel in terms of a sum of all the individual layers, an iterative approach to a generalised multi-layer ray tracer was developed. This obtains the refracted path length between an antenna and a pixel. By using the refracted path in the Backprojection algorithm, a refraction compensated image is obtained. This has two benefits over the more common approach of calculating the wall transmission function: first, it is easily generalisable to multiple layers and antenna configurations, secondly, it is a mathematically simpler approach.

It has been shown, via simulation, that for a single point target compensating the image using the correct wall properties produces the best focused image. This is in agreement with the literature. That said, it has also been shown that when there are multiple targets in close proximity to the wall, that this is no longer true. This is due to two factors, the interaction between the targets PSFs, and the fact that any scatterer assumed to be part of the wall structure is compressed by the refraction compensation. This leads to a bias towards larger assumed wall parameters if one were to use the image quality as a metric for evaluating the wall properties. Consequently, to obtain the wall properties from a SAR image, one should already have a good estimation of what the refractive index and thickness should be. This is so that targets are not subsumed into the wall structure. In addition, one should endeavour to isolate an individual signature on which to evaluate the image quality.

This improvement in focusing, while numerically supported, is not immediately obvious when looking at the laboratory SAR imagery. This is true for monostatic, bistatic, and multistatic imagery. The main point of the refraction compensation is to correct the positioning of the signatures within the image. An improvement in image quality is a by-product of this and should not be thought of as the main benefit.

8.5 Spatially Variant Basebanding and Upsampling

A novel method of upsampling planar and volumetric SAR imagery has been introduced and discussed in Chapter 7. The process has shown great promise as a method to significantly reduce the computation time associated with forming highly sampled SAR imagery.

The benefits to a reduced computation time are readily apparent, and methods for faster Backprojection do exist, be it via algorithmic changes [180–183] or effective parallelisation [174,185–189]. The upsampling method discussed in Chapter 7 does not place limitations on the nature of the SAR collection, such as a requirement that the measurement be far-field, and there is no reason why it cannot be combined with effective parallelisation to further accelerate the process.

The upsampling process has been shown to incur a minor reduction in image quality when compared to an image formed using standard Backprojection. This is not immediately apparent when applying the spatially variant basebanding but becomes more apparent when the basebanding is either not applied or conventional basebanding is used. For this reason, spatially variant basebanding should be applied to any image before it is upsampled.

With regards to Through-Wall imagery, it has been noted that signatures that exhibit very little angular diversity, such as a wall, cause an overzealous shift in the spatial-frequency support of the image when spatially variant basebanding is applied. This is an interesting phenomenon and has yet to be addressed. It would provide an interesting problem for future work.

8.6 Place in the literature

This thesis fills out omissions in the literature concerning generalisations to bistatic wall parameter extractions, allowing for a more versatile technique capable of gathering SAR imagery with approachable cross-range resolution. Thus, the thesis has fused what can reasonably be thought of as a 'wall-only' technique with the actual business of Through-Wall surveillance. In keeping with that theme, clutter is something that has previously been avoided. By adding clutter, the thesis helps to bridge a gap between laboratory and real-world measurements.

Throughout this body of work gathered results, both experimental and simulation, have broadly agreed with the literature. The refractive index of the concrete was shown to be within the range commonly attributed to concrete. That said, there is commonly a lack of clarity as to how precise the material properties are known. As an example, Fereidoony *et al* [131] do not provide uncertainty estimations for either their extracted parameters, or their supposedly correct comparison measurement. Endeavouring to remain transparent as to where numbers are coming from, and how precisely they are known, has constituted a significant portion of this work. Unfortunately, how precisely positioned the antennas are is rarely addressed. The sensitivity analysis performed in Chapter 4.6 therefore places some doubt as to the precision of previously reported experiments.

8.7 Future Work

Recommendations for future work have been made periodically throughout the thesis. A list of recommendations in no particular order is as follows:

- **Evolving the spatially variant basebanding operation.**
  Currently, spatially variant basebanding operates without any knowledge of the content of the scene beyond pixel coordinates and an image centre. Modifying the basebanding such that it can cope with changes in refractive index and different scattering phenomena would both make the basebanding more effective and reduce the sampling rate required to avoid wrapping in the spatial-frequency domain. Particular points of investigation would include how to appropriately calculate the bistatic vector going to each pixel and how to deal with points of reflection migrating throughout the SAR collection

- **Investigating more varied bistatic and multistatic geometries.**

  It has been remarked multiple times that SAR images do not show visible defocusing when outside of simulation. Part of the reason for this is a lack of angular separation between antennas. A greater variation in bistatic angle would result in greater defocusing. This would also be true for multistatic images. Since the bistatic parameter extraction discussed in Chapter 4 is applicable to a diverse bistatic geometry, applying it to a wider range of geometries would be of significant interest, both from a usability perspective and in the pursuit of finer measurement precision.

- **Including a MIMO measurement system as part of the parameter extraction.**

  Due to practical limitations, a truly generalised bistatic measurement was never taken. In all the bistatic measurements taken, one antenna was always at a fixed location. Two or more independently moving antennas would allow the investigation of a fully generalised Through-Wall scenario. An imagined use case is a swarm of remotely controlled drones, however for the precise extraction of any wall properties, the drones must include a very good navigation and positioning system.

- **Investigate piecewise parameter extraction from multi-layered walls.**

  It was left out of this thesis due to practical limitations with regards to construction, but a multi-layer wall parameter estimation procedure has been developed and discussed in Chapter 0. Due to the sensitivity of the extraction to positional errors, and in particular the assumed angle of the SAR system with respect to the wall, precise estimations of the refractive index and thickness for more than one layer would prove challenging. That said, if a method by which the angles of each layer could be established with respect to each other was developed, reasonable precision may yet be attainable.

9 References

1. Wiley CA. 3196436: Pulsed Doppler Radar Methods And Apparatus. USA; 1965.

2. Cumming IG., Wong FH. Digital Processing of Synthetic Aperture Radar Data: Algorithms and Implementation. Norwood, MA, USA: Artech House Inc; 2005.

3. Osgood B. Lecture Notes for EE 261 - The Fourier Transform and its Applications. Stanford, CA, USA; 2007.

4. Bracewell RN. The Fourier Transform And Its Applications. 3rd edn. McGraw-Hill; 2000.

5. Carrara WG., Goodman RS., Majewski RM. Spotlight Synthetic Aperture Radar - Signal Processing Algorithms. Boston, MA, USA: Artech House Inc; 1995.

6. Sullivan R. Synthetic Aperture Radar. In: Skolnik MI (ed.) Radar Handbook. 3rd edn. McGraw-Hill; 2008.

7. Jakowatz, Charles V J., Wahl DE., Eiche PH., Ghiglia DC., Thompson PA. Spotlight-Mode Synthetic Aperture Radar: A Signal Processing Approach. New York, NY: Springer; 1996.

8. Abedi H., Zakeri B. Through-the-Multilayered Wall Imaging Using Passive Synthetic Aperture Radar. IEEE Transactions on Geoscience and Remote Sensing. IEEE; 2019; 57(7): 4181–4191.

9. Feynman R., Leighton R., Sands M. The Feynmann Lectures on Physics, Volume 1. New Millen. Basic Boos; 2010.

10. Zhao W., Forte E., Pipan M., Tian G. Ground Penetrating Radar (GPR) attribute analysis for archaeological prospection. Journal of Applied Geophysics. Elsevier B.V.; 2013; 97: 107–117.

11. Paz C., Alcalá FJ., Carvalho JM., Ribeiro L. Science of the Total Environment Current uses of ground penetrating radar in groundwater-dependent ecosystems research. Science of the Total Environment. Elsevier B.V.; 2017; 595: 868–885.

12. Lombardi F., Griffiths HD., Balleri A. Landmine internal structure detection from

ground penetrating radar images. 2018 IEEE Radar Conference, RadarConf 2018. Oklahoma City, OK, USA: IEEE; 2018. pp. 1201–1206.

13. González-huici MA., Catapano I., Soldovieri F. A Comparative Study of GPR Reconstruction Approaches for Landmine Detection. IEEE Journal of Selected Topics in Applied Earth Observations and Remote Sensing. IEEE; 2014; 7(12): 4869–4878.

14. Pieraccini M., Miccinesi L. Ground-based radar interferometry: A bibliographic review. Remote Sensing. 2019; 11(9).

15. Yiğit E. Compressed sensing for millimeter-wave ground based SAR/ISAR imaging. Journal of Infrared, Millimeter, and Terahertz Waves. 2014; 35(11): 932–948.

16. Hu R., Min R., Pi Y. A Video-SAR imaging technique for aspect-dependent scattering in wide angle. IEEE Sensors Journal. IEEE; 2017; 17(12): 3677–3688.

17. Fortuny J. Efficient Algorithms for Three-Dimensional Near-Field Synthetic Aperture Radar Imaging. Electrical Engineering. University of Karslruhe, Germany; 2001.

18. Doerry AW. Basics of Polar-Format Algorithm for Processing Synthetic Aperture Radar Images. Sandia National Laboratories report SAND2012-3369. 2012.

19. Goh AS. Bistatic Synthetic Aperture Radar Data Processing and Analysis. University of Adelaide; 2012.

20. Doerry A. Basics of Polar-Format Algorithm for Processing Synthetic Aperture Radar Images. Sandia National Laboratories report SAND2012-3369. 2012.

21. Dogaru T., Le C. Synthetic Aperture Radar Techniques for Through-the-Wall Imaging. In: Amin MG (ed.) Through-The-Wall Radar Imaging. Boca Raton, Fl, USA, Fl, USA: CRC Press; 2011. pp. 307–343.

22. Chen VC., Smith GE., Woodbridge K., Baker CJ. Radar Micro-Doppler Signatures for Characterization of Human Motion. In: Amin MG (ed.) Through-The-Wall Radar Imaging. 1st edn. Boca Raton, Fl, USA, Fl, USA; 2011.

23. Griffiths HD. New directions in bistatic radar. 2008 IEEE Radar Conference, RADAR 2008. Rome, Italy, Italy; 2008. pp. 1–6.

24. Pieraccini M., Miccinesi L. Bistatic ground-based synthetic aperture radar. EUSAR 2018; 12th European Conference on Synthetic Aperture Radar. Aachen, Germany: VDE; 2018. pp. 275–279.

25. Rossum WL Van., De Wit JJM. Forward scatter radar for remote intelligence of building interiors. Electronic Letters. 2017; 53(15): 995–997.

26. Cho B., Kong Y., Park H., Kim Y. Automobile-Based SAR / InSAR System for Ground Experiments. IEEE Geoscience and Remote Sensing Letters. 2006; 3(3): 401–405.

27. Sévigny P. Through-Wall Synthetic Aperture Radar (TWSAR): Overview of Canadian R&D. 2017. Available at: https://www.sto.nato.int/publications/pages/results.aspx?k=STO-MP-SET-247&s=Search All STO Reports&r=stopublicationtype%3D%22Meeting Proceedings Paper%22 (Accessed: 3 April 2020)

28. Sévigny P., Fournier J. Automated stationary human target detector for 3D through-wall radar imagery. Electronic Letters. 2017; 53(15): 987–991.

29. Graham LC. Synthetic Interferometer Radar For Topographic Mapping. Proceedings of the IEEE. IEEE; 1974; 62(6): 763–768.

30. Pepe A., Calò F. A review of interferometric synthetic aperture RADAR (InSAR) multi-track approaches for the retrieval of Earth's Surface displacements. Applied Sciences (Switzerland). 2017; 7(12): 1–40.

31. Madsen S., Zebker HA., Martin J. Topographic Mapping Using Radar Interferometry: Processing Techniques. IEEE Transactions on Geoscience and Remote Sensing. 1993; 31(1): 246–256.

32. Goldstein RM., Zebker HA., Werner CL. Satellite Radar Interferometry: Two-Dimensional Phase Unwrapping. Radio Science. 1988; 23(4): 713–720.

33. Ulaby FT., Long DG. Microwave Radar and Radiometric Remote Sensing.

University of Michigan Press; 2014.

34. Wessel B., Huber M., Wohlfart C., Marschalk U., Kosmann D., Roth A. Accuracy assessment of the global TanDEM-X Digital Elevation Model with GPS data. ISPRS Journal of Photogrammetry and Remote Sensing. The Authors; 2018; 139: 171–182.

35. Gruber A., Wessel B., Huber M., Roth A. Operational TanDEM-X DEM calibration and first validation results. ISPRS Journal of Photogrammetry and Remote Sensing. International Society for Photogrammetry and Remote Sensing, Inc. (ISPRS); 2012; 73: 39–49.

36. Lopez-sanchez JM., Member S., Fortuny-Guasch J. 3-D radar imaging using range migration techniques. IEEE Transactions on Antennas and Propagation. 2000; 48(5): 728–737.

37. Aria DD. Advanced Tomographic Tool for HYDRA Radar system 2 Acquisition system and Proces- sing chain. EUSAR 2018; 12th European Conference on Synthetic Aperture Radar. Aachen, Germany, Germany: VDE; 2018. pp. 484–486.

38. Lombardini F., Tebaldini S. Multidimensional SAR tomography: Methods and applications. International Geoscience and Remote Sensing Symposium (IGARSS). 2017; 2017-July(1): 2460–2463.

39. Faulkner BD. SPARSE THREE-DIMENSIONAL SYNTHETIC APERTURE RADAR (3D SAR) IMAGE FORMATION. Cranfield University; 2016.

40. Andre D., Faulkner B., Finnis M. Low Frequency 3D Synthetic Aperture Radar for the Remote Intelligence of Building Interiors. Electronics Letters. 2017; 53(15): 984–987.

41. Elgy J., Andre D., Finnis M., Blacknell D. Data Driven Corrections to Multistatic 3D Through-Wall Radar Imagery. Proceedings of the Institute of Acoustics. Lerici, Italy; 2018. pp. 199–208.

42. Zhao Y., Zhu Y., Su Y., Yang M. A Fast 2D-ESPRIT Super-Resolution Imaging Algorithm for Linear Array SAR. IET International Radar Conference. Hangzhou,

China: IET; 2015. pp. 1–5.

43. Cristofani E., Vandewal M. High-resolution 3D SAR imaging applied to non-destructive testing of multi-layered materials. Proceedings of the European Conference on Synthetic Aperture Radar, EUSAR. Nuremberg, Germany: VDE; 2012. pp. 493–496.

44. Ertin E., Austin CD., Sharma S., Moses RL., Potter LC. GOTCHA experience report: three-dimensional SAR imaging with complete circular apertures. Algorithms for Synthetic Aperture Radar Imagery XIV. 2007; 6568(May 2007).

45. AFRL. Gotcha Volumetric SAR Data Set Overview. 2019. Available at: https://www.sdms.afrl.af.mil/index.php?collection=gotcha (Accessed: 29 August 2019)

46. Penner JF., Long DG. Ground-based 3D radar imaging of trees using a 2D synthetic aperture. Electronics (Switzerland). 2017; 6(1): 1–13.

47. Vo Dai TK., Thai A., Phan T., Kilic O., Russo K. Construction of an Inexpensive Anechoic Chamber and Its Applications in Undergraduate Research [Education Corner]. IEEE Antennas and Propagation Magazine. IEEE; 2018; 60(4): 102–112.

48. Sato M., Zhou ZS., Hamasaki T., Boerner WM. Development of a Ground-based Synthetic Aperture Radar (GB-SAR) system and its applications to environment monitoring and disaster prevention. European Space Agency, (Special Publication) ESA SP. 2005; (586): 125–131.

49. Kelly SI., Davies ME. A fast decimation-in-image back-projection algorithm for SAR. IEEE National Radar Conference - Proceedings. Cincinnati, OH, USA: IEEE; 2014. pp. 1046–1051.

50. Xu H., Wang B., Zhang J., Liu L., Li Y., Wang Y., et al. Chaos Through-Wall Imaging Radar. Sensing and Imaging. Springer US; 2017; 18(6): 1–14.

51. Corbett B., Andre D., Muff D., Morrow I., Finnis M. Imaging SAR phenomenology of concealed vibrating targets. Proceedings of the European Conference on Synthetic Aperture Radar, EUSAR. Aachen, Germany: VDE; 2018.

pp. 291–295.

52. Corbett B., Andre D., Finnis M. Through-wall detection and imaging of a vibrating target using synthetic aperture radar. Electronics Letters. 2017; 53(15): 991–995.

53. Ground Penetrating Radar Equipment | StructureScan Pro | GSSI. 2018. Available at: https://www.geophysical.com/products/structurescan-pro

54. Haas A., Peichl M., Dill S. Characterization of building structures with SAR. EUSAR 2018; 12th European Conference on Synthetic Aperture Radar. Aachen, Germany, Germany: VDE; 2018. pp. 967–970.

55. Haas A., Peichl M., Dill S. Characterization of wall structures with microwaves. Proc. SPIE 10633, Radar Sensor Technology XXII. Orlando, Florida, United States: SPIE; 2018. p. 35.

56. Volker A., Hunter A. Data-driven imaging in anisotropic media. AIP Conference Proceedings. Durban, South Africa; 2012. pp. 753–760.

57. Hayt WH., Buck JA. Engineering electromagnetics. 8th edn. Engineering Electromagnetics. New York, NY: McGraw-Hill; 2011. 367–381 p.

58. Balanis CA. Advanced Engineering Electromagnetics. 2nd Ed. Hoboken, NJ, USA: Wiley; 2012.

59. Muqaibel AH., Alsunaidi MA., Mohammad Iya N., Safaai-Jazi A. Wall Attenuation and Dispersion. In: Amin MG (ed.) Through-The-Wall Radar Imaging. Boca Raton, Fl, USA: CRC Press; 2011. pp. 1–32.

60. Elbert BR. Introduction to Satellite Communication. Norwood, MA, USA, MA, USA: Artech House Inc; 1987.

61. Zhang W., Thajudeen C., Hoorfar A. Polarimetric Through-the-wall imaging. Symposium Digest - 20th URSI International Symposium on Electromagnetic Theory, EMTS 2010. Berlin, Germany: IEEE; 2010. pp. 471–474.

62. Bufler TD., Narayanan RM. Radar classification of indoor targets using support vector machines. IET Radar, Sonar & Navigation. 2016; 10(8): 1468–1476.

63. Doody SG., Hughes N., Mak E., Muff DG., Nottingham MR. Low-frequency synthetic aperture radar data-dome collection with the Bright Sapphire II instrument. Electronic Letters. 2017; 53(15): 981–983.

64. Jackson JD. Classical Electrodynamics. 3rd Editio. John Wiley & Sons, Ltd; 1999.

65. De Wolf DA. Essentials of Electromagnetics for Engineering. Cambridge, UK: Cambridge University Press; 2001.

66. Robert A. Dielectric permittivity of concrete between 50 Mhz and 1 GHz and GPR measurements for building materials evaluation. Journal of Applied Geophysics. 1998; 40(1–3): 89–94.

67. Soutsos MN., Bungey JH., Millard SG., Shaw MR., Patterson A. Dielectric properties of concrete and their influence on radar testing. NDT and E International. 2001; 34(6): 419–425.

68. Inga Leonie Rittner WGF. Design and Evaluation of a Measurement Procedure to obtain the Electric Permittivity and the Magnetic Permeability. Revista Elektron. 2018; 2(1): 30–38.

69. Weir WB. Automatic Measurement of Complex Dielectric Constant and Permeability. Proceedings of the IEEE. 1974; 62(1).

70. Morrow IL., Finnis M V. Determination of the permittivity and permeability for some low-loss and high-loss microwave materials. 2016 Loughborough Antennas and Propagation Conference, LAPC 2016. Loughborough; 2017. pp. 1–4.

71. Karim MNA., Malek MFA., Jamlos MF. Permittivity measurement of different types of soil for ground penetrating radar applications. 2014 2nd International Conference on Electronic Design, ICED 2014. Penang, Malaysia, Malaysia: IEEE; 2014. pp. 479–482.

72. Guihard V., Taillade F., Balayssac J-P., Steck B., Sanahuja J. Permittivity measurement of cementitious materials and constituents with an open-ended coaxial probe: combination of experimental data, numerical modelling and a capacitive model. RILEM Technical Letters. 2019; 4: 39–48.

73. Guihard V., Taillade F., Balayssac J., Steck B., Sanahuja J., Deby F. Modelling the Behaviour of an Open-ended Coaxial Probe to Assess the Permittivity of Heterogeneous Dielectrics Solids. 2017; : 22–25.

74. Agilent Technologies. Basics of Measuring the Dielectric Properties of Materials. 2006.

75. Filali B., Boone F., Rhazi J., Ballivy G. Design and calibration of a large open-ended coaxial probe for the measurement of the dielectric properties of concrete. IEEE Transactions on Microwave Theory and Techniques. 2008; 56(10): 2322–2328.

76. Chung KL., Yuan L., Ji S., Sun L., Qu C., Zhang C. Dielectric characterization of Chinese standard concrete for compressive strength evaluation. Applied Sciences (Switzerland). 2017; 7(2).

77. Chung KL., Liu R., Li Y., Zhang C. Monitoring of Mix-Proportions of Concrete by Using Microwave Permittivity Measurement. 2018 IEEE International Conference on Signal Processing, Communications and Computing, ICSPCC 2018. IEEE; 2018. pp. 1–5.

78. Blackham D V., Pollard RD. An Improved Technique for Perimittivity Measurements Using a Coaxial Probe. IEEE Transactions on Instrumentation and Measurement. 1997; 46(5): 1093–1099.

79. Nicolson AM., Ross GF. Measurement of the Intrinsic Properties Of Materials by Time-Domain Techniques. IEEE Transactions on Instrumentation and Measurement. 1970; 19(4): 377–382.

80. Baker-Jarvis J., Vanzura EJ., Kissick WA. Improved technique for determining complex permittivity with the transmission/reflection method. IEEE Transactions on Microwave Theory and Techniques. 1990; 38(8): 1096–1103.

81. Packard H. Product Note 8510-3, Materials Measurement: Measuring the Dielectric Constant of Solids With the HP 8510 Network Analyzer. 1985.

82. Ghodgaonkar DK., Varadan V V., Varadan VK. Free-Space Measurement of

Complex Permittivity and Complex Permeability of Magnetic Materials at Microwave Frequencies. IEEE Transactions on Instrumentation and Measurement. 1990; 39(2): 387–394.

83. Luukkonen O., Maslovski SI., Tretyakov SA. A Stepwise Nicolson–Ross–Weir-Based Material Parameter Extraction Method. IEEE Antennas and Wireless Propagation Letters. 2011; 10: 1295–1298.

84. Boughriet AH., Legrand C., Chapoton A. Noniterative stable transmission/reflection method for low-loss material complex permittivity determination. IEEE Transactions on Microwave Theory and Techniques. 1997; 45(1): 52–57.

85. Blakney TL. Comments on 'Automatic measurement of complex dielectric constant and permeability at microwave frequencies'. Proceedings of the IEEE. 1975; 63(1): 203–205.

86. McGraw D. The measured of the dielectric constant of three different shapes of concrete blocks. International Journal of Recent Research and Applied Studies. 2015; 25(3): 82–102.

87. Ozturk M., Sevim UK., Akgol O., Unal E., Karaaslan M. Determination of physical properties of concrete by using microwave nondestructive techniques. Applied Computational Electromagnetics Society Journal. 2018; 33(3): 265–272.

88. Venkatesh MS., Raghaven GS. An overview of dielectric properties measuring techniques. Canadian Biosystems Engineering. 2005; 47(7): 15–30.

89. Bendaoued M., Terhzaz J., Mandry R., Bendaoued M. Determining the complex permittivity of building dielectric materials using a propagation constant measurement. International Journal of Electrical and Computer Engineering. 2017; 7(4): 1681–1685.

90. Sagnard F., Zein GE. In situ characterization of building materials for propagation modeling: frequency and time responses. IEEE Transactions on Antennas and Propagation. October 2005; 53(10): 3166–3173.

91. Grosvenor CA., Johnk RT., Baker-Jarvis J., Janezic MD., Riddle B. Time-domain free-field measurements of the relative permittivity of building materials. IEEE Transactions on Instrumentation and Measurement. 2009; 58(7): 2275–2282.

92. Muqaibel AH., Safaai-jazi A. A new formulation for characterization of materials based on measured insertion transfer function. IEEE Transactions on Microwave Theory and Techniques. 2003; 51(8): 1946–1951.

93. Ong GKC., Akbarnezhad A. Microwave-Assisted Concrete Technology: Production, Demolition and Recycling. 1st edn. Press C (ed.) 2018. 111–115 p.

94. Cemex UK. 1400 Solid Lightweight Readyblock - Standard Finish. Cemex Material Datasheet. 2017. pp. 1–2. Available at: https://www.cemex.co.uk/documents/45807659/45840219/masonry-readyblock-1400-dense-lightweight-readyblock-standard-finish.pdf (Accessed: 1 March 2017)

95. Maxwell Garnet JC. XII. Colours in metal glasses and in metallic films. Philosophical Transactions of The Royal Society A. 1904; 203(359–371): 385–420.

96. Dobson MC., Ulaby FT., Hallikainen MT., El-Rayes MA. Microwave Dielectric Behavior of Wet Soil-Part II: Dielectric Mixing Models. IEEE Transactions on Geoscience and Remote Sensing. 1985; GE-23(1): 35–46.

97. Ogunsola A., Reggiani U., Sandrolini L. Shielding effectiveness of concrete buildings. IEEE 6th International Symposium on Electromagnetic Compatibility and Electromagnetic Ecology, 2005. Saint Petersburg, Russia, Russia: IEEE; 2005. pp. 65–68.

98. Gonzalez-Lopez G., Blanch S., Romeu J., Jofre L. Debye Frequency-extended Waveguide Permittivity Extraction for High Complex Permittivity Materials. Concrete Setting Process Characterization. IEEE Transactions on Instrumentation and Measurement. 2019; 9456(c): 1–1.

99. Thajudeen C., Hoorfar A. Wall Parameters Estimation using a Hybrid Time-Delay-Only and Reflected Wave Ratio Technique. IEEE Antennas and Propagation

Society International Symposium (APSURSI). Orlando, FL, USA: IEEE; 2013. pp. 526–527.

100. Protiva P., Mrkvica J., MacHáč J. Estimation of wall parameters from time-delay-only through-wall radar measurements. IEEE Transactions on Antennas and Propagation. 2011; 59(11): 4268–4278.

101. Li X., Huang X., Jin T. Estimation of wall parameters by exploiting correlation of echoes in time domain. Electronics Letters. 2010; 46(23): 1563–1565.

102. Jamil M., Hassan MK., Al-Mattarneh HMA., Zain MFM. Concrete dielectric properties investigation using microwave nondestructive techniques. Materials and Structures/Materiaux et Constructions. 2013; 46(1–2): 77–87.

103. Taylor JR. An Introduction To Error Analysis. 2nd edn. University Science Books; 1997.

104. Vicente AN., Dip GM., Junqueira C. The step by step development of NRW method. SBMO/IEEE MTT-S International Microwave and Optoelectronics Conference Proceedings. 2011. pp. 738–742.

105. Amin MG. (ed.) Through-The-Wall Radar Imaging. Boca Raton, Fl, USA: CRC Press; 2011.

106. Stuchly SS., Matuszewski M. A Combined Total Reflection-Transmission Method in Application to Dielectric Spectroscopy. IEEE Transactions on Instrumentation and Measurement. 1978; 27(3): 285–288.

107. ITU-R. Effects of building materials and structures on radiowave propagation above about 100 MHz P Series Radiowave propagation. Recommendation ITU-R P.2040. 2013; 1.

108. Smith EK., Weintraub S. The Constants in the Equation for Atmospheric Refractive Index at Radio Frequencies. Proceedings of the IRE. 1953; 41(8): 1035–1037.

109. Pisa S., Piuzzi E., Pittella E., Atanasio PD., Zambotti A., Sacco G. Power Budget and Reconstruction Algorithms for Through the Wall Radar Imaging Systems.

2018 IEEE International Microwave Biomedical Conference (IMBioC). IEEE; 2018; (2): 208–210.

110. Villain G., Ihamouten A., Dérobert X. Determination of concrete water content by coupling electromagnetic methods: Coaxial/cylindrical transition line with capacitive probes. NDT and E International. Elsevier Ltd; 2017; 88(July 2016): 59–70.

111. Asp A., Valkama M., Pikkuvirta J., Hujanen A., Huhtinen I. Impact of Concrete Moisture on Radio Propagation : Fundamentals and Measurements of Concrete. 2019; : 542–547.

112. Wang G., Amin MG., Zhang Y. New approach for target locations in the presence of wall ambiguities. IEEE Transactions on Aerospace and Electronic Systems. 2006; 42(1): 301–315.

113. Wang G., Amin MG. A new approach for target location of through the wall radar imaging in the presence of wall ambiguities. Proceedings of the Fourth IEEE International Symposium on Signal Processing and Information Technology, 2004. 2004. pp. 183–186.

114. Wang G., Amin MG. Imaging through unknown walls using different standoff distances. IEEE Transactions on Signal Processing. 2006; 54(10): 4015–4025.

115. Ahmad F., Amin MG., Kassam SA. Synthetic aperture beamformer for imaging through a dielectric wall. IEEE Transactions on Aerospace and Electronic Systems. IEEE; 2005; 41(1): 271–283.

116. Ahmad F., Zhang Y., Amin MG. Three-dimensional wideband beamforming for imaging through a single wall. IEEE Geoscience and Remote Sensing Letters. 2008; 5(2): 176–179.

117. Ahmad F., Amin MG., Mandapati G. Autofocusing of through-the-wall radar imagery under unknown wall characteristics. IEEE Transactions on Image Processing. 2007; 16(7): 1785–1795.

118. Dehmollaian M., Sarabandi K. Refocusing Through Building Walls Using

Synthetic Aperture Radar. IEEE Transactions on Geoscience and Remote Sensing. 2008; 46(6): 1589–1599.

119. Chen X., Chen W. A simple method for image autofocusing in through-wall radar imaging. IEEE Antennas and Propagation Society, AP-S International Symposium (Digest). 2013. pp. 530–531.

120. Jin T., Chen B., Zhou Z. Image-domain estimation of wall parameters for autofocusing of through-the-wall SAR imagery. IEEE Transactions on Geoscience and Remote Sensing. 2013; 51(3): 1836–1843.

121. Solimene R., Soldovieri F., Prisco G., Pierri R. Three-dimensional through-wall imaging under ambiguous wall parameters. IEEE Transactions on Geoscience and Remote Sensing. 2009; 47(5): 1310–1317.

122. Solimene R., Napoli R Di., Soldovieri F., Pierri R. TWI for an Unknown Symmetric Lossless Wall. IEEE Transactions on Geoscience and Remote Sensing. IEEE; 2011; 49(8): 2876–2886.

123. Solimene R., Rajvanshi T., Aversano A., Buonanno G., Dell’Aversano A. Microwave imaging through an unknown wall by a MIMO configuration and SVD approach. Proc. SPIE 11059, Multimodal Sensing: Technologies and Applications. Munich, Germany; 2019. p. 3.

124. Aftanas M., Sachs J., Drutarovský M., Kocur D. Efficient and Fast Method of Wall Parameter Estimation by Using UWB Radar System. Frequenz. 2009; 63(11–12): 1–4.

125. Thajudeen C., Hoorfar A., Zhang W. Estimation of frequency-dependent parameters of unknown walls for enhanced through-the-wall imaging. IEEE Antennas and Propagation Society, AP-S International Symposium (Digest). IEEE; 2011; : 3070–3073.

126. Morrison K., Andre D., Blacknell D., Muff D., Nottingham M., Stevenson C., et al. Hyperspectral 10-50GHz SAR imaging of building materials. 2016 IEEE Radar Conference, RadarConf 2016. IEEE; 2016; : 1–5.

127. Repko M., Gamec J., Kurdel P., Gamcova M. Estimation of the Wall Thickness and Relative Permittivity by Radar System. ICETA 2018 - 16th IEEE International Conference on Emerging eLearning Technologies and Applications, Proceedings. Stary Smokovec, Slovakia: IEEE; 2018. pp. 469–474.

128. Protiva P., Mrkvica J., Šafařík M., Šikl R., Vlasák V., Macháć J. An Improved Technique for Estimating Wall Parameters from Time-Delay Through-Wall Radar Measurements. Radioelektronika (RADIOELEKTRONIKA), 2012 22nd International Conference. Brno, Czech Republic: IEEE; 2012. pp. 1–4.

129. Fereidoony F., Chamaani S., Sebt MA., Mirtaheri SA. Efficient method for estimation of the thicknesses and complex dielectric constant of wall. Antennas and Propagation (EuCAP), 2014 8th European Conference on. The Hague, Netherlands: IEEE; 2014. pp. 3085–3088.

130. Fereidoony F., Mirtaheri SA., Chamaani S. High-resolution range estimation using time delays in ultra-wideband M-sequence radar. IET Microwaves, Antennas and Propagation. 2017; 11(10): 1332–1339.

131. Fereidoony F., Mirtaheri SA., Chamaani S. M-Sequence Sensor and Continuous Basis Estimator for Wall Parameter Estimation Utilizing Through the Wall Sensing. IEEE Sensors Journal. IEEE; 2017; 17(13): 4083–4091.

132. Odendaal JW., Barnard E., Pistorius CWI. Two-Dimensional Superresolution Radar Imaging Using the MUSIC Algorithm. IEEE Transactions on Antennas and Propagation. 1994; 42(10): 1386–1391.

133. Yoon YS., Amin MG. High-resolution through-the-wall radar imaging using beamspace MUSIC. IEEE Transactions on Antennas and Propagation. 2008; 56(6): 1763–1774.

134. Schmidt R. Multiple emitter location and signal parameter estimation. IEEE Transactions on Antennas and Propagation. 1986; 34(3): 276–280.

135. Zhang P., Li Z., Chen Q. 2D UESPRIT superresolution SAR imaging algorithm. International Geoscience and Remote Sensing Symposium (IGARSS). 2010; (2): 4067–4070.

136. Li D., Yao D. Application of ESPRIT Method to Stepped Frequency Radar for Scattering Centre Extraction. IET International Radar Conference. 2009. pp. 1–4.

137. Lu Y., Song W., Lu J., Wang X., Tan Y. An Examination of Soil Moisture Estimation Using Ground Penetrating Radar in Desert Steppe. 2017; : 1–11.

138. Guo C., Zhao L., Chen Y., Li W., Liu RC. Extraction of the Pavement Permittivity and Thickness from Measured Ground-Coupled GPR Data Using a Ground-Wave Technique. IEEE Geoscience and Remote Sensing Letters. IEEE; 2017; 14(3): 399–403.

139. Liu CRR., Li J., Gan X., Xing H., Chen X. New model for estimating the thickness and permittivity of subsurface layers from GPR data. IEE Proc.- Radar Sonar and Navig. 2002; 149(6): 315–319.

140. Clair JS., Holbrook WS. Measuring snow water equivalent from common-offset GPR records through migration velocity analysis. 2017; : 2997–3009.

141. Bradford JH., Harper JT., Brown J. Complex dielectric permittivity measurements from ground-penetrating radar data to estimate snow liquid water content in the pendular regime. Water Resources Research. 2009; 45(8): 1–12.

142. Elgy J., Andre D., Morrow IL., Finnis M. Remote Determination of Building Material Characteristics Using Asymmetric Bistatic Radar Geometries. EUSAR 2018; 12th European Conference on Synthetic Aperture Radar. Aachen, Germany: VDE; 2018. pp. 843–846.

143. Thajudeen C., Hoorfar A. A Hybrid Bistatic-Monostatic Radar Technique for Calibration-Free Estimation of Lossy Wall Parameters. IEEE Antennas and Wireless Propagation Letters. IEEE; 2017; 16: 1249–1252.

144. Kobayashi H., Takaoka SI., Kawamura RI., Cui Y., Yamaguchi Y. Permittivity estimation of multilayered dielectrics by wall-thru radar image. ISAP 2014 - 2014 International Symposium on Antennas and Propagation, Conference Proceedings. Institute of Antenna Engineers of Taiwan; 2015. pp. 123–124.

145. Maser KR., Scullion T. Automated Pavement Subsurface Profiling Using Radar:

Case Studies of Four Experimental Field Sites. Transport Research Record. 1992; 1344: 148–154.

146. Morrison K., Andre D., Blacknell D., Muff D., Nottingham M., Stevenson C. Material Identification Using Extreme Wide - Band SAR Imaging 2 Reflectivity Measurements 3 Resonance Effects. EUSAR 2016: 11th European Conference on Synthetic Aperture Radar, Proceedings of. Hamburg, Germany: VDE; 2016. pp. 722–725.

147. Lynch P. The Dolph–Chebyshev Window: A Simple Optimal Filter. Monthly Weather Review. 1997; 125(4): 655–660.

148. Nyquist H. Certain topics in telegraph transmission theory (Reprinted from Transactions of the A. I. E. E., February, pg 617-644, 1928). Proceedings of the Ieee. 2002; 90(2): 280–305.

149. Shannon CE. Communication In The Presence Of Noise (Republished). Proceedings of the IEEE. 1998; 86(2): 447–457.

150. Morrison K., Bennett JC. Virtual bandwidth SAR (VB-SAR) for centimetric-scale sub-surface imaging from space. International Journal of Remote Sensing. Taylor & Francis; 2015; 36(7): 1789–1808.

151. Edwards-smith A., Morrison K., Zwieback S., Hajnsek I. Verification of the Virtual Bandwidth SAR Scheme for Centimetric Resolution Subsurface Imaging From Space. IEEE Transactions on Geoscience and Remote Sensing. IEEE; 2017; 56(1): 1–10.

152. Gorham L a., Moore LJ. SAR image formation toolbox for MATLAB. SPIE Algorithms for Synthetic Aperture Radar Imagery. Orlando, FL, USA; 2010. pp. 769906-769906–769913.

153. Kiusalaas J. Numerical Methods in Engineering with MATLAB. Engineering. Cambridge, UK: Cambridge University Press; 2005. 434 p.

154. Lagaris IE., Tsoulos IG. Stopping Rules for Box-Constrained Stochastic Global Optimization. : 1–15.

155. Boender CGE., Rinnooy Kan AHG. Bayesian Stopping Rules for Multistart Global Optimization Methods. Mathematical Programming. 1987; 37: 59–80.

156. Sengul O. Use of electrical resistivity as an indicator for durability. Construction and Building Materials. Elsevier Ltd; 2014; 73: 434–441.

157. Fulham-lebrasseur R., Sorelli L., Conciatori D. Development of electrically conductive concrete and mortars with hybrid conductive inclusions. Construction and Building Materials. Elsevier Ltd; 2020; 237: 117470.

158. Presuel-Moreno F., Wu YY., Liu Y. Effect of curing regime on concrete resistivity and aging factor over time. Construction and Building Materials. 2013; 48: 874–882.

159. Rees WG. Physical Properties of Remote Sensing. 2nd Editio. Cabridge University Press; 2001.

160. Hajnsek I., Papathanassiou K. Rough surface scattering models. 2005. Available at: https://earth.esa.int/documents/653194/656796/Rough_Surface_Scattering_Models.pdf (Accessed: 21 January 2020)

161. A-Info. A-Info LB-10180 Horn Antenna Specifications. 2018. Available at: http://ainfoinc.com.cn/en/pro_pdf/new_products/antenna/Broadband Horn Antenna/tr_LB-10180.pdf (Accessed: 16 January 2021)

162. Hoppe RHW. Sequential Quadratic Programming. Optimization 1. Houston, TX, USA: University of Houston; 2006.

163. Yegulalp AF. Fast backprojection algorithm for synthetic aperture radar. Proceedings of the 1999 IEEE Radar Conference. Radar into the Next Millennium. Waltham, MA, USA: IEEE; 1999. pp. 60–65.

164. Dehmollaian M., Thiel M., Sarabandi K. Through-the-wall imaging using differential SAR. IEEE Transactions on Geoscience and Remote Sensing. 2009; 47(5): 1289–1296.

165. Yoon YS., Amin MG. Spatial filtering for wall-clutter mitigation in through-the-

wall radar imaging. IEEE Transactions on Geoscience and Remote Sensing. IEEE; 2009; 47(9): 3192–3208.

166. Wang M., Cui G., Yi W., Kong L., Yang X., Yuan L. Time-division MIMO through-the-wall radar imaging behind multiple walls. IEEE National Radar Conference - Proceedings. Arlington, VA, USA: IEEE; 2015. pp. 1144–1148.

167. Zoofaghari M., Tavakoli A., Dehmollaian M. Imaging Through a Wall with Corrugated Surfaces. IEEE Geoscience and Remote Sensing Letters. 2016; 13(3): 394–398.

168. Khorashadi-Zadeh V., Dehmollaian M. Through a cinder block wall refocusing using SAR back projection method. IEEE Transactions on Antennas and Propagation. IEEE; 2019; 67(2): 1212–1222.

169. Khorashadi-zadeh V., Dehmollaian M. Refocusing Through Cinder Block Walls. 2017 Iranian Conference on Electrical Engineering (ICEE). Tehran, Iran: IEEE; 2017. pp. 2062–2065.

170. Chen X., Ye X. Through wall imaging: Inverse scattering approach. Proceedings of 3rd Asia-Pacific Conference on Antennas and Propagation, APCAP 2014. IEEE; 2014; : 796–797.

171. Li L., Zhang W., Li F. A novel autofocusing approach for real-time through-wall imaging under unknown wall characteristics. IEEE Transactions on Geoscience and Remote Sensing. 2010; 48(1): 423–431.

172. Wu S., Zhou H., Liu S., Duan R. Improved through-wall radar imaging using modified Green's function-based multi-path exploitation method. Eurasip Journal on Advances in Signal Processing. EURASIP Journal on Advances in Signal Processing; 2020; 4(2020)(1): 1–13.

173. Jaya V., Gopikakumari R. IEM : A New Image Enhancement Metric for Contrast and Sharpness Measurements. International Journal ofComputer Applications. 2013; 79(9): 1–9.

174. Elgy J., Andre D. GBSAR-Proc. 2019. Available at:

DOI:10.17862/cranfield.rd.9693581.v2 (Accessed: 25 November 2019)

175. Jin T., Yarovoy A. A Through-the-Wall Radar Imaging Method Based on a Realistic Model. International Journal of Antennas and Propagation. 2015; 2015.

176. Li Y., Zhao Y., Xiang Y., Ding Z., Liu H., Liu Q. Three-dimensional optimal focusing imaging algorithm for wall-penetrating radar. The Journal of Engineering. 2019; 2019(19): 6063–6066.

177. Gennarelli G., Solimene R., Soldovieri F., Amin MG. Three-Dimensional Through-Wall Sensing of Moving Targets Using Passive Multistatic Radars. IEEE Journal of Selected Topics in Applied Earth Observations and Remote Sensing. IEEE; 2016; 9(1): 141–148.

178. Zhang W., Hoorfar A. Three-Dimensional Real-Time Through-the-Wall Radar Imaging With Diffraction Tomographic Algorithm. IEEE Transactions on Geoscience and Remote Sensing. IEEE; 2013; 51(7): 4155–4163.

179. Sevigny P., Difilippo DJ. A multi-look fusion approach to through-wall radar imaging. IEEE National Radar Conference - Proceedings. Ottawa, Canada: IEEE; 2013.

180. Xiao S., Munson DC., Bressler. An N^2 log N Back-Projection Algorithm for SAR Image Formation. Simulation. 2000; (May): 3–7.

181. Ding Y., Munson DCDC. A fast back-projection algorithm for bistatic SAR imaging. Image Processing. 2002. Proceedings. 2002 International Conference on. Rochester, NY, USA: IEEE; 2002. pp. 449–452.

182. Basu S., Bresler Y. Filtered backprojection reconstruction algorithm for tomography. IEEE Transactions on Image Processing. 2000; 9(10): 1760–1773.

183. Zhang H., Tang J., Wang R., Deng Y., Wang W., Li N. An accelerated backprojection algorithm for monostatic and bistatic SAR processing. Remote Sensing. 2018; 10(1).

184. Park J., Tang PTP., Smelyanskiy M., Kim D., Benson T. Efficient backprojection-based synthetic aperture radar computation with many-core processors. Scientific

Programming. 2013; 21(3–4): 165–179.

185. Que R., Ponce O., Scheiber R., Reigber A. Real-time processing of SAR images for linear and non-linear tracks. Proceedings International Radar Symposium. Krakow, Poland; 2016.

186. Hu K., Zhang X., Wu W., Shi J., Wei S. Three GPU-based parallel schemes for SAR back projection imaging algorithm. Proceedings - 17th IEEE International Conference on Computational Science and Engineering, CSE 2014, Jointly with 13th IEEE International Conference on Ubiquitous Computing and Communications, IUCC 2014, 13th International Symposium on Pervasive Systems,. IEEE; 2014; : 324–328.

187. Wei P., Du J., Sui S., Chen Y. The Research on Parallel Optimization of SAR Imaging R-D Algorithm Based on CUDA. 2018 10th International Conference on Communication Software and Networks, ICCSN 2018. IEEE; 2018; : 526–530.

188. Fasih A., Hartley T. GPU-accelerated synthetic aperture radar backprojection in CUDA. IEEE National Radar Conference - Proceedings. IEEE; 2010; : 1408–1413.

189. Chapman W., Ranka S., Sahni S., Schmalz M., Moore LJ., Majumder U., et al. Backprojection algorithms for multicore and GPU architectures. Multicore Computing: Algorithms, Architectures, and Applications. 2012. pp. 391–412.

190. Blacknell D. The Resampling of Synthetic Aperture. In: Brooks SR (ed.) Mathematics in Remote Sensing. Oxford: Oxford University Press; 1989. pp. 173–188.

191. El-Darymli K., McGuire P., Power D., Moloney C. An algorithm for upsampling spotlight SAR imagery: a Radarsat-2 SLC perspective. Algorithms for Synthetic Aperture Radar Imagery XX. 2013; 8746(May 2013): 874607.

192. El-Darymli K., McGuire P., Gill E., Power D., Moloney C. Errata: Effect of detection on spatial resolution in synthetic aperture radar imagery and mitigation through upsampling. Journal of Applied Remote Sensing. 2014; 8(1): 089997.

193. Andre D., Morrow IL. A new spatially variant SAR basebanding technique. EUSAR 2018; 12th European Conference on Synthetic Aperture Radar. Aachen, Germany: VDE; 2018. pp. 1066–1069.

194. Andre D., Blacknell D., Finnis M. An Improved SAR-Near-Field Spatially Variant Basebanding Technique. Proceedings of the Institute of Acoustics. Lerici, Italy; 2018. pp. 173–180.

195. Blacknell D., Andre D. Life in the frequency domain: SAR CCD over mountains and the physics of vibrating targets. Proceedings of the Defence Applications of Signal Processing. 2011.

196. Elgy J., Andre D., Finnis M. Volumetric SAR near-field upsampling and basebanding. Electronic Letters. 2020; 56(12): 622–624.

197. Rudd R., Craig K., Ganley M., Hartless R. Building Materials and Propagation: Final Report. Ofcom. 2014.

Appendix A Derivations

A.1 Derivation For $\boldsymbol{\alpha}$ and $\boldsymbol{\beta}$ and $\boldsymbol{n}$

We start with Maxwell's Equations in differential form.

$$\nabla \cdot \mathbf{E} = \frac{\rho}{\varepsilon}$$ Gauss' Law for Electricity **A-1**

$$\nabla \cdot \mathbf{H} = 0$$ Gauss' Law for Magnetism **A-2**

$$\nabla \times \mathbf{E} = -\mu \frac{\partial \mathbf{H}}{\partial t}$$ Faraday's Law **A-3**

$$\nabla \times \mathbf{H} = \varepsilon \frac{\partial \mathbf{E}}{\partial t} + \mathbf{J}$$ Ampere's Law **A-4**

Where **E** is the electric field vector and **H** is the magnetic field vector, ρ is the charge density while ε and μ are the permittivity and permeability of the medium respectively. **J** is the current density and is defined in terms of the conductivity and electric field as $\mathbf{J} = \sigma\mathbf{E}$.

Consider a transverse electromagnetic wave traveling in the Z direction that only has an amplitude in the x plane. The electric field vector for such a wave will be $\mathbf{E} = E_x\mathbf{a_x}$. The magnetic field will be orthogonal to the electric field for a uniform plane wave, ergo the magnetic field can be expressed as $\mathbf{H} = H_y\mathbf{a_y}$. Using Faraday's Law, we can equate the curl of **E** with **H**:

$$\nabla \times \mathbf{E} = \frac{\partial E_x}{\partial z}\boldsymbol{a}_y = -\mu \frac{\partial H_y}{\partial t}\boldsymbol{a}_y \qquad \textbf{A-5}$$

And using Ampere's Law, we can write the curl of **H** in terms of **E**.

$$\nabla \times \mathbf{H} = -\frac{\partial H_y}{\partial z}\boldsymbol{a}_x = \varepsilon \frac{\partial E_x}{\partial t}\boldsymbol{a}_x + \sigma E_x \boldsymbol{a}_x \qquad \textbf{A-6}$$

By selectively differentiating equations **A-5** and **A-6** with respect to either z or t, we can eliminate the magnetic field term and derive an equation relating the spatial derivative of

E with its temporal derivative. First, we differentiate equation **A-5** with respect to z to get:

$$\frac{\partial^2 E_x}{\partial z^2} = -\mu \frac{\partial^2 H_y}{\partial t \partial z} \qquad \textbf{A-7}$$

Secondly we differentiate equation **A-6** with respect to time:

$$-\frac{\partial^2 H_y}{\partial z \partial t} = \varepsilon \frac{\partial^2 E_x}{\partial t^2} + \sigma \frac{\partial E_x}{\partial t} \qquad \textbf{A-8}$$

We can substitute equation **A-8** into equation **A-7** to arrive at the standard wave equation for an inhomogeneous medium used by [107].

$$\frac{\partial^2 E_x}{\partial z^2} = \mu\varepsilon \frac{\partial^2 E_x}{\partial t^2} + \mu\sigma \frac{\partial E_x}{\partial t} \qquad \textbf{A-9}$$

$$\nabla^2 \mathbf{E} - \frac{1}{v^2}\ddot{\mathbf{E}} = \mu\sigma\dot{\mathbf{E}} \qquad \textbf{A-10}$$

The solution to this second order ordinary differential equation is the standard sinusoidal equation for a complex transverse wave, $\mathbf{E} = E_0 e^{i(\omega t - k\boldsymbol{r})}$, by substituting this into equation **A-9**, an equation for the wavenumber k can be derived.

$$-k^2\mathbf{E} + \mu\varepsilon\omega^2\mathbf{E} = i\mu\sigma\omega\mathbf{E} \qquad \textbf{A-11}$$

$$k^2 = \mu\varepsilon\omega^2 - i\mu\sigma\omega \qquad \textbf{A-12}$$

$$k^2 = \mu\varepsilon\omega^2\left(1 - \frac{i\sigma}{\varepsilon\omega}\right) \qquad \textbf{A-13}$$

Equation **A-13** shows that in an inhomogeneous medium, the wavenumber is complex. There are numerous different approaches for expressing the complex term. For example, [57, pp.372–377] uses the time-harmonic form of Maxwell's Equations, thus introduces a complex term for the dielectric constant as $\varepsilon = (\varepsilon' - i\varepsilon'')$. This derivation follows [58, p.139] and [105], wherein the permittivity and permeability terms are considered to be real – note that [58] uses a different notation when referring to either permittivity or complex permittivity.

Now that the wave number has been shown to be complex, we can separate it into its real and imaginary components. For $ik = \alpha + i\beta$ where $\alpha, \beta \in \mathbb{R}$ then we can write equation **A-13** as:

$$(ik)^2 = -k^2 = -\omega^2\mu\varepsilon + \omega\mu i\sigma \qquad \textbf{A-14}$$

$$(\alpha + i\beta)^2 = -\omega^2\mu\varepsilon + \omega\mu i\sigma \qquad \textbf{A-15}$$

Expanding the bracketed term gives $(\alpha + i\beta)^2 = \alpha^2 - \beta^2 - 2i\alpha\beta$, substituting this into **A-15** allows us to separate the real and imaginary parts;

$$(\alpha^2 - \beta^2) + 2i\alpha\beta = -\omega^2\mu\varepsilon + \omega\mu i\sigma \qquad \textbf{A-16}$$

$$(\alpha^2 - \beta^2) = -\omega^2\mu\varepsilon \qquad \textbf{A-17}$$

$$2\alpha\beta = \omega\mu\sigma \qquad \textbf{A-18}$$

Equation **A-18** can be rearranged to provide an equation for β, this can then be substituted into equation **A-17** to give an equation for α that is independent of β.

$$\beta = \frac{\omega\mu\sigma}{2\alpha} \qquad \textbf{A-19}$$

$$\alpha^2 - \frac{\omega^2\mu^2\sigma^2}{4\alpha^2} + \omega^2\mu\varepsilon = 0 \qquad \textbf{A-20}$$

We can multiply the entirety of equation **A-20** by α^2, this puts the equation into the form of a quadratic, that can then be solved for using the quadratic formula $\frac{-b\pm\sqrt{b^2-4ac}}{2a}$:

$$\alpha^4 + \omega^2\mu\varepsilon\alpha^2 - \frac{\omega^2\mu^2\sigma^2}{4} = 0 \qquad \textbf{A-21}$$

Since α and β are assumed to both be positive real numbers [58, p.108], only the positive root is considered. Using the quadratic formula, the solution for α^2 is:

$$\alpha^2 = \frac{-\omega^2\mu\varepsilon + \sqrt{\omega^4\mu^2\varepsilon^2 + \omega^2\mu^2\sigma^2}}{2} \qquad \textbf{A-22}$$

$$\alpha = \sqrt{\frac{\omega^2\mu\varepsilon\left(\sqrt{1+\frac{\sigma^2}{\omega^2\varepsilon^2}}-1\right)}{2}} \qquad \textbf{A-23}$$

Since a square root can be either positive or negative, we could conceivably have a negative value for α, this would correspond to an increase in the amplitude of the electric field rather than a damping. This is referred to as a gain rather than as an attenuation.

Substituting equation **A-23** into equation **A-17** provides an equation for β.

$$\beta^2 = \alpha^2 + \omega^2\mu\varepsilon \qquad \textbf{A-24}$$

$$\beta = \sqrt{\frac{\omega^2\mu\varepsilon\left(\sqrt{1+\frac{\sigma^2}{\omega^2\varepsilon^2}}+1\right)}{2}} \qquad \textbf{A-25}$$

From equations **A-23** and **A-25**, we can infer that there are 4 possible combinations of $\alpha + i\beta$ corresponding to positive or negative values for α and β. These combinations describe the direction of the traveling wave and if it is experiencing a loss or a gain in amplitude.

A further analysis reveals that the phase velocity of the wave would be the ratio between ω and β. This is done by extracting α from the equation for a traveling wave.

$$\mathbf{E} = E_0 e^{i\omega t-(\alpha+i\beta)r} = E_0 e^{\alpha r} e^{i(\omega t-\beta r)} \qquad \textbf{A-26}$$

This can be rewritten to group the amplitude terms together into a single value, dependent on ***r***.

$$E_0 e^{\alpha r} e^{i(\omega t-\beta r)} = A(\boldsymbol{r}) e^{i(\omega t-\beta r)} \qquad \textbf{A-27}$$

Equation **A-27** shows that the phase of the traveling wave is completely independent of α, therefore the phase velocity of the wave is also independent of α. Since it is an oscillating wave, at the peak of each wave front, ωt must equal $\beta\boldsymbol{r}$. This leads to the phase velocity being [57, p.310]:

$$v_p = \frac{\boldsymbol{r}}{t} = \frac{\omega}{\beta} \qquad \textbf{A-28}$$

For a constant refractive index, the phase velocity does not change, therefore

$$n = \frac{c}{v_p} = \frac{\left(\frac{\omega}{\beta_0}\right)}{\left(\frac{\omega}{\beta}\right)} = \frac{\beta}{\beta_0} \qquad \textbf{A-29}$$

Where β_0 represents the phase in a vacuum and $n \in \mathbb{R}$ being the refractive index. This leads to an equation for the refractive index that inherently includes a consideration for the conductivity of the medium:

$$n = \frac{\beta}{\beta_0} = \sqrt{\frac{\varepsilon\mu}{2\varepsilon_0\mu_0}\left(\sqrt{1 + \frac{\sigma^2}{\omega^2\varepsilon^2}} + 1\right)} \qquad \textbf{A-30}$$

Assuming that the magnetic susceptibility of the material is zero, equation **A-30** can be rewritten as:

$$n = \sqrt{\frac{\varepsilon_r}{2}\left(\sqrt{1 + \frac{\sigma^2}{\omega^2\varepsilon^2}} + 1\right)} \qquad \textbf{A-31}$$

Where ε_r represents the relative dielectric of the material.

Symbol	Exact Equation	Conductor: $\left(\frac{\sigma}{\omega\varepsilon}\right)^2 \gg 1$	Insulator: $\left(\frac{\sigma}{\omega\varepsilon}\right)^2 \ll 1$
n	$\sqrt{\frac{\varepsilon\mu}{2\varepsilon_0\mu_0}\left(\sqrt{1+\frac{\sigma^2}{\omega^2\varepsilon^2}}+1\right)}$	$\sqrt{\frac{\sigma\mu}{2\omega}}c$	$\sqrt{\frac{\varepsilon\mu}{\varepsilon_0\mu_0}}=\frac{c}{v}$
β	$\sqrt{\frac{\omega^2\mu\varepsilon}{2}\left(\sqrt{1+\frac{\sigma^2}{\omega^2\varepsilon^2}}+1\right)}$	$\sqrt{\frac{\omega\mu\sigma}{2}}$	$\sqrt{\omega^2\mu\varepsilon}=\frac{\omega}{v}$
α	$\sqrt{\frac{\omega^2\mu\varepsilon}{2}\left(\sqrt{1+\frac{\sigma^2}{\omega^2\varepsilon^2}}-1\right)}$	$\sqrt{\frac{\omega\mu\sigma}{2}}$	$\frac{\sigma}{2}\sqrt{\frac{\mu}{\varepsilon}}$[12]
λ	$\frac{2\pi}{\beta}$	$\sqrt{\frac{8\pi^2}{\omega\mu\sigma}}$	$\frac{2\pi v}{\omega}$

Table A-1 – Summary of the main transmission equations. Given as exact solutions and as approximations for conductors and insulators.

---

[12] Obtained via binomial expansion of α [58, p.142].

A.2 Derivation of Slab Waveguide Transmission Function

Following Hayt's [57, pp.479–486] derivation of slab dielectric cutoff frequencies, consider a rectangular dielectric waveguide.

For propagation in the 3 spatial dimensions, the wavevector, $\boldsymbol{K}$, can be represented as a sum of vector contributions, $\boldsymbol{K} = \boldsymbol{K_x} + \boldsymbol{K_y} + \boldsymbol{K_z} = [K_x, K_y, K_z]$. The magnitude of the wavevector is therefore:

$$K = \sqrt{K_z^2 + K_x^2 + K_y^2} \quad \textbf{A-32}$$

If one were to only consider propagation in the z dimension, then K can be simplified by grouping the x and y terms together as:

$$K = \sqrt{K_z^2 + K_{mp}^2} \quad \textbf{A-33}$$

$$K_z = \sqrt{K^2 - K_{mp}^2} \quad \textbf{A-34}$$

Where the subscripts m and p represent integer modes of propagation, ultimately culminating in specific allowed directions.

From the wave equation, the following expression must hold:

$$\nabla^2 \boldsymbol{E} + K^2 \boldsymbol{E} = 0 \quad \textbf{A-35}$$

$$\frac{\partial^2 E_z}{\partial x^2} + \frac{\partial^2 E_z}{\partial y^2} + \left(K_z - K_{mp}\right) E_z = 0 \quad \textbf{A-36}$$

A suitable solution to the wave equation is a complex sinusoid, best expressed by Euler's equation:

$$E(x, y, z) = F_m(x) G_p(y) e^{iK_z z} \quad \textbf{A-37}$$

The functions F_m and G_p are currently undefined. Substituting equation A-37 into equation A-36 produces, via the product rule[13]:

$$G_p(y)\frac{d^2F_m(x)}{dx^2}+F_m(x)\frac{d^2G_p(y)}{dy^2}+K_{mp}^2F_m(x)G_p(y)=0 \tag{A-38}$$

Rearranging equation A-38 provides an equality whereby all the x terms are grouped and all the y terms are grouped:

$$\frac{1}{F_m(x)}\frac{d^2F_m(x)}{dx^2}+\frac{1}{G_p(y)}\frac{d^2G_p(y)}{dy^2}=-K_{mp}^2 \tag{A-39}$$

Since the first term is only dependent on x, and x and y are independent of each other, it follows that the first and second terms must both be constant, I.e.

$$\frac{d^2F_m(x)}{dx^2}+F_m(x)\kappa_m^2=0 \tag{A-40}$$

$$\frac{d^2G_p(y)}{dy^2}+G_p(y)\kappa_p^2=0 \tag{A-41}$$

where κ_m and κ_p are constants. Solving this pair of second order differential equations gives the functions $F_m(x)$ and $G_p(y)$ as:

$$F_m(x)=A_m\cos(\kappa_m x)+B_m\sin\,(\kappa_m x) \tag{A-42}$$

$$G_p(y)=C_p\cos(\kappa_p y)+D_p\sin\,(\kappa_p y) \tag{A-43}$$

This gives an electric field equation as:

$$\begin{aligned}E(x,y,z)=(A_m\cos(\kappa_m x)+B_m\sin(\kappa_m x))(C_p\cos(\kappa_p y)\\+D_p\sin\,(\kappa_p y))e^{iK_z z}\end{aligned} \tag{A-44}$$

The electric field is constrained by the waveguide such that $E=0$ at the waveguide boundaries, $x=0$, $y=0$, $x=a$, and $y=b$. These conditions imply that the cosine terms must not contribute towards the field. Therefore $A_m=0$ and $C_p=0$.

---

[13] Since $F_m(x)$ is being differentiated with respect to x and $G_p(y)$ with respect to y, the partial derivatives become full derivatives.

For the sinusoidal terms to equal 0 at the boundaries, either both B_m, and D_p equal 0, or $\kappa_m x$ and $\kappa_p y$ are both integer multiples of π. Setting both B_m, and D_p to 0 is a valid solution to the boundary value problem; it is simply the case where the is in fact no electric field. Such a scenario rather defeats the purpose of a waveguide however, so it is more informative to take the latter option, ergo:

$$\kappa_m = \frac{m\pi}{a} \qquad \textbf{A-45}$$

$$\kappa_p = \frac{p\pi}{b} \qquad \textbf{A-46}$$

The variables m and p represent integer modes of propagation. I.e. $p = 0,1,2,3 \ldots$ and $m = 0,1,2,3, \ldots.$

From equation A-39, $K_{mp}^2 = \kappa_m^2 + \kappa_p^2$. Therefore the modal wavenumber for a rectangular waveguide is:

$$K_{mp} = \sqrt{\left(\frac{m\pi}{a}\right)^2 + \left(\frac{p\pi}{b}\right)^2} \qquad \textbf{A-47}$$

By substituting equation A-47 back into equation A-32, the phase constant for a given mode is:

$$K_z = \sqrt{K - \left(\frac{m\pi}{a}\right)^2 + \left(\frac{p\pi}{b}\right)^2} \qquad \textbf{A-48}$$

If $K = \omega\sqrt{\mu\varepsilon}$, and $K_{mp} = \omega_c\sqrt{\mu\varepsilon}$, then equation A-48 can be rewritten as:

$$\omega_c = \frac{1}{\sqrt{\mu\varepsilon}}\sqrt{\left(\frac{m\pi}{a}\right)^2 + \left(\frac{p\pi}{b}\right)^2} \qquad \textbf{A-49}$$

$$K_z = \omega\sqrt{\mu\varepsilon}\sqrt{1 - \left(\frac{\omega_c}{\omega}\right)^2} \qquad \textbf{A-50}$$

Equation A-49 can be rewritten in terms of the material refractive index by noting that $\sqrt{\varepsilon\mu} = \frac{n}{c}$.

$$\omega_c = \frac{c}{n}\sqrt{\left(\frac{m\pi}{a}\right)^2 + \left(\frac{p\pi}{b}\right)^2}$$ **A-51**

The cutoff wavelength λ_c inside the waveguide is therefore:

$$\lambda_c = \frac{2\pi c}{n\omega_c} = \frac{2}{\sqrt{\left(\frac{m}{a}\right)^2 + \left(\frac{p}{b}\right)^2}}$$ **A-52**

Equation A-52 is an important result, as it demonstrates that the cutoff wavelength inside the waveguide is independent of the electrical properties of the material. This entire approach has reduced to a geometry problem concerning a simple two-dimensional standing wave. This is to be expected, since the electric field has been defined to be 0 at the block boundaries. The integers m and p therefore represent the harmonics in a fixed end standing wave.

Substituting equation A-52 into equation A-50 provides a metric for the phase term K_z that is consistent with Weir, Morrow, and others:

$$K_z = 2\pi\sqrt{\frac{n^2}{\lambda^2} - \frac{1}{\lambda_c^2}}$$ **A-53**